Global Modelling of Cloud, Convection and Precipitation Influences on Trace Gases and Aerosols

Dissertation

zur Erlangung des Doktorgrades (Dr. rer. nat.)
der Mathematisch-Naturwissenschaftlichen Fakultät
der Rheinischen Friedrich-Wilhelms-Universität Bonn

vorgelegt von
Holger Tost
aus Siegburg

Bonn, 29. März 2006

Angefertigt mit Genehmigung der Mathematisch-Naturwissenschaftlichen Fakultät der Rheinischen Friedrich-Wilhelms-Universität Bonn

1. Gutachter: Prof. Dr. Jos Lelieveld
2. Gutachter: Prof. Dr. Andreas Bott

Tag der Promotion: 19. Juni 2006

Diese Dissertation ist auf dem Hochschulschriftenserver der ULB Bonn
`http://hss.ulb.uni-bonn.de/diss_online` elektronisch publiziert.

Erscheinungsjahr: 2006

Abstract

In atmospheric chemistry modelling increasing attention has been paid to the effects of aqueous phase chemistry in the last decade. Even though wet deposition is a considerable sink in the atmospheric budgets of several trace species, it has been parameterised with highly simplified approaches. With increasing computer capacity global atmospheric chemistry and climate models have become more comprehensive allowing more detailed consideration of aqueous phase chemistry. The chemical processes within clouds and precipitation droplets do not only contribute to sinks for gas phase constituents, they can alter the chemical composition because reaction pathways can be quite different from the gas phase. Products, formed in the droplets, can be released into the gas phase and undergo reactions with other gaseous species. The droplets futhermore provide a surface for heterogeneous surface reactions. Additionally, precipitation can vertically redistribute gas phase trace species due to uptake and subsequent release back into the gas phase.
An adequate simulation of the hydrological cycle is a basic requirement for cloud and precipitation chemistry modelling. Since convective clouds cannot be resolved by the coarse grid size of global models, atmospheric convection is described with parameterisations. From a variety of available schemes for the calculation of convection, four have been selected and implemented into the atmospheric chemistry general circulation model ECHAM5/MESSy. The effects of the alternative convection schemes on the hydrological cycle and consequently on the simulated climate system have been analysed. A strong dependence of the precipitation distribution on the selected convection parameterisation has become apparent from the comparison with global observations. A similar comparison for water vapour columns obtains consistent results. The temperature distribution can be sensitively modified, resulting in substantial local average surface temperature changes, while the overall energy budget of the atmosphere is hardly affected. Generally, convection is of major importance for the distribution of trace species in the atmosphere, owing to enhanced vertical transport, the production of reactive nitrogen species in the upper troposphere by lightning, and scavenging and wet deposition. In this thesis these processes are analysed with different convection schemes and different descriptions of the scavenging process. To also address multiphase chemistry the new scavenging submodel SCAV has been developed, and has been applied in several studies under idealised as well as realistic conditions, including comprehensive gas and aqueous phase chemistry. The main factor that alters wet deposition distributions as a result of replacing the convection scheme is the modified precipitation distribution, both in the occurence and the intensity of rain events. The observed wet deposition patterns of nitrate, ammonia, and sulphate are captured accurately by the model with respect to the location and the approximate total amount. Comparisons of the model results with observed vertical profiles of trace gases show that the most comprehensive aqueous phase chemistry representation reproduces the mixing ratios and distributions of gaseous compounds most realistically.

Contents

Chapter 1

Introduction

The lower atmosphere of the Earth is a highly complex system undergoing continuous changes. It is on the one hand characterised by the effects studied in the field of meteorology, dealing with the motion and thermodynamics of air, and on the other hand by its chemical composition. The major chemical constituents are N_2, O_2, noble gases (mainly Argon), water vapour and carbon dioxide (CO_2). The first three compounds hardly participate in radiation absorption and chemical reactions in the lower atmosphere, whereas the latter two have large impact, since both contribute significantly to the greenhouse effect. Especially the increasing CO_2 content of the atmosphere, caused by anthropogenic emissions, has led to an increase of the global mean surface temperature (Houghton et al. (2001), IPCC). However, the atmosphere contains such a large amount of these two compounds that short term changes of their mixing ratio have only little effect. The changes induced by mankind in the gaseous envelope of the Earth instead lead to a higher burden of methane (CH_4), nitrious oxide (N_2O) and tropospheric ozone (O_3). After the emission restrictions of chlorofluorocarbos (CFCs) through the Montreal Protocol in 1990, which are responsible for the stratospheric ozone hole (e.g., Goodman, 2005), these three trace species gained increasing importance since they also act as greenhouse gases (e.g., Lelieveld et al., 1993; Brühl, 1993; Stevenson et al., 1998; Brasseur et al., 1998). Their combined influence is similar to the impact of CO_2.

As a feedback process, the observed temperature increase results in a higher atmospheric storage capacity for water vapour. Consequently, enhanced cloud formation and precipitation can occur. The uncertainty in the different processes causing climate change, as published in the IPCC-report (Houghton et al., 2001), includes not only the by now well known effects of the greenhouse gases, but also the effects of the atmospheric aerosol (direct and indirect effects (e.g., Ramanathan et al., 2001; Lohmann and Feichter, 2005)), for which a lower level of scientific understanding is noted. Furthermore, the effects of clouds resulting from a possible higher atmospheric burden of water vapour, which are not included in the indirect aerosol effects, are even more uncertain (Houghton et al., 2001).

A substantial fraction of all precipitation originates from convective events. The description of convection in the atmosphere goes back to Bjerkness (1938). From the 1970s on, when global modelling of the atmosphere became an increasingly important topic in atmospheric sciences, convection has been described with the help of parameterisations, i.e., the description of a subgrid-scale processes based on grid resolved quantities. Even though there has been a large development within the last 40 years (Arakawa, 2004), the problem of convection modelling is not yet solved (Randall et al., 2003). Since the occurence of more and stronger precipitation events causing floods in future due to climate change is

very likely (at least in the northern hemisphere, Houghton et al. (2001)), an adequate description of precipitation is required, not only for weather forecasting, but also for climate impact studies.

Atmospheric chemistry is generally dominated by oxidation processes that involve trace gases, i.e., compounds with low mixing ratios in the troposphere. The main oxidant is the OH radical produced mainly by the reaction of $O(^1D) + H_2O \rightarrow 2OH$ with the $O(^1D)$ originating from ozone photolysis. Nitrogen oxides (NO and NO_2, often treated together as NO_x) together with volatile organic compounds (VOCs) are important for the formation of tropospheric ozone. Additionally, the NO_x species are a main source of acidity in the atmospheric aerosol, clouds and precipitation, because they can react to nitric acid (HNO_3), which is a major component of acid rain. These nitrogen oxides are emitted naturally from soils and lightning (about 20 %) and anthropogeneously by industry and traffic (about 80 %). With growing industrialisation the anthropogenic emissions of sulphuric compounds, mainly sulphur dioxide (SO_2), which is also degassed from volcanoes into the atmosphere, led to an increased sulphur content of the atmosphere. These emissions also contribute efficiently to the acidity.

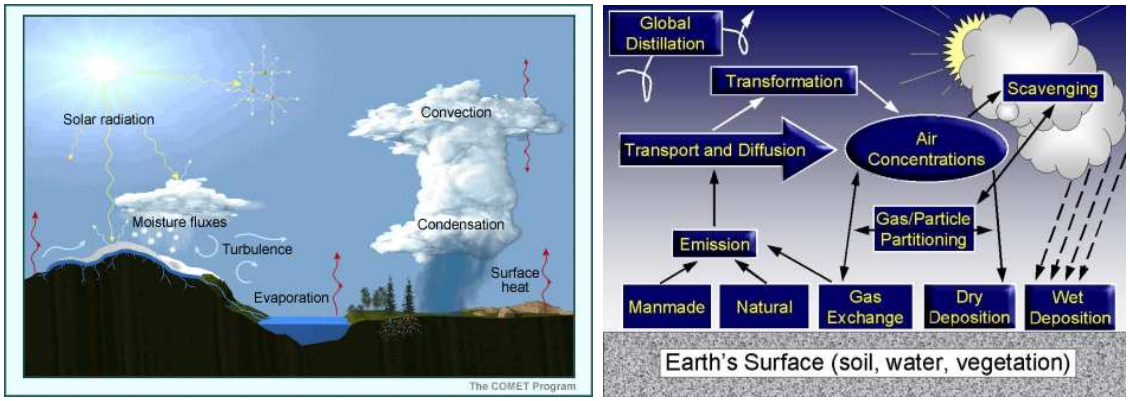

Figure 1.1: Sketch of meteorological (left, graphic from: `http://meted.ucar.edu/mesoprim/mesodefn/print.htm`) and chemical (right, graphic from: `http://www.msc-smc.ec.gc.ca/arqp/process_e.cfm`) atmospheric processes influencing trace gas budgets.

In the natural atmosphere chemical trace species are influenced by a large variety of meteorological and chemical processes, which are sketched in Figure 1.1. The left panel depicts mainly the meteorological aspects such as dynamics and turbulence and thermodynamics (energy fluxes, cloud processes), while the right one highlights the direct interactions among compounds (chemical reactions) and with the environment (photolysis, emission, and deposition).
Generally, the atmosphere reacts on a large scale to a change in a trace gas constituent, since many trace species interact with each other through rapid transport and mixing processes. Even if there is no direct connection between them, there may be an indirect coupling by common reaction precursors or products. An analysis of individual reactions and the interactions of single compounds is possible in a laboratory under controlled conditions. However, in the real atmosphere only measurements of the atmosphere as a whole entity, i.e., of individual species given the mixing ratios of all species and meteorological

parameters, can be performed. Therefore, observations are sometimes ambigious. Since a variety of processes influences the individual trace gas budgets, studies involving several processes together, but analysing their effects separately, can only be performed with computer model simulations of the atmosphere. Furthermore, only with computer models feedback studies of individual processes can be performed. However, measurements are required for testing and verifying the model results.

The role of clouds in atmospheric chemistry has been investigated in detail for almost two decades. The environmental problems arising from liquid phase chemistry, mainly acid rain and fog, were more serious in the 1980s and early 1990s; but even though they are no longer in the public media, the problems which they are causing are still not solved. Acid deposition results mainly from the dissolution of sulphuric and nitric acid. With increasing industrial emissions, the atmospheric load of these species has become higher, resulting in increased acid deposition. The first occurence of acid rain and its relationship with industrial pollution has been determined in 1852 in England, when Angus Smith analysed the chemical composition of rainwater and found a high sulphate content in a region with heavy industry. A notorious event of acid fog occured in London in December 1952 (Wilkins, 1954), when the meteorological situation has been characterised by foggy conditions, that together with the smoke from coal burning industries with high sulphur content led to sulphuric acid formation. This resulted in disasterous conditions, later on referred as London-type smog, causing the immediate death of more than 4000 people. After the rapid determination for the reasons for these conditions and the further increase of the industrial emissions it has been concluded that acid deposition is an international problem. Consequently, 1979 the 'Long-Range Transboundary Air Pollution Treaty' has been signed in Europe and reverified in 1983. In the following years several protocols have been signed to reduce the emissions of sulphur and nitrogen oxides. In eastern Asia, these reductions have been hardly considered in the last century, but from the year 2001 onwards at least continous measurements have been performed. However, the environmental damage dealt by acid rain is tremendous, affecting forests, lakes and swamp regions, but also the structure of buildings and human health. This damage did not only occur close to the pollution emission sources, but even long distances away, e.g., in Scandinavia the emissions are relatively low, but the transport of pollutants from England and other countries substantially contributes to acid deposition and the destruction of forest and lake ecosystems.
Additionally, the effect of cloud and precipitation chemistry might be important for another type of atmospheric pollution, i.e., photo-smog, resulting from the high emissions of VOCs leading to high ozone (O_3) surface concentrations under high NO_x conditions. Ozone is a toxic agent, affecting plants and also human health (e.g., Mauzerall et al., 2005; Bates, 2005). However, the influence of these processes on ozone is still not determined, since the previous studies came to ambigious conclusions. For instance, Lelieveld and Crutzen (1991) assigned a large importance for ozone to liquid phase chemistry in contrast to Liang and Jacob (1997), who deduced a minor impact. By now, only very few studies exist (e.g., Dentener, 1993), in which the cloud and precipitation chemistry is treated in detail on the global scale.
The increasing burden of aerosol particles in the atmosphere (e.g., Huebert et al., 2003), most pronounced in East Asia, substantially decreases the visibility and air quality. Additionally, the aerosol particles have a major impact on human health (e.g., Kaiser, 2005). The particles originate both from natural (dust) and anthropogenic (nitrate, sulphate)

sources, while the first supply reaction surfaces for the latter (Sun et al., 2005). Both, soluble and insoluble aerosol particles are removed from the atmosphere efficiently by clouds and precipitation, providing an additional process of anthropogenic pollution and its interactions with the liquid phase in the atmosphere.

1.1 Convection in the atmosphere

Convection plays a major role in the global meteorology of the Earth's atmosphere, even though it is mostly a small scale phenomenon. Single convective clouds are usually not larger than about 25 km^2, and non precipitating cumulus clouds not larger than a few km^2. The process of convection stabilises the atmosphere, i.e., it changes the energy distribution and affects the stratification within the atmosphere by exchange of air masses and latent heat. Strong convection is usually accompanied by precipitation. In the tropics most of the precipitation results from convection, but also in the midlatitudes a significant fraction of the total amount of precipitation originates from convective events.

Convection occurs almost everywhere in the Earth's troposphere. The most important regions for convection are the tropics, especially the Inner Tropical Convergence Zone (ITCZ). Here large cumulonimbus tower-like clouds are formed, regularly reaching up to the top of the troposphere. They can occur as single cells, but also in organised forms (multicells, squall lines). The causes for the strong convection are relatively high temperatures near the surface, strong evaporation (i.e., high content of water vapour in the atmosphere) and the resulting large fluxes of latent heat from the surface into the atmosphere. These can destabilise the atmosphere leading to the exchange of air resulting in convection. Other important regions for convection are the midlatitude storm tracks. In these mean flow patterns the air is often mixed from different sources with different moisture contents, also leading to a possible destabilisation of the atmosphere. Additionally, extratropical cyclones are generally characterised by frontal systems. These fronts can force the quick lifting of air, leading to condensation, and thus being a trigger mechanism for convective activity. Therefore, both the convection and the synoptic scale processes contribute to the precipitation formation.
In Figure 1.2 the circulation of one hemisphere (e.g., the northern hemisphere) is sketched. There are two convergence zones, first the ITCZ close to the equator and second in the midlatitudes where warm air currents from the subtropical regions meet cold air masses from the polar regions. These are the two major regions where strong convection occurs. In the subtropics at around 30° there is a strong downward motion of air effectively suppressing convective activity.
The ITCZ is the region with the strongest convection, being part of a larger scale phenomen, the Hadley circulation. This circulation is characterised by the transfer of heat from the tropics (highest incoming radiation leads to heat source) in the upper troposphere, and the transport of moisture in the lower troposphere towards the equatorial regions (e.g., Trenberth and Stepaniak, 2003). Due to the high moisture content the atmosphere tends to be conditionally unstable. The Hadley cell is a symmetrical phenomenon in both hemispheres with the ITCZ at its center. According to the convergent flow of air and the moisture transport into the ITCZ from both hemispheres convection is triggered. As mentioned above, convection occurs in a conditionally unstable atmosphere, and because of the transport of heat into the middle and upper troposphere and the drying

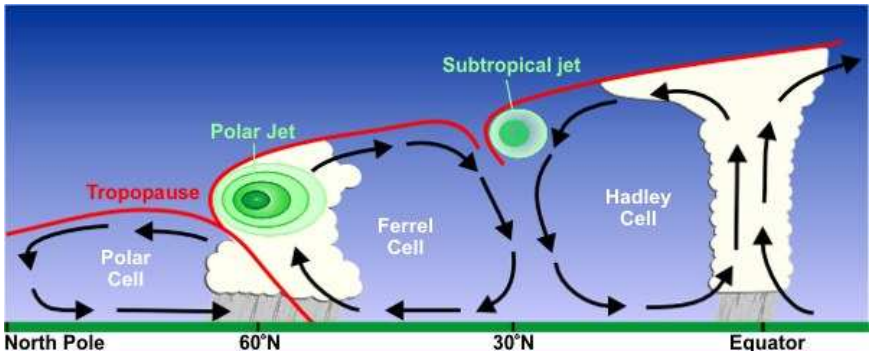

Figure 1.2: Sketch of the circulations of the northern hemisphere (graphic from: `http://www.srh.weather.gov`)

by precipitation in the convective clouds, the atmosphere is 'on average' pushed towards a so-called 'radiative-convective equilibrium state' (Manabe and Strickler, 1964).
Since convective clouds in the tropics occur in regions with the highest incoming solar radiation and additionally tend to spread out over large areas in their anvil regions, they are important for the radiation budget of the atmosphere (Fu et al., 1995).
Convection is known for creating gravity waves that propagate through the troposphere into the stratosphere (Eitzen and Randall, 2005), where these waves can influence the flow patterns. In the troposphere the gravity waves can act to reduce convective activity, but also trigger new convective events. Mapes (1993) found that there is an organisation of convective cells, originating from these gravity waves. This is proven valid and quantified by Liu and Moncrieff (2004).
In the midlatitudes the role of convection is still uncertain. Stensrud and Anderson (2001) discuss the forcing of midlatitude convection by the mean flow and the feedback on the flow itself, but do not come to an unambigious answer whether convection is responsible for characteristics of the mean extratropical flow. Over the South American continent the influences from both tropical convection and frontal systems contribute significantly to the variability of convective events in that region (Siqueira and Machado, 2004, and references therein).

The process of convection in the atmosphere has been described since several decades. The basic aspects can be reviewed from parcel theory. The simplest way of understanding this process is considering a bubble of warm air. The most important aspect of convection is that this bubble is warmer than the surrounding air. This might result from various sources, e.g., differential heating, because of different soil albedo, evaporation, orographically forced lifting, lifting forced by air currents in frontal systems, etc.. Because of its higher temperature and because the pressure of an air parcel is in rapid equilibrium with its surroundings (due to the expansion of sound waves) the air has a lower density (ideal gas law):

$$\rho = R \cdot T/p, \tag{1.1}$$

with p denoting the pressure, T the air temperature, R the gas constant and ρ the air density. Therefore it is buoyant and wells up. During its ascent it finally reaches a point in the atmosphere where this buoyancy is balanced by the gravitational force and no further lifting occurs.
An additional aspect to consider is that this air 'parcel', as it is usually called, mixes with

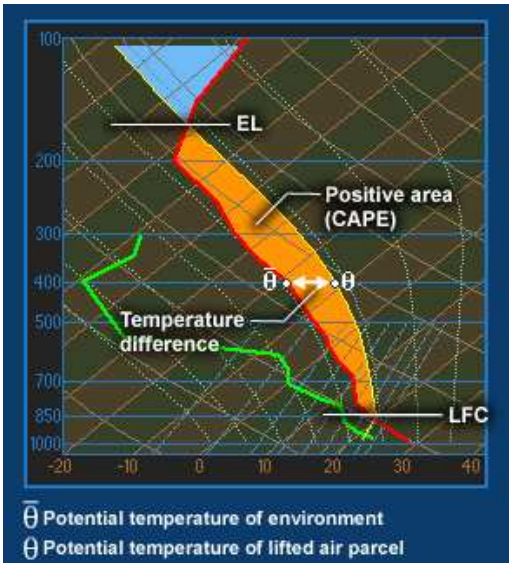

Figure 1.3: Vertical temperature profiles of an air parcel (yellow line), the environment (red line), and the humidity (green line) on Skew-T-Diagram. The orange area represents the CAPE (see text and Equation 1.2)(graphic from: `http://meted.ucar.edu`).

surrounding air. It entrains air from the environment around the parcel and together with air molecules also water vapour and trace gases. Therefore the air parcel can change its composition and water content.
It is important to recall that this is a very simplified view of the events occuring in deep convection and that the reality is much more complex (e.g., Warner, 1970; Baker et al., 1980; Doswell and Markowski, 2004).
Usually one differentiates between shallow and deep convection. The major difference is the height of the convective cloud tops and their vertical extension. Shallow and also shallow mid-level convection, i.e., convection that has its cloud base at higher altitude, usually consist only of small clouds, with a vertical extension of not more than 1 km, while deep convection results in high cumulonimbus cloud towers with their tops at a maximum height of up to 16 km in the tropics.
The other major difference is the production of precipitation: shallow convective clouds are usually non-precipitating, while deep convection is able to produce large amounts of precipitating water.
This difference, the efficient production of liquid water and ice, is responsible for the development of the individual types of convective clouds. With the idealised parcel theory the process can be described as follows (see Figure 1.3, where the yellow line depicts the temperature of the parcel and the red one of the environment). If an initially cooler air parcel is forced to rise, it will expand and therefore cool (its temperature following the yellow line). Since the air parcel is only slowly diluted compared to the upward air motion, it still contains most of the water vapour from its original source. With decreasing air temperature the saturation mixing ratio for water vapour can be reached and the water condenses. This results in a release of latent heat which additionally warms the air parcel and therefore increases its bouyancy. Due to this process the upward motion can continue. Above the crossing of the yellow and the red line, which is called the level of free convection (LFC), the parcel is buoyant relative to the environment and rises spontaneously. In this

example sounding the air parcel needs an external forcing to start its ascent because it is colder than the environment in the boundary layer.
If the temperature decreases further the freezing point of water is reached and the liquid water starts to freeze or the water vapour directly condenses onto ice crystals. The freezing enthalpy is an additional source of latent heat. A fraction of the liquid and frozen water precipitates. The upward motion is finally stopped if the surrouding air temperature decreases more slowly than the temperature of the air parcel or is even constant. This happens if the surrounding air shows an inversion in the temperature profile: it can be the inversion at the top of the planetary boundary layer (common for shallow convection), but finally all convection will stop at the strong inversion at the tropopause. As can be seen from Figure 1.3 this happens close to the 200 hPa isosurface. Even though in shallow convection the condensation and consequently cloud formation also takes place, the released energy is not sufficient for the air parcel to reach the LFC. Consequently, the convection does not become deep, but the ascent is stopped by the stable temperature profile.
A quantification of the strength of convection based on the stability of the atmosphere can only be determined theoretically. A common measure is CAPE (**C**onvective **A**vailable **P**otential **E**nergy) in J/kg which can be calculated from:

$$CAPE = \int_{LFC}^{ETL} \frac{T_v^u - T_v^e}{T_v^e} g dz. \tag{1.2}$$

In this equation LFC is the 'level of free convection', the altitude from where the parcel can rise from its own buoyancy, ETL the 'equilibrium temperature level' (also known as equilibrium level (EL) or level of neutral buoyancy (LNB)), where parcel temperature and environment temperature are equal, T_v^u is the virtual temperature of the upward moving parcel, and T_v^e the virtual temperature of the environment. By using the virtual temperature T_v ($T_v \approx (1 + 0.61q)T$) with T the temperature and q the specific humidity, the influence of humidity on the parcel density can be considered. Graphically CAPE can be interpreted as the orange region between the yellow and red line in Figure 1.3.
An additonal process necessary to consider is the formation of downward moving air, originating from the evaporation of some of the precipitating water. This evaporation requires heat, and therefore the air is cooled. If it is cooler than the environment, the air becomes negatively buoyant and starts sinking.

1.2 Scavenging and aqueous phase chemistry

The process of scavenging desribes the uptake of gas phase and aerosol species into cloud and precipitation droplets and snow/ice crystals. As a direct consequence of the uptake a fraction of the scavenged species is deposited to the surface by precipitation. Therefore, wet deposition and scavenging must be treated together in one common approach. In the budget of a chemical species c this is usually described by one term:

$$\begin{aligned}\left(\frac{\partial c}{\partial t}\right)_{total} &= \left(\frac{\partial c}{\partial t}\right)_{advection} + \left(\frac{\partial c}{\partial t}\right)_{convective\ transport} \\ &+ \left(\frac{\partial c}{\partial t}\right)_{gasphase\ chemistry} + \left(\frac{\partial c}{\partial t}\right)_{emission} \\ &+ \left(\frac{\partial c}{\partial t}\right)_{dry\ deposition} + \left(\frac{\partial c}{\partial t}\right)_{scav/wet\ deposition}\end{aligned} \tag{1.3}$$

Additionally, the release of species from the droplets/crystals has to be taken into account, either during evaporation or as an equilibrium process (see next paragraph).
Taking into account the process of scavenging in global chemistry climate modelling is very important, because it has many direct and indirect effects:

- Large sink term in the budget of many trace gases and aerosols of the atmosphere;
- The oxidation of reduced and partly oxidised gases, leading e.g., to the production of acid rain;
- Chemical composition of the cloud condensation nuclei influences precipitation formation;
- Aqueous phase chemistry can alter the mixing ratios of gas phase consituents by both alternative reaction pathways, and by providing sources and sinks of reactants.
- Vertical re-distributions of species.

These processes do not only depend on the properties of the species that are scavenged (solubility, chemical reactivity in the liquid phase, i.e., reaction rate coefficients, available chemical reaction partners, i.e., mixing ratios in both gas and liquid phase), but also of those of the scavenger (droplet size, shape and number, concentrations of dissolved species, liquid water content). This results in a large number of required input values to describe this process properly. However, some of these can be parameterised, especially for the microphysical parameters, or are well documented in the literature (e.g., reaction rates).

1.2.1 Henry's law

Clouds and precipitation can contain of a considerable amount of liquid water. According to Henry's law

$$[A]_{aq} = K_H p_g \tag{1.4}$$

after an infinite time the gas phase concentration of a species can be assumed in equilibrium with the concentration in the liquid phase. Therefore a fraction of the gas phase species will be transferred into the liquid. In this equation $[A]_{aq}$ denotes the liquid concentration of a species A, K_H the Henry coefficient of that species and p_g the partial pressure of that species in the gas phase.
The detailed treatment of this process is described in Section 6.2.1. Since in Equation 1.4 the gas phase as well as the aqueous phase content of a species are used, the equilibrium is dependent on concentration changes due to gas phase and liquid phase chemistry. For instance, if a chemical reaction takes place that effectively decreases the aqueous phase

concentration, the effective uptake increases. This effect is discussed in Section 1.2.2.1. The droplets, in which the chemical gaseous species can be taken up, can vary in size by orders of magnitude, from cloud droplets with an approximate radius < 20 μm to rain droplets with a radius of up to several mm.

1.2.2 On aqueous phase chemistry

Since the transition of gas phase species into the droplets depends on the concentration in the liquid phase, aqueous phase chemistry determines the scavenging potential. Two different types of reactions are of main importance:

1. Acid - Base - Equilibria;
2. Redox - Reactions.

The theories of these reactions can be found in common textbooks of chemistry in liquid solutions (e.g., Riedel, 1999). In addition, other reactions, e.g., the heterogeneous reactions on surfaces or photolysis reactions in the liquid phase, are possible, too (see Section 1.2.2.3). The importance of aqueous phase chemistry for the atmosphere has been reviewed by Jacob (2000).

1.2.2.1 Acid - Base - Equilibria

These reactions describe the deprotonisation of an acidic species in a water containing solution and do not include any electron transfer, i.e., the oxidation numbers of any atom in the participating molecules do not change. The reaction can generally be described by:

$$\mathrm{HA} + \mathrm{H_2O} \rightleftharpoons \mathrm{H_3O^+} + \mathrm{A^-}. \tag{1.5}$$

In this equation HA denotes a proton donating acid with H as the proton and A the residual base. Together with water (H_2O) a positively charged Hydronium - Ion (H_3O^+) and a negatively charged anion of the base are formed in the solution. These ions are stabilised by a surrouding cluster of water molecules. On the other hand an alkaline component B reacts with water as a proton acceptor according to:

$$\mathrm{B} + \mathrm{H_2O} \rightleftharpoons \mathrm{OH^-} + \mathrm{HB^+}. \tag{1.6}$$

Since water itself can act either as an acid or a base, a neutralisation reaction in droplets is always possible.

$$2\mathrm{H_2O} \rightleftharpoons \mathrm{OH^-} + \mathrm{H_3O^+}. \tag{1.7}$$

Since not every acid and base have the same strength of dissociation, each follows an individual dissociation equilibrium. A list with the applied dissociation coefficients can be found in Appendix C. Additionally, each dissociation reaction is linked via the H_3O^+-ion concentration, e.g. if there is an acid with high dissociation tendency and one with a low one, the one with the low one will dissociate only to a smaller fraction as if it is the only acid in the solution. In descriptions of chemical reactions usually only H^+ is used (also in this thesis), even though in the solution only H_3O^+-ions exist. A common measure for the H_3O^+-ion concentration is is the pH - value, defined as follows:

$$\mathrm{pH} \;=\; -\log_{10}\left[\mathrm{H_3O^+}\right]_{\mathrm{aq}}. \tag{1.8}$$

The most abundant acidic species in the atmosphere is carbon dioxide (CO_2). In the aqueous phase it dissociates:

$$\begin{aligned} CO_2 + H_2O &\rightleftharpoons H^+ + HCO_3^- \\ HCO_3^- &\rightleftharpoons H^+ + CO_3^{2-}. \end{aligned} \tag{1.9}$$

Even though carbonic acid is a relatively weak acid, it leads to an average pH - value of cloud and precipitation water of about 5.5 (in equilibrium state of unpolluted air and droplets) and is therefore a source of 'natural' background acidity. Dissociation of stronger acids like nitric acid (HNO_3) or sulphuric acid (H_2SO_4) result in much lower pH - values. For these acids the dissociation equilibrium is almost complete on the side of the dissociated products. One aspect to consider is the buffering effect of the weak acids. If the solution becomes more acidic than the equilibrium value for CO_2, the effective pH - value does not change much at the beginning. First the equilibrium 1.9 is shifted towards the production of CO_2 which is released to the gas phase. If the acidification is too strong the same will happen also to other weak acids, e.g., formic acid (HCOOH) or acetic acid (CH_3COOH). Even the strong hydrochloric acid can act as a buffer as shown by Kerkweg (2005) for liquid aerosols, releasing HCl to the gas phase.
Neutralisation of the acidic species in the atmosphere mostly originates from ammonia emissions. Even though NH_3 is only moderately soluble, in an acidic solution it dissociates into ammonium:

$$NH_3 + H_2O \rightleftharpoons OH^- + NH_4^+ \tag{1.10}$$

The produced OH^- reacts with H^+ according to Equation 1.7 to water. Thus Equilibrium 1.10 is pushed towards the side of the products (principle of LeChatelier). When no acids or much more ammonia than acidifying compounds are available Equation 1.10 can lead to even higher pH values than 7 (neutrality).
An additional source of alkalinity for clouds and precipitation is the scavenging of freshly emitted sea salt aerosol containing hydrogen carbonate compounds (e.g., Kerkweg, 2005; von Glasow et al., 2002a,b).

The dissociation equilibria also determine the phase transfer of species, as mentioned in section 1.2.1, e.g., due to the almost complete dissociation of HNO_3 the effective concentration of HNO_3(aq) is close to zero, resulting in an almost complete uptake from the gas phase. Only if the solution becomes very acidic, the dissociation comes to an equilibrium resulting in a constant HNO_{3aq} concentration, that limits the uptake. This is even more important for species of only moderate solubility, e.g., NH_3. Because of Equation 1.10 the NH_3(aq) concentration in acidic droplets is very low, resulting in a very efficient uptake of ammonia into acidic droplets according to Equation 1.4.

1.2.2.2 Redox - Reactions

For these reactions there is no general description possible. The aspect they have in common is that one participating reagent is reduced while another one is oxidised (Redox). Therefore in these reactions, there is a change of the oxidation numbers of at least two reacting atoms. A large variety of reactions exist with their reaction speed determined by the potential difference of the reacting compounds.
In this work one of the main aspects is the oxidation of sulphuric components. These

mainly originate from SO_2. The oxidation of this component by the OH radical (the main reaction partner) in the gas phase is rather slow and therefore only of minor importance (Warneck, 1999). In the aqueous phase, however, this species first reacts as an acid, which then can be oxidised at much higher rate by H_2O_2 and ozone:

$$\begin{aligned} SO_2 + H_2O &\rightleftharpoons H^+ + HSO_3^- \\ HSO_3^- &\rightleftharpoons H^+ + SO_3^{2-} \\ HSO_3^- + H_2O_2 &\rightarrow HSO_4^- + H_2O \\ HSO_3^- + O_3 &\rightarrow HSO_4^- + O_2 \end{aligned} \tag{1.11}$$

This reaction path is much faster and leads to sulphate formation in the droplets. Interactions between nitrate and sulphate occur in the solution as well as reactions containing organic species. Even reactions with transition metals take place in the droplets, but they will not be considered in this study. A complete list of the considered Redox reactions can be found in Appendix C.

1.2.2.3 Additional types of reactions

Heterogeneous reactions on the surface of droplets are also of importance. The best understood important example is the conversion of gaseous N_2O_5 on the droplet surface into nitrate, that is dissolved in the droplet according to:

$$N_2O_5 \downarrow + H_2O \rightarrow 2\ H^+ + 2\ NO_3^- . \tag{1.12}$$

Additionally, photolysis reactions can occur in the liquid phase. Due to the multiple scattering and reflection of photons it is assumed that the effective photolysis rates are higher than the equivalent rate would be in the gas phase. Therefore, as commonly done in aqueous phase chemistry models (e.g., von Glasow et al., 2002b), photolysis rates are multiplied by a factor according to the work of Ruggaber et al. (1997).

1.2.3 Aerosol scavenging

The scavenging of aerosol particles can usually be divided into two parts: the activation of soluble aerosol particles and their subsequent growth to cloud droplets, which is known as 'Nucleation Scavenging' (NS) and the incorporation of soluble and insoluble aerosol particles in falling precipitation, known as 'Impaction Scavenging' (IS). Both processes will be explained in detail in Section 6.2.2.

1.3 Thesis structure

This thesis is divided into two parts. The first one deals with convection and its parameterisations in global models, and the second one with scavenging, aqueous phase chemistry and wet deposition. Both topics are closely linked, since deep convection is usually characterised by strong precipitation events.
The scavenging is dependent on the precipitation distribution. In contrast to a box or column model in which the precipitation can be used as a prescribed input value, in global model studies of scavenging and aqueous phase chemsitry an accurate description of the

rainfall patterns is a requirement. Since some weaknesses in the precipitation distribution of the general circulation model ECHAM5 (Roeckner et al., 2003, 2004) have been analysed in a previous study (Hagemann et al., 2006), a replacement of the convection parameterisation, responsible for a part of the precipitation formation, is an attempt to either improve the rainfall distribution or at least to systematically determine the uncertainties originating from this process. Since generally the use of parameterisations implies several simplifications, the impact of these can be analysed.
Several other processes in global atmospheric chemistry modelling are linked to the results from the convection parameterisations.

1. The convective clouds are characterised by strong upward motion, resulting in an effective transport mechanism in the troposphere. The strength of this transport is difficult to determine absolutely. However, applying several convection parameterisations uncertainties in the transport processes can be addressed directly. Since the convective mass fluxes are not accessible by observations, the transport of tracers, e.g., ^{222}Rn, provides a good possibility for the analysis.

2. The parameterisation of lightning activity is essential for the NO_x modelling, because it causes in situ production of NO in the upper troposphere due to the high temperature of the flashes. However, the flashes cannot be resolved explicitely. Therefore the frequency is calculated either from the convective cloud top height, the updraft velocity or the convective precipitation formation.

3. The nucleation and impaction scavenging of trace species are highly dependent on the available convective cloud and precipitation water. This affects not only the mixing ratios of the compounds themselves, but also the vertical transport, especially for soluble compounds.

This thesis is structured as follows: Chapter 2 briefly describes the Atmospheric Chemistry General circulation Model (AC-GCM) ECHAM5/MESSy applied. In Chapter 3 the issue of convection parameterisations is analysed and the results of several simulations with alternative convection schemes are presented. The transport of trace gases is addressed in Chapter 4. Simulations of global lightning distributions are briefly analysed in Chapter 5, taking into account the uncertainties arising from the convection parameterisations. The main focus of Chapter 6 is on scavenging, aqueous phase chemistry and wet deposition, divided into three parts. First, a description of the newly developed comprehensive scavenging scheme (see Section 6.2 and Tost et al. (2006)) is given, followed by an application of this scheme under idealised atmospheric conditions (Section 6.3) and an application of this scheme under realistic atmospheric conditions (Section 6.4). Final remarks, conclusions and an outlook are presented in Chapter 7.

Chapter 2

Model description

2.1 ECHAM5

The General Circulation Model (GCM) ECHAM, developed at the Max Planck Institute for Meteorology (MPI-MET) in Hamburg, Germany, is originally based on the weather predicition model of the European Centre for Medium-range Weather Forecasts (ECMWF) in Reading, United Kingdom. The modifications implemented at the MPI-MET aim at the transformation into a climate model. The version 5.3.01 of this model (further denoted as ECHAM5 (Roeckner et al., 2003)) is used and extended at the Max Planck Institute for Chemistry (MPI-C) in Mainz, Germany. The climate model simulates the dynamics and thermodynamics of the atmosphere. At the MPI-C ECHAM5 has been combined with the Modular Earth Submodel System (MESSy) (Jöckel et al., 2005). MESSy mainly deals with either questions of atmospheric chemistry or extend the ECHAM5 model, both by coupling of the chemical processes to the dynamics or extending the model physics with respect to aspects that are relevant for investigations of atmospheric chemistry.
Simulations with ECHAM5 can be performed in several resolutions. As the dynamical core calculations are performed in spectral space, the resolution is defined by the triangular truncation of the waves. The coarsest applicable resolution is T21 (T for the triangular truncation) which corresponds to a grid box size of about 5.6 x 5.6 degrees. Technically, every truncation is possible, but only some designated are used. These range from T21 to T159. Higher resolutions are possible, but rarely used for application in a climate model. The vertical coordinate is a hybrid pressure grid, which uses terrain-following levels close

Resolution	Number of Boxes lon x lat	approximated Box Width ° x °	approximated Box Width km	Time Step s
T21 L19	64 x 32	5.6 x 5.6	621	2400
T31 L31	96 x 48	4.2 x 4.2	467	1800
T42 L31	128 x 64	2.8 x 2.8	311	1200
T63 L31	192 x 96	2.1 x 2.1	233	720
T85 L31	256 x 128	1.4 x 1.4	156	480
T106 L31	320 x 160	1.1 x 1.1	122	360
T159 L31	480 x 240	0.7 x 0.7	81	180

Table 2.1: The standard resolutions of the ECHAM5 model for tropospheric studies.

to the surface, and constant pressure levels for the upper troposphere and stratosphere. Standard vertical resolutions cover 19, 31 or 60 levels for tropospheric model simulations up to a height of 10 hPa. Additionally, a middle atmosphere mode of ECHAM5 (MA-ECHAM5) is selectable with 39 or 90 layers reaching up to 0.01 hPa. The time step length for the model simulations is dependent on the horizontal and vertical resolution to fulfill the Courant-Friedrich-Levi criterion and can be seen from Table 2.1 for the tropospheric resolutions.
For numerical reasons a semi-implicit time integration scheme with two time levels, the so-called 'leapfrog scheme', is applied. Prognostic variables calculated with the set of primitive equations for a moist atmosphere are temperature, divergence and vorticity, the logarithm of the surface pressure, and water vapour, cloud water and cloud ice. Advection is performed with a semi-lagrangian flux form scheme (Lin and Rood, 1996), but other advection algorithms are additionally available in the ECHAM5 model. This advection algorithm has the advantage of being mass conserving by definition, but the application on the ECHAM5 vertical grid may cause small errors as described by Jöckel et al. (2001). The microphysical and moist processes of large scale condensation and convection of the ECHAM5 model will be explained later in detail because they are of special importance within this work and also part of MESSy submodels.
More detailed information about the ECHAM5 model can be found in Roeckner et al. (2003) and on the ECHAM5 website of the MPI-MET[1].

2.2 MESSy

2.2.1 Overview

The Modular Earth Submodel System (MESSy), developed at the MPI-C, with contributions from the Deutsches Zentrum für Luft und Raumfahrt (DLR), has been described in detail by Jöckel et al. (2005). The fundamental idea is to build up a comprehensive Earth System Model in a highly structured, modularised way. With the same structure many different scientific tasks within the Earth system can be adressed. The currently implemented processes focus mainly on the atmosphere, comprising emissions, atmospheric chemistry, transport mechanisms and diagnostic tools. MESSy is generally structured into four layers: the base model layer (BML), consisting of the base model, which is currently the GCM ECHAM5. The second layer is the base model interface layer (BMIL), which includes the central management interface of the MESSy submodels and the data interface that collects the required data for each of the individual submodels and allows the exchange of data within the submodels. Additionally, the data import interface is part of this layer. The submodels are included in the third and the fourth layer: the submodel interface layer (SMIL) and the submodel core layer (SMCL). The SMIL comprises the internal procedure for the submodels, e.g., the call of individual routines contained within a submodel, and the internal data handling for each individual submodels, e.g., unit transformations. In addition to this the communication via the BMIL is coordinated for each submodel individually within the SMIL module of the respective submodel. The fourth layer, the SMCL, contains the main calculations of each submodel independently of the the layers above, e.g., they can be applied for a box model as well as for a GCM as a base model. The data transfer, i.e., the results of the SMCL routines, is only allowed via the submodel interface and from there the results can be accessed via the MESSy data

[1] `http://www.mpinet.mpg.de/en/extra/models/echam/echam5.php`

interface.
The present MESSy version 1.1. was released in January 2006. The system is currently undergoing an extensive evaluation process (Jöckel et al., 2006). The model studies in this work are performed with an extended version of the evaluation version ECHAM5/MESSy 1.1.

Table 2.2: List of MESSy submodels currently available in MESSy-version 1.1. Submodels used in this study are in bold face. People responsible for the respective submodels are from MPI-C, contributions of other institutes are listed in footnotes.

Submodel Name	Function	Responsible
AIRSEA	air-sea exchange over oceans	A. Pozzer
CLOUD[a]	CLOUD model	H. Tost
CONVECT[b]	CONVECTion model	H. Tost
CVTRANS	new ConVective tracer TRANSport	H. Tost
DRADON	^{222}Rn (diagnostics)	P. Jöckel
DRYDEP	DRY DEPosition of gases and aerosols	A. Kerkweg
EMDEP	EMissions and DEPosition	L. Ganzefeld
H2O	stratospheric H_2O and feedback	C. Brühl
HETCHEM	HETerogeneous CHEMistry (reaction rates)	B. Steil
JVAL	calculates J-VALues	R. Sander
LNOX	Lightning NO_x	P. Jöckel
M7[c]	Modal aerosol model	A. Kerkweg
MECCA	calculation of gas phase chemistry	R. Sander
MECCA-MBL	calculation of aerosol phase chemistry	A. Kerkweg
OFFLEM	OFFLine EMissions	P. Jöckel
ONLEM	ONLine EMissions (gas and aerosol)	A. Kerkweg
PHOTO	calculation of PHOTOlysis rate coefficients	C. Brühl
PSC	Polar Stratospheric Clouds	J. Buchholz
PTRAC	Passive TRACer (diagnostics)	P. Jöckel
QBO[d]	'Quasi Biannual Oszillation' nudging	P. Jöckel
SCAV	SCAVenging and wet deposition of gases and aerosols	H.Tost
SEDI	SEDImentation of aerosols	A. Kerkweg
TNUDGE	Tracer NUDG(E)ing	P. Jöckel
TROPOP	diagnostic of TROPOPause and boundary layer height	P. Jöckel

[a] the original routines have been part of ECHAM5
[b] some of the routines have originally been part of ECHAM5
[c] original box model from Vignati et al. (2004), see section 2.2.2.5
[d] original code from MPI-MET

In Table 2.2 an overview of the available submodels is presented. For the present work not all of them were required and used. Therefore only the used submodels (bold in the table) will be explained in detail in the next section.
As a major part of this thesis four new submodels were developed, either by the development and implementation of a new process description, or by modifying existing code. These are the submodels CLOUD, CONVECT, CVTRANS and SCAV.

CLOUD covers the calculation of the large-scale microphysical properties and cloud cover (see Section 2.2.2.8).
CONVECT, as described in Section 3.2, deals with the topic of convection and the implementation of several convection parameterisation schemes.
CVTRANS addresses the transport of trace species within the convective clouds and is described in Section 4.2.
SCAV, explained in detail in Tost et al. (2006) and Section 6.2, contains a parameterisation of scavenging and wet deposition of trace gases and aerosols in clouds and precipitation. Additionally, cloud and precipitation chemistry can be calculated.
Currently, MESSy is connected to ECHAM5, which is further denoted as ECHAM5/MESSy. More information can be found on the MESSy website[2] and in the literature (Jöckel et al., 2005).

2.2.2 MESSy - Submodels

2.2.2.1 MECCA - The Gas Phase Chemistry Submodel

The gas phase chemistry in MESSy is calculated with MECCA (Module Efficiently Calculating the Chemistry of the Atmosphere). It has been developed by Sander et al. (2005). The basic entity of this submodel is a box, and the implementation in a three dimensional global model is straightforward.
MECCA consists of a coupled set of differential equations automatically coded and solved by the Kinetic PreProcessor (KPP) (Damian et al., 2002). The species and reactions to be considered have to be selected before the simulation. The user can choose from a wide range of chemical compounds and their reactions. All of these are selectable from an equation set that describes stratospheric chemistry following Steil et al. (1998) (ECHAM4/CHEM), and tropospheric chemistry including Non-Methane HydroCarbon (NMHC) species following von Kuhlmann et al. (2003). Additionally, sulphur and halogen chemistry from von Glasow et al. (2002b) is included. Kerkweg (2005) added the option to calculate liquid phase aerosol chemistry on a prognostic aerosol distribution, but this is not used in this work. The reactions to be considered for a specific model simulation are selected from the comprehensive chemical equation set with an automated shell-script. Therefore the MECCA submodel can be applied to a wide range of tasks in the field of atmospheric chemistry.
Each chemical reaction requires a rate coefficient that can be dependent on meteorological and chemical parameters, e.g., temperature, pressure, concentration of a species X. All required values are collected and the rate coefficients are calculated before the chemical integration.
Photolysis reactions require the photolysis rate for the individual species that have to be imported from another submodel which calculates these rates (currently JVAL or PHOTO, see Section 2.2.2.3).
Simplified heterogeneous chemistry on aerosol surfaces can be considered in addition. The reaction coefficients for those reactions are calculated in the HETCHEM module which uses very simplified assumptions for describing the aerosol properties. This approach is less detailed than the aerosol chemistry of Kerkweg (2005) for the sake of higher computational efficiency.
The chemical integration is performed within the KPP generated code. It requires a nu-

[2] `http://www.messy-interface.org`

merically stable integration method. Tests by Sandu et al. (1997a,b) have shown that Rosenbrock solvers are suited best for this task. Since the same integration method is used in the SCAVenging submodel, this will be explained in detail in Section 6.2.
More details about the MECCA submodel can be found in Sander et al. (2005), the electronic supplement therein, or on the MECCA website[3]. A list of the chemical gas phase reactions used in this work can be found in Appendix D.

2.2.2.2 Radiation

The radiation routines of ECHAM5 have been adapted and slightly modified in the submodel RAD4ALL (B. Steil, unpublished, see also the MESSy-website[4]). The original code is as well selectable as an interactive coupling to trace gases (instead of climatological values). The processes and parameterisations of the original code are described in the ECHAM5 documentation (Roeckner et al., 2003).

2.2.2.3 Photolysis

As mentioned above the photolysis rates for the chemical integration scheme have to be provided by an external module. In this work the submodel JVAL is used for this purpose. Its core routines are based on the work of Landgraf and Crutzen (1998). Using a spectral approach the photolysis rate coefficient J_X of the species X can be determined by the following integral:

$$J_X = \int_I \sigma_X(\lambda_w)\Phi_X(\lambda_w)F(\lambda_w)d\lambda_w. \tag{2.1}$$

In this equation, $F(\lambda_w)$ is the actinic flux, λ_w the wavelength, $\sigma_X(\lambda_w)$ the absorption cross section for the species X and $\Phi_X(\lambda_w)$ the quantum yield. For computational purposes the photochemical active spectral interval, i.e., 178.6 nm $< \lambda_w <$ 752.5 nm, is subdivided into eight spectral bands. This selection of bands is based upon the simplificating assumption that each of those bands can be calculated individually. With this approach, Equation 2.1 can be written for each band i:

$$J_{i,X} = \int_{I_i} \sigma_X(\lambda_w)\Phi_X(\lambda_w)F(\lambda_w)d\lambda_w. \tag{2.2}$$

Since the photolysis rate is dependent on absorption and scattering, this has to be considered, too. Except for the Schumann-Runge-Band (178.6 nm $< \lambda_w <$ 202.0 nm) this effect is taken into acount by modifying the actinic flux for a purely absorbing atmosphere $F^a(\lambda_{w,i})$ at an adequate fixed wavelength for each of the bands with a factor δ_i to get the actual actinic flux $F(\lambda_{w,i})$:

$$F^a(\lambda_{w,i}) = \delta_i \cdot F(\lambda_{w,i}). \tag{2.3}$$

With this assumption the total photolysis rate of a species can be approximated by the following equation:

$$J_X = J^a_{1,X} + \sum_{i=2}^{8} J^a_{i,X} \cdot \delta_i. \tag{2.4}$$

A great advantage of this technique is that the J-values for the purely absorbing atmosphere $J^a_{i,X}$ can be precalculated, and only the factor δ_i has to be determined during the

[3] http://www.mpch-mainz.mpg.de/~sander/messy/mecca/
[4] http://www.messy-interface.org

integration depending on the meteorological conditions in the particular grid box of the model atmosphere. This is done by radiative transfer modelling, considering absorption and scattering by gas molecules, particles, cloud droplets and the earth's surface. A more detailed description can be found in the original work of Landgraf and Crutzen (1998).

2.2.2.4 Emissions

Emissions in MESSy are treated by the four submodels OFFLEM, ONLEM, LNOX and TNUDGE. A distinction is made between emissions from precompiled emission inventories, that are independent of the actual model state of the atmosphere, and those emissions, that do depend on actual meteorological conditions. The first are treated with the OFFLEM submodel, the latter with the ONLEM submodel. TNUDGE comprises pseudo-emissions of long lived species. Instead of an emission flux, a mixing ratio is provided as an external source. The tracer mixing ratio is relaxed towards this prescribed value, resulting in a pseudo-emission. Detailed descriptions of those three submodels can be found in Kerkweg et al. (2006) and on the MESSy website[5]. NO_x emissions from lightning are calculated separately in the additional submodel LNOX.

The OFFLEM submodel provides multi-dimensional fields, e.g. an emission flux or a mixing ratio field in the required model resolution. For that purpose the NCREGRID tool (Jöckel, 2006) is applied. An emission flux can be applied directly by adding a tendency to the tracer's mixing ratio in the respective grid box, or by converting it into a lower boundary condition which is processed by the calculations for boundary layer meteorology and vertical diffusion.
Offline emissions are used for CO, HCHO, HCOOH, CH_3OH, higher hydrocarbons (i.e., C_2H_4, C_2H_6, C_3H_6, C_3H_8, C_4H_10, CH_3CHO, CH_3COOH, CH_3COCH_3, $CH_3COC_2H_5$), SO_2, NH_3 and anthropogenic NO_x.
Most of the data is taken from the EDGAR-database[6] (version 3.2 FASTTRACK 2000). The emissions from biomass burning are also from the EDGAR - database and already included in the trace gase specific emission fluxes.
NH_3 emission data are fom the GEIA inventory emission set[7] according to Bouwman et al. (1997).
Additionally, NO_x emissions from aircraft based on Schmitt and Brunner (1997) are applied.
The NO_x is distributed to NO and NO_2, dependent on a selection in the OFFLEM namelist (see manual of Kerkweg et al. (2006)).

The ONLEM submodel calculates those emissions that are dependent on the meteorological parameters. In this work those are:

- the emission of Dimethylsulphide (DMS), depending on the DMS seawater concentration (a climatological distribution is provided by OFFLEM) and the windspeed (Liss and Merlivat, 1986),
- the emission of biogenic produced NO in the soil, depending on soil parameters, radiation, precipitation, etc. (Ganzeveld et al., 2002a,b),

[5] `http://www.messy-interface.org`
[6] `http://www.arch.rivm.nl/env/int/coredata/edgar/`
[7] `http://www.geiacenter.org`

- the emission of isoprene, also depending on soil properties, radiation, precipitation, etc. (Ganzeveld et al., 2002a,b),
- aerosol emission of sea-salt, depending on the windspeed (Monahan, 1986; Guelle et al., 2001),
- aerosol emission of dust, depending on the windspeed and soil properties (Balkanski et al., 2004).

Additionally, pseudo-emissions are calculated from prescribed boundary conditions with the submodel TNUDGE. This is applied for the methane (CH_4), the chlorofluorocarbons (CFCs), N_2O and H_2. However, the latter compounds are mainly important in stratospheric chemistry, and are not analysed in detail within this thesis work.

The LNOX submodel calculates the emission of NO_x during lightning activity based on the calculated flash frequency. Two paraterisations following different approaches are implemented.
One applies an empirically determined relationship between observed flashes and convective cloud top height with different parameters over land and sea, comprehensively described in Price et al. (1997). The other uses a relation between the updraft strength within the convective clouds to determine the flash frequency (Grewe et al., 2001).
Both approaches distinguish between intra-cloud (IC) and cloud-to-ground (CG) flashes. Since there are large uncertainties in the amount of nitrogen atoms produced in a lightning strike, this parameter can be adjusted in the LNOX namelist to adjust the calculated amount of NO_x source from lighting within the expected range of 2 to 10 Tg N/yr.
Vertically, the lightning emissions are distributed following a C-shape profile proposed by Pickering et al. (1998). This approach is desirable because of the process splitting in ECHAM5/MESSy: the convection and the convective tracer transport tendencies are calculated earlier, so that without the C-shape approach a wrong vertical emission profile is predicted due to neglect of the influence of convection.

2.2.2.5 Aerosol Microphysics - M7

A submodel for calculation of aerosol microphysical processes is M7. This is originally a box model developed at the Joint Research Center of the European Comission (JRC) in Ispra, Italy (Wilson et al., 2001; Vignati et al., 2004), and has been implemented into MESSy by Kerkweg (2005). This submodel distributes the atmospheric aerosol particles into seven lognormal modes: four soluble and three insoluble modes. For each mode independently the mass and number density are determined prognostically, as well as the mean dry and ambient radius. The standard deviations of the radius distributions are constant ($\sigma = 2.0$ for the coarse mode and $\sigma = 1.69$ for the other modes). The four soluble modes include the nucleation mode ($r < 5$ nm), the Aitken mode (5 nm $< r <$ 50 nm), the accumulation mode (50 nm $< r < 500$ nm) and the coarse mode ($r > 500$ nm). The nucleation mode consists of sulphate aerosol only and therefore the particles are completely soluble. The other modes contain sulphate, organic and black carbon, dust and seasalt, the latter two only in the two larger modes. In the insoluble modes there is organic and black carbon in the Aitken mode and dust in the accumulation and coarse mode.
M7 calculates the nucleation of sulphate particles in the nucleation mode. The mechanism

for this process can be found in Vehmakäki et al. (2002). Additionally, the condensation of sulfuric acid H_2SO_4 on all modes is considered. This can result in a growth of the mean radius as well as a transfer from an insoluble to a soluble mode. The coagulation of aerosol particles of different and the same sizes is possible. The resulting aerosol particle is of the same size for equal sized coagulation partners or of the size of the larger one in other cases. If a soluble and an insoluble aerosol particle coagulate the resulting particle is soluble. Since the particle radius can increase, the aerosol particles can shift from one mode to the other, which maintains the lognormal modal structure.
More details about this submodel can be found in the work of Wilson et al. (2001) and Vignati et al. (2004). Additionally, the M7 module is implemented into ECHAM5 in a different way by Stier et al. (2005) at the MPI-MET.

2.2.2.6 Sedimentation

The sedimentation of aerosol particles is treated by the submodel SEDI. It is based on the theory of aerosol sedimentation presented in Pruppacher and Klett (2000) and was developed by Kerkweg (2005). It determines the terminal velocity v_t of aerosol particles of a given size by:

$$v_t = v_{Stokes} \cdot f_{Slinn} \cdot f_{Cun} \tag{2.5}$$

with

$$v_{stokes} = \frac{2}{9} r(k)^2 \frac{g}{\eta} (\rho_{aero}(k) - \rho_{air}) \tag{2.6}$$

$$f_{Cun} = 1 + 1.257 \frac{\lambda}{r(k)} + 0.4 \frac{\lambda}{r(k)} exp\left(-1.1 \Big/ \frac{\lambda}{r(k)}\right) \tag{2.7}$$

$$f_{Slinn} = \begin{cases} 1 & \text{for bins} \\ \sigma(k)^{2 \ln \sigma(k)} & \text{for lognormal modes} \end{cases} . \tag{2.8}$$

In this set of equations k represents the aerosol mode, $r(k)$ the ambient aerosol radius of the individual modes, $\sigma(k)$ the standard deviation of the aerosol radius distribution and $\rho_{aero}(k)$ the aerosol density; η denotes the viscosity of air, λ the mean free path of air molecules and g the graviational acceleration. The Cunningham-slip-flow correction F_{Cun} is applied to take into account that the aerosol particles may be non-spherical and therefore their aerodynamic behaviour deviates from ideal spheres. For the lognormal aerosol distribution the Slinn factor (Slinn and Slinn, 1980) is applied to consider the difference between the mean settling velocity and the settling velocity of a particle with the mean radius.

2.2.2.7 Dry Deposition

The process of dry deposition, i.e., the loss of gas molecules and aerosol particles from the atmosphere onto the earth's surface by turbulent transfer and uptake processes in absence of precipitation or clouds is calculated with the submodel DRYDEP. This sink process in the surface layer is implemented following Ganzeveld and Lelieveld (1995) for gas phase species and Stier et al. (2005) for aerosol tracers.

Gas Phase species
Dry deposition of trace gases is applied according to the 'Big-Leaf Approach' following Ganzeveld et al. (1998). The submodel calculates a dry deposition velocity for specific

gases, namely O_3, NO, NO_2, HNO_3 and SO_2. This velocity for the species X is determined using a multi-resistance approach:

$$v_d(X) = \frac{1}{R_{aero} + R_{qbr}(X) + R_{surf}} \tag{2.9}$$

R_{aero} represents the physical state of the atmosphere, i.e., the atmospheric resistance taking into account atmospheric stability, roughness length, friction velocity and additional parameters determined from the boundary layer meteorology calculations. R_{surf} denotes the chemical, physical and biological properties of the surface to allow an uptake of a gas molecule. It has to be determined individually for different surface classes: a) water (with distinction between sea-ice cover and open water) and land (with distinction between snow/ice covered, water in the wet skin reservoir, bare soil, and vegetation. Detailed information can be found in the literature (e.g., Ganzeveld and Lelieveld, 1995, and references therein). $R_{qbr}(X)$ considers the molecular diffusion of a species X and is mostly much smaller than the other two resistances and therefore often neglected.
With this dry deposition velocity for a specific species X ($v_d(X)$) a deposition flux F_{drydep} can be determined by multiplying the velocity with the surface layer concentation of this species $c_g(X)$:

$$F_{drydep} = c_g(X) \cdot v_d(X). \tag{2.10}$$

For other trace gases the dry deposition velocity and the uptake resistance are interpolated according to their solubility and reactivity compared to SO_2 and O_3.

Aerosol particles
Dry deposition of aerosol particles is also applied following the 'Big-Leaf Approach'. The implementation is based on the work of Stier et al. (2005). This is only suitable for aerosol distributions with lognormal modes. The deposition velocity is calculated accounting for six different surface types, the mean ambient aerosol radius, the standard deviation of the corresponding radius distribution, and the meteorological parameters.

2.2.2.8 Cloud microphysics

The cloud processes associated with large-scale upshift are treated in the CLOUD submodel, developed as a part of this thesis, and it integrates a number of routines available in ECHAM5. This submodel provides an interface for selectable cloud microphysical schemes. It calculates the cloud droplet number concentrations, the large-scale cloud cover, condensation, and precipitation formation and evaporation. Water vapour, cloud water and cloud ice are prognostic variables in the ECHAM5 model and their changes due to the processes mentioned above result in a tendency that is applied in the ECHAM5 integration scheme. At present only the original cloud and cloud cover calculating parametrisations from the ECHAM5 model are implemented. These are described in detail by Roeckner et al. (2003), based on work by Lohmann and Roeckner (1996). The prognostic cloud cover scheme is derived from Tompkins (2002).
The scheme provides the liquid/ice water content and the precipitation formation and evaporation rates, precipitation flux from each model level and cloud cover, which are all required for the scavenging scheme. Currently, the cloud droplet number concentration is constant and independent of the aerosol distribution, being the default in ECHAM5.

2.2.2.9 Radon

The submodel DRADON, developed by P. Jöckel (unpublished), describes the source and decay of radioactive Radon ^{222}Rn. This trace species is emitted over land surfaces according to the emission inventory of Schery and Wasiolek (1998), or with a constant flux selectable in the namelist, e.g., a flux of 1 atom/(cm^2 s) as applied in several other model studies (e.g., Jacob and Prather, 1990; Jacob et al., 1997). Since its sources and the decay as the only sink are relatively well known and it is not chemically reactive, the tracer ^{222}Rn is well suited for studying transport processes in the atmosphere (e.g., Jacob and Prather, 1990). The decay of ^{222}Rn can be calculated either as a first order loss process or, as applied in this work (Section 6.3), as the complete decay chain to lead ^{210}Pb. For the mathematical description of this decay chain the general Bateman (1910) solution of a radioactive decay chain is applied (Pressyanov, 2002).

2.2.2.10 Data Assimilation

A simplified type of data assimilation of the meteorological quantities, i.e., the temperature, surface pressure, vorticity and divergence is possible. Its aim is to push the model towards an observed state. For that purpose this data can be introduced from an external source, e.g., ECMWF analysis or reanalysis data (ERA15, ERA40). The assimilation of these quantities is performed by adding an additional tendency $\partial X/\partial t$ to the respective variables, which is the difference of the (re-)analysed to the modelled value $X_{\text{analy}} - X$ and a certain relaxation coefficient $G(X)$, that includes the relaxation time.

$$\left(\frac{\partial X}{\partial t}\right)_{\text{nudge}} = G(X) \cdot [X_{\text{analy}} - X] \tag{2.11}$$

This so-called 'nudging' can be applied in various strength for each model layer, depending on the relaxation coefficients. More of the method can be found in Jeuken et al. (1996). Its application and implementation are described in more detail in van Aalst (2005) and Buchholz (2005).
However, in such a nudged simulation the model physics are disturbed by this additional tendencies, that might lead into instabilities or discrepancies compared to simulations without nudging (Hagemann et al., 2002; Bengtsson et al., 2004).

Chapter 3

Convection

3.1 Overview

As mentioned in the introduction, convection plays a key role in atmospheric thermodynamics with strong feedbacks on the general circulation. A major problem is its description in a large-scale model, e.g., a general circulation model (GCM). In such a model, as can be seen from Chapter 2.1, the grid box size is much larger than the single convective clouds. Therefore a parametrisation, i.e., an approximate description of the small scale process influenced by and feeding back on the grid-scale variables, is required. The problem becomes even worse when the microphysical effects in those convective clouds are considered, which then comprises processes of a length-scale of several orders of magnitude from the μm size of cloud droplets to the 400 km size of the model grid box.
A second aspect of the problematic description of convection is that in contrast to the commonly used approach of individual convective cells, these are often connected and organised into mesoscale convective systems (Houze, jr., 2004). Although a comprehensive solution for this aspect is still not found, Donner et al. (2001) and Yano et al. (2004) try to overcome it by modifying the mass flux approach with an additional term describing the influence of mesoscale effects.

Over the last fifty years different parameterisations have been tested, but the perfect solution for the problem has not yet been found (Randall et al., 2003). Especially in numerical weather prediction (NWP) models, but also in climate models it is crucial to achieve realistic precipitation from the convective clouds as well as water vapour transport into the upper troposphere. For coupled chemistry climate models (CCMs) the requirements are even stronger because the convection is linked to vertical tracer redistribution, scavenging, cloud and radiation properties and other physical processes, e.g., lightning activity. A comprehensive overview of the development of convection theories can be found in Arakawa (2004) and will be reviewed only shortly in this thesis.

The first convection parameterisations have been based on the concept of 'moist adiabatic adjustment' (e.g., Manabe et al., 1965). Parameterisations of that type try to adjust the atmosphere's unstable temperature profile to a neutral or almost neutral stratification by changing the temperature and water vapour, but nowadays they are rarely used, though sometimes in combination with other convection schemes.
The principles of 'mass-flux schemes', first proposed by Arakawa and Schubert (1974), which explicitely treat the vertical mass transport due to convective overturning, is the

theoretical basis of several contemporary convection parameterisations. Large differences occur in the closure assumptions of these schemes, required to achieve an applicable algorithm for a computer model. The closure assumptions of the parameterisations used here will be explained in detail in the relevant descriptions (see Chapter 3.2). Arakawa (2004) tries to classify these schemes according to their closure asumptions, but some schemes cannot be unambigiously categorised. These categories are:

- *Diagnostic closure schemes based on large-scale moisture or mass convergence, or vertical advection of moisture (e.g., Kuo (1974), Tiedtke (1989))*
- *Diagnostic closure schemes based on quasi-equilibrium (e.g., original Arakawa and Schubert (1974), Donner et al. (2001))*
- *(Virtually) instantaneous adjustment schemes (e.g., modified Arakawa and Schubert (1974), modified Manabe et al. (1965))*
- *Relaxed and/or triggered adjustment schemes (e.g., Hack (1994), Zhang and McFarlane (1995), Bechtold et al. (2001))*
- *Prognostic closure schemes with explicit formulations of transient processes (e.g., Emanuel and Zivkovic-Rothman (1999))*
- *Stochastic closure schemes (e.g., Lin and Neelin (2000, 2002, 2003)).*

Most of these schemes can show reasonable agreement with observations with respect to temperature profiles in GCMs and to a somewhat lesser extent also moisture sinks and humidity profiles, but fail in the treatment of the mesoscale processes associated with deep convection (Donner et al., 2001). According to Donner et al. (2001) the agreements with observations might originate from some compensating errors, e.g., neglecting the proper description of cloud microphysics or radiative effects in convective clouds. Instead of an ensemble of mass fluxes as assumed by Arakawa and Schubert (1974), Donner et al. (2001) describe a spectrum of clouds in their approach.
The alternative, a cloud resolving model (CRM) with a resolution of about 1 km, to compute the properties of convective clouds performs quite well, but these models are computationally expensive and therefore they are mostly not applicable on a global scale, especially not on the timescales of a climate model. Consequently, a convection parameterisation is still required at present and also in the near future.
Krishnamurti and Sanjay (2003) propose a new approach by using a superensemble, i.e., they use a set of six convection parameterisations that are non-uniformly weighted, dependent on the location of the convective grid column. These weights are calculated with a 'training set' of 85 model simulations. This weighted superensemble achieves good forecast skill rankings according to Krishnamurti and Sanjay (2003). However, this scheme has the disadvantage that it was trained on model output. For NWPs, which simulate the real atmosphere at present conditions, this is acceptable, but for climate models, calculating future scenarios with unknown meteorological conditions there is no evidence that those weights remain acceptable under future conditions.
Grell and Deeveny (2002) propose a combination of ensemble and data assimilation techniques, but since there is no data for future calculations available this also does not seem to be a solution for the problem.
Naveau and Moncrieff (2003) address the description of the convective mass flux by a probabilistic approach, based on extreme-value theory. They use the vertical velocity as

a key parameter. Since this is a prognostic variable only in non-hydrostatic models, the application in a GCM is not appropriate at the present.
A completely different approach is proposed by Nober and Graf (2005). Instead of developing a parameterisation based on observations, they use a theoretical concept: an ensemble of clouds is treated from the view of self-organisation. This is done by calculating cloud properties, followed by applying interactions on the basis of population dynamics. The authors show that their approach works without much tuning in the climate model ECHAM5 (Roeckner et al., 2003), but it is not yet tested for long term climate simulations.
Another new approach, the so-called 'superparameterisation', introduced by Grabowski and Smolarkiewicz (1999) and Grabowski (2004), makes use of the better process description of convection by CRMs. For this approach, a (simplified, two dimensional) CRM is used in every grid-box of the global model. This is computationally very expensive, but might become a future perspective for global climate models (Randall et al., 2003) with increasing computer power. The application in a chemistry climate model has to be delayed further into the future, because the chemistry and tracer transport calculations are usually very expensive and the additional costs of a CRM in such a model do not seem affordable within the next few years.

In the past convection scheme comparisons have been performed in several studies (e.g., Mahowald et al., 1995; Xie et al., 2002). However, mostly the different parameterisation schemes are implemented in single column models (SCMs), and their results are then compared to results from cloud resolving models or meteorological observations. Typical convection simulation experiments are performed, e.g., tropical oceanic convection, or continental convection in a time frame that is also covered by observations. As a result specific convection schemes are judged as *good performing*, but these results must be treated with care, since the objective result is *good performing under the given conditions*.
Xie et al. (2002) conclude that some of the large discrepancies of some convection schemes are associated with the deficiencies in the triggering of convection.
In none of the comparisons mentioned above the influence of convection on the larger scales is assessed. This can only be done with a larger scale model, specifically a global model. Only in such a model framework the interaction of the convection scheme with the large-scale cloud scheme due to the transport of water vapour can be taken into account. Under certain conditions the large-scale cloud scheme stands in for the convection parameterisation resulting in modelled precipitation fields that are close to observations.
Mapes et al. (2004) compare several convection parameterisations in a regional model over a 10-day period. This model is applied in a tropical region covering ocean as well as continental areas. Even though the outer regions of their model domain are strongly influenced by the boundary conditions (reanalysis data from ECMWF), the core region is more dependent on the selected convection scheme. Mapes et al. (2004) find large differences in precipitation and wind divergence, but are not able to define an overall 'best convection scheme' for their model domain and simulation period.
A study by Mahowald et al. (1997) investigates, how the two convection schemes of Tiedtke (1989) and Arakawa and Schubert (1974) behave in the 'offline' chemistry transport model (CTM) MATCH (Rasch et al., 1997), driven by different reanalysis data, but the performance of the schemes concerning the hydrological cycle is not discussed in detail.
A global study covering a simulation period of 32 months with different convection parameterisations has been done by Lee et al. (2003). They conclude that the tropical intra-seasonal oscillations (strong convective activity periods (e.g., Madden and Julian,

1994, and references therein), stretching from the Indian Ocean to the central Pacific and the South Pacific Convergence Zone (SPCZ)) are highly dependent on the choice of the scheme, both for an aqua-planet, on which they perform most of their investigations, as well as in the real Earth's atmosphere. Additionally they admit that the *'cumulus parameterisation remains a key issue for improving GCM simulations of both mean tropical rainfall and its intraseasonal variability'*.

3.2 Convection Schemes: Model description

As one part of this thesis the submodel CONVECT was developed. MESSy provides an interface to handle the data transfer required by a convection scheme. In the submodel Interface Layer (SMIL) the required input parameters for the selected scheme are calculated and supplied. The submodel currently comprises four different convection schemes with several additionally selectable characteristics. These schemes are all fully coupled to the other physical processes of the model, using input parameters from the GCM, and returning their ouput to the GCM. Therefore, only one scheme can be used at the same time to give a consistent view of the behaviour of the convection parameterisation in the global model.
The different schemes are:

- The convection scheme of Tiedtke (1989) with the additions of Nordeng (1994), which is the default for the ECHAM5 model. Additionally, two different closure assumptions are selectable: the original closure of Tiedtke (1989) and a so-called hybrid closure.

- The convection scheme of the ECMWF operational global weather forecast model (Tompkins et al., 2004) (IFS cycle 29r1b), originally also based on the Tiedtke (1989)-scheme.

- The convection scheme of Zhang and McFarlane (1995) and Hack (1994), as applied in the chemistry transport model MATCH (e.g., Rasch et al., 1997; Lawrence et al., 1999).

- The convection scheme of Bechtold et al. (2001), with only slight modifications.

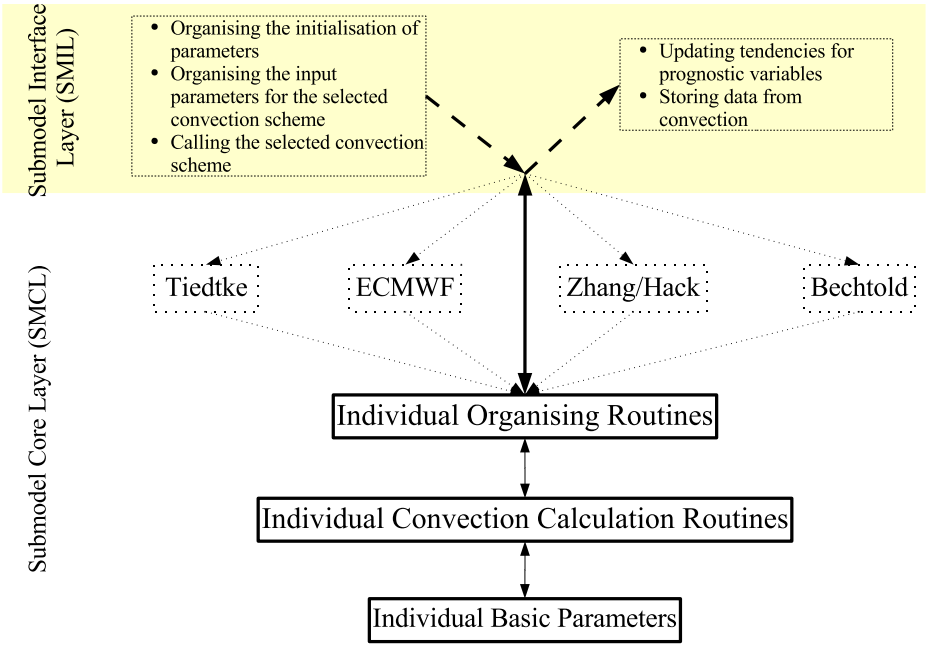

Figure 3.1: Sketch of the CONVECT submodel

This is sketched in Figure 3.1. Since none of the schemes is a new development, they will be explained only shortly referencing to the literature. The main difference between the schemes will be outlined.

3.2.1 The Tiedtke - Scheme

As mentioned above, this scheme is based on the work of Tiedtke (1989). The standard scheme of ECHAM5 is developed further by the additions of Nordeng (1994). It contains most of the assumptions of the original work, but also several updates. First the basic Tiedtke scheme (also still included in the original ECHAM5 model), is explained, followed by the additions.
Following the approach of Arakawa and Schubert (1974) the convection is described by an ensemble of clouds modifying the equations for the large-scale budget of the environmental dry static energy $\bar{s}$ ($s = c_p T + gz$) and the specific humidity $\bar{q}$:

$$\begin{aligned} \frac{\partial \bar{s}}{\partial t} + \bar{\mathbf{v}} \cdot \nabla \bar{s} + \bar{w} \frac{\partial \bar{s}}{\partial z} &= -\frac{1}{\rho} \frac{\partial}{\partial z} \Big(M_u s_u + M_d s_d - (M_u + M_d) \bar{s} \Big) \\ &\quad + L(c_u - e_d - \tilde{e}_l - \tilde{e}_p) \\ &\quad - \frac{1}{\rho} \frac{\partial}{\partial z} (\bar{\rho} \overline{w' s'})_{tu} + \bar{Q}_r \end{aligned} \tag{3.1}$$

$$\begin{aligned} \frac{\partial \bar{q}}{\partial t} + \bar{\mathbf{v}} \cdot \nabla \bar{q} + \bar{w} \frac{\partial \bar{q}}{\partial z} &= -\frac{1}{\rho} \frac{\partial}{\partial z} \Big(M_u q_u + M_d q_d - (M_u + M_d) \bar{q} \Big) \\ &\quad + (c_u - e_d - \tilde{e}_l - \tilde{e}_p) \\ &\quad - \frac{1}{\rho} \frac{\partial}{\partial z} (\bar{\rho} \overline{w' q'})_{tu} \end{aligned} \tag{3.2}$$

In these equations $\bar{\mathbf{v}}$ denotes the two-dimensional, horizontal windfield, w the vertical wind velocity, ρ the air density, M_u the upward and M_d the downward mass flux, L the latent heat of condensation. The condensation of water vapor in the updraft is represented by c_u, while the three terms e_d, $\tilde{e}_l$ and $\tilde{e}_p$ represent the evaporation of detrained water, cloud water, and precipitation, respectively. The boundary layer turbulence is considered by $-\frac{1}{\rho} \frac{\partial}{\partial z} (\bar{\rho} \overline{w' s'})_{tu}$ and $\bar{Q}_r$ denotes the impact of radiation. Barred quantities represent the environmental state of the atmosphere.

Even though a cloud ensemble is assumed, only bulk values for a steady state are calculated in the scheme. These are:

$$\frac{\partial M_u}{\partial z} = E_u - D_u \tag{3.3}$$

$$\frac{\partial (M_u s_u)}{\partial z} = E_u \bar{s} - D_u s_u + L \bar{\rho} c_u \tag{3.4}$$

$$\frac{\partial M_u q_u}{\partial z} = E_u \bar{q} - D_u q_u - \bar{\rho} c_u \tag{3.5}$$

$$\frac{\partial M_u l}{\partial z} = -D_u l + \bar{\rho} c_u - \bar{\rho} G_p \tag{3.6}$$

Entrainment E_u and detrainment D_u of the updraft consist of a turbulent and an 'organised' part. The turbulent part is parameterised with constant values times the mass flux.

The liquid water l has the precipitation formation G_p as an additional loss term. For the downdrafts M_d the equations 3.3 to 3.5 can be formulated analogously:

$$\frac{\partial M_d}{\partial z} = E_d - D_d \tag{3.7}$$

$$\frac{\partial (M_d s_d)}{\partial z} = E_d \bar{s} - D_d s_d + L\bar{\rho} e_d \tag{3.8}$$

$$\frac{\partial M_d q_d}{\partial z} = E_d \bar{q} - D_d q_d - \bar{\rho} e_d \tag{3.9}$$

Entrainment E_d and detrainment D_d in the downdrafts are assumed with a constant value times the mass flux.
The Tiedtke-scheme differentiates between three types of convection:

1. penetrative or deep convection, i.e., convection, mostly triggered in the boundary layer by convergent flow, reaching several kilometers in altitude,
2. shallow convection, mostly triggered by subcloud layer turbulence,
3. midlevel convection, i.e., convection with its origin at higher altitudes, e.g., frontal convection in extratropical cyclones.

The organised entrainment and detrainment for all three respective types are parameterised differently:

1. The entrainment is proportional to large-scale moisture convergence.
2. 70 % of the updraft air mass is detrained in the cloud top layer, the rest in the layer above.
3. Here, the same assumptions are made as for penetrative convection, the cloud base mass flux is determined by the large-scale flow.

This formulation of the entrainment rate contains the required closure assumptions, i.e., the convection of the Tiedtke-scheme is highly dependent on large-scale moisture convergence.
The precipitation formation G_p is parameterised in a very simplified way from the amount of cloud water:

$$G_p = K(z) l, \qquad \text{with :} \tag{3.10}$$

$$K(z) = \begin{cases} 0, & \text{if } z < Z_b + 1500 \text{ m} \\ 2.0 \cdot 10^{-3} & \text{if } z > Z_b + 1500 \text{ m}. \end{cases} \tag{3.11}$$

This leads to a total precipitation of

$$P(z) = \int_{z}^{cloud\ top} (G_p - e_d - \tilde{e_p}) \bar{\rho} dz, \tag{3.12}$$

with e_d the detrained precipitation and $\tilde{e_p}$ the evaporation of precipitation in subcloud layers.
The convection scheme is triggered by determining the temperature of an air parcel and comparing it with the environmental temperature in the LFC. If it is warmer by 0.5 K,

i.e., bouyant to the surrounding air, the convection scheme is activated.

The additions of Nordeng (1994) contain a new treatment of organised entrainment and detrainment for penetrative convection, as well as a new closure assumption based on CAPE and a relaxation time. Additionally, the vertical transport of momentum is implemented, assuming a similar behaviour compared to moisture.
The organised entrainment is now defined by the bouyancy b, vertical velocity w_0, air density ρ and the mass flux M:

$$E^{org} = \left\{ \frac{b}{2(w_0^2 + \int_0^z b \; dz)} + \frac{1}{\bar{\rho}} \frac{\partial \bar{\rho}}{\partial z} \right\} \cdot M, \tag{3.13}$$

with $w_0 = 1$ m/s and $b = g/\bar{T}(T_v - \bar{T}) - gl$. Organised detrainment can be calculated from the fractional cloud cover σ_{cv} and the mass flux:

$$D^{org} = -\frac{M}{\sigma_{cv}} \frac{\partial \sigma_{cv}}{\partial z}. \tag{3.14}$$

The cloud cover is estimated from the levels where detrainment starts and the cloud top by:

$$\sigma_{cv} = \sigma_{cv,0} \cos\left(\frac{\pi}{2} \frac{z - z_d}{z_t - z_d} \right). \tag{3.15}$$

Additionally the closure assumption has been replaced, which could be easily done after changing the entrainment/detrainment. This is done with an adjustment closure using CAPE. This is defined differently than in equation 1.2 by additionally considering the effect of liquid water l:

$$CAPE = \int_{LFC}^{ETL} \left(\frac{T_v - \bar{T}_v}{\bar{T}_v} g - gl \right) dz. \tag{3.16}$$

With the help of this equation the cloud base mass flux can be defined by:

$$M_B = \frac{CAPE}{\tau} \frac{M_B^*}{\int_{cloud} \left(\frac{(1+\delta q)}{c_p T_v^e} \frac{\partial \bar{s}}{\partial z} + \delta \frac{\partial \bar{q}}{\partial z} \right) M^* \frac{g}{\bar{\rho}} dz} \tag{3.17}$$

Here M^* is an estimated starting value for the first computation of the updraft. From this computation $CAPE$ is approximated, and the real updraft with the correct cloud base mass flux can be calculated. For the value of M^* the old calculation from the moisture convergence approach is used.

3.2.2 The ECMWF - Scheme

This convection scheme, introduced by Tompkins et al. (2004), is used operationally in the global weather forecast model of the ECMWF, Reading. It is based on the same scheme of Tiedtke (1989), but it has been modified according to Gregory et al. (2000). These are similar to the modifications of the above mentioned scheme by Nordeng (1994), but they result in a slightly different formulation of the updraft mass flux M_B at the cloud base.

$$M_B = \frac{\frac{CAPE}{\tau}}{\int g(\eta_u - 0.3\eta_d) \left(\frac{1}{\bar{T}} (\frac{\partial \bar{T}}{\partial z} + \frac{g}{c_p}) + \frac{0.608}{1+0.608\bar{q}} \frac{\partial \bar{q}}{\partial z} \right) dz} \tag{3.18}$$

The symbols η_u and η_d denote the variation of the mass fluxes with height, derived from the entraining/detraining plume model of convection. Additionally, the turbulent entrainment rates for deep and shallow convection have been slightly modified, i.e., for deep convection it was increased while for the shallow convection formulation a decrease of the entrainment rate was assumed.
In addition to this, the triggering of deep convection has been modified according to Bechtold et al. (2004), based on the updraft velocity. First, a check for shallow convection is made, considering a strongly entraining parcel, followed by a check for weakly entraining deep convection. If successful, the shallow convection result is replaced by this.
Furthermore, the precipitation conversion factor is increased.
The shallow convection can be used with two closure assumptions: first, a classical closure, depending on the temperature and humidity profiles, and second an approach calculating a characteristic velocity w^* using the sensible heat and moisture flux as input parameters (Grant and Brown, 1999).

3.2.3 The Zhang - McFarlane - Hack - Scheme

The convection scheme of Zhang and McFarlane (1995) for deep and of Hack (1994) for shallow and midlevel convection has been initially developed for the Community Climate Model (CCM3). Considering deep convection, the equations 3.1 and 3.2 are also valid for this scheme.
Additionally, the standard equations for the convection scheme 3.4 to 3.6 are applied with minor modifications. The differences occur in the formulations of entrainment and detrainment and the precipitation formation. In this scheme the ensemble approach is much more visible. The updraft is defined as:

$$\begin{aligned} M_u &= M_b \int_0^{\lambda_0} \frac{1}{\lambda} e^{\lambda(z-z_b)} d\lambda \\ &= \left(\frac{M_b}{\lambda_0(z-z_b)}\right)(exp\{\lambda_d(z)(z-z_b)\}-1) \end{aligned} \tag{3.19}$$

M_b symbolizes the ensemble cloud base mass flux, while $\lambda_d(z)$ is the fractional entrainment rate of the updraft plume that detrains at height z. λ_0 is the maximum allowed entraining rate and z_b the height of the cloud base. $\lambda_d(z)$ is evaluated from the difference in moist static energy of the ambient and saturated air. With this expression the updraft detrainment D_u can be calculated:

$$D_u(z) = -\frac{M_b}{\lambda_0}\frac{\partial \lambda_d}{\partial z} exp\{\lambda_d(z)(z-z_b)\}. \tag{3.20}$$

The corresponding entrainment E_u is calculated from the equations 3.19 and 3.20 in the equation 3.3:

$$E_u = \frac{\partial M_u}{\partial z} - D_u. \tag{3.21}$$

The precipitation formation is parameterised by:

$$R_r = C_0 M_u l, \tag{3.22}$$

with C_0 as a constant.
Downdraft formulation is analogous to 3.19:

$$M_d = \left(\frac{-\alpha M_b}{\lambda_m(z_d - z)}\right)(exp(\lambda_m(z)(z_d - z)) - 1). \tag{3.23}$$

λ_m, the maximum downdraft entrainment rate, is fixed to $\lambda_m = 2\lambda_0$, but limited by $\lambda_m < 2/(z_d - z_b)$ with z_d as the height of the convective downdraft top layer. Evaporation of precipitation can occur in the downdraft to maintain a state of saturation.
For the closure it is again assumed that CAPE is consumed within a relaxation time τ, defining the cloud base mass flux:

$$M_b = \frac{CAPE}{\tau F}, \tag{3.24}$$

with F as the CAPE-consumption rate.

The shallow and midlevel convection are parameterised according to Hack (1994). Mass flux and precipitation are calculated using the moist static energy h from the theory of adjustment. It is important to note that the Hack scheme always uses three layers to determine the convective adjustment of each model level. These three layers are subsequently applied to all model levels, calculating the effective convection all over the atmosphere. The updraft mass flux for each layer is assumed to be:

$$\begin{aligned} M_{u,k} &= (h - \bar{h}_k^*)\Bigg(g\tau\Bigg\{\frac{1+\gamma_k}{\Delta p_k}\{(s - \bar{s}_{k+\frac{1}{2}} + Ll_k) \\ &\quad -\beta(s - \bar{s}_{k-\frac{1}{2}})\} - \frac{1}{\Delta p_{k+1}}(\bar{h}_{k+\frac{1}{2}} - h)\Bigg\}\Bigg)^{-1} \end{aligned} \tag{3.25}$$

The index k in this equation denotes the vertical layers. Due to the discretisation, the values at the interfaces of the three layers are required. The liquid water of this layer is represented by l_k, and Δp is the pressure difference of this layer.
Rain water production R for each layer and precipitation P are similary approached:

$$\begin{aligned} L \cdot R &= (L(1-\beta)M_u l \\ &= 1 - \beta M_u\left(\bar{s} - s + \frac{1}{1+\gamma}(h - \bar{h}^*)\right) \end{aligned} \tag{3.26}$$

$$P = \frac{1}{\rho_{H_2O}} \int\limits_{cloud} R dz. \tag{3.27}$$

In these equations β is the detrainment parameter, γ represents $(L/c_p)(\partial\bar{q}^*/\partial\bar{T})_p$, and the quantities with an * denote the saturated state. The parameter β can be determined from the buoyancy and the liquid water budget.
The actual calculation is working as follows: first β is determined by a first guess from buoyancy, then the mass flux is calculated using 3.25, the budget of all quantities are checked and then adjusted.

Additionally, Wilcox (2003) proposed an enhanced evaporation of convective precipitation for the CCM3 model because of the unsaturated areas in mesoscale convective cloud systems. Since this convection scheme does not take into account the organisation of

convective clouds, it is a proposal to adjust the precipitation fluxes with respect to that issue. This evaporation can be calculated following the equation

$$Evap = k_e(1 - RH)R_r^{1/2}, \tag{3.28}$$

in which $Evap$ denotes the rate of evaporation, RH the relative humidity, $k_e = 10^{-5}$ and R the precipitation formation rate. This equation is only applied in grid cells with low total cloud cover.
In the CCM3 the effect of this is an enhancement of evaporation of surface precipitation of 10%, corresponding to a better representation of mesoscale convective systems in the tropics, as described by Gamache and Houze, jr. (1983). This results in less light rain, but an enhancement of strong precipitation events. Lang and Lawrence (2005a) applied this additional evaporation in the MATCH model (Rasch et al., 1997) and found an improvement in the precipitation and integrated water vapour columns (IWVC) compared to satellite data.

3.2.4 The Bechtold - Scheme

This scheme (Bechtold et al., 2001), applied in the French Meso-NH model, was also developed originally for the global scale. It uses the same equations 3.1 and 3.2 as basic assumptions. Also all quantities considered to be changed by convection follow, slightly modified, the approach of 3.4 to 3.6. This scheme has many similarities with the convection scheme of Kain and Fritsch (1990).
The triggering of convection is determined by checking the stability of an air parcel at the Lifting Condensation Level (LCL). This is done by evaluating:

$$\overline{\Theta_v^{mix}} - \overline{\Theta_v} + \Delta T/\Pi > 0 \tag{3.29}$$

$\overline{\Theta_v^{mix}}$ represents the virtual potential temperature in a more than 60 hPa deep layer above ground, Π is the Exner function ($\Pi = (p/p_0)^{R_d/c_p}$), and ΔT is proportional to the large-scale vertical motion.
The updraft computations originate from the LCL with starting parameters for the moist static energy ($h = s + Lq$), water and the mass flux defined by:

$$M_u(LCL) = \bar{\rho} w_{\mathrm{LCL}} \pi R_0^2, \tag{3.30}$$

with $w_{\mathrm{LCL}} = 1$ m/s and $R_0 = 1500$ m updraft radius for deep and $R_0 = 50$ m updraft radius for shallow convection.
Simplified cloud microphysics allows glaciation of water in the temperature range of 248-268 K. Precipitation is formed by converting cloud ice and cloud water to precipitation P:

$$\Delta r_r + \Delta r_s = (r_u^c + r_u^i)\{1 - exp(-c_{pr}\Delta z/w_u)\} \tag{3.31}$$

$$P = \sum_{LCL}^{CTL} = M_u(\Delta r_r + \Delta r_s), \tag{3.32}$$

with $c_{pr} = 0.02$ s^{-1}, r_r as the liquid and r_s the ice precipitation formation rate, and a detailed calculation of the vertical velocity w_u. r_u^c denotes the cloud water and r_u^i the cloud ice mixing ratio in the updraft.
The entrainment and detrainment for the updraft are described following an approach of

Kain and Fritsch (1990), that uses fractional entrainment f_ϵ rates defined by a gaussian distribution:

$$
\begin{aligned}
E_u &= \Delta M^t f_\epsilon, && (3.33)\\
\text{with :}\quad \Delta M^t &= M_u c_{etr} \Delta z / R_0, && (3.34)\\
\text{with :}\quad c_{etr} &= 0.2 \\
f_\epsilon(z) &= A(exp\{-(z-m)^2/2\sigma_b^2\} - k), && (3.35)\\
\text{with :}\quad A &= (0.97\sigma_b\sqrt{2\pi})^{-1}, \\
\sigma_b &= 1/6 \\
k &= e^{-4.5}, \\
m &= 0.5.
\end{aligned}
$$

The equations for the detrainment are derived analogously.
Calculations for the downdraft are highly dependent on the total downdraft precipitation evaporation rate. The downdraft properties are described by:

$$
\begin{aligned}
E_d &= -M_d(LFS)c_{etr}\Delta z/R_0 && (3.36)\\
D_d &= 0, \qquad \text{except in the detrainment layer} && (3.37)\\
\Delta M_d &= E_d && (3.38)\\
\Delta(M_d\Theta_{e,d}) &= E_d\bar{\Theta}_e && (3.39)\\
\Delta(M_d r_{w,d}) &= E_d\bar{r_w}. && (3.40)
\end{aligned}
$$

Evaporation occurs wherever the relative humidity sinks below a threshold of 90%. In case of no evaporation in the whole column no downdrafts are allowed.
The closure assumption is again based on the decrease of CAPE. However, in contrast to other CAPE closures, here the equivalent potential temperature is used. Finally, all the quantities are adjusted with the change in CAPE over the adjustment time.

3.2.5 Differences between the schemes

In the following Table 3.1 the main differences of the used convection schemes are shortly summarised:

Table 3.1: Differences between the convection schemes

-	Tiedtke	ECMWF	Zhang-McFarlane-Hack	Bechtold
Closure (deep)	CAPE / moisture convergence	CAPE	CAPE	CAPE
Entrainment	turbulent and organised	turbulent	turbulent	turbulent
Closure (shallow)	moisture convergence	1.) CAPE 2.) w* (Grant and Brown, 1999)	moist static energy	CAPE
Triggering	$T_v^p + \Delta T > T_v^{env}$ $\Delta T = 0.5\ K$	$w_u > 0$ with w_u from entrainment and buoyancy (Jakob and Siebesma, 2003)	Zhang-McFarlane: $T_v^p + \Delta T > T_v^{env}$ $\Delta T = 0.5\ K$ Hack: $h_c - h_k^* > 0$	$\Theta_v^p + \frac{\Delta T}{\Pi} > \Theta_v^{env}$ $\Delta T = 6 \cdot \lvert\bar{w}\rvert^{1/3}$
Precipitation formation	$\Delta r = r_u^c/(1 + c_t \cdot \Delta z)$	more detailed decription, including the 'Bergeron-Findeisen' process	Zhang-McFarlane: $\Delta r = c_0 \cdot r_u^c$ Hack: $\Delta r = (1 - \beta) \cdot r_u^c$	$\Delta r_r + \Delta r_s = (r_u^c + r_u^i) \cdot \{1 - exp(-c_{pr}\Delta z/w_u)\}$

This table is far from being complete, but shows the major differences between the parameterisations.
The computational costs of each scheme are very similar, only the Bechtold scheme is a little more expensive ($< 5\%$ compared to the other convection schemes), but still much cheaper than other processes of a GCM, e.g., radiation calculations.

3.3 Convection Scheme Comparisons

3.3.1 Simulation setup

The aim of this study is to investigate the dependence of rainfall patterns, and in more general the hydrological cycle, including the integrated water vapour columns, evaporation and the effect on temperature using different convection schemes. All simulations for this part of the thesis are performed under the same conditions. The horizontal resolution is T42 with 31 layers in the vertical. In addition to the basic ECHAM5 without the original cloud and cover (calculating large-scale microphysics), radiation and convection routines, the MESSy submodels CLOUD, RAD4ALL and CONVECT are used. Additionally the CVTRANS and LNOX submodels are applied for diagnostic purposes, even though there have been no tracers in the simulation setup.
The simulations start in October 1994 and end in January 2001. However, these dates are artificial, since no nudging is applied and the GCM runs in a climatological mode. The first three months are used as 'spin-up time' of the model and are not taken into account for the results. Initial conditions are derived from ERA40 data.
All simulations of this study are performed with the same executable. The only differences are the applied convection schemes that can be selected via the namelist of the submodel CONVECT.
Those are, as described in Section 3.2:

- T1 - the default convection scheme of ECHAM5, following Tiedtke-Nordeng;
- T2 - the original Tiedtke scheme;
- T3 - the Tiedtke scheme with the so-called 'hybrid closure';
- EC - the scheme of the integrated forecasting system (IFS) at ECMWF with the closure for shallow convection according to Grant and Brown (1999);
- EC2 - the scheme of the integrated forecasting system (IFS) at ECMWF with the traditional shallow convection closure;
- ZH - the convection scheme following Zhang-McFarlane-Hack;
- ZHW - the convection scheme following Zhang-McFarlane-Hack with the extended evaporation routine according to Wilcox (2003);
- B1 - the convection scheme of Bechtold without treatment of ice;
- B2 - the convection scheme of Bechtold including the treatment of ice.

In all schemes the different types of convection (shallow, deep, and if treated differently midlevel) are allowed. Updrafts and downdrafts are considered. There are differences in the formation of precipitation, but these are part of the individual convection schemes. For all simulations except for ZH and ZHW (due to a lack of the corresponding routine) the transport and change of momentum is considered.
All simulations are performed with climatological sea surface temperatures (SST) (average SST from 1990 to 2000 from the Atmospheric Model Intercomparison Project[1] (AMIP)).

[1] `http://www-pcmdi.llnl.gov/projects/amip/`

3.3.2 Results

3.3.2.1 Comparison of the precipitation with climatological observations

First the precipitation at the surface is compared between the simulations with the different convection schemes and with observations from the Global Precipitation Climatology Project (GPCP) (Huffman et al., 1997). The observational data is a composite of rain-gauge and satellite measurements. A detailed description of the observational dataset can be found on the project website[2]. The version-2 of the dataset, that is applied in this study, is presented by Adler et al. (2003). The observations are regridded to the same resolution as the model.

Although the convective precipitation can be modeled separately, in the observations a distinction between large-scale and convective rain is difficult. On the other hand, this distinction is partly artificial from the model calculations and dependent on the grid size of the model. Furthermore, often weak precipitation from the convection scheme in the model is compensated by large-scale precipitation, which results together in a stabilised atmosphere with realistic water vapor content. Therefore only the total precipitation is analysed, consisting of large-scale rain, snow and graupel, and convective rain and snow.

First, the global precipitation intensity is compared in Figure 3.2. This figure shows the horizontally integrated precipitation in Tg/s, calculated as monthly mean values averaged over the whole simulation time. The main conclusion drawn from this figure is that compared to the observations (dark blue with crosses), all schemes produce substantially too much precipitation: the largest overestimation is up to 20%. Both ZH and EC simulations with and without their additional modifications achieve values closer to the total amount of observed precipitation.

The simulation with the default convection scheme of the ECHAM5 model (T1, black) is one of the strongly overestimating ones, while with the other closures of the Tiedtke-scheme the performance is slightly better with respect to the total precipitation amount.

[2]http://precip.gsfc.nasa.gov/

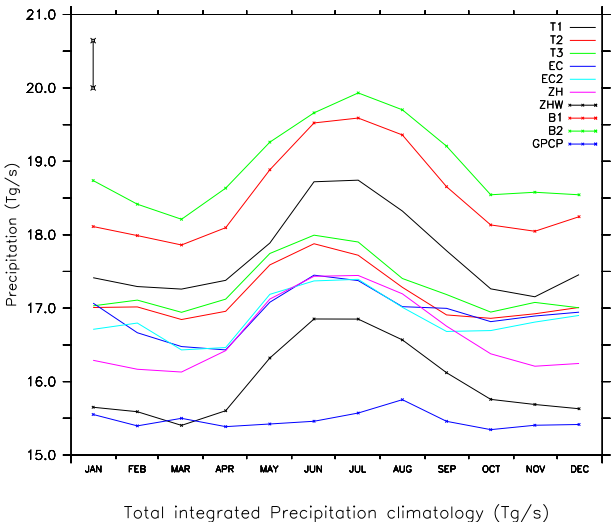

Figure 3.2: Total precipitation climatology (Tg/s) of the different simulations and observations. The bar in the upper left corner indicates the average monthly standard deviation (σ) of all schemes.

The simulations with the Bechtold scheme (B1 and B2, red with crosses and green with crosses) perform even worse.
All schemes produce a strong annual cycle with a pronounced maximum during boreal summer, which is not evident from the observations. The average variability within each month of all simulations is indicated by the bar in the upper left corner of Figure 3.2.
Since the global total precipitation hardly gives any evidence for the judgment of 'poor simulation' results, the spatial distribution of precipitation is investigated in Figure 3.3 and Figure 3.4. All data is averaged over the six year simulation time. The resulting values are given in mm precipitation per day at the surface.
Figure 3.3 shows the zonal (averaged over all longitudes) temporal averaged precipitation for the four seasons. Almost all simulations reproduce the general shape of the observations, i.e., low precipitation in the polar regions, a relative maximum in the midlatitudes (storm tracks), a minimum in the subtropical regions and the maximum of precipitation in the ITCZ. The maximum is shifted from about 15°S in winter to about 15°N in summer,

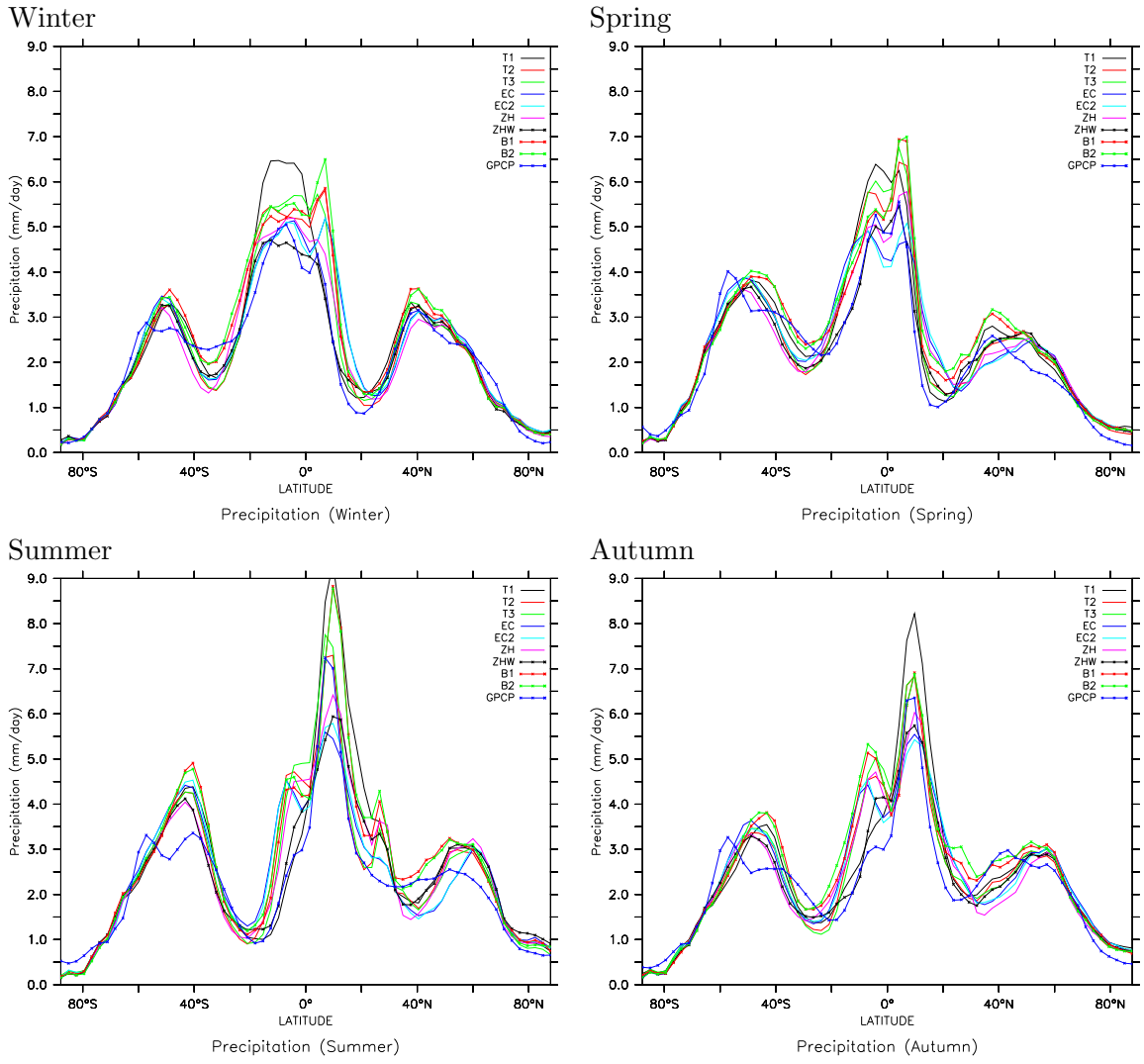

Figure 3.3: Zonal average precipitation in mm/day for the four seasons (6 year average): for boreal winter (DJF), spring (MAM), summer (JJA) and autumn (SON).

with intermediate positions in the two other seasons. This means that the annual cycle of the ITZC is well captured by all simulations.
One of the main characteristics in all seasons is that almost all schemes overestimate the maximum precipitation in the tropics, sometimes by more than 25%. This contributes significantly to the total overestimation shown in Figure 3.2.
However, in comparison with the observations the model simulations are highly correlated with respect to the zonal precipitation distribution. Since the same base model, i.e., the same formulation of all other processes, is applied, the differences between the individual simulations in the zonal averages which are determined by the global circulations are small. Despite the overestimation in the tropics by most of the convection schemes, in the midlatitudes the simulations with the different schemes behave even more similar to each other.
In the Figure 3.4 the horizontal precipitation patterns are presented for the different simulations. All schemes are able to reproduce the main characteristics of the observations. These include a sharply discernable ITCZ in the equatorial Pacific, and the maximum precipitation over the land masses in the Indonesian region. Additionally, high precipitation values are observed in Amazonia. Over the tropical central Africa there is also a maximum, but this is smaller than in the other tropical continental areas. Several regions that link the tropical with extratropical flow are distinct: from the Pacific warmpool to the storm tracks in the North and South Pacific and the South Pacific Conversion Zone (SPCZ). In the Atlantic such regions are less intense. In the midlatitudes the highest rainfall rates are observed over the oceans in the storm track areas. Most of the schemes produce high precipitation values in the tropics, especially over the warm pool region in southeast Asia.
T1 shows a region with very high rainfall over Indonesia and the Pacific Ocean east of the islands. Over the Central Pacific the ITCZ is clearly detectable and sharply separated from the surrounding regions. Heavy rainfall is simulated in Central America and the northern part of South America. Additionally, in Central Africa there is strong precipitation, even though it is significanly less than in Amazonia. An area with very high precipitation values can be found in the Himalaya and the Tibetean plateau. In the midlatitudes on the northern hemisphere the storm tracks are easy to identify: following the Gulf Stream in the North Atlantic to the Norwegian coast and from the islands of Japan to the West coast of northern Canada, describing the flow from the tropical to extratropical regions with high content of moisture evaporated from the oceans. In the southern hemisphere a precipitation band is detected at the southern end of the continents at about 50°S, with inflow regions from the Pacific warm pool and South America. The simulation T2 shows a similar picture. In contrast to T1 the heavy precipitation east of Indonesia is reduced, but in this simulation heavy rainfall west of Indonesia is calculated. The model simulation using the T3 scheme yields results close to the other two Tiedtke schemes, with no specific additional characteristics.
Applying the EC scheme in the model, there are no large differences between the EC and EC2 simulations. Therefore only EC is presented here. The strongest precipitation can be found in the Pacific ITCZ. In the Indian Ocean from Indonesia to northern Madagascar high values are uniformly simulated. In Indonesia there is much less precipitation, especially over the islands than in the other simulations, even compared to the observations. Over the tropical contintents of South America and Central Africa a good representation of the observations is found. The ITCZ in the Pacific, Atlantic and in the Indian Oceans is clearly defined, but not characterised by such strong precipitation as in the Tiedtke sim-

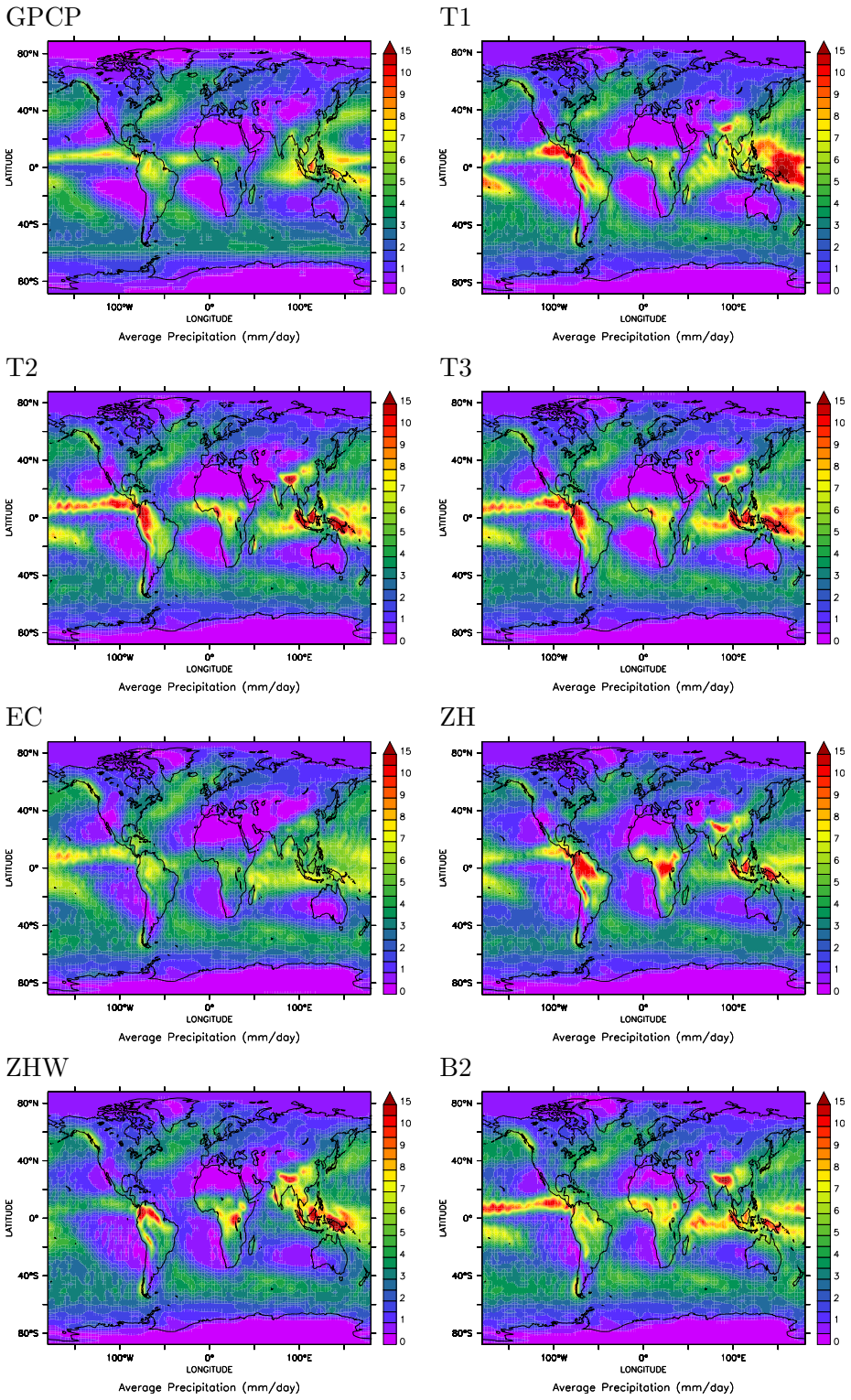

Figure 3.4: Observed and simulated horizontal distribution of precipitation in mm/day (6 year average). The upper left panel shows the GPCP (observational data), the other panels the individual simulations.

ulations. Comparable to all simulations, the ITCZ in the Atlantic is underestimated. The strong rainfall in the Himalaya reagion does not occur. The patterns in the midlatitudes are similar to the Tiedtke simulations and the observations.
In the ZH simulation again strong precipitation occurs over the land masses of Indonesia, but weaker rainfall over the ocean. In Central Africa and Amazonia high precipitation values are calculated, too. The identification of the ITCZ in the Pacific and the Indian Ocean is possible even though it is weaker than in the Tiedtke simulations, but in the Atlantic it can hardly be seen. Again strong rainfall in the Himalaya region is detected. The precipitation in the northern hemispheric storm tracks is a bit weaker than in the other schemes. The additional evaporation that is applied in the ZHW simulation reduces the maxima of the ZH simulation. This becomes most obvious in Amazonia and Central Africa, but also in the ITCZ in the Pacific and over the warm pool. The precipitation in the storm tracks, mostly produced by the Hack convection is very similar to the ZH simulation. Again, high values in the Himalaya region are calculated.
The simulations with the Bechtold schemes B1 and B2 are very similar. Thus, only B2 is shown in Figure 3.4. Again heavy rainfall over the land in the Indonesian area is computed. The ITCZ with strong rainfall is defined more sharply in the western part of the Pacific and is clearly separated over all tropical oceans. In the Indian Ocean stronger precipitation occurs, similar to T3, but it is located almost as much in the West as in EC. Central Africa and Amazonia are characterised by weaker rainfall than in the other schemes, but still significantly higher than in EC. Again, in the Himalaya highest precipitation values are simulated. The midlatitudes are captured likewise as in the Tiedtke simulations.

An evaluation of the hydrological cycle, using the convection scheme applied in T1, has been done by Hagemann et al. (2006). They conclude that the model captures the climatological precipitation quite well, but do not further investigate the overestimation in the tropics or other problems. Since the T1 simulation is almost identical to their model setup except for the resolution (they use T106 L31), similar conclusions as presented in the article of Hagemann et al. (2006) can be drawn. In their results they also mention the overestimation at steep mountain slopes (e.g., Himalaya) and the overestimation in the tropics. Therefore, the reduced horizontal resolution cannot be the major reason for the weaknesses of most simulations.

For detailed investigations of the discrepancies, the differences between the observations and the model results are shown in Figure 3.5.
For comparison the upper left panel depicts again the observations, this time on a slightly different scale. The other pictures show analogously the different model simulations, but this time the absolute difference to the observations (model simulation minus GPCP). Each difference higher than ± 5 mm/day is displayed as a difference of the highest category.
As in Figure 3.4, the T1, T2 and T3 simulations show almost the same patterns. T1 shows the strongest overestimation east of Papua New Guinea, in the Himalayan area, northeast of Madagascar in the Indian Ocean and in Central Africa. Additionally, in the western part of Amazonia and west of the coast of Central America too high rainfall values are simulated. On the other hand, west of Indonesia and in the tropical Atlantic, higher precipitation amounts are observed than predicted by the model. T2 and T3 show only similar differences to the observations as T1. In south-east Asia, the model tends to underestimate the precipitation locally, while it overestimates in the vicinity. In the

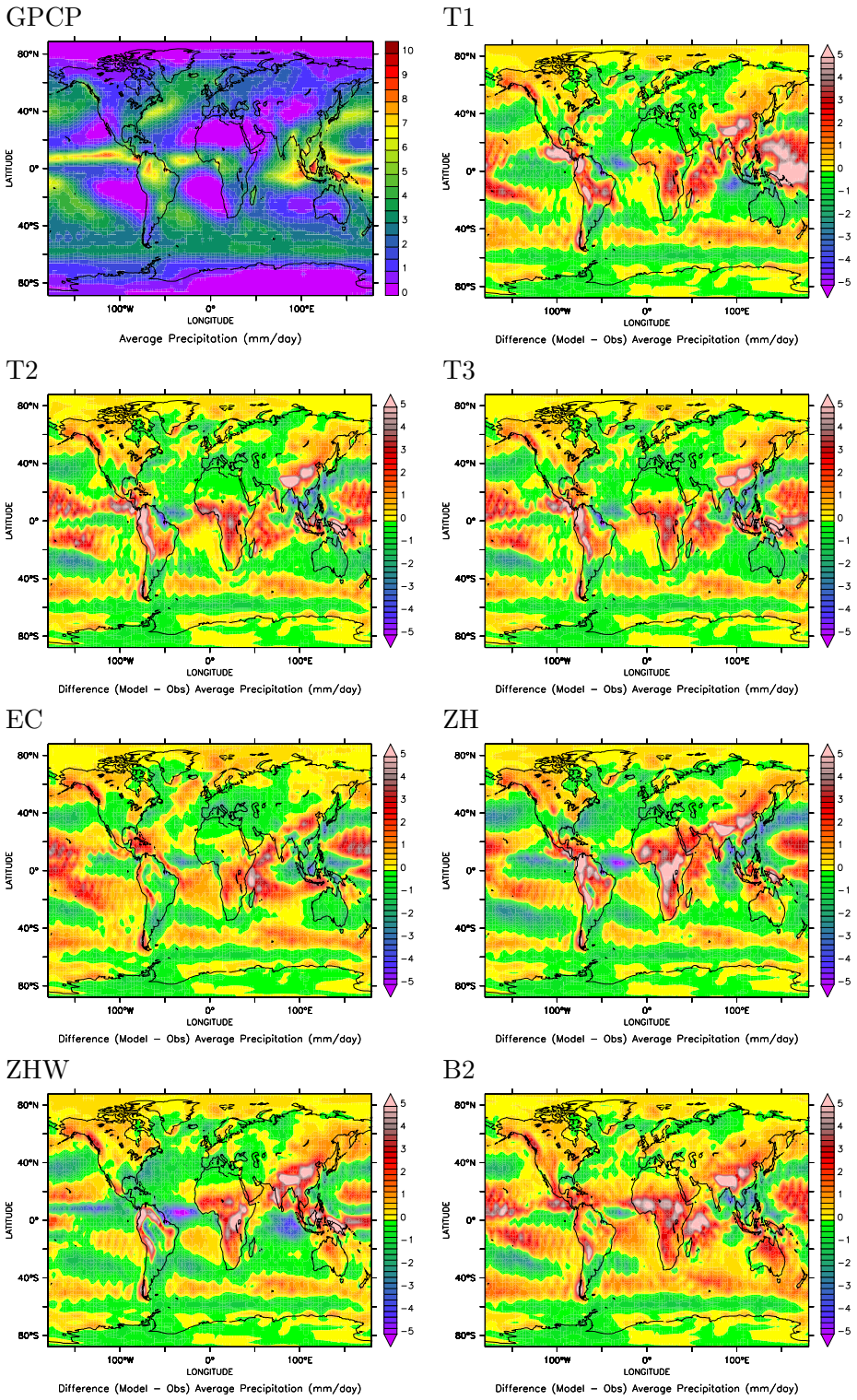

Figure 3.5: Differences (model simulation - GPCP) of the horizontal precipitation distribution in mm/day (differences between 6 year averages). The upper left panel shows the observational data, the other panels denote the differences for the individual simulations.

northern Pacific there is an underestimation detectable. On the other hand, over west Africa and also in the central Pacific an overestimation is diagnosed. The region between 20° to 40°S and 125° to 160°E is characterised by an underestimation compared to the observations of the GPCP dataset.
Even though the differences in the formulations of these three convection schemes are very small they lead to significant differences in the results. Since the formulation of the precipitation production is identical this can only be a result from the different treatment of entrainment and detrainment and the closure assumptions. Especially the frontal convection in the storm tracks of the northern hemisphere are captured better in the T1 simulation. Since the convection requires less moisture for precipitation production than the large-scale cloud parameterisation as a subgrid-scale process, it seems that the convection is significant for the total amount of rainfall in those regions, too. The more effective triggering in the T1 simulation leads to a more realistic precipitation formation.
In the simulation with the EC scheme the strong overestimation north of Madagascar is as obvious as in the tropical central Pacific. Over the Indonesian islands as well as over the tropical Atlantic a slight underestimation is simulated. On the other hand, over a large area in the SPCZ, but also several subtropical subsidence regions the precipitation is generally overestimated. This is a result of the interaction with the large-scale cloud scheme: in the subtropical subsidence areas this computes light, drizzle-like precipitation, which is not observed. Even though an overestimation in east Asia is observed it is not in the Himalaya region as in the other simulations and less significant.
The ZH scheme is characterised by the strongest differences compared to the observations: heavy overestimation over the tropical continents, but underestimation in the ITCZ over the ocean. Additionally, with this scheme the highest underestimations of all simulations in the northern Pacific storm tracks occur. To a somewhat lesser extent this can also be detected in the North Atlantic storm track close the American coast. Again in the Himalaya region too high rainfall values are simulated compared to the observations. Since this scheme consists of two separate parts (Zhang-McFarlane and Hack) it is not easy to identify which one is in general responsible for the differences to the observations. Roughly the Zhang-McFarlane part is dominant in the tropical precipitation production, while the Hack scheme has more relevance in the midlatitudes. Since the Hack scheme is basically an adjustment scheme, the moisture is adjusted until a more stabilised state of the atmosphere is reached. This happens before the precipitation production of this model simulation becomes efficient enough to reflect the observations. The differences in the tropics, mostly produced by the Zhang-McFarlane part, might originate again from the different triggering: over the continents the triggering is too fast, resulting in overestimated rainfall, while over the oceans the convection scheme is activated not often enough. Since the planetary boundary layer (PBL) height is used as one of the input parameters in the triggering, a parameterised value (the PBL height) is used as input for a second parameterisation. This is a source for large uncertainties. In the simulation with the ZHW scheme, the overestimations of ZH in South America and Central Africa are lower and cover smaller areas. On the other hand, the underestimation over the tropical oceans is more severe. The Himalaya overestimation is similar to the ZH simulation. However, the midlatitude storm tracks, especially in the North Pacific, are captured much better. Since the additional evaporation leads to a higher content of moisture in the atmosphere, which is not reduced by precipitation that efficiently, in the overestimation areas the model calculation gets closer to the observations. In the regions of underestimation the same mechanism increases the discrepancies to the observations.

The Bechtold simulations B1 and B2 (again only B2 is shown) suffer from the problem in the Himalaya region as well. Northeast of Madagascar the overestimation is as obvious as in Central Africa and in the ITCZ west of Central America. To some extent in South America there is an overestimation, too, though this is not in Amazonia, but rather shifted more to the south. On the other hand, underestimations occur as in T2 and T3 in southeast Asia and especially in the Atlantic ITCZ. In the central Pacific there is a tendency to overestimate the total rainfall. The drizzling precipitation that also occurs in the EC scheme from the large-scale cloud parameterisation is responsible for some overestimation in the subtropics.

Summary of the precipitation analysis

Most of the schemes tend to overestimate precipitation in the tropics, especially over the warm pool region in Southeast Asia. Almost all schemes behave quite similar in the midlatitudes. Even though in those regions the large-scale precipitation plays a significant role in the total rainfall, still a large fraction of the rain is produced by convective activity. Over Europe and North America almost all simulations are able to reproduce the annual average daily precipitation values of the observations. A weak point in almost all parameterisations can be found in the northern storm tracks over the Pacific Ocean. Even though its end at the North American coast is simulated well, the precipitation is underestimated in the flow from the islands of Japan to the middle of the Pacific. All simulations produce strong precipitation at the southern end of Chile on the South American coast that cannot be seen in the observations. This is independent of the choice of the convection scheme, and must therefore either be attributed to an effect caused by other components of the ECHAM5 model (an input parameter for the convection) or to a common flaw of all parameterisations. A severe problem occurs in the Himalya region for the simulations T1, T2 and T3, as well as for ZH, ZHW, and B1 and B2. There, the convection is heavily overestimated. This may be due to the orographic effects of the Tibetean plateau leading to too effective triggering of convection in that region. As already mentioned above, in the EC and Bechtold simulations the areas with very weak precipitation (< 0.5 mm/day) are not that sharply separated. These are the regions west of the southern hemisphere continent borders and also at the Californian coast, all dominated by large-scale subsidence. Additionally, light precipitation is calculated over the Arabian peninsula (also in the ZH simulations). The light precipitation in those regions originates from the large-scale cloud scheme. In the simulations this can be seen directly when only the large-scale rainfall is considered (not shown here). This may be a result of the lack or the underestimation of convection in those regions that leads to too high water vapor mixing ratios. These will trigger the large-scale cloud scheme. Almost all schemes have problems in representing the observations well based on the timescale and resolution of this model experiment. Nevertheless, the simulations EC and ZH seem to be closest to the observations in describing the total precipitation amount, while T1, EC and B2 are better with respect to the horizontal distribution. Overall, the EC scheme seems to be best suited to simulate precipitation patterns.

3.3.2.2 Statistical analysis

To achieve a more objective view of the performance of the different convection schemes, a statistical analysis (see Appendix A) is performed, calculating the mean values, the bias and the root mean square error (RMSE) compared to the observations, as well as the

Data	Mean [mm/day]	Bias [mm/day]	Bias %	RMSE [mm/day]	Correlation R^2	Slope	Intercept with y-axis
GPCP	2.62	-	-	-	-	-	-
T1	3.00	0.38	14.5	1.52	0.70	1.13	-0.01
T2	2.91	0.29	11.0	1.43	0.69	1.07	0.05
T3	2.93	0.31	11.7	1.37	0.72	1.09	0.03
EC	2.87	0.25	9.5	1.11	0.72	0.90	0.40
EC2	2.86	0.24	9.0	1.12	0.70	0.88	0.45
ZH	2.82	0.20	7.6	1.52	0.57	0.87	0.42
ZHW	2.71	0.09	9.0	1.44	0.60	0.87	0.36
B1	3.14	0.52	19.8	1.32	0.68	0.98	0.43
B2	3.21	0.59	22.5	1.33	0.67	0.98	0.46

Table 3.2: Statistics of the precipitation analysis from the model simulations compared with the GPCP observations.

correlation and the corresponding linear regression. The results are presented in Table 3.2.
The mean value of the observations is 2.62 mm/day. As already shown above in Figure 3.2, all schemes overestimate this value. The simulations EC, EC2, ZH and especially ZHW have much lower biases. The RMSE of all simulations is relatively high with the best values for the EC simulations. This indicates that the horizontal distribution is captured best by those schemes. None of the simulations is highly correlated ($R^2 > 0.8$) with the observations. Additionally, in Figure 3.6 a Taylor diagram (Taylor, 2001) is shown for the precipitation analysis relating the representation of the spatial patterns and the amplitude of the spatial variability using the standard deviation and the correlation (see Appendix A). Even though T3 and EC have the highest correlation, they are not best with respect to slope and intercept. These two parameters are best in the T2 simulation, but T3 and EC are not significantly different. However, in none of the simulations this slope is close to 1. The normalised standard deviation is close to 1 for both the EC simulations, and as mentioned above the RMSE (the distance to the point perfectly representating the observations with normalised $\sigma = 1$ and $R = 1$) is smallest. Since none of the schemes is able to perfectly reproduce statistically the precipitation observations, it is difficult to rate the 'best' convection scheme from this analysis. Each simulation tends to perform well in some regions of the Earth while in others the performance is rather poor. Nevertheless, again the EC schemes seem to perform 'relatively best in this study' because of the highest correlation together with a low bias and the best capturing of the amplitude of the spatial variation.

3.3.2.3 Integrated water vapour column

The next parameter under investigation is the vertically integrated water vapour column (IWVC). With the help of this quantity it is possible to decide whether the whole hydrological cycle is still in balance or if the atmosphere in general becomes too moist or too dry. The IWVC can be observed from space with satellite measurements and therefore a complete global dataset can be retrieved. Since the water vapour concentrations in the stratosphere are very low, it can be assumed that almost 100% of the vertically integrated H_2O is located in the troposphere. The observational data originate from the

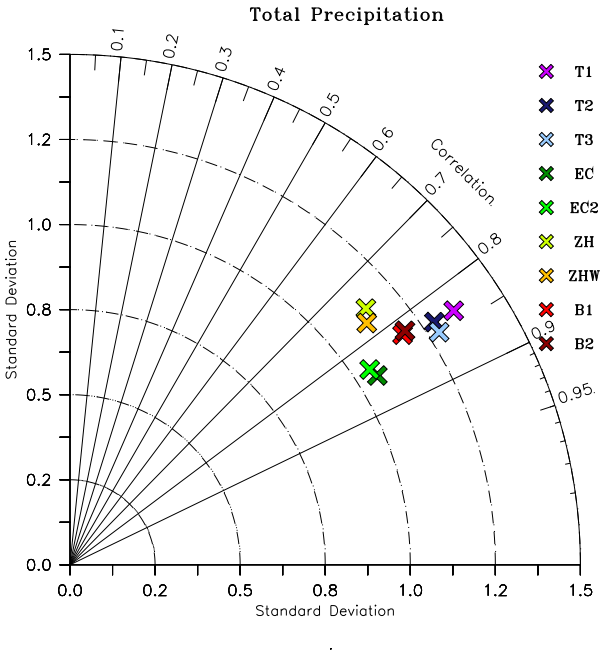

Figure 3.6: Taylor diagram for the average total global precipitation. The standard deviation of the model calculations is normalised with the observational standard deviation. The various simulations are indicated by different colors.

Global Ozone Monitoring Experiment (GOME, Burrows et al. (1999)) on the Second European Remote Sensing Satellite (ERS-2). The retrieval of the water vapour is described by Noël et al. (1999). In addition to the GOME measurements, data from Special Sensor Microwave/Imager (SSM/I, Wentz (1997, and references therein) is used in the dataset. A detailed description of the dataset of the IWVC can be found in Lang and Lawrence (2005b, and references therein). The observational data is given as monthly average values starting in August 1995 until August 2002. Climatological values are compiled from the data as well as from the model simulations.
In Figure 3.7 the zonal average of the modelled and observed IWVC from a six year climatology is shown. In winter (left panel), in the southern hemisphere all the simulations fit quite well to the observations. Only in the tropics the observed values are a bit higher than in the simulations, with ZHW and the ECs being the exception, instead overestimating the observed IWVC values. The T1 simulation is closest, while in most other simulations the total value is underestimated by almost 0.5 cm, i.e., about 10%. Additionally, the maximum water vapour column is shifted by 5° to 10° northwards to the equator. In the northern hemisphere at about 40°N all the simulations overestimate the observed IWVC. Except in the tropics, the shape of the observations is reproduced almost identically by all the applied convection schemes. In summer, on the other hand (right panel of Figure 3.7), the simulations with exchanged convection schemes behave differently. First of all, in the southern hemisphere at about 40°S they overestimate by almost 0.5 cm, which is close to 30%. In the tropics, some schemes are able to correctly reproduce the maxima (T2, B1) while others overestimate (T1, T3, EC, EC2, and significantly ZHW) or underestimate (B2 and ZH). In the northern hemisphere north of 40°N the simulations with the individual convection schemes are not that uniform any more, but show a spread of almost 0.6 cm, which is up to 40%. Some schemes fit well with the observations (B1 and

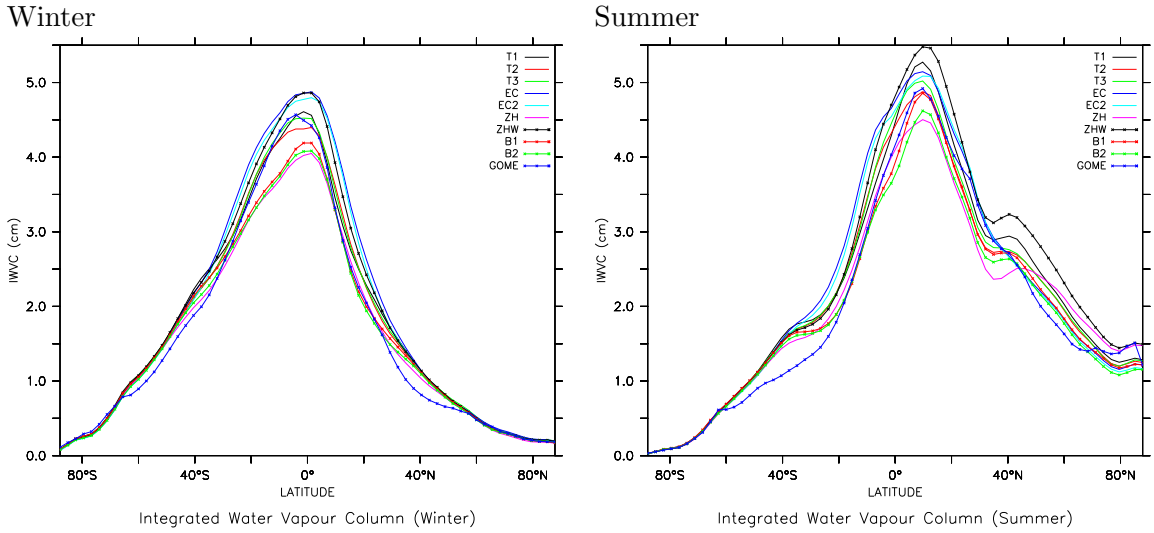

Figure 3.7: Zonal average values of the IWVC in cm for winter (DJF) (left) and summer (JJA) (right).

B2) in that region, others overestimate significantly (T1 and ZH, ZHW even worse) and others underestimate the absolute values of the observed IWVC (EC). Especially in the polar regions there are large discrepancies, but these should be treated with care, since also the observations close to the pole with satellite retrievals have high uncertainties. All simulations produce a secondary maximum in summer around 40°N, not found in the observations.

Additionally, the horizontal distribution is examined here. For that purpose the 6 year annual average IWVC of the observations and the model simulations are shown in Figure 3.8. The isolines depict the observations from the GOME/SSMI dataset. The upper left panel shows the highest water vapour column values in the tropics, as expected from Figure 3.7. The maximum values are above 5.5 cm. Polewards the IWVC values show a strong gradient. The subsidence regions, characterised by almost no precipitation in Figure 3.4, can also be detected in this figure. They are characterised by low IWVC values. Because of the subsidence, the exchange of moisture with higher altitude is limited, even though the evaporation is substantial. The highest values occur over the ocean in the convergence regions (ITCZ, warm pool, and SPCZ), where the ocean as an unlimited reservoir of atmospheric moisture representing a strong source overlaps with the effects of the transport of moisture from the subtropics (Trenberth and Stepaniak, 2003). Especially the warm pool east of Indonesia, characterised by strongest convection, i.e., convergence of air masses, shows the highest moisture content.

The T1 simulation creates a pattern that looks quite similar and captures all the characteristics of the observations. Nevertheless, in most of the tropics the IWVC is slightly higher than in the observations, especially over the warm pool and most parts of the ITCZ over the oceans. This is also the case over central Amazonia. In the midlatitudes even smaller regional patterns are simulated well compared to the satellite data, e.g., the low values over North America originating from the influences of dry polar air currents.

Again the mean characteristics can be reproduced by the EC simulations. Even though in these simulations in the tropics the horizontal distribution is spatially consistent with the observations, slightly higher values are achieved. These higher values in the tropics cause

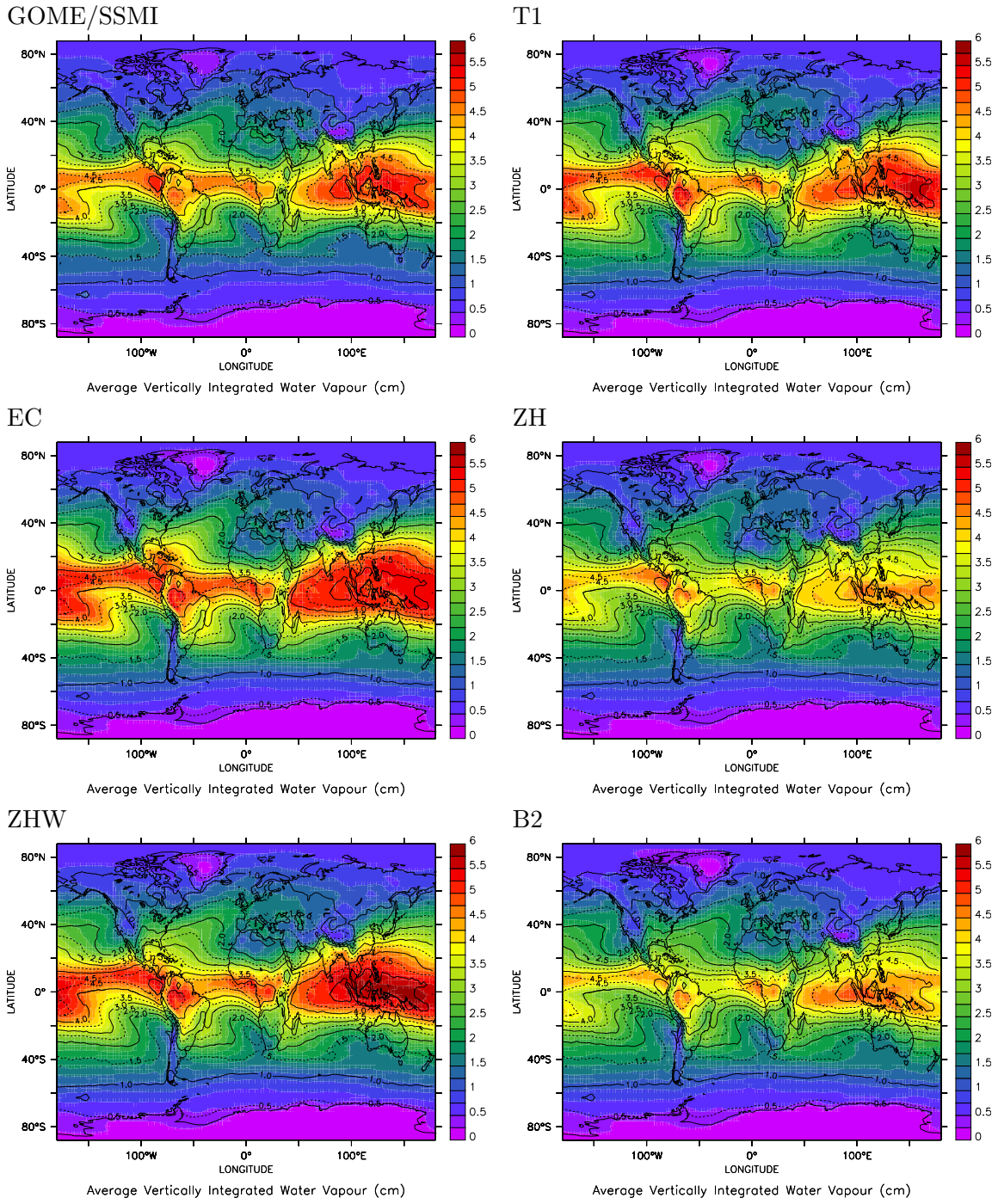

Figure 3.8: Horizontal distribution of the annual average of the IWVC (cm) of the model simulation (colors) and the observations (isolines). The observations are displayed in the upper left panel, the individual model simulations in the other panels.

consistently higher values further polewards, too. This is consistent with the modelled weaker precipitation compared to the T1 simulation (compare Figure 3.4).
With the ZH convection scheme lower values are calculated in the tropics, but a good representation is found in the midlatitudes and polar regions. In the tropics the underes-

Name	Mean [cm]	Bias [cm]	Bias %	RMSE [cm]	Correlation R^2	Slope	Intercept with y-axis
GOME	2.33	-	-	-	-	-	-
T1	2.51	0.17	7.4	0.30	0.94	1.01	0.13
T2	2.44	0.11	4.8	0.28	0.94	0.97	0.16
T3	2.48	0.15	6.3	0.27	0.94	0.99	0.14
EC	2.66	0.33	14.2	0.36	0.94	1.09	0.09
EC2	2.62	0.28	12.2	0.33	0.94	1.07	0.08
ZH	2.26	-0.07	-3.0	0.35	0.91	0.86	0.23
ZHW	2.67	0.34	14.4	0.31	0.95	1.09	0.10
B1	2.31	-0.02	-0.7	0.33	0.93	0.90	0.19
B2	2.25	-0.09	-3.7	0.35	0.92	0.87	0.19

Table 3.3: Statistics of the IWVC analysis of the model simulations compared with the GOME/SSMI observations.

timation is significant, as already seen in Figure 3.7 for all seasons. Again, the meridional distribution patterns are similar to both observations and the other model simulations. In the ZHW simulation the patterns of the observations are reproduced, too. Especially in the tropics, but also in midlatitudes generally the IWVC has much higher values than in the other simulations. The effect is most obvious in the tropics and from there it spreads out into the midlatitudes of both hemispheres. This feature is also visible in Figure 3.7.
The B2 simulation also exhibits the problem of underestimation of the IWVC over the tropical oceans while over the continents the values are almost correct. Again, this is self-consistent, because the precipitation is generally overestimated (compare Figure 3.4): too much rain is produced, resulting in too low values of the remaining water vapour.
All simulations are able to reproduce the observational patterns of the IWVC even though the values are usually a bit lower in the tropics. Overall it seems that the ZH and the B2 scheme tend to underestimate the IWVC, while the EC schemes and especially ZHW overestimate the moisture content of the atmosphere. It is remarkable that the exchange of the convection scheme, which yields strong effects in the precipitation, seems to have only a small effect on the average IWVC spatial distribution patterns. On the other hand, the absolute values are highly dependent on the choice of the convection scheme.
Table 3.3 shows the statistical analysis for the integrated water vapour column values. The mean value for the observation is 2.33 cm. Except the ZH, B1 and B2 simulations all the others show a positive bias in the order of a few %. As mentioned above, ZHW heavily overestimates and therefore shows a large positive bias, but the EC simulation is almost similar in the overestimation resulting from more widespread higher IWVC values. The overestimation is located mainly in the tropics, but the decreasing gradient towards the poles is of similar strength in the observations and all simultaions leading to a shift of higher values polewards. The RMSE is relatively small (best for T3) and the correlation with all values being above 0.91 quite high (best for ZHW), indicating a good representation of the patterns. This is further supported by almost unity slope and only small offsets (best for T1 and T3). A remarkable result from the statisical analysis is that the correlation is best for the ZWH simulation, with the slope much worse than other simulations: this confirms that a high correlation on its own does not necessarily mean best results; the bias needs to be taken into account as well. Even though in Figure 3.8 the B2

simulation seems to heavily underestimate the IWVC values, the statistical analysis shows that the underestimation is less significant; only the maximum values in the tropics are underestimated while in the extratropics the IWVC is overestimated. A best performing scheme cannot be derived from this analysis, although it must be mentioned that only the EC and ZHW schemes have biases in excess of 10%.

3.3.2.4 Evaporation

To 'close' the atmospheric hydrological cycle, the evaporation is also analysed. This quantity can be measured only locally and shows a strong heterogeneity. A global dataset of evaporation fluxes to evaluate a GCM does not exist at present. Therefore only the different simulations can be compared. For the statistical analysis the T1 simulation is chosen as the reference, since this convection scheme and its performance have been validated in the climate studies of Roeckner et al. (2004).
The upper left panel of Figure 3.9 shows the daily average evaporation flux of the T1 simulation taken from the six year climatology. The main water vapour sources for the atmosphere, i.e., regions with high evaporation fluxes, are over the quasi-unlimited moisture reservoir of the oceans. They are located in regions with high sea surface temperature (SST): the tropical and subtropical areas, but not directly in the ITCZ. As mentioned above the water vapour is transported towards the ITCZ from the subtropics. Additionally, relatively high evaporation is calculated over the rain forest of Amazonia. The Sahara, the deserts of Arabia and Mongolia as well as the North and South American deserts are characterised by almost zero evaporation. With the decrease of solar radiation fluxes towards the poles the evaporation shows a corresponding gradient. White regions, which occur on the map in Greenland and Antarctica, depict areas where the evaporation is negative, i.e., water vapour does not evaporate from the ice, but rather condenses on it. However, the latter fluxes are very small. The isolines in all pictures show the evaporation from the T1 simulation as a reference.
Even though the T2 simulation also uses the Tiedtke approach, the evaporation shows differences, mostly calculating lower values. The maxima are located in the same positions. The simulation with the EC scheme (middle left panel) yields slightly different results. In the Indian Ocean the evaporation is lower by more than 10%; this is similar in the west Pacific and in the SPCZ region. In the east Pacific of the northern hemisphere even higher values than in the T1 simulation occur. The evaporation over the tropical continents is slightly lower explaining the smaller precipitation fluxes of these regions, which correspond better to the observations of the GPCP data (compare Figure 3.4).
The ZH simulation, presented in the middle right panel, shows the same patterns as T1, but has remarkably lower values than the reference simulation. Since the maxima are located in the same positions there is only a significant bias resulting in overall lower total evaporation. Again, this is consistent with the overall lower simulated precipitation fluxes. The evaporation in the ZHW simulation is even lower than in the ZH simulation, and therefore significantly lower than in T1, though the patterns are still well-correlated. Especially over the tropical continents the evaporation yields lower values than ZH, resulting in the reduction of the precipitation in those regions (compare Figure 3.4).
The patterns of T1 are also produced by the B2 simulation (lower right panel). However, the areas with low evaporation are not as sharply distinct as in the T1 simulation, resulting in the weak precipitation that is diagnosed for these regions. The maxima are located in the same positions, even though they are lower than in T1, too. However, the

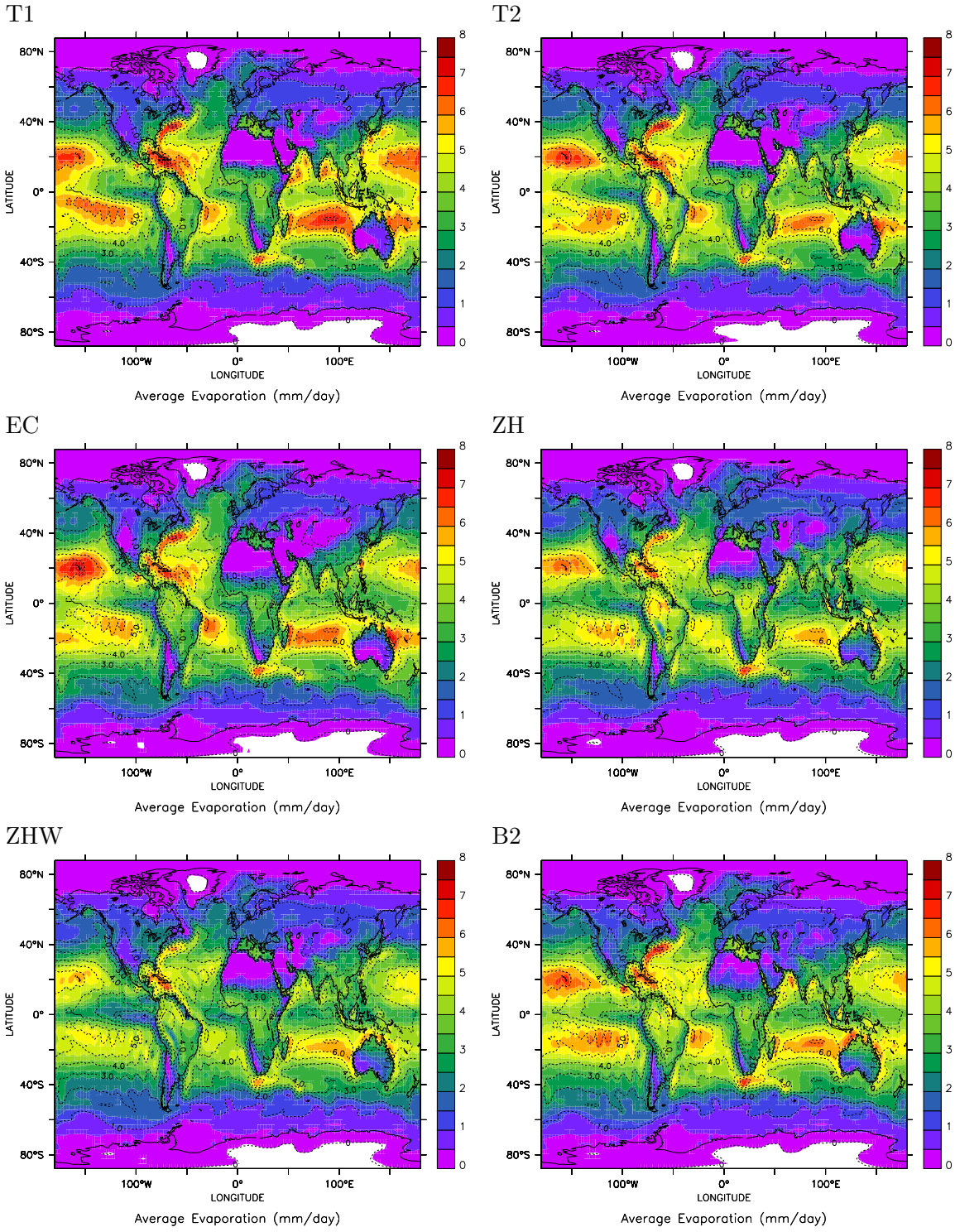

Figure 3.9: 6 year average evaporation fluxes of the model simulations in mm/day for the different simulations. The isolines depict the values of the reference simulation T1.

poleward gradient is not that steep in this simulation, resulting in stronger evaporation in the midlatitudes.
Overall, the patterns are reproduced very similarly, but with the alternative convection

Data	Mean [mm/day]	Bias [mm/day]	Bias %	RMSE [mm/day]	Correlation R^2	Slope	Intercept with y-axis
T1	3.00	-	-	-	-	-	-
T2	2.90	-0.10	-3.2	0.42	0.97	0.94	0.08
T3	2.93	-0.07	-2.4	0.34	0.98	0.96	0.05
EC	2.94	-0.06	-1.9	0.52	0.95	0.93	0.16
EC2	2.91	-0.09	-3.0	0.55	0.94	0.91	0.18
ZH	2.83	-0.17	-5.8	0.74	0.91	0.84	0.25
ZHW	2.68	-0.32	-10.7	0.62	0.94	0.82	0.20
B1	2.95	-0.05	-1.7	0.59	0.94	0.88	0.23
B2	3.05	0.05	1.7	0.57	0.94	0.92	0.23

Table 3.4: Statistics of the evaporation analysis of the model simulations compared to the T1 simulation.

schemes the total evaporation seems to be lower than in the reference simulation T1. To quantifiy these results, the statistics are summarised in Table 3.4. The highest mean values are calculated in the B2 simulation, the reference T1 is slightly lower. The differences in the global means show relatively a high variability (about 15% differences from the lowest (ZHW) to the highest average evaporation (B2)). This results in a different moisture source for the atmosphere, which consequently explains some of the variability detected in the precipitation analysis. The patterns are reproduced very well, resulting in high correlations ($R^2 > 0.9$) and a good linear regression for all the simulations. Only the extreme values of the T1 scheme are less sharply distinct in most of the other simulations, e.g., the maximum evaporation of the B2 simulation is significantly lower than in T1, although the mean value is even higher.

3.3.2.5 Effects on temperature

Since the exchange of the convection scheme is generally a strong modification of the model physics of a GCM, it must be investigated how strongly the simulated climate system is affected. Therefore, in addition to the hydrological cycle, the three dimensional temperature fields are analysed. For that purpose, the results of T1 are taken as the reference, since it is very similar to the climate setup of the investigations by Roeckner et al. (2004). During the evaluation process, this model is 'tuned' to reflect a temperature distribution and an energy budget close to observations by modifications of the longwave radiation parameterisation. Note that the SSTs are prescribed and the same for all simulations, which suppresses some of the model differences.
In order to investigate the 'climate change' resulting from the application of alternative convection schemes the 3D - temperature is analysed. This is done by a correlation analysis of the monthly mean temperatures at all altitudes. Since the schemes T1, T2, T3 and B1, B2 and EC, EC2 do not differ much in terms of precipitation and T1 is used as the reference climate, this analysis is shown for the EC, ZH, ZHW and B2 simulations only.
In Figure 3.10 the monthly mean temperatures of T1 on the horizontal axes are compared with the corresponding values of EC, ZH, ZHW and B2 on the vertical axes. For this graph, all the temperatures are averaged onto a $10^\circ \times 10^\circ$ grid in all model levels. Additionally the correlation and the linear regression between reference simulation (T1) and one with an alternative scheme are shown. Since the linear regression is very close

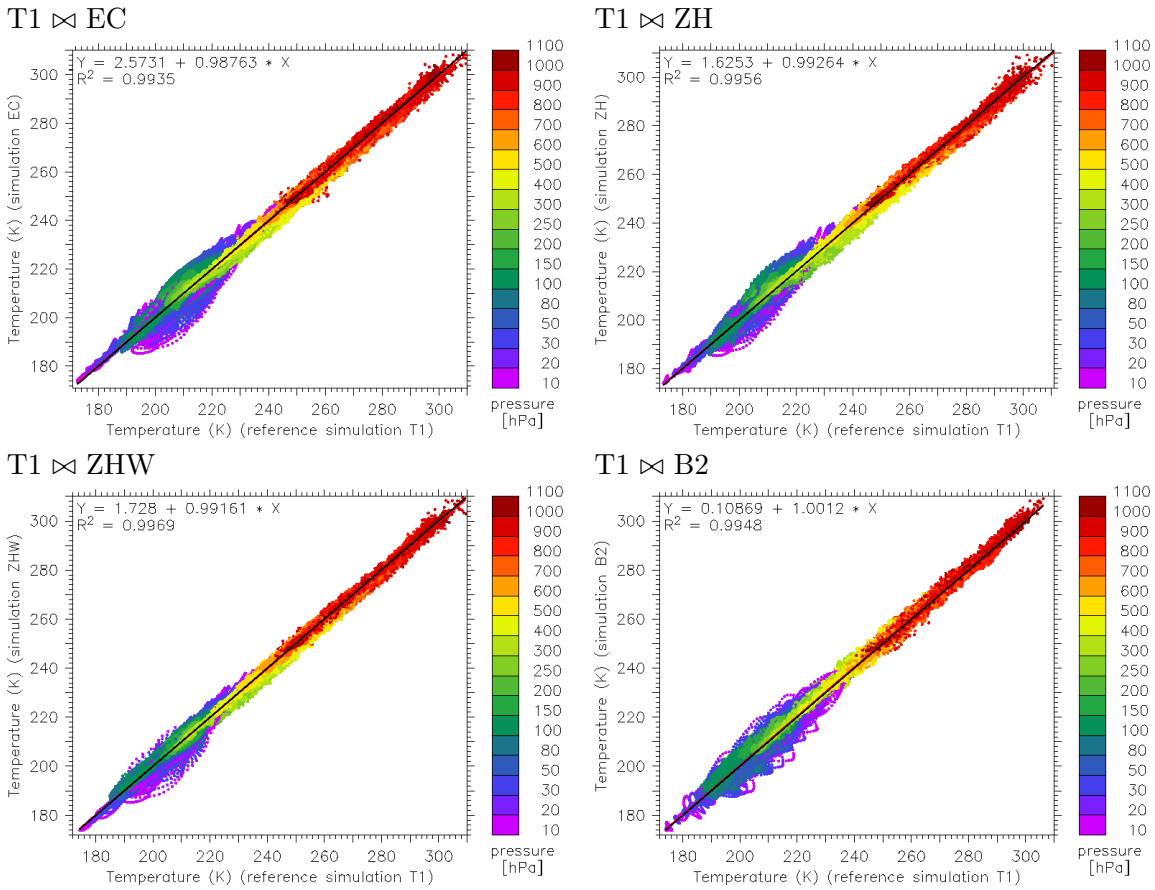

Figure 3.10: Correlation of the monthly mean temperatures with the reference simulation T1, color-coded with the pressure altitude for the simulations EC, ZH, ZHW, and B2.

to the ideal (one-by-one, black line) correlation with no offset, their differences are hardly distinguishable. The color-coding represents the corresponding pressure height (in hPa) of the grid boxes.

This analysis is performed for the whole model atmosphere, even though the stratosphere is probably less influenced directly by the selected convection scheme. If there would be large differences that will deteriorate the simulated climate of the stratosphere, the scheme will not be applicable in this model setup. As a consequence, the correlation at higher altitudes should be almost equal to 1. However, the transport of water vapour into the upper troposphere by convection is dependent on the selected parameterisation, and consequently a different distribution in the lower tropical stratosphere is possible.

The overall correlation is very high ($R^2 > 0.993$) for all simulations. The slope of the linear regression is close to one, with small variation for the individual simulations. The differences in the intercept are slightly higher, except for B2 with almost no offset. This shows that the overall temperature is not significantly disturbed (< 5 K variability) when a different convection parameterisation is used. On the other hand the varying offset indicates that there is some variation due to the selected scheme.

The upper left panel of Figure 3.10 depicts a high variation in the tropopause region and a little aloft. This refers to a different injection of tropospheric air masses into the upper troposphere and lower stratosphere (UTLS). A possible consequence is a changed water

Simulation Name	Correlation R^2	Slope	Intercept with y-axis
T1	-	-	-
T2	0.997	0.999	0.50
T3	0.997	0.996	1.10
EC	0.994	0.988	2.57
EC2	0.995	0.992	1.76
ZH	0.996	0.993	1.63
ZHW	0.997	0.992	1.73
B1	0.996	0.992	2.27
B2	0.995	1.001	0.11

Table 3.5: Statistics of the temperature (as in Figure 3.10) of the model simulations compared with the T1 reference simulation.

vapour content in this UTLS region, that can result in strong changes of the temperature patterns influenced by the radiation. The panel on the upper right (T1 $\bowtie$ ZH) shows a slightly stronger variation and a shift to higher temperatures above 295 K. This is equivalent to the lower troposphere regions, especially the surface and the boundary layer. Since convection and its triggering play a major role in the formulation of boundary layer parameterisations there is a strong coupling with the exchange of sensible and latent heat and a feedback on the intensity of the convection itself. Again, there is large variation in the UTLS region.
The correlation plot in the lower left panel of Figure 3.10 shows a slightly lower variation in the lower atmosphere, while in the upper atmosphere the picture is is very similar compared to the ZH correlation. This means that the temperature changes of the surface temperature will be less significant.
The lower right panel again shows only small variation in the lower atmosphere, but high variation in the upper troposphere and lower stratosphere.

As will be explained in detail in the transport section (see Chapter 4), the Tiedtke scheme indeed shows weaker transport of air into the tropical tropopause region and the convection does not reach up that deep as in the simulations with the alternative convection parameterisations. This is consistent with higher values of water vapour in the UTLS region (pictures are not shown), that occur in most other simulations.
The corresponding statistics (for all model layers) for all the simulations are listed in Table 3.5. In summary, the overall correlation is almost one, indicating a weak dependence of the global temperature on the choice of the convection scheme.
The small differences in the mean, vertically averaged temperature of the model atmosphere and the small bias show that the energy budget of the atmosphere is not severely disturbed. These results are presented in Table 3.6. The almost perfect correlation and the low RMSE values indicate that the global climate is not changed much by the exchange of the convection scheme.
However, the intercept with the y-axis shows high offset of up to 25 K, indicating some influence on the local temperature, even though it is not of that magnitude.
A second indication for local temperature changes originates from the broadness of the correlation plots of Figure 3.10. Even though the linear regression is almost perfect, a

Simulation Name	Mean [K]	Bias [K]	RMSE [K]	Correlation R^2	Slope	Intercept with y-axis
T1	245.8	-	-	-	-	-
T2	245.6	-0.14	0.39	0.998	1.04	-9.24
T3	245.9	0.11	0.44	0.999	1.05	-11.59
EC	246.6	0.79	0.82	0.998	1.10	-24.72
EC2	246.2	0.46	0.72	0.998	1.09	-21.10
ZH	246.0	0.27	0.55	0.997	1.05	-12.93
ZHW	246.1	0.30	0.42	0.997	1.02	-4.15
B1	245.3	-0.50	0.30	0.998	0.98	3.42
B2	245.0	-0.78	0.32	0.999	0.98	4.02

Table 3.6: Statistics of the vertical average temperature analysis of the model simulations compared with the T1 simulation.

Simulation Name	Mean [K]	Bias [K]	RMSE [K]	Correlation R^2	Slope	Intercept with y-axis
T1	287.3	-	-	-	-	-
T2	287.2	-0.10	0.49	0.99	1.01	-3.64
T3	287.3	-0.00	0.42	0.99	1.01	-3.17
EC	287.0	-0.30	0.97	1.00	1.01	-3.74
EC2	286.8	-0.49	0.96	1.00	0.99	2.47
ZH	287.0	-0.26	0.94	0.99	1.00	-1.33
ZHW	287.1	-0.19	0.85	0.99	1.00	-0.59
B1	286.9	-0.40	0.65	0.99	0.99	1.14
B2	286.6	-0.66	0.80	0.99	1.00	-1.17

Table 3.7: Statistics of the temperature in the lowest model level of the model simulations compared with the T1 simulation.

range of ±5 K is visible.
Therefore, the change in the temperature close to the surface is investigated next. Table 3.7 lists the calculated statistics for the temperature of the lowest model level, i.e., usually about 70 m above the surface. The maximum change in the mean 'surface' temperature is 0.7 K globally, but most of the simulations calculate smaller differences. The correlation is almost one, and the RMSE is relatively small. Even though a direct comparison is not possible, the observations of the last century of climated change indicated by an increasing temperature of 0.6 ± 0.2 K over the last 100 years as referenced in the IPCC report (Houghton et al., 2001), are of the same magnitude as the calculated values from the different model simulations. This indicates that the uncertainties resulting from the convection parameterisations are as high as from several other processes and should be considered for climate modelling.

The horizontal temperature differences close to the surface compared to the T1 simulation are shown in Figure 3.11. As before, climatological 6-year averages of the different simulations are compared.
For an overall impression on the average 'surface' temperature field, the values of the ref-

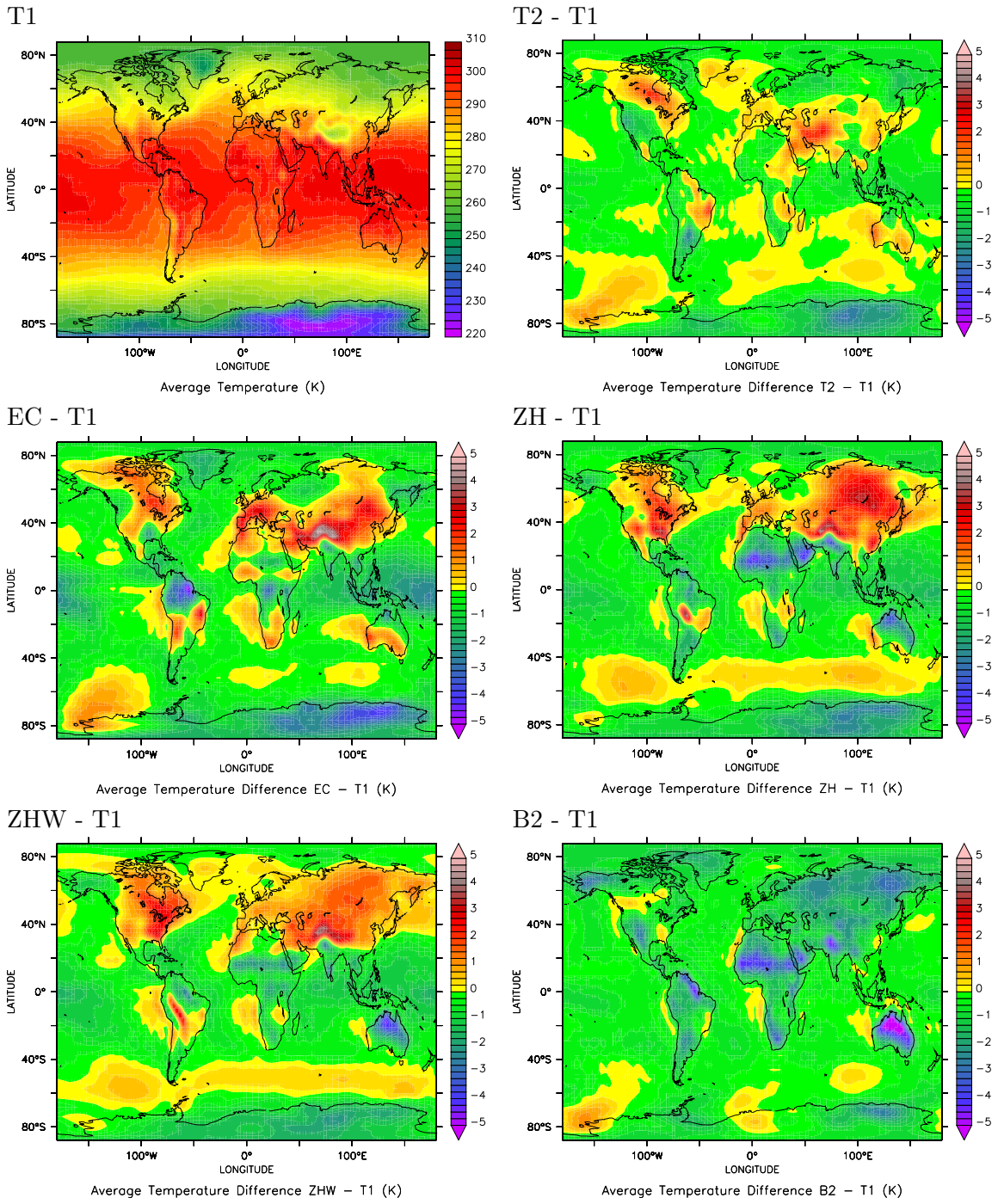

Figure 3.11: Climatological temperature in the lowest model level of the reference simulation (upper left panel) and the differences (Alternative convection scheme - Reference Setup) to the simulations with other convection schemes for T2, EC, ZH, ZHW and B2.

erence simulation are shown in the upper left panel.
The T2 simulation (upper right panel) results locally in differences of already up to 2 K, even though the convection parameterisation is very similar to the reference T1. The largest changes are in western Russia and eastern Siberia as well as in central North

America, i.e., in these regions the T2 simulation results in lower temperatures. Higher temperatures than in the reference experiment are calculated in Alaska, Central Africa and eastern China.
The changes, using the EC simulation, are much more distinct. As seen from the statistics of Table 3.7 the global mean is only 0.3 K lower. Nevertheless, regions with differences of about ±5 K occur. Lower values are calculated in Antarctica, the warm pool region east of Indonesia, Amazonia and to lesser extent Central Africa. On the other hand higher temperatures than in the reference simulation are calculated for northern Canada and central Asia, especially the Tibetean plateau, and central Europe. Over almost all oceans the temperature is slightly lower than in the reference simulation. The local differences are much higher than indicated by the 0.3 K of the global mean value.
The simulation with the ZH scheme, with almost the same bias as the EC scheme, shows again some regions with considerably lower values (up to 4 K difference) than T1 in northern Africa and Australia. As before, over the oceans the surface temperature is lower as in the T1 reference, except in the northern and southern storm tracks. On the other hand, higher values are obtained in central Asia, Siberia, North America and central South America.
The results for ZHW are similar, but the absolute differences are mostly lower both for increases and decreases of the 'surface' temperature. Neither the changes in northern Africa nor in Siberia are that large. Only north of India, locally higher temperatures than in ZH are simulated.
The B2 simulation with the highest bias of -0.66 K shows almost nowhere regions with higher surface temperatures than the reference simulation. The largest differences in the temperature fields of the B2 simulation occur in northern Australia, northern Africa and Siberia. On the other hand, only in the subsidence regions at continental shores slightly higher temperatures than in the reference simulation are calculated. Even though all over the globe the differences are less extreme, the lower values almost everywhere cause the calculated bias.
It should be mentioned that the sea surface temperature is consistently prescribed as a boundary condition in all the simulations. Therefore, the main differences in the temperature of the lowest model level consequently occur over the continents as analysed. In the EC simulation the differences over the oceans are larger than in the other calculations. This can be explained by the different treatment of the sensible and latent heat fluxes and their importance for the convection triggering using the Grant and Brown (1999) closure.
Overall, the global 'surface' temperature shows strong variations dependent on the choice of the convection scheme, but represents still a very sreasonable, stable state of the atmosphere within the uncertainties of global long-term measurements. No drift to higher or lower temperatures during the simulation period has been detected.

3.4 Discussion

The present investigations show the dependence of precipitation patterns on the convection parameterisation. A large dependence has been detected, not only on a day-to-day basis, but also for long-term averages. For consistency, the IWVC and temperature have been analysed.
First of all, it is important to mention that all alternative convection schemes are applied without any 'tuning' of the GCM to predict present day climate. Note that the T1 scheme is applied as standard scheme in the ECHAM5 model and therefore the model system has

been tuned (Roeckner et al., 2004). This has been the reason for selecting T1 as reference simulation in the comparisons. Usually, during the evaluation procedure of a GCM, some parameters in the longwave radiation scheme are modified, until a realistic energy budget of the atmosphere is achieved. This 'tuning' is always critical, because in principle it is only valid for one specific simulation setup. A change in solar activity, an increasing CO_2 concentration, a different land-use inventory or the application of nudging techniques can destroy this tuning by efficiently modifying existing or even adding an additional energy term (positive or negative) into the system. Especially for calculating scenarios, such a 'tuning' is not possible because of the lack of knowlegde about the future state of the atmosphere. Therefore its influence should be as small as possible. The result that no additional tuning of the energy budget is required to maintain stability of the simulated present day climate with different convection parameterisations supports the physical consistence of the ECHAM5/MESSy model system.
In none of the simulations a long term drift towards higher or lower temperatures or precipitation values has been detected. Therefore it is concluded that all schemes are able to produce a stable atmospheric state.
Even though the system maintains stability, the global average temperature close to the surface is changed significantly (see Figure 3.11) by exchanging the convection parameterisation. This illustrates some of the uncertainty in modelling the present day atmosphere. A question that comes up should be mentioned here is: How do the alternative convection schemes perform under perturbed conditions, e.g., a CO_2-doubling? From this study this cannot be answered and therefore an extrapolation of the variation in the surface temperatures of this study to future scenario calculations is not allowed.
The temperature changes for present day calculations with alternative convection schemes are in the same range as the observed temperature increase within the last century as mentioned by Houghton et al. (2001). Therefore, it should be an aspect considered carefully that a change of the same magnitude is proposed as a possible change of surface temperatures in the calculation of future scenarios with other climate models, as mentioned in the IPCC-report (Houghton et al., 2001). Relative changes owing to model forcings may still be relevant and significant. However, if a modification of the model physics by exchanging the convection parameterisation yields results that show uncertainties of the same magnitude without any 'tuning' of the model, the absolute values of such a scenario temperature change may not be (statistically) significant. This study tries to points out the uncertainties in the model physics dependent on only one of the parameterised processes, i.e., the subgrid-scale convection.
Even if the model with an alternative convection scheme is 'tuned' in the usual way, it cannot be guaranteed, that a similar change in the surface temperatures is achieved due to the reasons mentioned above. For long time integration periods over several hundred years, such a tuning is probably useful or required, but at least on the relatively short timescales of this study, this seems not necessary.
In addition to the temperature, the dependence of the precipitation patterns on the choice of the convection scheme is substantial. Although an interannual variability is present, no trend of decreasing or increasing global precipitation from year to year in any of the schemes occured. Therefore it seems that in terms of the water budget the system is also stable.
With respect to the precipitation it is difficult to judge which scheme performs best under the given conditions of this simulation. Even though the T1 and B2 simulations overestimate the total precipitation by far, the patterns of the observations are reproduced quite

well. On the other hand, the ZH schemes (ZH and ZHW) which reproduces best the total precipitation amount show weaknesses in the horizontal distribution. The EC simulations (EC and EC2) *perform best in this study* when both the total amount and the horizontal distribution are taken into account, both qualitatively and by statistical analysis.
The analysis for the detailed reasons for the large local differences go beyond the scope of the study. However, the different trigger mechanisms for the individual schemes (i.e., one scheme might activate the convection calculations in a specific gridbox and another does not, even though the vertical profile is identical) and the different simplified descriptions of the microphysical processes are likely the sources of discrepancies. Such an evaulation would be better performed in single column model experiments, with fixed prescribed boundary conditions, because in a GCM a difference to a reference simulation occuring in one timestep in one grid box will result in different conditions in every grid box later on because of the non-linearity of such a coupled model. However, Xie et al. (2002) in their SCM study also conclude that the different trigger mechanisms play an important role.
Additionally, it must be admitted that the GPCP dataset for precipitation is not the only global rainfall observation inventory. There is also the Merged Analysis of Precipitation dataset from the Climate Prediction Center (CMAP) (Xie and Arkin, 1997), which additionally includes model simulation output. If this dataset were to be taken as the reference observations, the results of the comparison with observations possibly would be different. Nevertheless, the differences of the results between the individual schemes would still remain. This is true also for the water vapour column as compared with the selected satellite data set.
The extension of Wilcox (2003) in the ZHW simulation results in an improvement in the precipitation patterns compared to ZH, but in contrast to the results of Lang and Lawrence (2005a) the IWVC is notably overestimated, though better correlated to the observations. Therefore this extension seems not to be generally appropriate, but apparently depends on the interactions with other physical parameterisations in the model.
This issue seems to be important for all applied convection schemes, because most of them require input parameteres from other physical processes, e.g., exchanges of moisture and energy with the surface, boundary layer processes, interactions with large-scale condensation processes and radiation. Therefore it is difficult to judge a convection scheme in a global model on its own.
In conclusion, it can be stated that an exchange of the convection parameterisation yields a stable system of the atmosphere with large local variations compared to the standard ECHAM5 model. This indicates the large uncertainty resulting from the convection parameterisations that could be conceived as an 'error bar' for the influence of convective activity. Especially for regional climate impact studies, the high variability of the 'surface' temperature requires a detailed analysis of the uncertainties originating from the convection parameterisations to improve the models performance with respect to convective activity.

Chapter 4

Convective Transport

4.1 Overview

The issue of convective tracer transport is less frequently addressed in the literature than convection itself. Generally, chemical species are transported following the same mechanism as water vapour and air masses along with the calculated convective mass fluxes, e.g., as described for momentum in the modifications of the Tiedtke (1989) scheme by Nordeng (1994).
This approach using bulk quantities originates from the concept of Yanai et al. (1973) and is applied in most GCM convection transport mechanisms. As a result from combined observations and model studies it is concluded, that most of the properties of convective clouds can be described sufficiently well by using their bulk quantities. Convection schemes using 'the ensemble of convective plumes' approach of Arakawa and Schubert (1974) can determine the bulk qunatities by summing up the effects of all plumes. Although initially derived for moisture and energy, it is assumed that this approach is also applicable for trace species.
In general, the convection parameterisations are developed with the goal to represent the hydrological and energetic aspects of subgrid-scale clouds, and less effort is spent on a realistic vertical redistributions of trace species in the atmosphere. Since the original implementations for clouds do not necessarily imply that the vertical redistribution is positive definite, though tracer mixing ratios have only positive values, an extension for the Tiedtke (1989) - Nordeng (1994) scheme has been developed by Brinkop and Sausen (1996) to guarantee positive definite tracer mixing ratios.
Lawrence and Rasch (2005) propose in contrast to the commonly used bulk transport a plume ensemble approach, following the basic idea of Arakawa and Schubert (1974) of an ensemble of mass fluxes. They show that their new approach results in significantly different tracer mixing ratios in the upper troposphere, and generally different vertical profiles.
The chemical tracer ^{222}Rn has proven a useful quantity to investigate the vertical transport by convection (Jacob and Prather, 1990), since it is chemically inactive and not soluble. The only sink is its radioactive decay. A similar indicator, methyl iodide (CH_3I) is proposed by Bell et al. (2002) for convection in marine environment, but since its sources are hardly known, it is of more limited value. Since ^{222}Rn is mostly restricted to land and CH_3I to marine regions, both species complement each other as indicators for convective activity.
One of the first steps to include the transport of trace species within convective clouds

into photochemical models has been proposed by Gidel (1983). Even though the model applied in that study is very simple compared to state-of-the-art modelling, the author is able to reproduce observed vertical profiles.
Mahowald et al. (1997) show strong differences for the distribution of ^{222}Rn between various simulation setups. Due to the fact that not only different convection schemes, but also different analysis data are used to drive their offline CTM, the relative effect of the selected convection parameterisation cannot directly be addressed.
A study by Collins et al. (2002) shows that using a Lagrangian model with two different descriptions of convective transport, the vertical distribution of ^{222}Rn is highly dependent on the choice of the scheme, but a conclusion on which scheme is overall performing better was not possible.
A large model intercomparison focusing on vertical transport of trace species, especially using ^{222}Rn, is described by Jacob et al. (1997). One of the main conclusions is that the vertical mixing by convection is essential. The problem of such a model intercomparison is that it is difficult to distinguish the origin of the differences of tracer mixing ratios. Even though several different convection parameterisations are applied, it is not possible to attribute the deviations directly to the convection scheme and its effects on the transport, since each model produces its own state of the atmosphere. On average all compared models calculate similar Radon mixing ratios. The two-dimensional models participating in this study however, tend to heavily underestimate the vertical transport.
Since convective transport for soluble species must always be addressed together with scavenging these two processes and their interaction are described together in Chapter 6, while in the next section the convective transport is analysed on its own, as for insoluble compounds.

4.2 CVTRANS: Submodel description

The submodel CVTRANS, which was developed as a part of this thesis, treats the ConVective tracer TRANSport. This is an online transport submodel for vertical transport in convective columns, using the bulk approach. It is based on Lawrence and Rasch (2005), but has been extensively modified. The modifications include a conversion to FORTRAN90 and the application to mass fluxes, entrainment, and detrainment rates independent of the convection scheme. It requires the mass fluxes (upward and downward) and the corresponding entrainment and detrainment rates at each model level as input parameters. These have to be provided by the convection scheme. Using the MESSy structure a straightforward coupling of this submodel with the CONVECT submodel is applied.
This submodel is equipped with a closure routine that guarantees that the mass fluxes in each model level k are properly closed, i.e.:

$$F_u^k = F_u^{k+1} + E_u^k + D_u^k. \tag{4.1}$$

In this equation F_u^k denotes the updraft mass flux, F_u^{k+1} the mass flux from the layer below, E_u^k the entrainment flux and D_u^k the detrainment flux in this layer. All fluxes are in kg/(m^{2}s). This closure had to be reformulated as well, and now it is more robust. The scheme is monotonic, positive definite and mass conserving. To assure this, the mass flux of air in a grid box must not exceed the available grid mass in one model timestep. If this occurs a priori, the scheme adjusts the mass fluxes and entrainment and detrainment

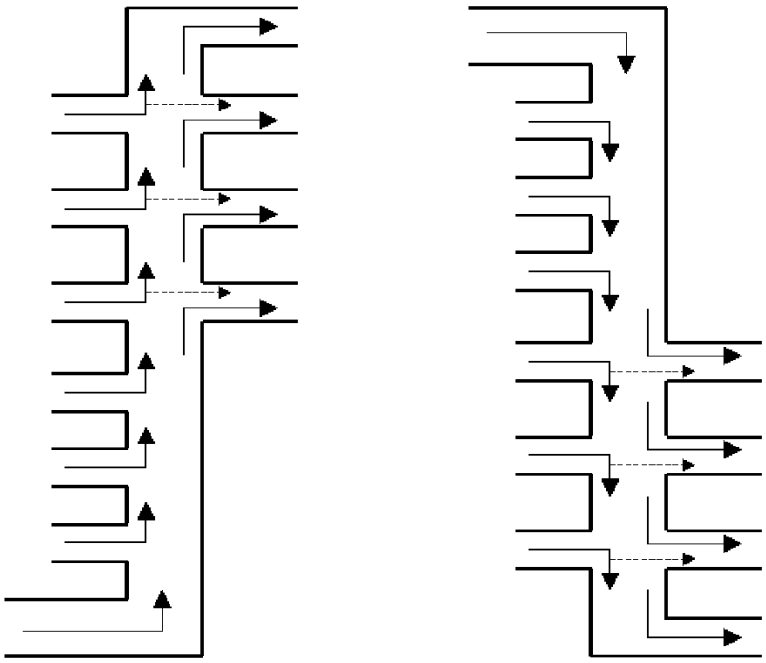

Figure 4.1: Sketch of the convective tracer tranport scheme for upward (left) and downward (right) transport.

rates so that this limit is reached.
The transport routine itself calculates the tracer mixing ratio in the updraft and downdraft (i.e., the tracer mass fluxes) and the detrained tracer mass fluxes, considering entrainment in each layer. Additionally, a fraction of the entrained tracer mixing ratio can directly be detrained in the same level. This can be seen in Figure 4.1. Theoretically detrainment from the updraft is possible in each layer, but usually significant detrainment occurs only in the upper troposphere. For downward transport in the convective downdrafts the calculations are performed analogously. The detrainment from the convective downdrafts usually occurs in the lowest model layers only.
The calculations for the updraft are described by the following equations (downdrafts follow the same principle):

$$M_u^k(X) = \frac{(F_u^{k+1} - (D_u^k - p_e \cdot E_u^k)) \cdot M_u^{k+1}(X) + (1 - p_e) \cdot E_u^k \cdot M_{env}^k(X)}{F_u^{k+1}} \quad (4.2)$$

$$M_{ud}^k(X) = \frac{(D_u^k - p_e \cdot E_u^k) \cdot M_u^{k+1}(X) + p_e \cdot E_u^k \cdot M_{env}^k(X)}{D_u^k} \quad (4.3)$$

In these equations $M_u^k(X)$ denotes the tracer updraft mixing ratio of species X in level k. In this case, it is irrelevant if these ratios are given in mol/mol or kg/kg. $M_{env}^k(X)$ represents the environmental mixing ratio of species X outside of the convective plume. The parameter p_e specifies the fractions of the entrained air which is detrained immediately in the same model layer. $M_{ud}^k(X)$ is the mixing ratio in the updraft detrainment flux.
The equations for the downdraft mixing ratio $M_d^k(X)$ und downdraft detrained mixing ratio $M_{dd}^k(X)$ are derived analogously. With those quantities the new tracer mixing ratio of the species X in each layer, $M^k(X)$, can be described by:

$$
\begin{aligned}
M^k(X) \;=\; & \Big\{(M^k_{\text{air}} - (M^k_u - M^k_d + D^k_u + D^k_d)\cdot\Delta t)\cdot M^k(X) \\
& +(M^k_u - M^k_d)\cdot\Delta t\cdot M^{k-1}(X) \\
& +D^k_u\cdot\Delta t\cdot M^k_{ud}(X) \\
& +D^k_d\cdot\Delta t\cdot M^k_{dd}(X)\Big\} \\
& /M^k_{\text{air}}.
\end{aligned} \tag{4.4}
$$

In this equation Δt denotes the model timestep and M^k_{air} the column air mass per m^2 within that particular grid box.
The first term on the right hand side in this equation determines the amount of the tracer X that is not affected by the convective activity, the second term the influence of air subsidence around the convective plume, the third the effect of the detrained updraft mixing ratio of the species and the fourth the detrainment from the downdraft.
This process is calculated sequentially for all trace species.
The largest benefit from this submodel is, that it can be used with various convection schemes. These might have their own transport schemes, but with this submodel the user can be sure that any difference analysed in trace gas mixing ratios originate only from the differences in the convection parameterisations, since the transport mechanism used for all the studies is identical. This is specifically valid for the simulations of Section 4.3.
The effect of scavenging and wet deposition on the convective transport and the coupling to those processes will be addressed in Section 6.2.

4.3 Comparisons of Convection Schemes - Implications on vertical transport

4.3.1 Simulation setup

For the analysis of convective transport five simulations with idealised tracers have been performed. Gas phase chemistry is neglected. The effect of the differences in tracer transport can be analysed with the help of the DRADON submodel with its corresponding tracer ^{222}Rn. The submodels used in this study are CLOUD, CONVECT, CVTRANS, (SCAV), OFFLEM, DRADON, DRYDEP, SEDI, LNOX and TROPOP. LNOX is used for diagnostics (see Chapter 5), and TROPOP for the calculation of the planetary boundary layer (PBL) height, which is required for the Zhang-McFarlane-Hack scheme, and the diagnostics of the tropopause height.
These simulations are:

- Simulation with the Tiedtke convection scheme T1 (C_T1), the reference simulation;
- Simulation with the ECMWF convection scheme EC2 (C_EC);
- Simulation with the Zhang-McFarlane-Hack convection scheme ZH (C_ZH);
- Simulation with the Zhang-McFarlane-Hack convection scheme with the additional evaporation of precipitation ZHW (C_ZHW);
- Simulation with the Bechtold convection scheme B2 (C_B2).

The convection schemes and their respective names are the same as in Chapter 3. Since the differences within the groups of the convection schemes T1, T2, T3 and EC, EC2 and

B1, B2 (see Section 3.3.2) are small, only one of each group is used here, namely T1, EC2 and B2, respectively.
The simulations are performed with climtological sea surface temperatures. The simulation period is 15 months, but only the last 12 months are used for the data analysis to avoid potential model spin-up effects.
The focus of this study is on the ^{222}Rn tracer and its three dimensional distribution.

4.3.2 Results

4.3.2.1 Convective mass fluxes

First, the zonal distributions of the updraft mass fluxes calculated with the different convection schemes are presented. Since this quantity is virtually impossible to observe, usually the Radon tracer mixing ratios are investigated to analyse the mass fluxes. However, these mixing ratios can also be influenced by other processes, e.g., advection. Therefore the analysis of the updraft mass fluxes are suitable for a model intercomparison to address vertical upward transport in a model as presented in Figure 4.2. The figure shows the annual zonal average of the updraft mass fluxes as calculated by the various convection schemes. Close to the surface the average zonal orography is displayed in dark grey. In the upper troposphere the simulated average tropopause height is marked with the turquoise line.
The C_T1 simulation, the reference simulation, shows the expected distribution of convection: deep convection in the tropics, only shallow upward motion in the subtropics and a more convectively active region in the midlatitude storm tracks, characterised by a combination of shallow and deep convection. Usually, the convection starts already at altitudes in or slightly above the planetary boundary layer (PBL). If convection is triggered considerably above the PBL this is described by the so-called midlevel convection of this scheme.
The shallow convection is characterised by stronger upward mass fluxes. It seldomly reaches higher than 800 hPa, a typical convective boundary layer height. Above this altitude, the mass flux shows much lower values of about half the strength only. In the C_T1 simulation the mass fluxes decrease with increasing altitude, due to detrainment of air from the mass fluxes and the dilution by entrainment, which reduces the buoyancy and consequently the strength of the vertical upward mass fluxes. The convective upward motion ends at about 200 hPa on average in the tropics with lower altitudes up to 400 hPa in the polar regions. This is effectively below the average tropopause height, denoted by the turquoise line, which ultimately limits convection due to the temperature inversion. There is hardly any convective transport across the tropopause, constraining the injection of tropospheric air into the stratosphere and vice versa. The subtropical regions with very rare convective activity are characterised by much lower upward motion. This can be explained by the subsidence in the Hadley circulation taking place in these regions (compare Figure 1.2).
In the C_EC simulation, the situation is different. Even though the horizontal zonal distribution is similar (highest values in the tropics and two secondary maxima), in this case the shallow convection is much stronger. In the southern storm tracks, the shallow convection is much more intense than in the northern hemisphere. The absolute values in the shallow convection are considerably higher, as noted by Grant and Brown (1999) and Tompkins et al. (2004). However, not only the shallow convection is stronger but also the deep convective mass fluxes reach values that are on average almost twice as high,

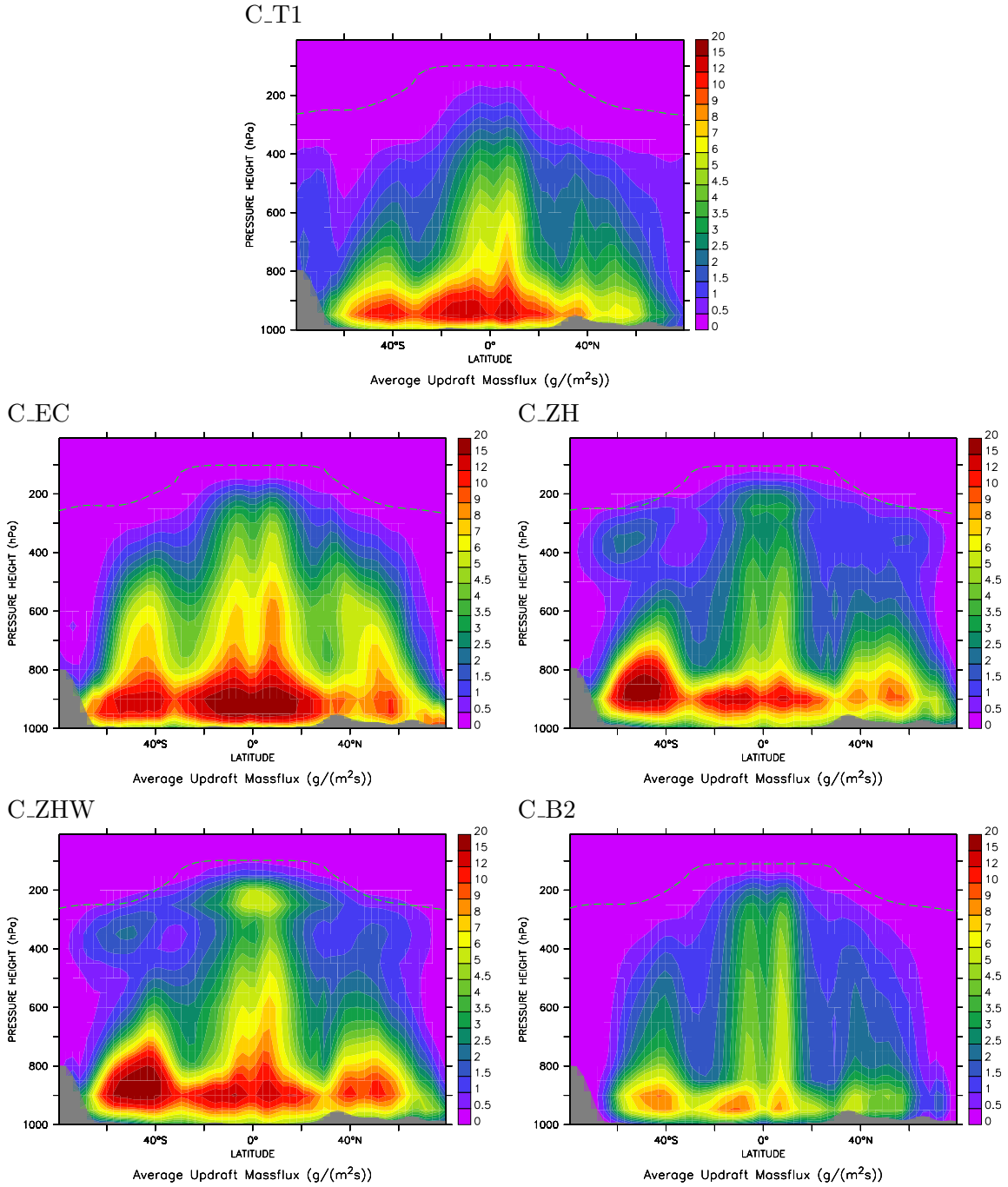

Figure 4.2: Annual zonal average of the convective updraft mass fluxes in g/(m^{2}s). The grey area depicts the zonally averaged orography.

resulting in more effective upward transport. The mass fluxes of C_EC reach up to almost 500 hPa in the midlatitudes with values twice as high as in the C_T1 simulation. In the tropics there is hardly any decrease of the mass flux strength with altitude up to 400 hPa. Above this height a decrease can be detected, but the vertical gradient of the mass flux is less step compared to C_T1. This results in upward mass fluxes of more than 6 g/(m^{2}s) compared to C_T1 with only 2 g/(m^{2}s) in an altitude of about 400 hPa. In the tropics two

separate updraft regions can be detected for C_EC, which are less distinct in the C_T1 simulation. Additionally, there is almost no convection above 800 hPa at the poles in C_EC, while the shallow convection is stronger than in C_T1 in the northern hemisphere. Since the shallow convection scheme of the ECMWF-scheme is substantially different from the Tiedtke-Nordeng-scheme, some discrepancies must be expected, but the strength of the shallow convective mass fluxes is almost a factor of two larger. The shallow convection closure of Grant and Brown (1999), known to produce even stronger shallow mass fluxes, is not applied in this study. It seems, that the applied entrainment formulation (turbulent entrainment only) hardly affects the updraft, resulting in deeper convection. The midlevel and deep convection of the extratropics is much more effectively triggered and stronger due to a different calculation of the cloud base mass flux. The tropopause is diagnosed at almost the same altitude, again providing an effective transport barrier, which is not crossed by significant convective updrafts.

For the C_ZH simulation, the tropical upward mass fluxes are calculated similarly compared to C_T1, but somewhat lower values for the middle troposphere can be detected (right panel in the middle row of Figure 4.2). In the tropics the convection reaches up to substantially higher levels, but still fades below the tropopause. Close to 200 hPa is a region where the mass fluxes even increase again. A possible explanation is, that this results not only from the Zhang-McFarlane scheme, but additionally from the Hack part, further stabilising the upper troposphere with high water vapour content transported by the Zhang-McFarlane part. The shallow convection and also the convection of the midlatitudes, mostly originating from the Hack scheme, are significantly stronger than in the C_T1, but weaker than in the C_EC simulation. This is partly due to the fact that the Hack scheme determines convective mass fluxes for each layer individually. With the help of the detrainment parameter β these layers are connected to achieve a total mass flux (Hack, 1994), but a direct plume ascent is not calculated. In the midlatitudes, where the tropopause height decreases as in the other simulations, convective mass fluxes are calculated which on average reach or even cross the average tropopause, leading to a penetration of the transport barrier. Even though the mass fluxes are relatively small and the subsequent transport of trace species and moisture into the lower stratosphere might be weaker compared to the exchange along the isentropes in those specific regions, this likely has an effect on the composition of the lower stratosphere.

The C_ZHW simulation shows a very similar mass flux distribution compared to C_ZH in the midlatitudes and also for the shallow convection with a little higher values than C_ZH. The convection of the tropics is stronger than in C_ZH, reaching similar values as C_EC in the middle troposphere. The upper tropopspheric maximum, as simulated by C_ZH, is even stronger while lower values occur between 500 and 350 hPa. Similar to the C_ZH simulation, the tropopause is almost reached in the tropics by average mass fluxes of about 1 g/(m^2 s) and in the midlatitudes convective transport across the tropopause occurs.

The Bechtold scheme applied in C_B2 shows again the maximum mass flux in the tropics, and a weak secondary maximum in the southern storm tracks, though the northern storm tracks are not characterised by such strong upward mass fluxes. Since the precipitation in these regions is captured quite well (compare Figure 3.4), this mainly results from large-scale precipitation. The shallow convection is weaker than in the other schemes. This must partly be attributed to the rather different descriptions of shallow convection. Additionally, in this simulation a much longer relaxation time (4 hours) compared to the other schemes for both shallow and deep convection is applied, resulting in weaker mass fluxes.

Simulation Name	Mean [g/(m^{2}s)]	Bias [g/(m^{2}s)]	RMSE [g/(m^{2}s)]	Correlation R^2	Slope	Intercept with y-axis
C_T1	2.53	-	-	-	-	-
C_EC	4.01	1.48	1.32	0.74	1.23	0.70
C_ZH	2.81	0.28	1.21	0.62	0.81	0.67
C_ZHW	3.45	0.92	1.14	0.77	1.16	0.42
C_B2	1.93	-0.60	0.91	0.79	0.75	-0.06

Table 4.1: Statistics of the annual zonal updraft mass flux averaged over all model levels of the individual model simulations compared with the C_T1 simulation.

Since the general shape of the mass fluxes is similar to most of the other simulations, a shorter relaxation time would result in mass fluxes of the same magnitude as in the other simulations. The two peaks in the tropics are much sharper than in the other convection schemes. The convective mass fluxes reach higher than in the C_T1 simulation, but do not reach or cross the tropopause as in C_ZH and C_ZHW.
The statistics of the mass fluxes using C_T1 as the reference are shown in Table 4.1. All schemes except for C_B2 calculate stronger upward mass fluxes than C_T1. On the other hand, the correlation R^2 is always higher than 0.6 indicating a similar spatial distribution. The slope and correlation indicate that C_B2 is closest to the reference C_T1, which is also a model result and not necessarily represents 'reality'.

In summary, the five simulations show large differences in the average updraft mass fluxes. Especially the differences in the shallow convection, which determines partly the mixing of the lower troposphere, have a substantial effect on water vapour and tracer concentrations. However, in the ECHAM5 model an additional process calculating the vertical mixing of compounds in the boundary layer is implemented. Therefore, the differences in the lower troposphere might not be that significant. An increased strength of the deep convective mass fluxes in the tropics will result in significantly higher concentrations of trace species and water vapour in the tropical tropopause region. This is critical, especially for the schemes that cross the average tropopause with convective mass fluxes, resulting in a much enhanced convective exchange of air masses between troposphere and stratosphere. This affects not only by the injection of tropospheric air into the lower stratosphere, but also the movement of stratospheric air into the upper troposphere by the mass balancing subsidence. Additionally, higher water vapour contents in the upper troposphere can lead to enhanced cirrus formation with feedbacks on radiation and therefore on the energy budget of the Earth.

4.3.2.2 Radon distributions

Next, the vertical distribution of Radon (^{222}Rn) is analysed. The zonal average vertical distribution of Radon with the different convection schemes is presented in Figure 4.3. The upper left panel in addition shows the annual average horizontal distribution in the surface layer. Since significant emission of ^{222}Rn occurs only over land, if it is not covered by ice, the highest values can be found over the land masses of the northern hemisphere. The mixing ratios are highest in the Sahara, because in the subtropics the winds close to the surface are lower than in the midlatitudes. As a consequence ^{222}Rn is less ventilated

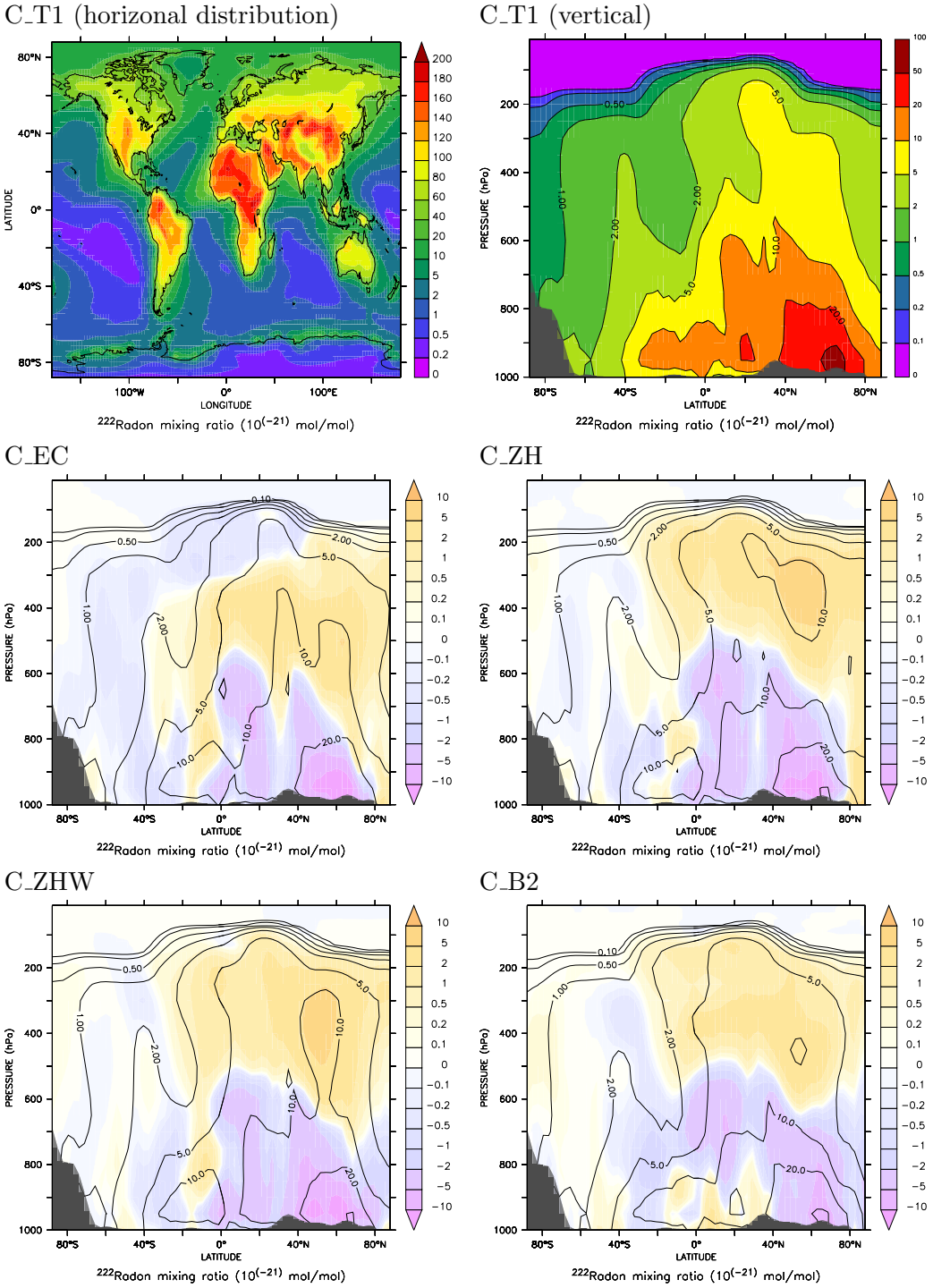

Figure 4.3: Simulated ^{222}Rn mixing ratio during summer (JJA) in 10^{-21} mol/mol. The upper left panel shows the annual average of the surface layer mixing ratio of the C_T1 simulation, the other panels show the zonal averages of the various simulations. The contour lines display the simulated mixing ratios of the individual simulations, the colors show the differences to the C_T1 reference simulation. The grey area close to the surface is the mean orography.

by advection from the source regions. Additionally, there is little convection in this region and therefore ^{222}Rn accumulates in the boundary layer.
The other panels show the zonal average mixing ratios. For comparison with the model results from the model intercomparison by Jacob et al. (1997), the average mixing ratio for the summer season (JJA) is displayed. The contour lines show the simulated mxing ratios for the individual simulations. In the upper right panel the colors show the same as the contour lines for the C_T1 simulation. In the other pictures the colors denote the difference to the C_T1 simulation.
The general shape is similar for all simulations: the highest ^{222}Rn abundance occurs in the northern hemisphere between 40°N and 75°N, resulting from the relatively large land masses in these latitudes. The emitted atoms are also vertically transported yielding significant mixing ratios in the upper troposphere of the northern hemisphere. The convection of the midlatitudes is indicated by the two peaks at about 40°N and 40°S. The ITCZ is not sharply reflected in the ^{222}Rn distribution.
The colors of the four lower panels of Figure 4.3, which show the differences to the C_T1 simulations, illustrate the differences in the vertical transport. As already seen in Figure 4.2, the transport into the upper troposphere is more effective in all simulations compared to the reference. This is mostly a direct effect of the convective vertical transport. Even though the Hadley circulation might be stronger in these simulations compared to C_T1, the mixing ratios cannot be affected by long-range transport because of the radon life time of only a few days. Only in regions close to convective activity, e.g., parts of the upper troposphere in subtropics, this can have a slight impact. In general, the circulation follows the pathways indicated in Figure 1.2. However, except for the convective updraft, which occurs within a timeframe of a few hours, most of the other transport processes are too slow (especially meridional transport), to substantially influence the tracer mixing ratios in the upper troposphere. These differences to C_T1 are lower in the B2 simulation than in the others.
The details, e.g., the height of the '$10 \cdot 10^{-21}$ mol/mol isoline' of all simulations differ substantially. Especially in C_ZH and C_ZHW this contour line reaches up to almost 200 hPa, while in the C_T1 simulation is is mostly located below 600 hPa. For comparison, in the study of Jacob et al. (1997) the ^{222}Rn distributions of the participating models with their different convection parameterisations differ as much. For instance, ECHAM3 shows a lower '$10 \cdot 10^{-21}$ mol/mol isoline' than the TM2 or GFDL models. In contrast, the '$2 \cdot 10^{-21}$ mol/mol isoline' has an almost comparable shape in all simulations of this study, which is not the case in the analysis of Jacob et al. (1997). This must therefore be attributed to other differences in the model physics of the participating models of the intercomparison, and cannot necessarily be explained by the different convection schemes alone.
Despite the high reaching mass fluxes of the C_ZH and C_ZHW simulations as diagnosed in Figure 4.2, the gradient at the tropopause and in the lower stratosphere is almost identical in all five simulations. This underlines that the differences in the ^{222}Rn mixing ratios are mostly due to the differences in the convective transport. Additionally, the uniform shape of the isolines plays down the importance of injection of tropospheric air into the stratosphere by convection. Even though this might occur, it is not reflected in the zonal average mixing ratios. First, this can be explained by the limited importance of this convective injections compared to the large-scale isentropic troposphere-stratosphere exchange. Moreover, in Figure 4.2 annual averages are shown, while in Figure 4.3 the summer mixing ratios are displayed. In general, in late autumn and winter, the convective

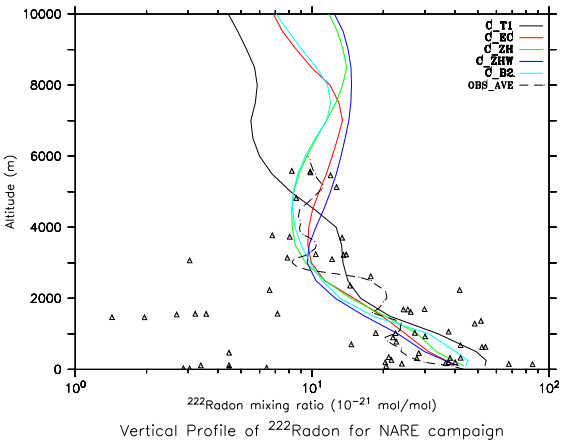

Figure 4.4: Vertical profile of the ^{222}Rn mixing ratio during the NARE campaign in 10^{-21} mol/mol as observed and simulated.

activity in the northern storm tracks is stronger than in boreal summer, probably resulting in no such cross-tropopause transport during this season. In the southern hemispheric storm tracks the occurence of a possible cross-tropopause transport in this seasson (winter in the southern hemisphere) is not obvious, since the mixing ratios are generally lower.

Vertical profiles of ^{222}Rn have been measured at various locations in the last fifty years. The compilation of data by Liu et al. (1984) is helpful for a general overview, but this data is not very useful for the comparison with model results, since the average profiles presented are constructed from measurements taken over long or not explicitly specified time periods. For the comparisons of model results with observations, measurement data from several field campaigns are used, adapted from the work of Olivié (2005).
For this purpose, the average mixing ratios of the model calculations within the region and time period of the campaign are calculated. Based on the observations a time averaged vertical profile is determined (dashed line). In addition, the individual measurements are marked with symbols. Since data of the years of the individual campaigns are compared with a simulation performed with a free running GCM forced by climatologcial sea surface temperatures only, a perfect match of observations and model calculations cannot be expected.
Figure 4.4 shows the observed radon mixing ratios (black symbols) with their average profile (black dashed line) from the NARE campaign (1993) over the North Atlantic and Canada as described by Zaucker et al. (1996). The colored lines show the corresponding results from the model simulations with the different convection schemes. Note the logarithmic scale on the horizontal axis. For the boundary layer, all simulations are within the variability of the observations, although some differences are apparent. This mainly reflects the differences in the description of the source of ^{222}Rn. Above about 1 km altitude the curves of the model simulations are very similar. Between 2 and 3 km the different simulations increasingly deviate, reflecting the transition to the free troposphere. Nevertheless, all simulations are within the variability of the observations. Above 5 km, where no observations are available, the profiles deviate significantly from each other, showing the effect of the different detrainment descriptions and strength of the convective mass fluxes.

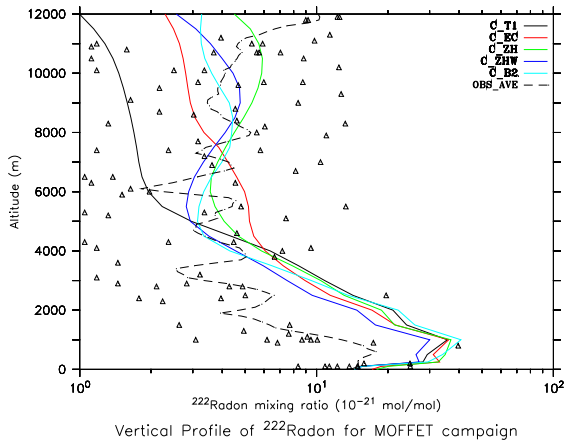

Figure 4.5: Vertical profile of the ^{222}Rn mixing ratio during the MOFFET campaign in 10^{-21} mol/mol.

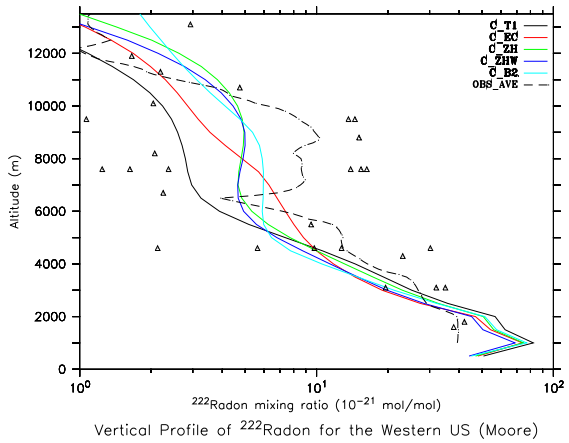

Figure 4.6: Vertical profile of the ^{222}Rn mixing ratio in the western USA (Moore et al., 1973) in 10^{-21} mol/mol.

A similar picture as above can be made for a flight campaign at Moffet Field, California, in summer 1994 (Kritz et al., 1998). For this data, a model calculation with a regional model has been performed by Stockwell et al. (1998). Again, the simulations are very similar in the boundary layer and the lower troposphere. All calculated mixing ratios are at the high end of the variability of the observations. Above 3 km the model calculations differ increasingly. While the mixing ratios of T1 are highest higher from 2 to 4.5 km they become much lower than the values of the other simulations above 6 km. They are, however, still in the range of observations, because the variability is very high for this campaign, but deviate most from the observational average. C_EC and C_B2 show a very similar shape, being somewhat lower than the observational average, while C_ZH and C_ZHW calculate slightly higher mixing ratios. At 12 km, the maximum altitude of the observations, the measured average shows an increase that is not found in any of the simulations.
Moore et al. (1973) provide an additional ^{222}Rn dataset. Observations took place in the western United States and the profiles originate from all seasons. This is presented in Figure 4.6. On average, the profiles are very similar below 6 km. Below 2 km altitude with only fery few measurements all the simulations show higher ^{222}Rn mixing ratios than the

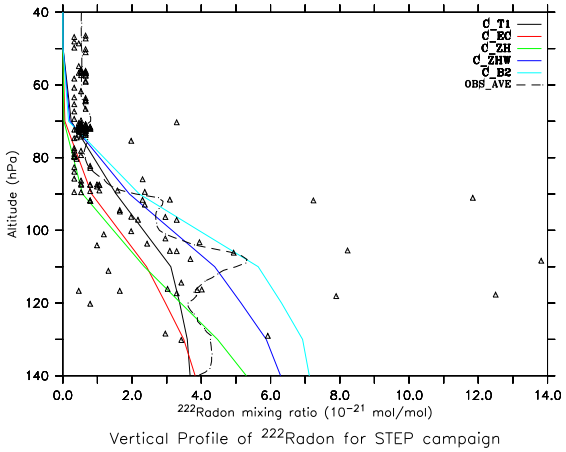

Figure 4.7: Vertical profile of the ^{222}Rn mixing ratio during the STEP campaign in 10^{-21} mol/mol.

observations. The shape is similar to the other profiles, reflecting the emissions and the PBL. Above 2 km the model results are slighlty lower than the observational average. As indicated above, the C_T1 simulation shows lower values above 6 km and does not capture the upper tropospheric maximum in the observations. Even though this maxmium is not sharply distinct in the other simulations the upper tropospheric mixing ratios are closer to the observations, especially for the C_ZH and C_ZHW simulation.
Also for the upper troposphere and lower stratosphere some vertical profiles are available. Those are from the STEP campaign (Kritz et al., 1993), north of Australia in January and February 1987 and shown in Figure 4.7. This time the mixing ratios are shown on a linear axis versus the pressure altitude ranging from 140 hPa to 40 hPa, representing the upper troposphere lower stratosphere region. In comparison to these observations the C_B2 simulation shows the highest values being at the upper limit of the observed variability. The other simulations calculate lower mixing ratios closer to the observational average, but also with distinct differences. Above 70 hPa the mixing ratios of all simulations decrease drastically, with a gradient much steeper than observed. This can partly be due to the fact that the upper limit of the model domain is at 10 hPa. Therefore, the stratospheric circulation is only roughly reproduced by the model. Furthermore, close to the model domain boundaries the results should be treated with care. Already the results between 140 hPa and 80 hPa are based on only few model levels and are interpolated linearly on the pressure axis. Even though convection can contribute to the injection of tropospheric air into the stratosphere (Mullendore et al., 2005), this does not occur regularly. Even if such a case was captured during the STEP measurements, it is highly unlikely that a model simulation without nudging reproduces such an event of extreme convection.

In summary, it can be stated, that all simulations are overall able to predict a reasonablly realistic average vertical profile of ^{222}Radon, but show significant differences between each other. The C_T1 simulation shows lower concentrations in the upper troposphere as a result of the weaker vertical transport.

4.4 Discussion

The aim of this study is to shed light onto the differences in convective transport as diagnosed by replacing the convection parameterisation. Again, it is not possible from the simulations to designate one of the schemes as 'best performing' with respect to reproducing observed vertical profiles of trace species influenced only by transport.
It is difficult to compare observed profiles and model simulations, especially if the local model meteorology is not identical to the observed conditions. For that purpose a simulation series with the nudging technique applied for the time of the individual campaigns would be required, but this is beyond the scope of this study. Especially for the STEP campaign focussing on troposphere-stratosphere-exchange processes, a higher model resolution in the vertical direction, e.g., the 90 layer middle atmosphere version, would be helpful.
The comparison of the results with the model intercomparison of Jacob et al. (1997) can only be used qualitatively, because in contrast to their results the differences in the ^{222}Rn mixing ratios of the simulations of this chapter can directly be assigned to the influence, i.e., the occurence and strength of convective events. A direct comparison with the findings of Jacob et al. (1997) is not possible because the model setup of both simulation series is not identical. Additionally, their simulations do not differ solely with respect to convection, but also more generally with respect to the model physics.

The issue of the transport of air masses across the tropopause by convection in some of the simulations must be considered. However, average mass fluxes are analysed as well as the average tropopause height. Therefore it cannot be guaranteed from this comparisons that there has actually been transport across the tropopause and exchange of air. However, a higher content of moisture in the upper troposphere originating from convection is simulated (these figures are not shown). This partly explains the temperature variations seen in Figure 3.10 because water vapour contributes to radiative cooling. The higher water vapour content also has feedbacks on the dynamics, partly due to more formation of cirrus clouds by the large-scale cloud scheme, and high ice clouds generally contribute to radiative heating. This may partly explain the instabilities in the upper tropical troposphere, which activate the Hack convection parameterisation in the C_ZH and C_ZHW simulations, as analysed in Figure 4.2.
In the midlatitudes the exchange of air across the tropopause occurs mostly along isentropes, while the effect of convection is thought to be of minor importance (Holton et al., 1995). Nevertheless, a recent model study by Mullendore et al. (2005) shows the occurence of tracer transport across the tropopause in extreme midlatitude convection and compared their results with observations from the STEP campaign (Kritz et al., 1993), concluding that locally convection can contribute to the injection of air from the troposphere into the stratosphere. However, it is questionable, if the very deep convection of the C_ZH and C_ZHW simulation in the midlatitudes predicts this process.

Chapter 5

Lightning

Lightning is of special importance in a global atmospheric chemistry climate model, since it is a source for NO_x in the upper troposphere. Due to this process reactive nitrogen can participate in the chemistry of the remote atmosphere, e.g., through effective ozone formation far from anthropogenic emission sources (Stockwell et al., 1999). Since the NO is produced at higher altitude, it is relatively slowly converted to soluble HNO_3 that would be efficiently scavenged. In contrast to surface NO_x emissions different reaction paths are possible in the upper troposphere, e.g., the formation of PAN which is thermally labile in the lower troposphere. Even though these NO_x emissions are less than 10% of the total nitrogen oxide emissions, they are important for the upper tropospheric chemical composition. Several studies (e.g., Stockwell et al., 1999; Tie et al., 2001; Labrador et al., 2004) show that lightning NO_x emissions have large effects on atmospheric chemistry in the upper troposphere.
Although global observations of lightning are available from the Lightning Imaging Sensor (LIS) and the Optical Transient Detector (OTD) a link with meteorological quantities is required for predicting flash rates in prognostic models.

5.1 Simulation setup

Since a GCM usually does not include the electrical circuit of the atmosphere and the process of electrification is still associated with large uncertainties, the flashes cannot be explicitely calculated by the model. Moreover, since the convective thunderstorms themselves are mainly unresolved on the coarse grid of a global model, the lightning can only be derived indirectly from resolved or parameterised quantities. In the applied model this process is parameterised following the approach of Price and Rind (1992) and Price et al. (1997) (see Section 2.2.2.4). As mentioned earlier, the parameterisation is derived from an empirical relationship of observed flash frequencies and convective cloud top heights, differentiating between continental and ocean grid boxes. This is expressed by the Equations 5.1 and 5.2, respectively:

$$F_c = 3.44 \cdot 10^{-5} \cdot H^{4.90} \quad (5.1)$$

$$F_m = 6.40 \cdot 10^{-4} \cdot H^{1.73} \quad (5.2)$$

F_c and F_m denote the flash frequencies in flashes per minute for continental and marine regions, respectively, and H is the convective cloud top height in km. Price and Rind

(1994) discuss that the calculated flash frequencies depend on the horizontal resolution and introduce a resolution dependent rescaling parameter to overcome this issue. This parameter has been multiplied by 1.5, as determined from previous studies of this model during the setup of the evaluation simulation (see Section 6.4.1). However, since in that simulation a different vertical resolution and nudging is applied, this parameter is not necessarily suitable for a different model setup.
The production of NO_x resulting from the modelled and observed lightning is even more uncertain, since, even if the flash frequency is simulated correctly, the rate of NO_x production per flash is highly uncertain. Neither the ratio of inter-cloud, intra-cloud and cloud-to-ground flashes is known and can be quantitavely determined from observations, nor the efficiency of each type for producing NO_x. These production estimates vary by two orders of magnitude in the literature. Furthermore, usually an average amount of NO_x production per flash is given, but the flashes themselves vary in their energy, and consequently in their potential of NO_x formation. This formation varies from $0.3 \cdot 10^{21}$ to $6.1 \cdot 10^{21}$ molecules/flash (Ridley et al., 1996) to values of $1.8 \cdot 10^{21}$ to $30 \cdot 10^{21}$ molecules/flash (Beirle et al., 2004) or even to $300 \cdot 10^{21}$ molecules/flash (Franzblau and Popp, 1989). Price et al. (1997) assume a value of $67 \cdot 10^{21}$ molecules/flash for cloud-to-ground and $6.7 \cdot 10^{21}$ molecules/flash for intra-cloud flashes. Due to these uncertainties the estimates of global NO_x production from lighting vary between 2 and 12 Tg N/yr (e.g., Tie et al., 2001; Labrador, 2005, and references therein).
Since the cloud top height is a diagnosed value from the convection scheme, an exchange of the convection parameterisation affects the simulated flash frequencies. The model simulations evaluated in this section are described in Section 4.3.1. The diagnostic output of the LNOX submodel is evaluated in this section.

5.2 Model calculated flash frequencies

Flash frequency data, used to test the ECHAM5/MESSy model results have been derived from a combined data set of LIS and OTD observations. A gridded data set with a horizontal resolution of 2.5° with daily values of the flash frequency can be obtained from the Global Hydrology Resource Center[1]. A description of the two instruments and the respective data can be found in Christian et al. (1999) and Thomas et al. (2000) for LIS, and Christian et al. (2003) for OTD data, respectively.

Table 5.1: Rescaling parameter and statistics of the lightning simulation

Data	Total Frequency flashes/s	Rescaling Factor RF	Correlation R^2
LIS & OTD	44.59	1	-
C_T1	14.42	3.09	0.342
C_EC	41.13	1.08	0.614
C_ZH	120.3	0.37	0.477
C_ZHW	135.9	0.33	0.445
C_B2	86.47	0.52	0.556

[1] `http://ghrc.mfsc.nasa.gov`

Since there are large differences between the simulated flash frequencies applying the various convection simulations with respect to intensity and distribution a rescaling factor RF has been calculated first. This is derived from the global total number of flashes per second of the observations ff_{obs} divided by the total number of flashes per second of the simulations ff_{model}.

$$RF = ff_{obs}/ff_{model} \tag{5.3}$$

Since the simulated frequencies are derived from empirical coefficients such a rescaling factor can be seen as a requirement for the selected convection scheme. The calculated values for RF are listed in Table 5.1.

This factor is very important, and it varies between 0.33 and more than 3, indicating a strong underestimation for one scheme (C_T1) and a strong overestimation for another (C_ZH and C_ZHW). The horizontal flash frequency distribution shown in Figure 5.1 are the simulated frequencies multiplied with RF for an investigation of the average spatial distribution of the lightning events.

The upper left panel depicts the observed flash frequencies per km^2 and year, i.e., the combined satellite observations (LIS & OTD), on a logarithmic scale. It shows the highest values over the tropical continents of Central Africa, South America and Indonesia. Also, in the southeastern USA and southeast Asia relatively high values are observed. In Europe, northern Asia, and Canada the flash frequency is typically more than an order of magnitude lower. Over the oceans there is much less lightning activity. Close to the continents the flash frequencies decrease by a factor of more than 10 while in remote marine regions it is lower by a factor of more than 100, even in the ITCZ and the SPCZ with high convective activity. There is only very little lightning activity in the southern storm tracks. This is due to the fact that there are no continents which induce stronger updrafts, higher cloud tops and increased lightning. From 75° polewards no data is available, because the orbital track of LIS is limited to ±35° (Christian et al., 1999) and the observations by OTD are restricted to ±75° by the orbital inclination and the instrument field of view (Christian et al., 2003).

The upper right panel shows the flash frequencies for the C_T1 simulation. Even though the rescaling has been applied, it differs from the observations. As in the observations, over the continents the values are higher than over the ocean. However, the maximum is not found in Africa, but in Indonesia and southeast Asia. There much higher values compared to the observations are obtained (more than a factor of 5). In Central America a weaker overestimation occurs. While in Amazonia a slight overestimation is found in the model simulation, in the southern part of the continent an underestimation occurs. An even stronger underestimation (50% compared to the observed values) is detected in Central Africa, where the observations show a maximum. The distribution in the extratropical northern hemisphere shows an overall underestimation. Therefore the spatial distribution is not represented well by this model configuration as can be seen from the relatively low correlation ($R^2 = 0.342$) in Table 5.1. The high rescaling factor required to obtain a similar global total flash frequency indicates an underestimation of the convective cloud top height, consistent with the results from the mass flux analysis (compare Figure 4.2).

A comparison of the C_EC simulation with the observations yields better results. Over the continents the main characteristics are represented relatively well. The maximum values are simulated in Central Africa, followed by South America. The spatial distribution from Amazonia to Argentina is captured better than in C_T1. Over Indonesia also an overestimation occurs, but this is not as strong as in the C_T1 simulation. In Europe and

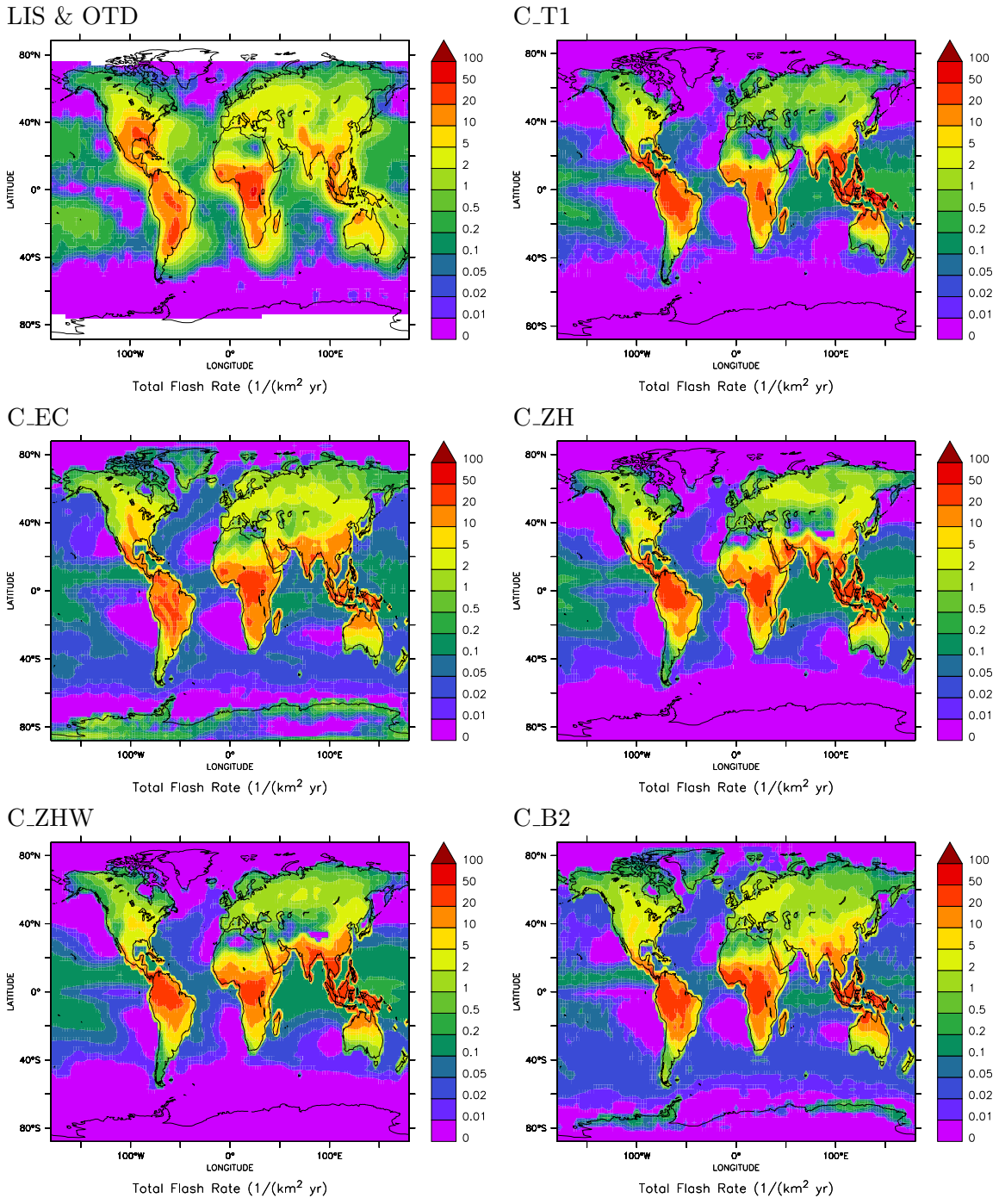

Figure 5.1: Observed and simulated annual average flash frequencies in $1/(\mathrm{km}^2\ \mathrm{yr})$.

northern Asia as well as in North America there is a slight underestimation, similar to the C_T1 simulation. Again, over the oceans, generally lower values are simulated than observed, especially close to the coasts. Additionally, there are some differences in the southern storm tracks, where more lightning is simulated than observed, and Antarctica and north of 70° N, where observations are missing. Nevertheless, with a rescaling factor of 1.08 the simulation with the C_EC convection scheme shows the highest correlation

($R^2 = 0.61$).
The C_ZH simulation (right panel in the middle row) also shows relatively high values, e.g., in southeast Asia, thus requiring a rescaling factor of 0.37. A similar overestimation is simulated for Central America, while in Africa the observed maximum is not represented properly. On the other hand in the USA the model underestimates the lightning activity significantly. Similar as in the C_T1 simulation there is an underestimation in northern Asia. As in the previous panels, over the oceans the flash frequency is underestimated. For this simulation the rescaling factor is 0.37, indicating a much higher average cloud top height predicted by the convection scheme, i.e., much deeper convection. This is consistent with the analysis of Figure 4.2. The spatial distribution with a correlation of $R^2 = 0.48$ is much better than in C_T1, but not as good as in the C_EC simulations.
A similar conclusion can be obtained for the C_ZHW simulation. The distribution looks similar to C_ZH, with slightly lower values in Amazonia and Central Africa. On the other hand, in southeast Asia the overestimation is even stronger. In northern Asia slightly lower flash frequencies are calculated. This results in a slightly reduced correlation ($R^2 = 0.45$), and a smaller rescaling factor (0.33 compared to 0.37).
The Bechtold scheme (lower right panel of Figure 5.1) is able to reproduce the maximum in Central Africa with the secondary maximum in South America of almost similar range. The lightning activity over Indonesia is overestimated as in the other simulations. However, in India, Thailand, Vietnam, Bangladesh, and southern China almost correct values are simulated. In Europe and northern Asia the observed flash frequency is slightly underestimated, while similar to the other simulations, the underestimation in North America is more significant. The lightning activity in the northern and southern storm tracks is comparable to the C_EC simulation, again too high in the southern storm tracks. Further polewards this cannot be evaluated due to the lack of observations. The rescaling factor of 0.52 indicates deeper convection as with the C_T1 scheme, but not as deep as in the C_ZH or C_ZHW simulation, again consistent with the mass flux analysis of Section 4.3.2.1. The spatial distribution is represented almost as good as in the C_EC simulation.
The statistical details are presented in a Taylor diagram in Figure 5.2. According to the statistics, with respect to both the normalised standard deviation and the correlation the C_EC simulation performs best. The simulation with the Bechtold scheme shows an overstimation of the amplitude of the spatial variation. This is even larger for the simulations using the ZH and ZHW convection scheme. The standard convection scheme T1 shows an even higher normalised standard deviation. The ranking with respect to the correlation is identical. The 'best' spatial representation of the observed flash frequencies is found in the C_EC simulation while with the C_T1 the correlation is significantly lower. Furthermore, C_EC is also 'best' with respect to the rescaling factor with RF close to 1.

5.3 Discussion

In summary, the additional rescaling factor dependent on the selected convection scheme is a requirement for a realistic simulation of flash frequencies. Since it is very dependent on the specific model setup a fixed number cannot be given, but must be determined individually. It may well be possible that the rescaling factors required by the alternative convection parameterisations are resolution dependent. This must not be mixed up with the resolution dependent rescaling parameter for the Price et al. (1997) lightning parameterisation.

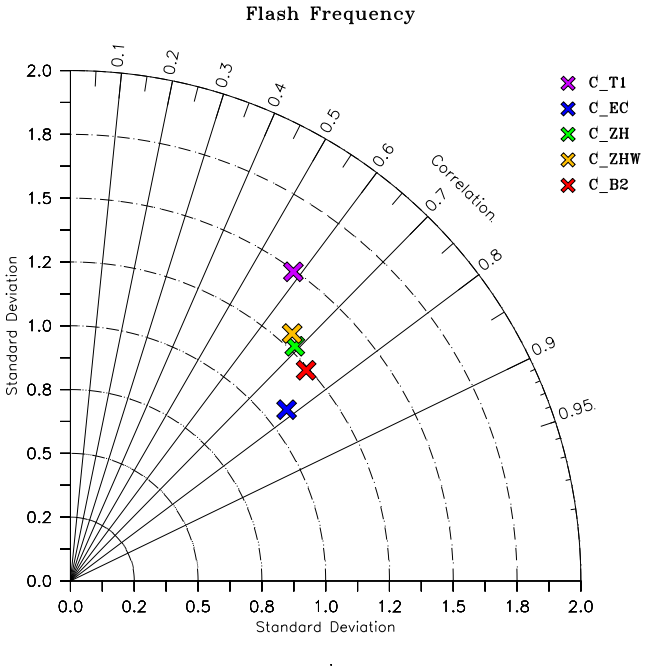

Figure 5.2: Taylor diagram for the modelled flash frequencies.

Evaluating the details of the spatial distribution is difficult. However, compared with a previous study (Labrador et al., 2005), the lightning over Indonesia, Europe and northern Asia is captured much better. Allen and Pickering (2002) compare three different parameterisations of lightning based on cloud top height, updraft mass fluxes and precipitation formation respectively. Since in this study no global statistical evaluation is performed, these results can be compared only qualitatively with the lightning distribution from the individual simulations. The differences with the different lightning parameterisations are much larger than the differences resulting from different convection schemes. In none of their simulations the maximum in Africa is captured appropriately, and both the mass flux and precipitation formation based scheme overestimate the lightning activity in the warm pool region and the Bay of Bengal. The cloud top height simulation of Allen and Pickering (2002) underestimates the lightning activity in South America and Central Africa. Again, the simulations of the present study capture these features much better.

As mentioned above, all simulations show problems in describing the observed flash frequencies over the ocean. This is a known problem of the Price and Rind (1992) parameterisation, discusssed in Grewe et al. (2001), in which a dependence of the flash frequency proportional to the updraft velocity rather than the cloud top height is proposed. Since this approach has not been applied in this study, it cannot be determined whether this would overcome this problem.

A possible improvement for future applications, especially with the Price and Rind (1992) parameterisation, would be a weighting of the simulated flash frequency with the fractional land-sea mask. At present time a grid box is considered as continental if the land fraction exceeds 10%. Especially for the Indonesian region in the relatively coarse horizontal resolution, this might substantially decrease the overestimation analysed for most of the simulations with the individual convection schemes.

Additionally, the model results are all from free-running simulations of only one year

with prescribed climatological sea surface temperatures as boundary conditions. A longer time series of simulated flash frequencies is a requirement for a more robust statistical performance analysis of the individual convection schemes with respect to lightning. Nevertheless, the presented analysis already gives some strong indications. Furthermore, the LNOX submodel has been applied in the simulations of Section 3.3, but only instantaneous values have been evaluated in the output. An average of these indicated the same results, but shows worse correlation. This is due to the fact that the ouput is restricted to specific times of the day, e.g., in Africa it is always in the evening hours while in South America it is about noon, distorting the real daily flash distribution.
Even though the total NO_x production is uncertain, a representation of the observed flashes by the model is a requirement for the correct spatial distribution of the emissions of reactive nitrogen species affecting the chemistry of the atmosphere, which is sufficiently achieved compared to state-of-the-art modelling.

Chapter 6

Scavenging and aqueous phase chemistry

6.1 Overview

Two approaches of cloud and scavenging atmospheric chemistry modelling have been followed in the past, i.e., the explicit calculation of the uptake of species in droplets, sometimes including aqueous phase chemistry, and the parameterisation of the effects of scavenging by applying scavenging ratios or efficiencies to trace gas concentrations in clouds and precipitation. These two approaches will be briefly reviewed.
An explicit calculation of the uptake of species has so far applied only in smaller scale models, i.e., in box models for the analysis of the chemical effects of clouds and in parcel models, and within the last decade also in regional models, for studies of chemistry, scavenging and deposition (e.g., Jacob (1986); Lelieveld and Crutzen (1991); Bott and Carmichael (1993); Monod and Carlier (1999); Fahey and Pandis (2001); von Glasow et al. (2002b); Ervens et al. (2003); Leriche et al. (2003)).
The theoretical basis for the phase transitions and its applicability to modelling is described in Schwartz (1986). One of the first model studies has been performed by Levine and Schwartz (1982). In this work the nucleation and impaction scavenging of nitric acid by clouds and rain is discussed based on a box model study, and a mathematical approach for the process decription is derived.
Flossmann et al. (1985) investigate the wet removal of atmospheric pollutants. In the first of a five paper series they restrict themselves to aerosol particles, but in the follow-up articles (Flossmann et al., 1987; Flossmann and Pruppacher, 1988; Alheit et al., 1990; Respondek et al., 1995), the uptake and oxidation of SO_2 is considered for liquid and mixed phase clouds. Additionally, feedbacks of the scavenging on the cloud properties are analysed.
Simplified cloud chemistry averaged over the whole cloud is calculated in the model of Chang et al. (1987). Even though some crude assumptions have been made (e.g., uniform distribution of all trace species within a cloud even though it contains several model layers), the basic aqueous phase chemistry was properly calculated.
Detailed cloud chemsitry has been calculated by Lelieveld and Crutzen (1991) in box model studies with cloud parameters derived from a statistical dataset. They find a significant reduction of several gaseous species, e.g., NO_x and H_2O_2, leading to a major influence on the ozone budget of the troposphere. This is contradictory to the results of Liang and

Jacob (1997) who conclude from box model studies that the effect on the ozone mixing ratios is only minor. By applying their box model in the regional model of Jacob et al. (1993), they did not find large differences compared to the original results without the aqueous phase chemistry.
The importance of the aqueous sulphur oxidation of SO_2 to SO_4^{2-} is well known (e.g., Warneck (1999)). Wang and Chang (1993b) point out the importance of the pH - value for this oxidation, and the relevance of the vertical redistribution of those trace species is shown, too (Wang and Chang, 1993a). Applying the same model, Wang and Crutzen (1995) find a significant reduction of SO_2 after a convective storm event with nucleation scavenging and impaction scavenging almost equally efficient. In their study the conversion of SO_2 to sulphate is of minor importance, but as the authors admit the mixing ratio of the main oxidant H_2O_2 is relatively low in their calculations.
Barth et al. (2002) analyse that *a weakness of most of the detailed chemistry model studies is an insufficient description of the microphysical properties of the clouds and precipitation.* They use a regional chemistry transport model to discuss the effect of cloud chemistry on ozone concentrations. In contrast to the studies mentioned above (e.g., Lelieveld and Crutzen, 1991; Chang et al., 1987) a detailed chemistry together with a detailed microphysical treatment of clouds is applied. They derive an ozone reduction by clouds between 6 and 17% in the cloud layers. Additionally, other trace gases, e.g., HCHO, CH_3OOH and HO_2 are depleted substantially by aqueous phase chemistry.
Barth et al. (2001) and Yin et al. (2001) investigate the effect of the vertical redistribution within convective clouds with different models for several artificial tracers with various solubility (ranging from the solubility of the almost insoluble CO to the very soluble HNO_3). The uptake of soluble species into clouds and the subsequent washout is important for the upper tropospheric composition. In the work of Yin et al. (2001), not only artificial tracers, but also atmospheric gases and their uptake and chemical reactions are considered. They show that for species with low solubility (e.g., NO or O_3) a much higher concentration can be found at the cloud top as for species like HNO_3 or H_2O_2.
Salzmann (2005) analyses from a series of simulations with a cloud resolving model that the uptake of soluble species is significant for the upper tropospheric composition, not only considering the liquid but also the ice phase. This corresponds with the results of Barth et al. (2001). Fahey and Pandis (2003) show that for a regional three dimensional model the aqueous phase chemistry can be calculated droplet size-resolved without too much extra computational effort, resulting in some variability in the trace gas mixing ratios (small differences over land, where comparisons with measurements are possible, but large over the oceans in areas without available observations).
Several more models with bulk aqueous phase chemistry exist (e.g., Chang et al. (1987); Hass et al. (1993); Liu et al. (1997); Matthijsen et al. (1997)), mostly using similar approaches as those mentioned above. The application of cloud and precipitation chemistry in a global model has not been studied yet in detail. Lawrence and Crutzen (1998) calculate the uptake of gaseous trace species in cloud and rain droplets acording to Henry's law, but do not consider chemical reactions in the aqueous phase. They include the gravitational settling of cloud droplets and show that it helps to reduce the overestimation of some trace species mixing ratios in the upper troposphere. The dissociation of acidic species is parameterised by applying a modified Henry coefficient. In a follow-up paper Crutzen and Lawrence (2000) present the effect of scavenging for the vertical transport of several species under different conditions, e.g., a varied pH - value. This affects the effective Henry coefficient, but chemical interactions or an online calculation of the pH is not

possible. Nevertheless, they conclude that the removal of several trace gases, e.g., SO_2, is highly dependent on the pH - value within the clouds and precipitation. The expansion of the same model to the chemistry of non-methane-hydrocarbons (NMHCs) (von Kuhlmann et al., 2003) uses the same algorithm for the organic acids, e.g., CH_3COOH.
The aqueous phase chemistry of sulphur in a global model is applied by Feichter et al. (1996), but the neglect of the presence of HNO_3 and neutralising compounds is a major weakness of their study. The first approach with basic aqueous phase chemistry in a global model is undertaken by Dentener (1993). Roelofs and Lelieveld (1995) explicitely calculate the uptake and dissociation equilibria of several species (e.g., HNO_3, H_2SO_4, H_2O_2, O_3), and the SO_2 oxidation. The disadvantage of this scheme is that it is hardly expandable since its programming structure is very topic specific. Some parts of this thesis are based on this work (Roelofs and Lelieveld, 1995).
As mentioned above, some model calculations use simplified parameterisations, applying scavenging efficiencies. This is commonly done for the aerosol scavenging, but in some model studies also for gaseous components. An example is the work of Stier et al. (2005), where the sulphur oxidation is simplified to achieve a realistic sulphate aerosol. A similar approach is described in Yu et al. (2003). Since the focus for both models is mainly the atmospheric aerosol, the liquid phase chemistry is of minor importance for their investigations. On the other hand, only with a properly described liquid phase chemistry the composition of the atmospheric aerosol can be simulated accurately, as will be explained later.

6.2 Scavenging Scheme: Model description

The SCAV submodel (also published in Tost et al. (2006)) calculates the process of scavenging of gas molecules and aerosol particles by clouds and precipitation. Additionally, aqueous phase chemistry and the chemical processing of aerosols in the clouds and the precipitation flux can be investigated.
The SCAV submodel is highly structured, and all calculations are performed in the smallest meaningful entity. For the physico-chemical process 'scavenging' this is a vertical column since the chemical composition of the rainwater that enters a grid box from above affects the scavenging in that particular layer as well as the layers below. The input for the SCAV submodel has to be provided by an external source, e.g., from a larger scale model or through prescribed values. If available, liquid water content and an average droplet size can be used as input data, otherwise they can be estimated from precipitation rates or fluxes, e.g., following Mason (1971). Calculation of scavenging for each droplet or even for droplet size bins is not feasible within most models over a longer simulation period due to computational constraints. Therefore, a monodisperse droplet spectrum is assumed for cloud droplets. For liquid precipitation a rain droplet size distribution according to Best (1950) has to be assumed, because of reasons to be described later (see Section 6.2.1).
In this work the often used terms of 'in-cloud' and 'below-cloud' scavenging are avoided as they do not represent a physical process but only its location. Instead the terms nucleation scavenging (NS) and impaction scavenging (IS) are used, providing a more accurate process description. NS represents the dissolution of species during the nucleation and growth of cloud droplets by microphysical processes that can result in precipitation formation. The term IS is used for falling rain droplets that impact with gas molecules and aerosols resulting in their uptake. This is more suitable because precipitation, formed at a higher altitude and falling into a cloud layer, leads to IS even though this may happen

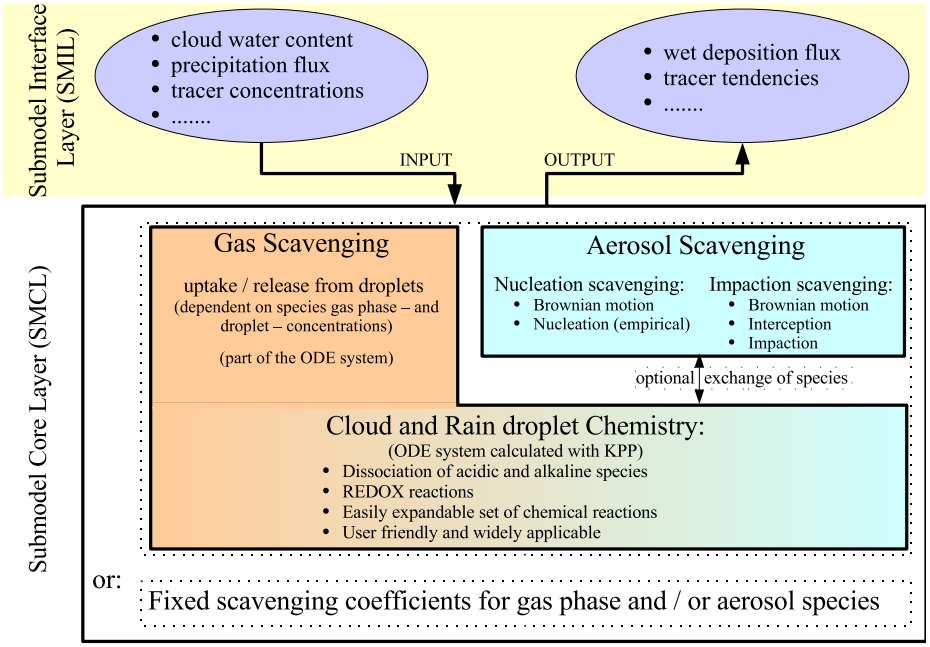

Figure 6.1: Schematic representation of the scavenging and multiphase chemistry scheme.

within a cloud. Both processes have to be strictly distinguished because the droplet diameter can differ by orders of magnitude.
Within the column, the scavenging process starts in the uppermost layer where a cloud is located (NS). In the layer below, the IS by the incoming precipitation flux is calculated first, followed by NS in that particular layer. If there are no clouds in this layer, the NS is neglected and only IS is calculated.
SCAV also calculates the aqueous phase chemistry in cloud droplets. Many reactions (e.g., the oxidation of SO_2) proceed at rates very different from those in the gas phase. The aqueous phase chemistry is calculated for both, precipitating and non-precipitating clouds, accounting for the chemical cloud processing of aerosols and air (for the latter after cloud evaporation).

The technical realisation for the scheme is sketched in Figure 6.1. The coloured boxes describe the new approach compared to the fixed coefficients commonly used in former models. The sketch also shows that input values (liquid water content (LWC), rain rate, etc.) for the clouds and precipitation are required. The coding standard defined by the MESSy structure (Jöckel et al., 2005) is strictly followed. The submodel interface layer (SMIL) organises the necessary data flow from the base model, which can be either a column model or a GCM, into the calculation of the scavenging process in the submodel core layer (SMCL).
The required input parameters are: temperature (K), pressure (Pa), cloud liquid water content (kg/kg), precipitation formation (kg/kg), cloud ice content (kg/kg), snow formation (kg/kg), rain and snow flux (kg/(m^{2}s)), cloud cover, tracer mixing ratios (mol/mol), aerosol radius (m) and mode width (for modal aerosol modules), photolysis rates for individual species (1/s), and some quantities describing the grid box (mass, volume, horizontal size). The submodel has its own species structure, as defined and used in the SMCL. The 'translation' into this structure is done in the SMIL and is largely automated by prepro-

cessing scripts.
User interaction controls the internal complexity of the submodel by setting switches in the FORTRAN90 namelist, namely:

- IS and / or NS
- gas phase and / or aerosol species scavenging
- scavenging by liquid water and / or ice

Additionally, the complexity of the scheme is selectable by both the choice of the aqueous phase chemistry mechanism (described later) and the scavenging parametrisations.
The output are tendencies for the tracer mixing ratios, the wet deposition fluxes for the considered species, and pH - values in clouds and precipitation.

6.2.1 Gas scavenging and liquid phase chemistry

The scavenging of gases can be calculated following two different approaches: First, in the classical approach with empirically determined, fixed scavenging coefficients (estimated from previous studies and Henry's law coefficients), and second by a system of coupled ordinary differential equations (ODE), explicitly describing the processes involved. The first has the advantage of being computationally efficient, e.g., in long-term climate simulations, whereas the second resolves feedback mechanisms between the multi-phase chemistry and transport processes involved. For the second approach the Kinetic PreProcessor (KPP) is applied including an adequate numerical equation solver (Damian et al., 2002; Sandu and Sander, 2005).
The processes of uptake and release of gases from the cloud or rain droplets is formulated following the Henry's law equilibrium and a correction for gas phase diffusion limitation and the accommodation coefficients.
Additional processes taking place in the liquid phase are:

- Transfer reactions (described in detail below);
- Dissociation of acidic and alkaline species (acid-base equilibria, see section 1.2.2.1);
- Redox reactions in the liquid (as mentioned in section 1.2.2.2);
- Photolysis reactions in the liquid phase (e.g., of H_2O_2);
- Heterogeneous reactions on the surface of the droplets (e.g., gaseous N_2O_5 reacts on an aqueous surface with H_2O to dissolved HNO_3).

These processes are described by a coupled system of ODEs. Using KPP, the chemical reaction system can easily be altered without changes in the code (only automated scripts need to be run) and therefore it is applicable to a wide range of tasks of various complexity. The available liquid phase reaction set is identical to that of Sander et al. (2005), with some additions from Ervens et al. (2003). The reaction rates are calculated at each model time step and in each model level, depending on the meteorological input data (i.e., temperature, pressure, liquid water content (LWC)). The selection is possible from a comprehensive set of chemical reactions, but very detailed liquid phase chemistry becomes computational intensive.
An adequate minimum scavenging mechanism for current tropospheric chemistry systems

contains the transfer of about 35 species into and out of the droplets, their dissociation equilibria and the liquid phase oxidation of SO_2 to SO_4^{2-} by O_3 and H_2O_2 (45 reactions). This is still computationally efficient while simulating the major known influences on tropospheric photochemistry. For further improvements and tests it is possible to calculate a comprehensive aqueous phase chemistry considering more than 70 inorganic and organic species with up to 130 reactions, or selecting even more chemical reactions, e.g., including transition metal chemistry.
A list of all reactions of the SCAV submodel used in this studies can be found in Appendix C. Those that are labeled with an 'Scm' are used in the smallest mechanism suitable for long term model simulations.

Technically, a liquid chemistry mechanism has to be selected before a simulation. This is done by an automated script similar to that described by Sander et al. (2005). This script applies the KPP software and automatically creates FORTRAN90 code for the calculation and solution of the chemical mechanism. Additionally, it builds the chemical species structure of the SMCL and creates the routines that manage the transfer from a different species structure into that of the submodel (part of the SMIL). The new liquid phase chemistry calculation code is part of the SMCL, too. After compilation the simulation takes into account scavenging as well as the cloud and precipitation chemistry of all selected reactions.
Because the model time step of global models is relatively long for chemistry integrations a model time step has to be subdivided into several sub-time-steps. Tests have shown that a Rosenbrock solver with automatic time step control is best suited for this specific task, since it can be applied to very stiff ODE systems (see also Sandu et al. (1997b,a)). Therefore in this work a 3rd order Rosenbrock solver with automatic time stepping control is used. Its most important feature is not the order, but the automatic time stepping control, allowing very small timesteps (e.g., 10^{-10} s) if required.
For every time step of the base model the entire tropospheric column of the model domain needs to be taken into account. This is essential, because the uptake of species from the gas phase is also limited by the amount which is already dissolved in the precipitation. For each layer the chemical composition of the precipitation falling from the layers above determines the starting concentrations in the liquid phase, while the gas phase concentrations are determined by the ambient values of the actual layer. The wet deposition flux from the lowest model layer represents the chemical composition of rain water. Since usually only a small fraction of a grid box is affected by clouds and precipitation, only the cloud covered part, or the part, in which the precipitation occurs, contributes to the scavenging, while the rest of the grid box remains unchanged. The cloud cover is one of the required input values. This bulk approach does not take into account the cloud structure in the grid box, since this information is often not provided by models, not even for cloud microphysics.
For very simple test cases also fixed scavenging coefficients are implemented in the scheme and can be selected in the namelist controlling the SCAV submodel. However, this approach is not recommended for regular atmospheric chemistry applications.
Within the chemical mechanism the reaction rates also include the transfer coefficients. These are limited by gas phase diffusion, which can be calculated from the atmospheric conditions and the molar mass of individual species following:

$$D_g = \frac{\bar{v} \cdot \lambda}{3} \tag{6.1}$$

Here $\bar{v}$ represents the mean molecular velocity from the Boltzmann velocity distribution (in m/s) and λ the mean free path (in m) at the particular atmospheric conditions resulting in the diffusivity D_g of the respective gas in the air in m^2/s.
For cloud droplets the transfer coefficient can be described by the following equation (Schwartz, 1986):

$$k_{mt} = \bar{v} / \left(r \cdot \left(\frac{r}{\lambda} + \frac{4}{3\alpha} \right) \right) \tag{6.2}$$

In this equation the transfer coefficient k_{mt} has the unit s^{-1}, r, the droplet radius is given in m and the accommodation coefficient α, is dimensionless. Even though the assumption of an average cloud droplet radius does not reflect the reality, the error made by this approach is sufficiently small, since the transfer velocity of gaseous species does not differ much in the size range of cloud droplets.
For falling rain droplets the equation originally derived by Frössling (1938) is used:

$$v_{tr} = \frac{D_g}{2r} \cdot \left(2 + 0.6 \sqrt{\frac{2 \cdot r \cdot u}{\nu}} \left(\frac{\nu}{D_g} \right)^{1/3} \right) \tag{6.3}$$

Here v_{tr} is the transfer velocity across the droplet surface in m/s, u (the terminal velocity of the falling droplets) is given in m/s and ν is the kinematic viscosity of air in m^2/s. Since the precipitation is not monodisperse, a droplet size distribution has to be assumed because an average droplet size would underestimate the effective transfer coefficient. Therefore an integrated transfer velocity over all droplet sizes weighted with the distribution function of Best (1950) is calculated. To obtain the same transfer coefficient as in Equation 6.2 a geometry factor has to be applied to transform the velocity across the surface into a reaction rate coefficient:

$$k_{mt} = \frac{3 v_{tr}}{r} \tag{6.4}$$

For the determination of the transfer reaction rate coefficients ($k_{\text{exf:f}}$ (forward) and $k_{\text{exf:b}}$ (backward), both in s^{-1}), k_{mt} has to be multiplied with the LWC (in m^3_{water} / m^3_{air}) for the forward and with the dimensionless Henry coefficient H_x for the backward reaction rate (Sander, 1999).

$$k_{\text{exf:f}} = k_{mt} \cdot LWC \tag{6.5}$$

$$k_{\text{exf:b}} = k_{mt} \cdot H_x \tag{6.6}$$

The dissociation reactions follow the Arrhenius formula, and the oxidation reaction rates are taken from the literature (see Appendix C). In this place it is emphasized that these chemical calculations are separated from the calculation of gas phase chemistry and are independent of it.

6.2.2 Aerosol scavenging

For this process SCAV also contains the dual approach using fixed coefficients or alternatively online calculated scavenging coefficients. The latter calculation, being recommended for atmospheric chemistry applications is dependent on aerosol and droplet radius. Different parametrisations are implemented for nucleation and impaction scavenging: the nucleation scavenging takes into account Brownian motion (following Seinfeld and Pandis (1998)) while the nucleation and growth to cloud droplets is parametrised with an empiric function shown in Figure 6.2. The aerosol nucleation scavenging ratio is plotted versus

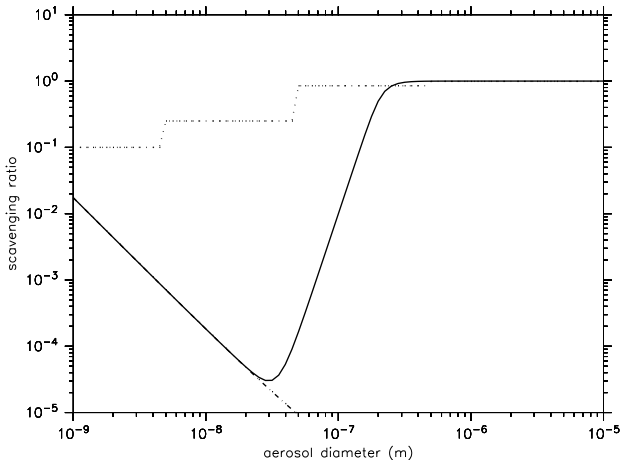

Figure 6.2: Nucleation scavenging based on an empirically fitted curve as a function of aerosol diameter (compare Equations 6.7 and 6.9; solid line: total scavenging efficiency; dashed line: effect of Brownian motion in a cloud with a LWC of 1 g/kg; dotted line: parametrisation by Stier et al. (2005)).

the aerosol radius. For the small particles the Brownian motion (dashed line) is dominant. For the larger particles, above a threshold of about 0.1 μm, the nucleation and growth of cloud droplets is dominant, rapidly reaching 100% aerosol scavenging ratio. The function for the larger aerosol particles has been empirically determined by measurements within clouds. Both processes in combination result in a ratio shown by the solid line. The dotted line shows a recently used parametrisation for NS in water clouds by Stier et al. (2005). For the small particles of the nucleation and Aitken mode the latter parametrisation yields much higher values.
Impaction scavenging depends on Brownian motion, interception, and impaction following a formula originally described by Slinn (1983). Its applicability has also been shown by Andronache (2003, 2004). Figure 6.3 shows the three major processes that control impaction scavenging, depicting the collection efficiency as a function of the aerosol radius for rain droplets with 1 mm radius. The double dashes show the Brownian motion induced scavenging, again dominant for the smallest particles. The dotted line depicts the interception and the short dashes the results of impaction. Impaction and interception are clearly dominant for the larger particles. The solid line shows the net effect. For comparison, a constant collection efficiency of 0.7 for all aerosol sizes, which is a commonly used parameter in simple parametrisations, is plotted (medium dashes). It is obvious that this does not represent the physical processes involved.
Both figures show the well known 'scavenging gap', being slightly shifted to the smaller particles for nucleation scavenging compared to impaction scavenging.
Since there is a dependency on rainfall intensity and droplet size, Figure 6.4 shows the scavenging coefficient for five rain rates (0.5 mm/h, 1 mm/h, 2 mm/h, 5 mm/h, 10 mm/h from lower to the upper curve, respectively). Following Mason (1971), the mean rain droplet radius depends on the rain rate, yielding radii of 0.32 mm, 0.37 mm, 0.42mm, 0.51 mm and 0.59 mm, respectively.

The parametrisations described above are part of the SMCL. The calculated aerosol concentrations in the base model are transferred in the SMIL into local fields of the SMCL,

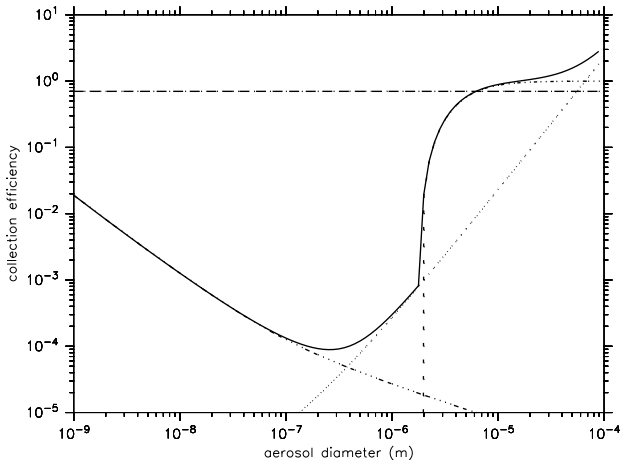

Figure 6.3: Impaction scavenging and the effect of contributing processes on the collection efficiency as a function of aerosol diameter as calculated by Equation 6.10 (solid line: total collision efficiency; double-dashed line: Brownian motion; dotted line: interception; short dashed line: impaction; medium dashed line: constant efficiency (for comparison only)).

similarly to the gas phase species. In each grid box NS and IS are calculated in the same way as described for the gas phase scavenging adopting the required input values in subroutines of the SMIL. Again the scavenged fraction is stored in the wet deposition flux separately for each aerosol species.
Within the SMCL for nucleation scavenging the Brownian motion effect is determined by the semi-empirical formula from Pruppacher and Klett (2000):

$$\Lambda_B = \frac{1.35 \cdot LWC \cdot D_p}{r_{\text{cloud}}^2} \tag{6.7}$$

Here Λ_B represents the scavenging coefficient for Brownian motion in s^{-1}, the LWC is in g/cm^3, D_p is the diffusivity of the particle in m^2/s and the unit of the cloud droplet radius r_{cloud} is m. This coefficient is applied in an exponential approach for each aerosol species:

$$C(t_0 + \Delta t) = C(t_0) \cdot \exp(-\Lambda_B \cdot \Delta t) \tag{6.8}$$

C is the concentration of a species and Δt the model time step in s. The empirical function for the nucleation of cloud droplets is applied in a different way. In this case it is not the scavenging coefficient, but the scavenging ratio, calculated by:

$$C = C_0 \cdot (1 - \arctan((5.0 \cdot 10^6 \cdot r_{\text{aer}})^6) \cdot 2/\pi) \tag{6.9}$$

For this parametrisation the aerosol radius r_{aer} is used in m. The scavenging ratio C/C_0 resulting from this equation is shown in Figure 6.2. The equation is derived from the measurements presented by Svenningsson et al. (1997) and Martinsson et al. (1999). While Equation 6.9 describes only the uptake of aerosol particles in cloud droplets, the actual removal of aerosol particles by the cloud depends on the ratio of precipitation production to the liquid water content of the cloud. Since the uptake is formulated without using cloud droplet attributes, an assumption about the cloud droplet distribution is not required.

It is assumed that the microphysical properties of the cloud and precipitation formation are already calculated by other submodels and can be used as input values. If

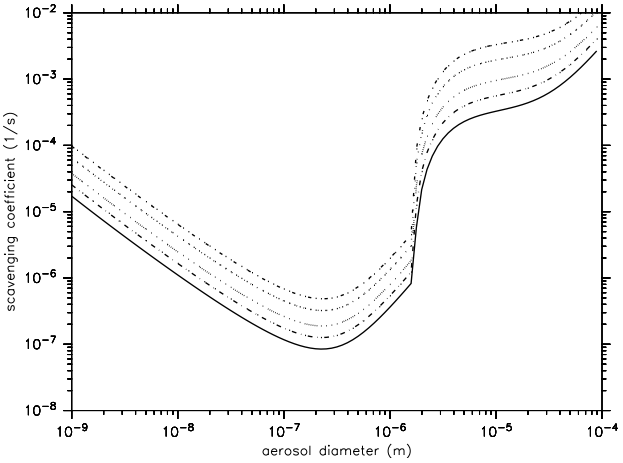

Figure 6.4: Impaction scavenging coefficient for various rain rates calculated according to Equation 6.10 (from bottom to the top: 0.5 mm/h, 1 mm/h, 2 mm/h, 5 mm/h, 10 mm/h) as a function of aerosol diameter.

the aerosol distribution is already used for this purpose and modified by this process, the aerosol nucleation scavenging of the submodel SCAV should not be applied. A formulation of aerosol-cloud interactions considering the supersaturation and chemical composition of the aerosol would be useful, but has not been implemented in the model system yet. Due to this lack, the simplified approach has been made.
For impaction scavenging the scavenging coefficient is calculated from the collision efficiency shown in Figure 6.3. This dimensionless efficiency E is determined by:

$$E = \frac{4}{ReSc}(1 + 0.4Re^{1/2}Sc^{1/3} + 0.16Re^{1/2}Sc^{1/2}) + 4\Phi(\omega^{-1} + (1 + 2Re^{1/2})\Phi) + \left(\frac{St - S^*}{St - S^* + 2/3}\right)^{3/2} \tag{6.10}$$

Re is the Reynolds number of the rain droplet, Sc the Schmidt number of the collected aerosol particle, St the Stokes number of the collected particle, Φ the ratio of radii of particle and droplet ($r_{\text{particle}}/r_{\text{droplet}}$), and ω the viscosity ratio of water to air. The parameter S^* is derived from the Reynolds number by:

$$S^* = \frac{1.2 + \frac{1}{12}\ln(1 + Re)}{1 + \ln(1 + Re)} \tag{6.11}$$

For this calculation the terminal velocity of the raindrops is computed following Beard and Pruppacher (1969). Parametrisations and definitions of all other required parameters can be found in the textbooks of Pruppacher and Klett (2000) and Seinfeld and Pandis (1998). Subsequently, the scavenging coefficient can be calculated by:

$$\Lambda = \frac{E}{r_{\text{rain}}} \cdot 0.75 \cdot F_{\text{rain}} \tag{6.12}$$

Here again Λ is the scavenging coefficient in s^{-1}, r_{rain}, the radius of the droplet, is given in mm, the effective precipitation flux F_{rain} in kg m^{-2} s^{-1}, pertaining to the fractional dimensionless part of the grid box covered by precipitating clouds. The coefficient Λ is applied as in Equation (6.8).

6.2.3 Coupling of aerosol scavenging and liquid phase chemistry

In case of a calculation of the chemical composition of the aerosol a coupling between the aerosol and gas phase scavenging is required because of the chemical interaction in the aqueous phase. Note that it is irrelevant whether a specific molecule originates from a dissolved aerosol particle or from gas phase species (e.g., sulphate, which can be transferred by sulphate aerosol particles, by the dissolution of gaseous H_2SO_4 or by the liquid phase oxidation of SO_2). Furthermore, the chemical cloud processing of aerosol particles which have not been removed from the atmosphere by wet deposition, but rather have been released through droplet evaporation can thus be addressed explicitly.

Technically, this is achieved as follows. The calculations in each column are performed stepwise. First, as described above, NS is calculated for aerosol species, afterwards the chemically active, scavenged fractions are used as initial concentrations for the species in the liquid. Effectively, there is only a different transfer mechanism for these species (dissolution of aerosol particles compared to diffusive uptake from the gas phase). Next, the gas phase concentrations from the base model are fed into the chemical core and assigned to the selected chemical species. Now the actual chemical integration is performed including the reactions and transfer mechanisms from and into the gas phase. If species of limited solubility enter a model layer with low gas phase concentration these can partly be transferred to the gas phase. Additionally, the aqueous phase chemistry in the droplets may cause a release of species produced within the droplets, e.g., chloride ions that have been reduced in chemical reactions can be released as volatile chlorine species to the gas phase. At the end of each time step it is assumed that the cloud completely evaporates and all volatile species will be released to the gas phase, while the ions are transferred to the aerosol phase, thus affecting the aerosol properties. As an example, the SO_2 oxidation to SO_4^{2-} can significantly increase the aerosol sulphate amount. The evaporation approach is used for numerical reasons, because the model would become computationally very expensive if in addition to the gas phase species all aqueous phase species including ions were to be transported together with the cloud water. Since usually longer time steps are used for transport compared to the chemistry substeps, the difference in the uptake time is expected to be of less importance. The ratio of the precipitation formation to the total cloud water content within one time step determines the fraction of the species actually scavenged, entering the next lower grid-box by the precipitation flux.
For the impaction scavenging the procedure is similar. First the aerosol impaction scavenging is calculated. Subsequently, for chemically active species (determined by the selected mechanism) the transformation of scavenged aerosol material into the rain water is performed and subtracted from the aerosol wet deposition flux. Then the chemical integration is performed and the species concentrations are stored in the wet deposition flux for the layer below.
Several degrees of coupling can be selected by the user, depending how detailed the information of the chemical composition of the aerosol can be provided. If there is no aerosol submodel available, assumptions are made to create a set of passive aerosol tracers (e.g., aerosol sulphate, nitrate, H^+ and ammonium) to ensure mass conservation. These are affected by the typical aerosol sinks, but microphysical aerosol properties are not assigned.

6.2.4 Evaporation of rain and release of dissolved species

If cloud or falling rain droplets evaporate completely the dissolved species are released. Any neutral, volatile compound is transferred to the gas phase. Scavenged aerosol particles are redistributed into the aerosol distribution. In many previous model approaches, the ions were neglected, assuming that they would stay attached to aerosols and eventually be scavenged by precipitation before they would be released back to the gas phase. Alternatively they were transferred back into the gas phase species from which they originate (e.g., NO_3^- is released as gaseous HNO_3). The former approach is not mass conserving and neither assumption is physically and chemically realistic. Due to the coupling with the aerosols this weakness has been overcome in the new scheme.

Note that the commonly used approach to release part of the dissolved species according to the effective evaporation rate (Roelofs and Lelieveld, 1995) is not applied. Rather a more mechanistic approach is followed. As long as there is liquid water available (LWC greater than a threshold value), the liquid phase chemistry is calculated as described above. In case of higher liquid phase concentrations than allowed according to Henry's law for equilibrium, these species are released into the gas phase via the phase change mechanism described above with respect to the gas phase diffusion limitation. For ions, the lower water content raises their concentrations. This changes the dissociation equilibria and the rates of reaction pathways. In case of the complete evaporation, i.e., if the LWC decreases below the threshold (droplet must then be considered as deliquesced aerosol), non-volatile species and ions produced by liquid phase chemical processes are transferred to aerosol species of the largest available mode. This also depends on the degree of coupling between the aerosol composition and the SCAV scheme. As a consequence new aerosol particles can be created. The volatile compounds are either directly released to the gas phase or through the chemistry scheme of the aerosol submodel, again dependent on the availability of a scheme that performs the process calculations.

6.2.5 Large-scale and convective precipitation

Usually global models distinguish between large-scale (i.e., grid size resolved) and convective (i.e., subgrid-scale) precipitation. Since in reality there is no difference in those types of rainfall, scavenging occurs in both. Therefore the same routines of the SCAV submodel can be applied with input parameters from the respective precipitation parameterisation. In convective clouds and precipitation it is necessary to consider the strong upward motion of the air and the tracers within. This is taken into account by the submodel CVTRANS (see Section 4.2). In such a case the upward motion of a soluble tracer is counteracted by the downward motion of the dissolved tracer in the precipitation. Therefore a simple application of the operator/process-splitting is not feasible, because either the soluble material will be transported along the clouds without any interference (first transport, then scavenging), or the scavenging and the vertical redistribution will be underestimated (first scavenging, then transport), since a large part of a soluble tracer will be scavenged only in the lowest layers, where the temperature is higher resulting in a lower solubility.
Therefore in the CVTRANS submodel it is selectable which process order should be applied. Even an iterative process sequence is possible, and in this work a scheme is used that allows convective transport to the top layer of rain production, then the scavenging and finally the transport of the modified tracer concentrations from the layer above the freezing point to the convective cloud top.

6.3 Scavenging: Idealised case studies

In this section the interaction of the different convection schemes with scavenging and wet deposition is investigated. The intention of this study is not to determine the scavenging rates for the individual components, but to show the dependence on the selected convection scheme contributing to convective transport and scavenging under 'almost realistic atmospheric conditions'. Since trace gas mixing ratios are modified by chemistry depending on the mixing ratios of almost all other species, in this idealised study the gas phase chemistry is neglected. Therefore, the differences between the simulations originate only from the effects of the different convection parameterisations. This includes both direct effects of transport and scavenging and the modified dynamics and thermodynamics of the atmosphere. Since it has been shown in Chapter 3 that replacing the convection parameterisation does not disturb the general circulation, as tested with the help of the temperature distribution, a significant part of the differences occuring in the study of this section can be assigned to the direct effects of transport and scavenging.

6.3.1 Simulation setup

The simulations performed for this study are described in Section 4.3.1. The analysed species are 'idealised' gas phase constituents, which have similar properties (molar mass, solubility, reactions in the liquid phase) as HNO_3, NH_3, HCOOH, HCHO, O_3 and CO. CO is not affected by scavenging at all. The scavenging is calculated with minimum aqueous phase chemistry (marked with **Scm** in Appendix C). To achieve realistic atmospheric concentrations of each component they are initialised with data from a comprehensive chemistry simulation and are continuously emitted (except for O_3) at the surface (OFFLEM). The applied emission rates are, however, different from those proposed by the EDGAR emission database, to take into account the chemical production.
Additionally, ^{210}Pb, the product from the radioactive decay of ^{222}Rn, is used for the analysis of aerosol scavenging, since it is known to stick to aerosol particles (e.g., Sanak et al., 1981; Liu et al., 2001).
For convenience the simulations and their respective abbreviations are repeated here:

- Simulation with the Tiedtke convection scheme T1 (C_T1), the reference simulation;
- Simulation with the ECMWF convection scheme EC2 (C_EC);
- Simulation with the Zhang-McFarlane-Hack convection scheme ZH (C_ZH);
- Simulation with the Zhang-McFarlane-Hack convection scheme with the additional evaporation of precipitation ZHW (C_ZHW);
- Simulation with the Bechtold convection scheme B2 (C_B2).

Again, only the one year data after the spin-up period of three months is used. It is emphasised, that the gas phase species O_3, HCHO, HNO_3 and NH_3 in these simulations are idealised tracers, even though in the following this is not always noted.

6.3.2 Idealised studies: Results

First, average profiles of the idealised tracers are analysed, followed by the associated wet deposition fluxes.

6.3.2.1 Vertical profiles of idealised tracers

The annual average vertical profiles of the mixing ratios (in nmol/mol) of the species comparable to O_3, HCHO and HNO_3 are shown as zonal average in the tropics (10°S to 10°N). This region is generally characterised by strong convection, including both convective updrafts and scavenging by convective clouds and precipitation.

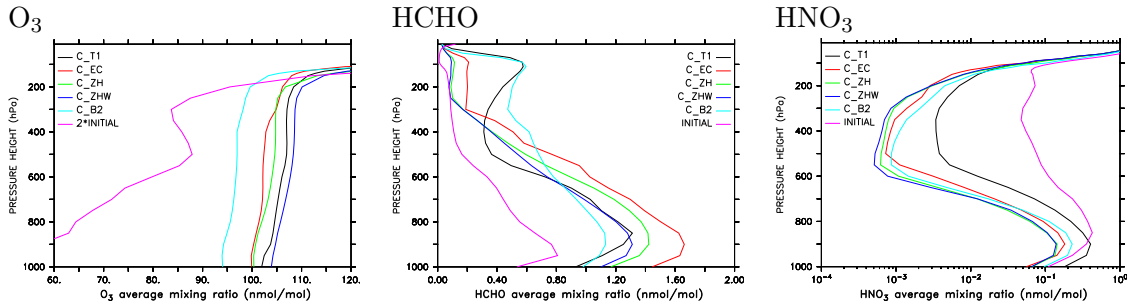

Figure 6.5: Annual average vertical profile in the tropics of idealised O_3, HCHO and HNO_3 in the simulations with the individual convection schemes (denoted by the color). The magenta line depicts the initial profile for all simulations (for O_3 multiplied by 2 to stay within the scale).

The left panel of Figure 6.5 shows the ozone mixing ratio. Since no gas phase chemistry is applied, and the solubility of ozone is low, it is hardly affected by scavenging, also because aqueous phase oxidation of SO_2 is not considered. Furthermore, the dry deposition of O_3 is neglected. Therefore, the differences between the simulations are mainly a consequence of the different convective transport. Due to convection an efficient mixing occurs in the troposphere. Above 200 hPa, the mixing ratio increases substantially because of the higher values in the stratosphere originating from the initialisation. However, the tropospheric values, especially close to the surface, are substantially higher for all simulations than the initial mixing ratios. This results from downward transport of ozone rich air from the stratosphere. According to Equation 4.4 the air raised by convection must be balanced outside the plume. In the UTLS region with increasing ozone mixing ratios with altitude this balancing leads to a downward transport of O_3. Depending on the strength of the convective upward motion of air containing less ozone, the mass balancing subsidence within the grid cell is enhanced. Therefore the highest mixing ratios occur in the C_ZHW (dark blue) simulation with the most intense convection in the tropics (compare Figure 4.2). Even though the C_ZH (green) simulation shows similar strong convection reaching almost as high, the tropospheric mixing ratios are lower than in the C_T1 (black) simulation. Therefore the O_3 values cannot be explained by convective transport alone. The strong convective activity in the C_ZH simulation is mostly restricted to the continents as analysed from the precipitation patterns. Therefore, on a global average the C_T1 simulation with a more uniform spatial distribution is as effective in the downward transport of ozone rich air from the UTLS region. The C_EC simulation (red line) shows slightly lower values in the middle troposphere, but similar O_3 mixing ratios near the surface. In the C_B2 simulation the ozone mixing ratios are slightly lower. The gradient is as steep as for the other simulations, indicating again a well mixed troposphere. Without the chemical sink processes, this can be explained only by weaker exchange with the stratosphere. Furthermore, it must be remembered that the values in Figure 6.5 are annual average vertical profiles. Since there is almost no loss process for ozone in this study (no chemistry and no

dry deposition), it can be transported from the stratosphere into the troposphere through tropopause folds in the midlatitudes, and then subsequently in the lower troposphere together with water vapour (Trenberth and Stepaniak, 2003) towards the equator.
The middle panel of Figure 6.5 depicts the vertical average profiles of idealised formaldehyde. HCHO is of medium solubility and therefore partly affected by the scavenging by clouds and precipitation. The initialisation and the emissions at the surface lead to a profile with decreasing values with altitude for all simulations. The upper tropospheric mixing ratios are in the range of 10% to 50% of the surface and boundary layer mixing ratios. In all simulations an increase in the boundary layer can be detected. This originates from the emissions and almost no sink processes in the lower troposphere. Even though there is impaction scavenging, the uptake into the droplets is relatively low due to the solubility and the warm air temperatures. There are hardly any precipitating clouds below 850 hPa, resulting in no effective nucleation scavenging and subsequent wet deposition in the lower troposphere. Above 850 hPa the mixing ratios in all simulations decrease almost linearly with altitude. Even though this is consistent with the initial profile, it reflects only a compensation of the reduced emissions and the neglection of gas phase chemistry. The C_T1 and the C_B2 simulations show a secondary maximum at about 100 hPa, that does not occur with the other convection schemes. Both the C_ZH and C_ZHW HCHO profiles are almost identical above 400 hPa. The C_EC scheme shows the highest mixing ratios in the lower troposphere. This is because of the lower total precipitation amount (compare Figure 3.4) in the tropics compared to C_T1 and C_B2, which results in a less efficient scavenging in C_EC of this compound. The C_ZH and C_ZHW show even lower total precipitation, but as mentioned above, the convection with strong precipitation is restricted to smaller areas over the continents. Since these are the same regions, in which emissions of this compound occur, this results in a more efficient scavenging and lower mixing ratios than in C_EC. The gradient is steeper for C_B2 indicating less influence of the scavenging in this simulation. In the upper troposphere, this might be a consequence of the explicit treatment of convective cloud ice, that is not considered with respect to scavenging. The positive or zero gradient in the upper troposphere occuring in all simulations can also be explained by the weaker scavenging in the upper troposphere due to lower liquid water content. While for the C_EC simulation almost no change in mixing ratio occurs above 300 hPa and for both simulations applying the ZH convection scheme above 250 hPa, the upper boundary of scavenging above is possibly lower for the C_B2 and the C_T1 simulation. The increase of the HCHO mixing ratios is consequently a result of the convective outflow.
The highly soluble HNO_3-like compound is shown in the right panel, with mixing ratios on a logarithmic axis. Similar to HCHO it shows increasing mixing ratios in the boundary layer, but a strong decrease in the middle troposphere and high values in the lower stratosphere. Since there is no chemical production of this compound, only the emissions are responsible for the high values in the boundary layer. The high values in the lower stratosphere originate mostly from the initialisation. Because of the chemical production the initial values in the stratosphere are much higher than in the troposphere, but also in the middle troposphere they are not as low as in the average profiles of the simulations. All simulations show an almost complete scavenging in the middle troposphere with mixing ratios decreased by more than two orders of magnitude, except for the C_T1 simulation. Even for the latter one the reduction is substantial. This is a consequecne of both nucleation and impaction scavenging of HNO_3. Subsidence and slow diffusion are responsible for the increasing mixing ratios above 200 hPa. In this region all simulations are very

similar. In the middle troposphere the shape of the profiles is analogue, too. For most of the simulations (except C_T1) the mixing ratios are also very similar. Even though the uptake of nitric acid on ice particles is neglected, this seems to be of minor importance for the total scavenging in this simulation setup, since the HNO_3 source is restricted to the surface and consequently mostly scavenged in the lower troposphere where sufficient liquid water is available. If gas phase chemistry would be considered, there would also be chemical production in the upper troposphere and the uptake on ice might be more significant.
Concluding, the convective transport alone determines the vertical mixing of insoluble trace species like O_3, while for soluble compounds the interaction of convective transport and scavenging determines the resulting vertical profiles. This results in an efficient mixing of the first type of species, while for the latter the scavenging dominates the vertical profiles. In case of higher values in the stratosphere, the intrusion of stratospheric air influences the troposphere; the strength of this effect is dependent on the convective transport as well.

6.3.2.2 Wet deposition fluxes of idealised tracers

Analysing the wet deposition fluxes, the first species under investigation is the tracer with similar characteristics as nitric acid (HNO_3). It represents a highly soluble tracer, that is scavenged very efficiently and acts as a strong acid in liquid solution. For that purpose, the one year accumulated wet deposition flux of nitrate (NO_3^-) and nitric acid from the C_T1 simulation as a reference is shown in Figure 6.6 in the upper left panel and the absolute differences of the other simulations to that reference in the lower left panels. On the right side of Figure 6.6, the same pictures are shown for the wet deposition flux of ammonia and ammonium (NH_3 and NH_4^+), again absolute values in the upper panel and the differences of the various simulations to C_T1 below.
Since the tracers used in this study are idealised, a comparison with measurements is not feasible. In order to get a realistic distribution, emissions have been assigned to the individual species comparable to their chemical formation (see Section 6.3.1).
Accordingly, the nitrate wet deposition is highest in the regions of high emissions, i.e., in eastern North America, Europe, India, China and Central Africa. As the upper left panel uses a logarithmic scale the wet deposition over the oceans remote from the sources is substantially lower.
The other panels of the left column of Figure 6.6 show the differences in the wet deposition flux of nitrate to the C_T1 simulation. In the simulation with the EC convection scheme significantly higher amounts are deposited over Europe, the USA and Central Africa. Additionally, there are significant differences west of the Californian coast, the African and Australian west coast. In these regions the deposition fluxes of the C_T1 simulation are relatively low. On the other hand, in C_EC significantly lower deposition fluxes are calculated for most parts of the ITCZ region and in the outflow regions from the continents in both hemispheres. The C_ZH simulation shows a similar picture. The largest differences with higher values are found in the US, Central Europe and Central Africa, but also in India and the same regions over the oceans as above. Lower values occur again in the tropics, the continental outflow regions and in northern Canada. Comparing the two simulations with the schemes based on the ZH convection scheme (C_ZH and C_ZHW) only small differences occur. The C_B2 simulation shows a different picture: even though

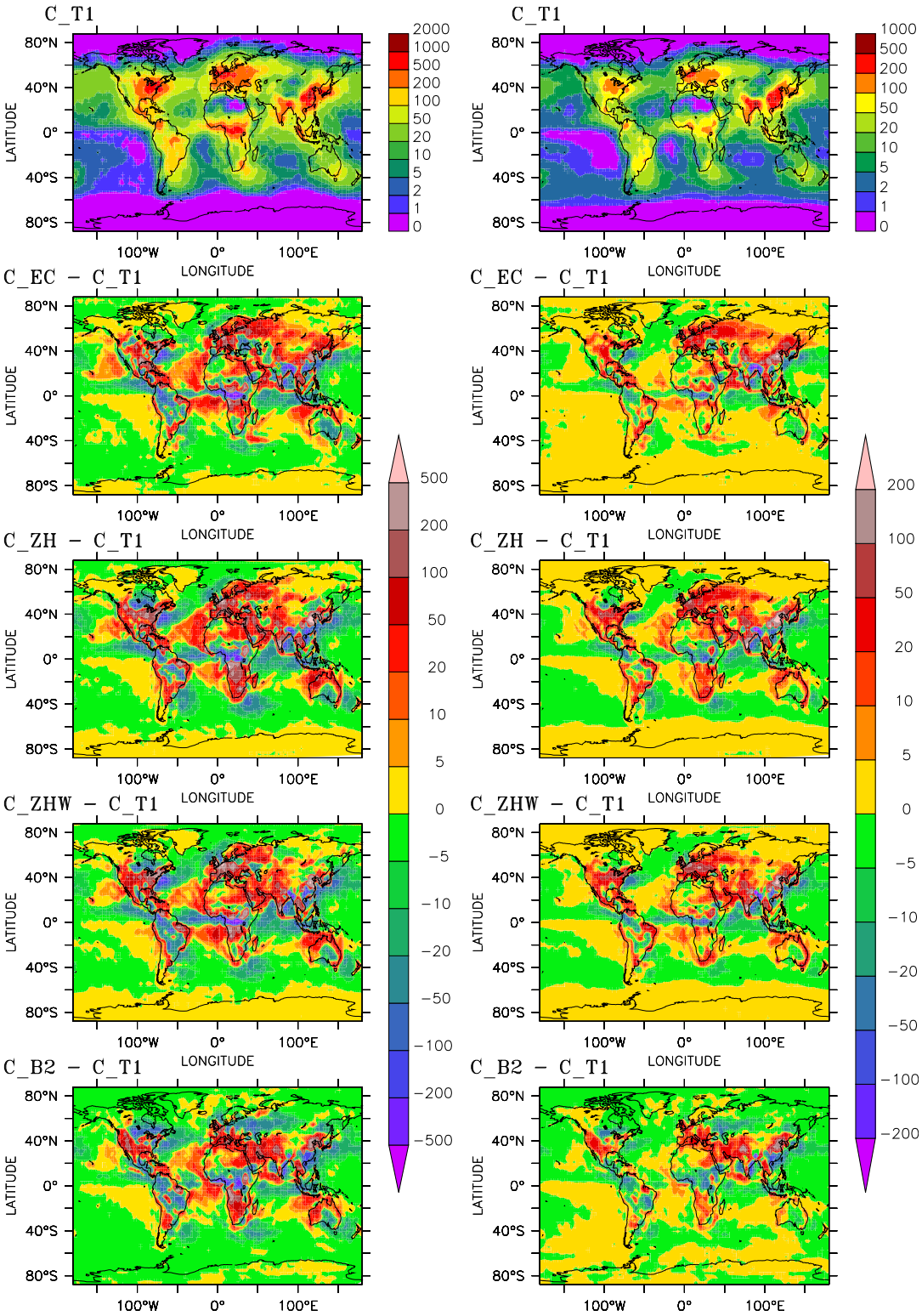

Figure 6.6: Annual sum of the wet deposition flux of nitrate (left) and NH_x (right) in mg N/m^2 of the simulation T1 (upper panels), and differences of the wet deposition fluxes to the reference simulation in mg N/m^2 (lower panels).

in Central Africa and the USA higher deposition values are simulated, the maxima of the differences are locally shifted more to the South or West respectively, compared to the other simulations. In Europe and eastern Canada lower values than in the reference simulation are calculated. The ITCZ and the outflow regions are again characterised by minimally lower wet deposition fluxes of nitrate than in C_T1.
The differences in the precipitation distribution (Figure 3.5) are mainly responsible for the shift of the wet deposition patterns, e.g., precipitation occuring in one specific region leads to effective deposition in that region because of the high solubility of nitrate species. Consequently, deposition of this species cannot occur further downwind, because it has been depleted almost completely during precipitation events, since the lifetime of nitrate with respect to scavenging and wet deposition is less than one model timestep during precipitation (Levine and Schwartz, 1982). The strength of the precipitation events is of minor importance, because generally moderate rainfall is sufficient for the efficient depletion of this compound.
The right column of Figure 6.6 shows the corresponding diagrams for a species similar to the reduced nitrogen compound NH_x (NH_3 + NH_4^+), including the dissociation and neutralising capabilities. As for nitrate, the emission patterns dominate the deposition flux distribution. In the upper right panel the absolute deposition values are presented for the C_T1 simulation. The fluxes are highest in China and India, and slightly lower in the eastern USA and Europe. Additionally, some remarkable deposition is found in the northernmost part of South America and in Central Africa. The latter two regions are characterised by strong precipitation (compare with Figure 3.4 in Section 3.3.2.1). The simulation C_EC shows substantially higher values of NH_x deposition in China and slightly higher values in Europe and the western USA. Almost everywhere over the ocean, with generally lower wet deposition, the absolute difference is small, with a tendency to higher values than in the reference simulation. In the eastern USA, Amazonia, the Bay of Bengal and the storm tracks of the northern hemisphere slightly lower values are calculated. The differences to the simulation with the ZH convection scheme indicate higher deposition fluxes again in China, Europe, the USA and some parts of South America and southern Africa. In the ITCZ region lower values occur. In contrast to the C_EC simulation not only the northern, but additionally the southern storm tracks are characterised by lower deposition fluxes than in the reference simulation. As for the nitrate-like compound, the differences of the C_ZHW simulation to the C_ZH are very small and occur mostly in the tropics due to the modified precipitation distribution because of the enhanced evaporation. In the C_B2 (lowest right panel) much higher deposition values occur in Arabia and eastwards to India. Additionally, more wet deposition than in the reference simulation is calculated for the western USA and southern Africa. Lower values are obtained in Central Africa, southeast Asia, and Amazonia. Furthermore, slightly less deposition is simulated over most of the oceans.
Since both compounds (HNO_3 and NH_x), if dissociation and neutralisation are considered, are highly soluble and effectively scavenged, the main differences between the individual simulations can be assigned to the simulated different precipitation distributions. Generally, the strength of the precipitation has a minor influence on the wet deposition patterns. Nevertheless, in some areas of high deposition the differences are up to 50%, resulting locally in strongly modified conditions. Generally, the overall deposition patterns are similar between all the simulations. Both species have emission sources at the surface. In contrast to ^{222}Rn (compare Section 4.3.2.2) these two compounds are influenced by both convective transport and scavenging. Therefore the effect of the differences in transport interact

with those in the precipitation distributions. Due to the effective scavenging a substantial fraction of the highly soluble compounds does not reach the upper tropsophere.
The differences in the precipitation become more important for species with lower solubility. The wet deposition fluxes of two of such compounds are investigated in Figure 6.7: the left column shows an almost insoluble species similar to O_3 without emission and chemical source, but realistic initial conditions from a previous simulation including comprehensive chemistry calculations with substantially higher values in the stratosphere and lower values in the troposphere. On the right, the wet deposition fluxes for a species with the characteristics of formaldehyde (HCHO) are shown. HCHO is of moderate solubility, and in this simulation setup it has an emission source at the surface.
The scavenging and wet deposition of O_3 is globally of almost negligible significance, especially if aqueous oxidation of sulphuric compounds is neglected. Therefore the wet deposition of this species in the individual simulations is an indicator for both the occurence of precipitation and its strength. The nucleation scavenging of O_3 reveals the occurence of precipitation producing clouds. Since the aqueous phase concentration depends on the gaseous mixing ratio according to Henry's law, it can be used as an indirect analysis tool for the gas phase concentrations.
The upper left panel of Figure 6.7 shows the annual wet deposition flux of ozone in $\mu g/m^2$. As expected the distribution patterns look very similar to the precipitation distribution (compare Figure 3.4), but weighted with the O_3 mixing ratios. Since there is no local chemical production and the import of ozone from the stratosphere is relatively slow, the absolute values on both hemispheres are similar, with slightly higher deposition in the northern hemisphere due to the intra-hemispheric asymetry of the gas phase mixing ratios originating from the initialisation. In the subsidence regions, with almost no precipitation in the T1 convection, only low deposition values occur while in the storm tracks with significant rainfall and ozone from the pollution centers of North America, Europe and Asia (also from the initialisation) higher values are calculated. Furthermore, ozone is transported from the stratosphere into the troposphere along isentropes and at tropopause folds in the midlatitudes. Even though there is strong precipitation in the tropics, the deposition values are lower because of lower ozone mixing ratios. Neither in the initialisation high mixing ratios occur, nor significant transport from the stratosphere occurs because the general circulation is characterised by upward motion of tropospheric air into the stratosphere in the tropics and subsidence further polewards with the intrusion of stratospheric air into the troposphere at tropopause folds, exchange on isentropes or propably small influences of convection (Holton et al., 1995). As identified in Section 4.3.2.1, the convection in the Tiedtke scheme does not reach up into the highest troposphere. Consequently, the mass balancing subsidence is not very effective as a transport process of ozone rich air from the UTLS region into the lower troposphere, especially in the tropics.
The differences that occur in the C_EC simulation show generally lower O_3 deposition values in the midlatitudes while there is more scavenging in the tropics. An exception are the regions where a significant overestimation of precipitation occurs in the T1 simulation (Figure 3.5), i.e., the warm pool east of Indonesia and Central and South America. The lower deposition in these regions is due to the lower precipitation water content leading to a reduced scavenging according to Henry's law. The lower deposition fluxes in the midlatitudes and higher ones in the remaining tropical regions can be attributed to lower and higher ozone mixing ratios, respectively. These originate partly from the downward transport by subsidence as mentioned above. Additionally, from the middle troposphere

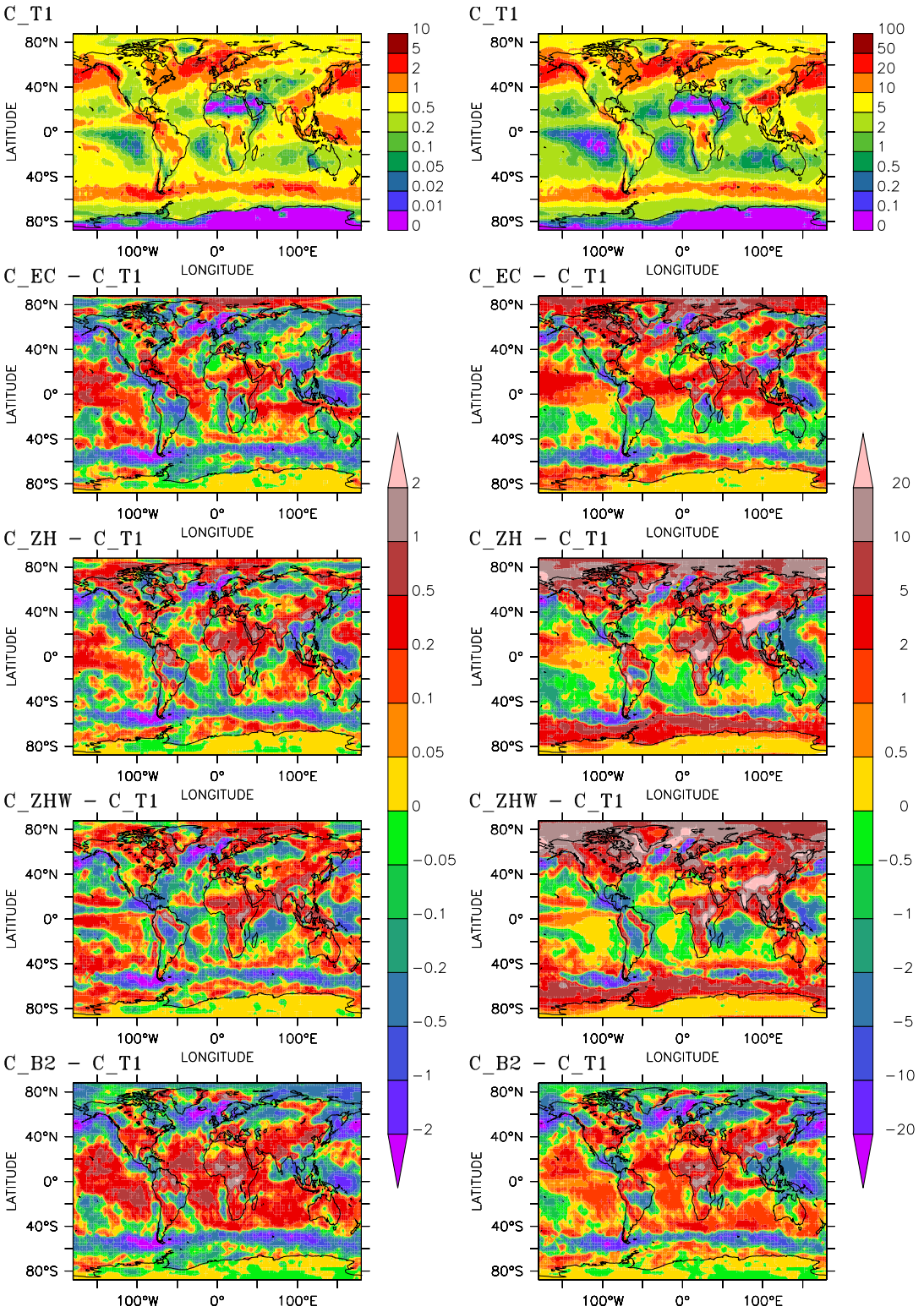

Figure 6.7: Annual sum of the wet deposition flux of ozone (left) in $\mu g/m^2$ and HCHO (right) in mg/m^2 of the simulation T1 (upper panels), and differences of the wet deposition fluxes to the reference simulation in $\mu g/m^2$ and mg/m^2, respectively (lower panels).

ozone can be carried to the lower troposphere by convective downdrafts, leading to higher mixing ratios in the lower troposphere.
This becomes more obvious in the C_ZH simulation with extremely deep convection over the tropical continents and less deep convection over the tropical oceans: over the continents significantly more ozone is deposited in rain compared to the C_T1 simulation, while over the oceans this is less significant. As for the C_EC scheme the lower precipitation values over the warm pool region lead to lower deposition in that region. As seen in the Figure 4.2 the updraft values in the uppermost troposphere in the tropics are substantially higher than in the other simulations. The mass-balancing results in stronger ozone downward transport in the regions of the extremely deep continental convection. Additionally, the precipitation in these regions is much stronger than in the reference simulation, and therefore increases the differences. Since this effect is reduced in the ZHW convection setup, the deposition values of the C_ZHW simulation are lower in these regions, but still higher than in the reference, since the convection is still much deeper.
Similar conclusions are drawn for the Bechtold simulation. Since there is much more precipitation in the tropics compared to the C_EC simulation, the effect of larger wet depositon fluxes in the tropics is even more obvious. In Central Africa, where the deepest convection occurs, substantial more ozone is scavenged than in the reference simulation. The reason for the lower deposition values in the storm tracks compared to the reference simulation occuring in all simulations is twofold. The differences can partly result from the precipitation patterns and the partitioning of the precipitation into rain and snow, modifying the liquid water available for the uptake and aqueous phase chemistry.
The right column of Figure 6.7 depicts the annual wet deposition of the formaldehyde-like compound in mg/m^2. Similar to the compounds analysed in Figure 6.6, the wet deposition is characterised on the one hand by the precipitation fluxes and on the other hand by the emissions. Since the emissions are mostly of industrial origin they are strongest in the northern hemisphere. The wet deposition flux shows highest values in the continental outflow regions of the storm tracks of the northern hemisphere, where both conditions are optimally fulfilled. Without active gas phase chemistry the decomposition of higher hydrocarbons does not contribute to the HCHO formation. Therefore, only the higher precipitation values in the southern storm tracks and over the tropical continents are the main reason for the high wet deposition in this regions.
The differences occuring in the C_EC simulation with significantly lower values over the Pacific in the northern storm tracks and over the warm pool reaching even into the SPCZ can be attributed to the weaker total precipitation in this specific region than in C_T1, as analysed in Figures 3.4 and 3.5. In the other parts of the ITCZ the wet deposition is stronger in the C_EC simulation, compensating the lower values of the warm pool. The weaker deposition in the warm pool region increases the atmospheric lifetime with respect to the considered processes, resulting in enhanced long-range transport. A similar explanation can be given for the northern storm tracks with lower values over the Pacific and the northern Atlantic but higher values over Canada and eastern Siberia. In the polar regions the differences in scavenging are caused by the different partitioning into snow and liquid precipitation. In the simulation using the ZH convection, much higher values occur in India, China, and Central Africa. The higher values in the tropics and in Asia are a direct consequence of the higher precipitation amount calculated in the C_ZH simulation. The differences in the polar region on the northern hemisphere as well as in the southern storm tracks are a consequence of no differentiation of the precipitation between liquid and solid type. Since the snowfall does not effectively take part in the scavenging, but

all convective precipitation produced by this scheme is liquid, higher deposition fluxes result. This occurs similarily also in the C_ZHW simulation. Since in Central Africa the convective precipitation is reduced relative to the C_ZH simulation, but still significantly higher than in C_T1, the wet deposition is accordingly higher than in the reference, but lower than in the C_ZH setup. In most other regions this simulation behaves similar to the C_ZH. The HCHO wet deposition in the C_B2 simulation (lowest panel on the right of Figure 6.7) shows lower values in the warm pool region and both storm tracks: in the Pacific this is a consequence of the reduced, more realistic precipitation (compare Figure 3.5), while in the subpolar regions the reduced deposition can be explained by the explicit treatment of convective cloud ice and snowfall. In the tropics almost everywhere, slightly higher values than in the reference are calculated. This results from the compensation of the lower values over the warm pool and the resulting extended transport. Furthermore, the total precipitation amount is higher than in the reference simulation (see Figure 3.2). In the subsidence regions of the subtropics in this simulation setup light precipitation is produced, which is less pronounced in the reference. Therefore there is hardly any wet deposition in C_T1, though some in this simulation setup.

Overall, for the species with low and medium solubility the differences in the wet deposition fluxes are a consequence of the shifted precipitation patterns as well as for the highly soluble compounds. However, even though these differences are small with respect to precipitation, they can have a much stronger impact on the less soluble trace species and their sinks. In contrast to the very soluble constituents, which are often completely depleted during precipitation, the strength of the precipitation events determines the wet deposition fluxes for species like HCHO and O_3. For the less soluble compounds the importance of convective transport for the vertical redistribution is largest. For O_3 the height of the convective cloud towers effectively determines the strength of the downward transport of ozone from the UTLS region, resulting in higher mixing ratios in the lower troposphere and boundary layers, if the convection penetrates deeper.

6.3.2.3 Wet deposition of ^{210}Pb

The tracer ^{210}Pb is known to stick to aerosol particles. Since in this study there is no real aerosol available, it is for simplicity assumed that there is an uniform aerosol with a radius of 0.75 μm, that is sedimenting, scavenged and dry and wet deposited. In Figure 6.8 the wet deposition is shown for the five simulations, again adopting C_T1 for the reference values and compare the differences for the simulations with the alternative convection schemes.
The wet deposition of lead in the C_T1 simulation is largest in Central Africa. Secondary maxima are found in India, China and Amazonia. Additionally, in North America there are two regions with more than 50 μg Pb/m^2, in agreement with the ^{222}Rn surface mixing ratios as presented in the upper left panel of Figure 4.3. In contrast to its precursor, ^{210}Pb is not restricted to the continents where the emission occurs, since deposition (dry and wet) is the only sink and the lifetime is longer than the radioactive decay of ^{222}Rn. Therefore the long-range horizontal transport of lead becomes more important than for its precursor. Downwind, i.e., west of northern Africa with a high radon load, in the ITCZ substantial wet deposition occurs over the Atlantic. This is similar for the northern storm tracks, both in the Pacific and the Atlantic. In the southern storm tracks this effect is less

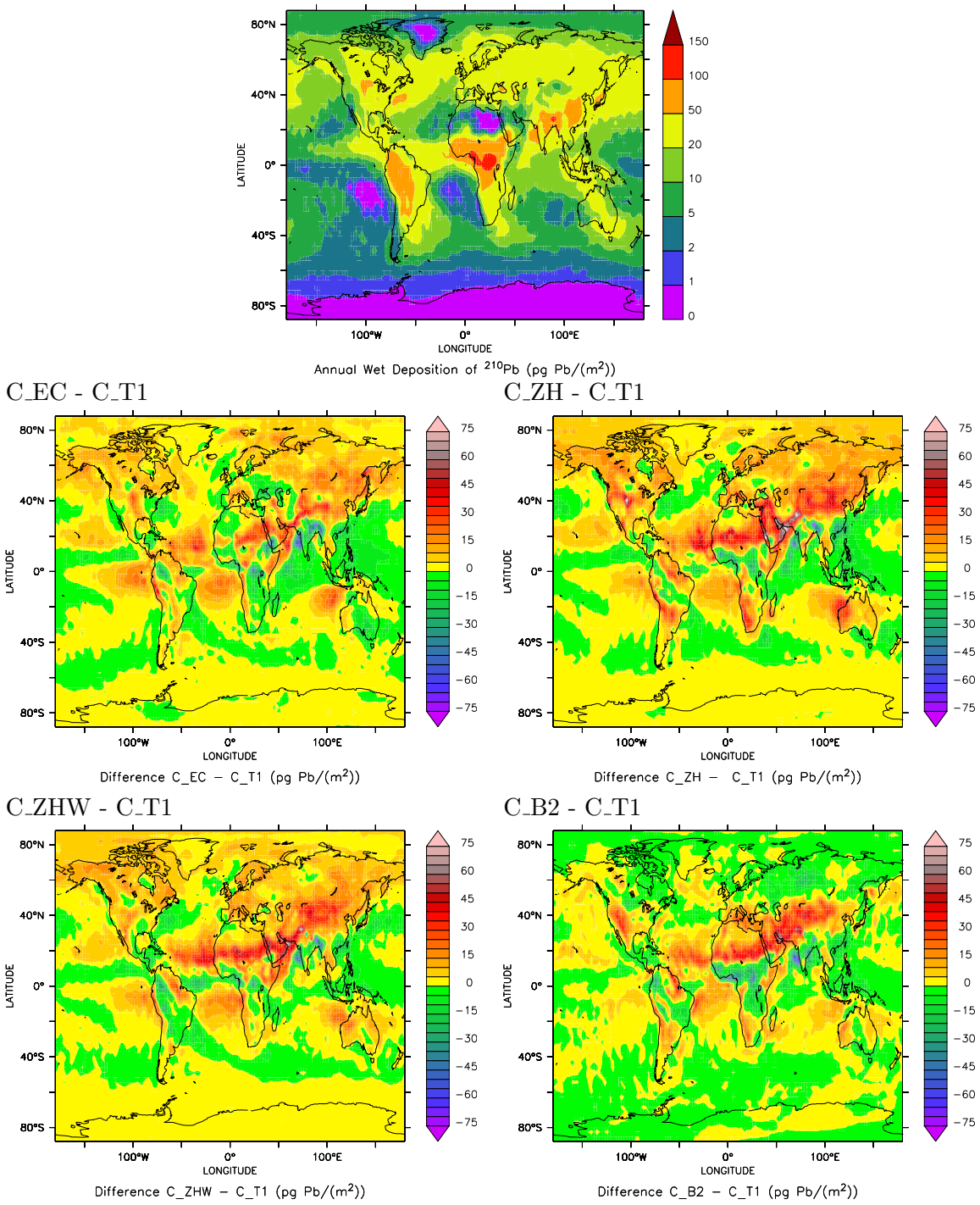

Figure 6.8: Wet deposition of ^{210}Pb

pronounced, because of the smaller continental masses and consequently the lower ^{222}Rn emission and subsequent ^{210}Pb production.
In the C_EC simulation wet deposition is more important over the continents while over the ocean the values are lower. In general, there is more wet deposition than in the reference simulation. This is, comparable to the gaseous compounds, mostly dependent on

Simulation Name	Wet Deposition [kg/month]	Dry Deposition [kg/month]	Sedimentation [kg/month]	Total Deposition [kg/month]	Burden [kg]
C_T1	0.76	0.07	0.26	1.09	0.11
C_EC	0.87	0.04	0.19	1.11	0.08
C_ZH	0.95	0.03	0.12	1.10	0.06
C_ZHW	0.92	0.04	0.14	1.10	0.05
C_B2	0.85	0.05	0.18	1.09	0.08
ECHAM4	0.91	0.11	-	1.02	0.23
CCM Ω	1.07	0.11	-	1.18	0.32
TOMCAT	1.10	0.07	-	1.20	0.32

Table 6.1: Deposition of ^{210}Pb of the five simulations and some reference values from another intermodel comparison (Rasch et al., 2000).

the different precipitation patterns, e.g., the lower rainfall in the warm pool region results in lower wet deposition fluxes of ^{210}Pb. The absolute strength of the precipitation is of secondary significance, since the precipitation flux enters only linearly in Equation 6.12. The dependence of the droplet radius, which has stronger influence on the scavenging efficiency, is relatively weak above a certain threshold value of the precipitation flux (about 1 mm/h). Even though the total precipitation is lower, the rainfall covers a larger area. Consequently, the total wet deposition is higher than in C_T1. The stronger upward transport as indicated in Figure 4.2 seems not to be reflected in the wet deposition fluxes. The largest differences occur in regions where in the reference simulation almost no wet deposition of lead occurs. A comparable conclusion can be drawn from the right panel in the middle row of Figure 6.8. Over the tropical oceans where less precipitation is calculated a slight reduction in the wet deposition flux of this compound is simulated, while over the continents the deposition is higher. As for the gaseous compounds the lack of differentiation between convective rain and snow in C_ZH leads to substantially higher scavenging in the northern hemisphere. In the southern hemisphere this is less pronounced because of the lower atmospheric burden of the precursor ^{222}Rn. However, in Amazonia and in Central Africa lower values are seen over parts of the continents, even though the precipitation is much stronger than in the reference simulation. This is a consequence of the more effective upward transport in the convective clouds without complete scavenging. The simulation C_ZHW shows in general the same picture as the C_ZH simulation. Small scale differences result from the modified precipitation patterns compared to C_ZH.
The C_B2 simulation yields an almost completely different result. In large regions slightly lower deposition values are calculated. The main differences result again from the precipitation distribution, e.g., the calculated light precipitation in northern Africa leads to scavenging that does not occur in the reference simulation, and in the Atlantic ITCZ higher precipitation occurs in this model setup leading to slightly higher depostion values.

In Table 6.1 the values from a model intercomparison (Rasch et al., 2000) for the scavenging of ^{210}Pb are compared with the results from the simulations of this study.
All five simulations C_T1 to C_B2 show a comparable total global deposition of about 1.09 to 1.11 kg/month. However, this total is composed of the individual sink processes and in each simulation each has different importance: in C_ZH the wet deposition is strongest, but sedimentation and dry deposition are lower than in the other model setups. Furthermore, the burden is lowest in C_ZH and C_ZHW. The reference simulation shows

the lowest global total wet deposition and consistently the highest burden. Even though the identical emission conditions are applied, the effective emissions differ slightly, partly influencing the differences in the burdens. In comparison with some exemplary selected models from the comparison of Rasch et al. (2000), the total deposition is in the same range (1.02 to 1.20 kg/month) as for the other models. Unfortunately, for these a separation for aerosol sedimentation and dry deposition does not exist.
The total load of ^{210}Pb is significantly lower in the simulation series of this study. Because of the lower load the residence time, calculated as burden divided by total deposition is lower than in most of the other models of the intercomparison. The most imporant difference is that the aerosol particles in this study have a constant radius for all regions and altitudes, while some of the models used in Rasch et al. (2000) apply a separate module to calculate the properties of the atmospheric aerosol in detail. Since the deposition in the studies of this thesis is similar, one reason must be assigned to the emissions. Even though in the referenced study also an emission of 1 atom/(cm^2 s) is applied, differences can occur in the ice covered regions where no emissions are calculated in the studies of this section. Even though the emissions in Rasch et al. (2000) occur only in ice-free regions, the applied ice mask (online or offline calculated) is not identical. Additionally, Rasch et al. (2000) propose lower emissions from 60° to 70° N of 0.5 atoms/(cm^2 s).

6.3.2.4 Summary

The influence of the exchange of the convection parameterisation results in obvious modifications in both the vertical profiles and wet deposition fluxes. For a low soluble compound like O_3 the convective transport determines the vertical redistribution. Additionally, the downward transport of stratospheric ozone resulting in a higher mixing ratios in the troposphere is dependent on the convection parameterisation. In all simulations there is almost no gradient within the troposphere, which is identical to a well mixed lower atmosphere. For highly soluble species like HNO_3 the scavenging leads to an almost complete depletion in the middle troposphere in all simulations. Even though this is less pronounced for the C_T1 simulation, it is still substantial (more than one order of magnitude). Differences in both convective transport and modifications due to altered precipitation patterns are hardly noticeable. For species of intermediate solubility like HCHO these differences are more important.
For highly soluble compounds the wet deposition distribution shows a high dependence on the occurence of precipitation, while for species with lower solubility the strength of the precipitation events has more significance. Furthermore, a smaller sink of a specific compound in one region results in more long-range transport and subsequent wet deposition further downwind.

6.4 Scavenging: Global chemistry studies

6.4.1 Long term simulation

6.4.1.1 Simulation setup

The ECHAM5/MESSy model has been used for a simulation from January 1998 to October 2005 (EVAL), with a horizontal resolution of T42 and 90 vertical layers up to 0.01 hPa. The data assimilation (nudging) technique is applied below 100 hPa with ECMWF - analysis data to represent the real state of the troposphere. All submodels described in Section 2.2 are used, except for an aerosol submodel. Additionally, some submodels that perform calculations only in the stratosphere are used. A detailed description of this simulation can be found in Jöckel et al. (2006). It is aimed at describing the atmospheric chemistry from the surface up to the mesosphere with one consistent model. The applied convection scheme is T1, being the default for the ECHAM5 model, for which the meteorology of the climate model has been evaluated (Roeckner et al., 2004). In this simulation the SCAV submodel is applied with a minimum number of reactions in the aqueous phase, the SCAV_SCM setup (as in the studies of Section 6.3, compare also Section 6.4.2 and Appendix C).

6.4.1.2 Results - Wet deposition fluxes

The wet deposition fluxes of the simulation period are compared with measurement data. There are some average values from measurements available for data from Europe and the USA from the years 1974 to 1998 gridded on a 0.5° x 0.5° grid[1]. A comparison with these values is shown in the Figures 6.9 and 6.10 for aqueous nitrate (NO_3^-(aq) and HNO_3(aq)) and total dissolved ammonium (NH_3(aq) and NH_4^+(aq)), respectively, from the National Atmospheric Deposition Program (NADP) network (in the USA). No statistical comparison is performed for this data, it is only shown as a first impression of the performance of the SCAV submodel. Even though in the EVAL simulation emission data for the year 2000 from the EDGAR 3.2 FASTTRACK database are applied, the nitrate wet deposition values from the simulation agree very well with the observations, both, with respect to the horizontal distribution and the absolute values (see Figure 6.9). The maximum is slightly higher in the model results and somewhat shifted eastward. However, since the resolution of the simulation with 2.8° is relatively coarser than the grid of the observations, the tendency of the model to artificially disperse the pollutants cannot be avoided. Nevertheless, the eastward increasing values east of 95°W are represented well by the model. Assuming that the emissions of nitrogen oxides in the USA did not change substantially over the simulation period, and the conversion of NO_x to nitrate is represented well, the model is able to capture well both the observed deposition patterns and absolute values.
A similar conclusions can be drawn from the comparison of the ammonium wet deposition of Figure 6.10. Again, the maximum west of the Great lakes is reproduced well by the model with respect to position and absolute value. The west-east gradient is simulated as well as the north-south distribution over the USA, although the pollution transport may be somewhat too efficient.

Recent global observations are provided by Dentener (2006, personal communication). With this data the wet deposition from the EVAL simulation is compared and a statisti-

[1] http://daac.ornl.gov/CLIMATE/guides/nitrogen_deposition.html

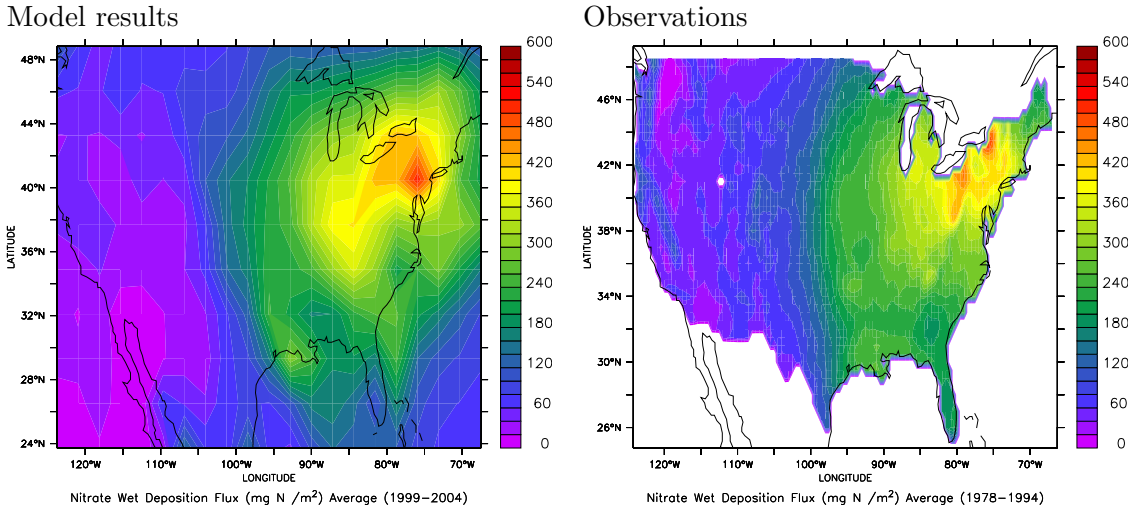

Figure 6.9: Average annual wet deposition flux of Nitrate in mg N/m^2 for the model sinulation (left) and observations (right) in the USA.

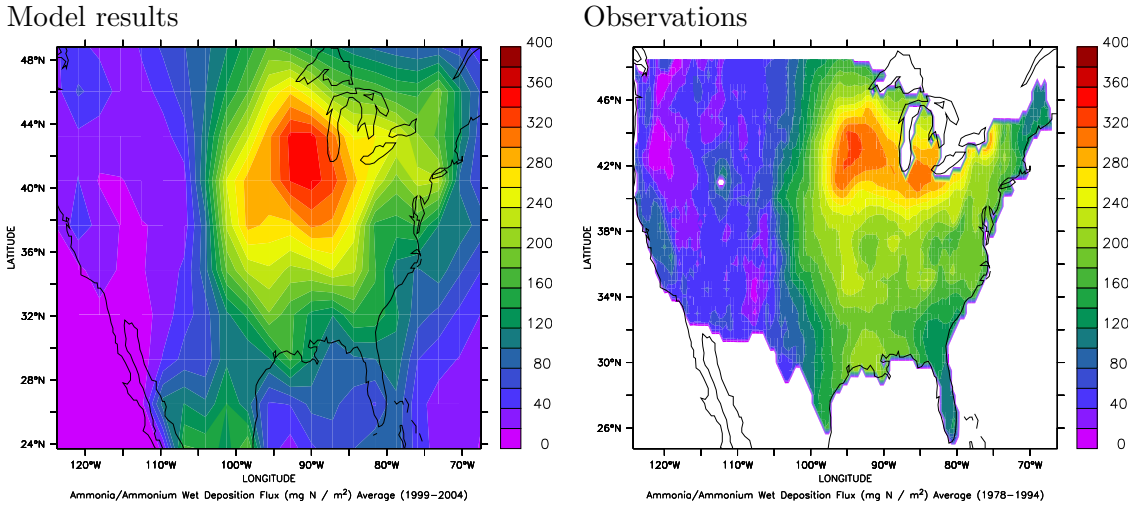

Figure 6.10: Average annual wet deposition flux of Ammonium and Ammonia in mg N/m^2 for the model sinulation (left) and observations (right) in the USA.

cal analysis is performed.
The measurement data is usually derived from a chemical analysis of the collected rain water. Data from several measurement networks is used, notably in the USA the extensive 'National Atmospheric Deposition Program' (NADP) network, in Europe the much less extensive 'Convention on Long-range Transboundary Air Pollution' (EMEP) network, in East Asia the smaller 'Acid Deposition Monitoring Network in East Asia' (EANET), and in Africa the limited 'Monitoring Network of Atmospheric Chemistry in Africa' (IDAF), plus additional data from South America and India. The data is mostly provided as averages of several years within the last decade. Nevertheless, there is no global coverage of measurement data available. Especially in Russia, Australia and Antarctica there are no measurements available. Even in Africa and South America there are only few measurement stations. The number of stations of each network used in this analysis is listed in

Table 6.2: Measurement stations of the individual networks with wet deposition data

Species	ALL	NADP	EMEP	EANET	IDAF	India	S. America
Nitrate	371	227	41	23	8	44	16
Ammonium	359	227	39	23	8	34	16
Sulphate	366	228	41	13	8	48	16

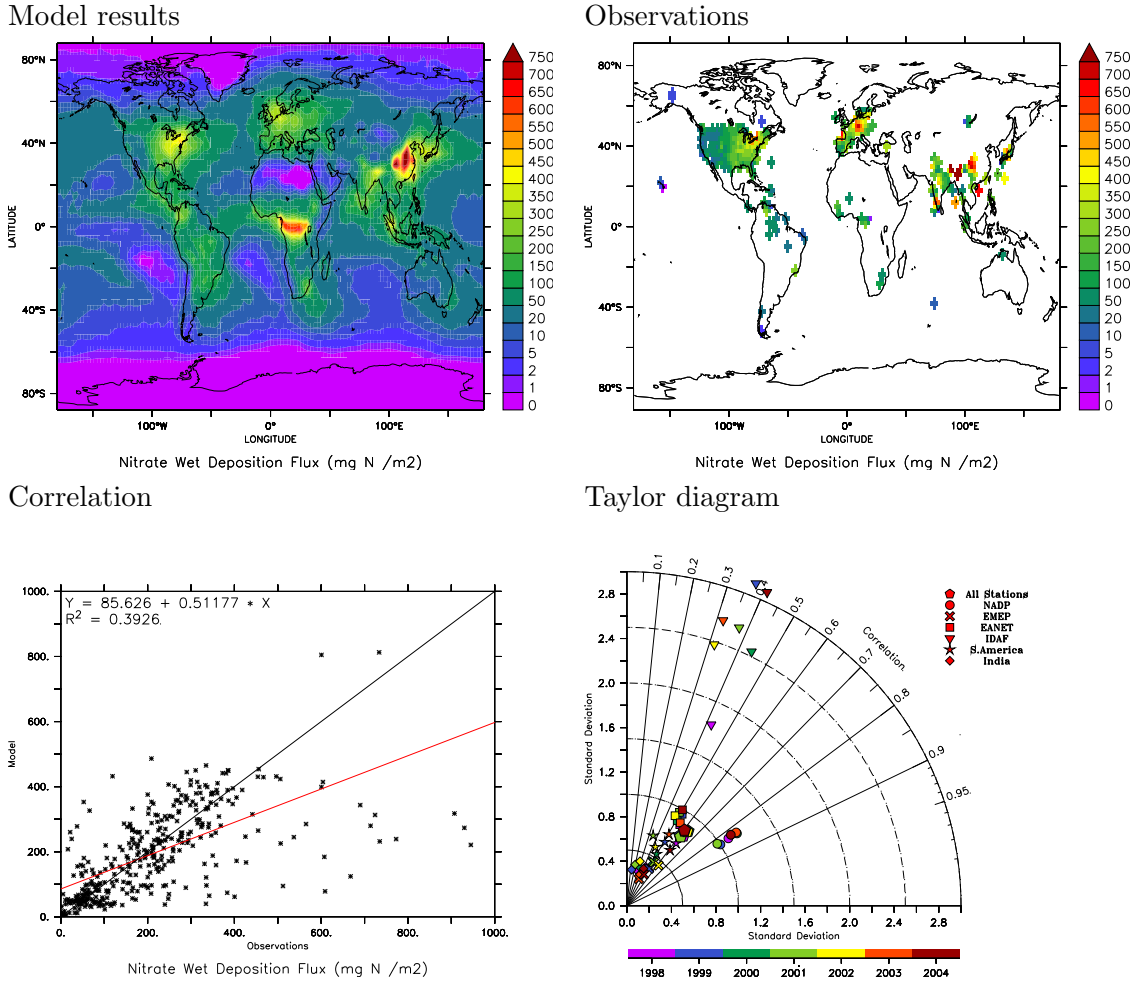

Figure 6.11: Average annual wet deposition flux of Nitrate in mg N/m^2 for the model sinulation (left) and observations (right) (upper panels) and statistical analysis (lower panels).

Table 6.2. Over the oceans (islands) hardly any long-term observations exist.

First, the nitrate wet deposition is investigated. The upper left panel of Figure 6.11 represents the average annually accumulated wet deposition flux of nitrate (i.e., NO_3^- and HNO_3(aq)) in mg N/year (a logarithimic scale is selected below 100 mg N/yr, above linear scale). There are four regions with substantially enhanced values: Central Africa, China and east India, the North American east coast, and western Europe.
The relatively high values in Africa are a consequence of the high biomass burning emissions in the region. Additionally, they are caused by biogenic soil emissions from the rain

forest. The lightning activity that produces NO_x relatively effectively in this region is about one order of magnitude lower than the biomass burning source. Due to oxidation (mostly by $NO_2 + OH \rightarrow HNO_3$) a major part is converted to gaseous HNO_3. As a very soluble species HNO_3 is very effectively taken up by clouds and removed by precipitation (mostly of convective origin). The efficient scavening process determines the wet deposition, since there are hardly any reducing mechanisms in the aqueous phase that can affect the liquid phase concentrations. In Europe, North America and east Asia the nitrate is mostly a product of the industrial emissions of nitrogen oxides. These are transformed by the same chemical mechanisms as the biomass and soil emissions. Wet deposition is the main sink, too.
The upper right panel of Figure 6.11 shows the observational data from the individual measurement stations. In North America, as already seen in Figure 6.9 a good agreement between the model and the observations can be detected. In Europe the simulated values are generally lower than the observations. The high simulated values in Africa are not evident from the observations. On first sight, the simulated values in South America and India agree well with the observations, while for the EANET data large differences are found.
The lower left panel of Figure 6.11 shows a scatter plot of the annual nitrate wet deposition of all observations on the x-axis and the model results (averaged over the simulation years) on the y-axis. The black line is the perfect linear regression, while the red line is the actual linear regression, calculated as decribed in Appendix A. A major contribution of the points originates from the NADP network, where a good representation can be found. These points are close to the perfect linear regression. The scatter is relatively large, leading to an overall linear regression of $y = 0.51 * x + 85.63$. The correlation of all data is $R^2 = 0.393$.
The lower right panel (Figure 6.11) shows a Taylor diagram, comparing each individual year of the model simulation with the observational data. The color coding represents the simulation year. In addition to the statistics for all stations together, the data from each network are indicated separately by the different symbols. The pentagons depict the data from all stations. As calculated above, the correlation for each of the years is slightly above 0.6 (note that the angle depicts R and not R^2). The amplitude of the spatial variation, as defined by the normalised standard deviation is above 0.8. The analysis of the individual measurement networks shows large differences in the different regions. As indicated above, the correlation of the NADP data (marked as circles) is above 0.8 and the normalised standard deviation close to 1, showing a good agreement between the distribution patterns of model and observations. The EMEP data, denoted with Xs, show a much smaller correlation and also the normalised standard deviation is below 0.5. This means that the spatial variation is underestimated by the model. The EANET data (quadrates) is correlated only with $R = 0.5$, but shows good agreement in the amplitude of the spatial variation. The data from Africa (triangles) is scattered relatively far from the other points. As mentioned above, the model fails in the description of the depostion patterns and values in this specific region. Additionally, it has to be noted that the interannual variability is largest for this data. The data from South America and India are both correlated only low and underestimate the spatial variation, too.

A similar analysis is performed for the wet deposited reduced nitrogen compounds (NH_3 and NH_4^+). Similar as in Figure 6.11, the upper left panel of Figure 6.12 shows the average annual sum of the simulated wet deposition of NH_x in mg N/year on a similar scale. The

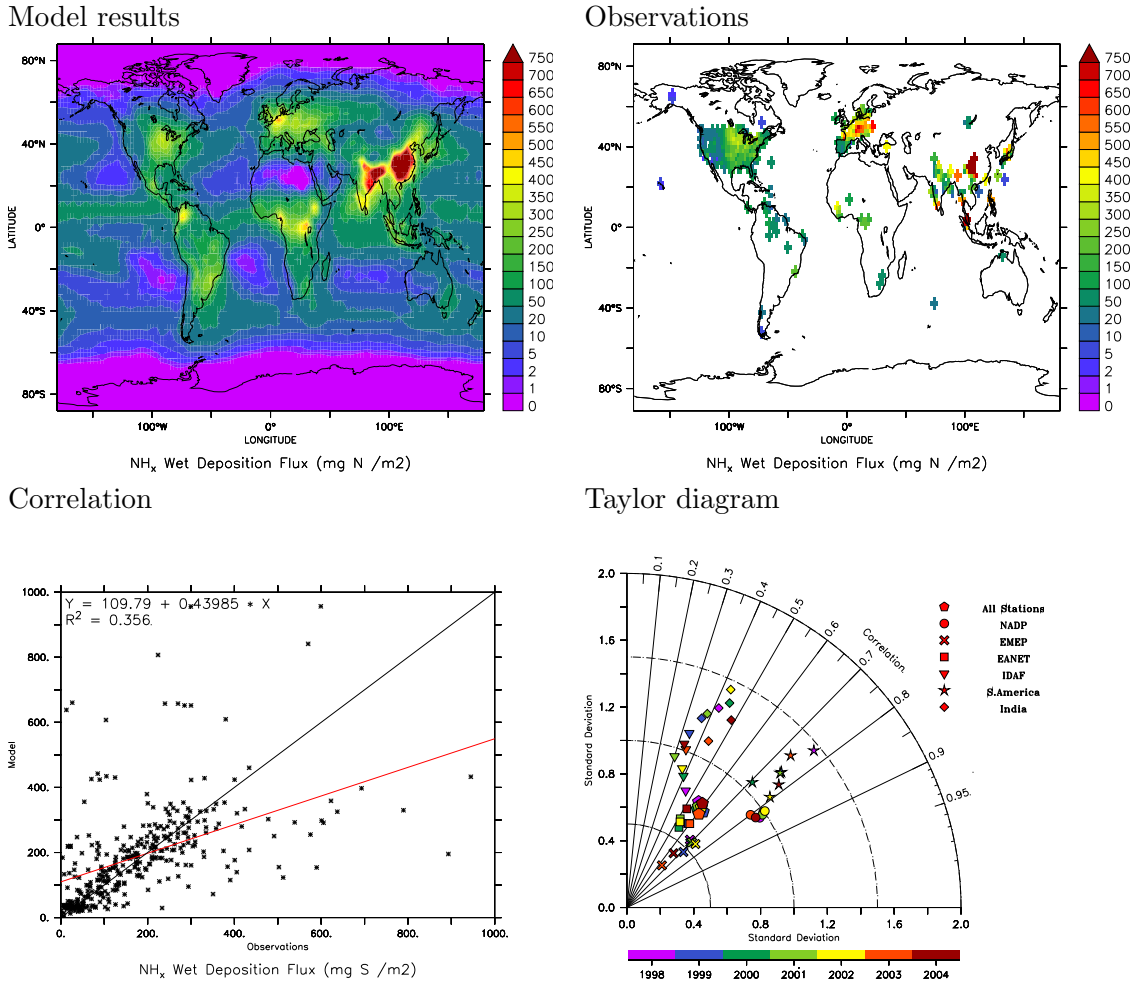

Figure 6.12: Average annual wet deposition flux of Ammonium / Ammonia in mg N/m^2 for the model simulation (left) and observations (right) (upper panels) and statistical analysis (lower panels).

highest simulated values occur in India and China. Secondary maxima are found in Europe, Central Africa, the northern South America and the region around the Great Lakes in North America. Some of these patterns can be attributed to high emissions, e.g., in Europe, especially in the Netherlands, but also in India and China, from both industrial and agricultural sources. The source in the USA is mostly industrial. The relatively high values in South America and Central Africa are mostly due to biomass burning. In the upper left panel of Figure 6.12 the precipitation distribution is more obvious than above for the nitrate deposition. This is a consequence of the fact that NH_3 does not participate in the gas phase chemistry and is therefore only affected by emissions (sources), transport, and dry and wet deposition (sinks). The ITCZ is clearly characterised by higher deposition values than the subtropics. Some of the regions with very high values (north of India, northernmost part of South America) are also regions in which very high precipitation rates occur with the selected convection scheme (T1), as analysed in Figure 3.5.
The observational data (upper right panel of Figure 6.12) shows similar values in East Asia and North America. In Europe higher values than in the simulation are observed.

The data in Africa and South America is similar to the model simulation, but again there are not enough measurements available to infer a good agreement.
The scatter plot in the lower left panel shows a large number of points close to the one-by-one line, but also several points where the observed values are much higher than calculated by the model. These are likely points from the EMEP network, where the two upper figures indicate an underestimation of the simulated values. The overall linear regression and correlation are of similar quality as for nitrate: $y = 0.44 * x + 109.79$ and $R^2 = 0.356$. Especially the high offset confirms the underestimation of the spatial variation by the model.
The Taylor diagram in the lower right panel shows for all stations (pentagons) only minor interannual variability. The overall correlation R is around 0.6, while the normalised standard deviation is around 0.75. Again there is a large range in the data from the individual measurement networks. The NADP data (circles) shows little scatter over the years with R close to 0.8 and an almost ideal standard deviation. The EMEP data (marked with X) are still relatively high with respect to the correlation with an R of about 0.7, but the standard deviation varies over the years between 0.2 to 0.6, denoting an underestimation of the horizontal variation. Such an underestimation is also found for the data from east Asia. However, this model data is less correlated with the observations. In the comparison with the data from India and Africa the correlation is even worse, while for Africa (triangles) the normalised standard deviation is around 1. The accurate biomass burning emissions of NH_3 obviously are the reason for this good agreement. Consequently the correlation with the South American data $R > 0.7$ is relatively good, even though there the spatial variation is slightly overestimated.

A third compound usually analysed in rainwater is sulphate (SO_4^{2-} and HSO_4^-), which is a product of the aqueous phase oxidation of dissolved SO_2 follwing the reactions 1.11. The gas phase oxidation of SO_2 to H_2SO_4 and subsequent uptake of sulphuric acid is of less relevance. Nevertheless, due to its high solubility gaseous H_2SO_4 is very effectively scavenged and removed from the atmosphere. Even though SO_2 is less soluble, it is quickly transformed into sulphite and sulphate, causing a relatively efficient scavenging. The reaction partners H_2O_2 and O_3 have very different scavenging behaviour. While H_2O_2 is highly soluble and efficiently removed from the atmosphere by scavenging, the scavenging of O_3 is almost negligible. Nevertheless, due to the relatively high concentrations of ozone there is sufficient available for the aqueous oxidation of sulphur dioxide.
The upper left panel of Figure 6.13 shows the simulated sulphate wet deposition flux. It shows strong maxima in the industrial regions of North America, Europe, India and East Asia. These are regions with strong emissions. Especially in Europe, the highest values of sulphate deposition occur in eastern Europe, where brown coal with a high sulphur content is used for energy production. The globally highest values are simulated in China as a consequence of air pollution from industry. Though the emissions are representative for the year 2000, they have high uncertainties, especially in China. The dependence on the precipitation distribution is less dominant as for the NH_x compounds.
The observations (upper right panel) show a very similar distribution pattern. Additionally, the absolute values are captured quite well for the USA and Europe. Despite the low numbers of measurements in India, a maximum is observed in the same region as in the model simulation. Since there is almost no data in China (only one point with very high values in the southern part), it is not possible to evaluate the model in that specific region.

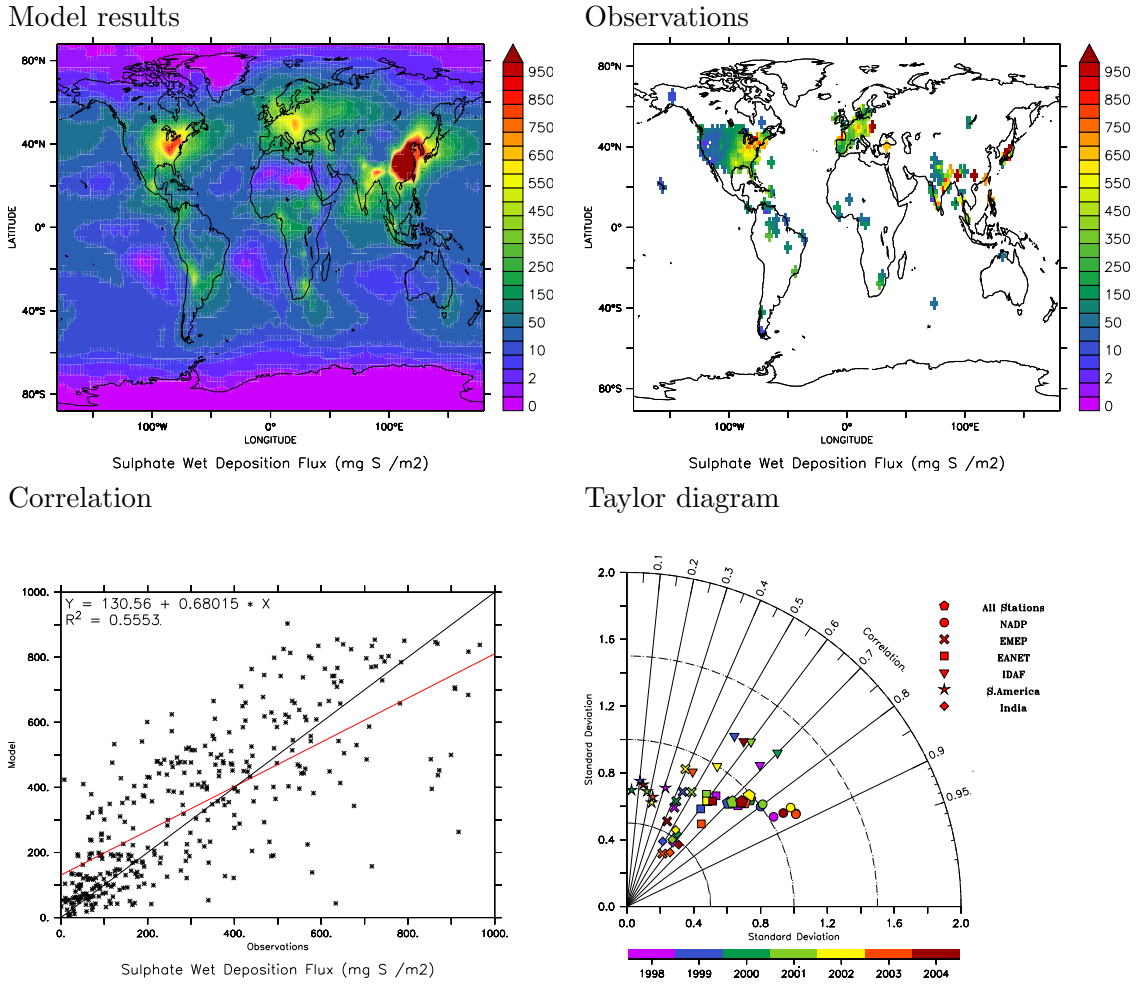

Figure 6.13: Average annual wet deposition flux of Sulphate in mg S/m^2 for the model sinulation (left) and observations (right) (upper panels) and statistical analysis (lower panels).

The scatter plot of all measurements and the corresponding averaged model values is shown in the lower left panel of Figure 6.13. Even though again a scattering around the one-by-one regression is found, it is more uniform than for the other analysed compounds. Also for the lower values observations and model correspond quite well. The overall regression can be described by: $y = 0.68 * x + 130.56$ and $R^2 = 0.555$.
The relatively good performance of the model is displayed by the Taylor diagram (lower right panel). The correlation R of all the stations is $R > 0.7$ with the normalised standard deviation close to 1. The data from the NADP network again has higher correlation values of more than 0.85, and the normalised standard deviation, determining the spatial variation, is slightly above one. As before, for the other measurement networks the model calculations deviate more from the observations. The European data show a correlation R between 0.4 and 0.5 and underestimate the spatial variation. The Asian data are correlated with an $R = 0.6$ and a slight underestimation of the spatial variation. The remote African stations, which are not affected by strong local industrial emissions, are also correlated relatively well. Here, a higher interannual variability is found. The distribution

patterns over South America are not well represented by the model, indicated by a low correlation.

Overall, the scavenging scheme appears to be able to realistically represent the global wet deposition patterns, compared to the observations. Even though there are some weak points, these cannot directly be attributed to a weakness of the scheme, but can be due to uncertainties in the emissions, local chemistry and transport. Especially in eastern Asia, the emissions are rather uncertain. Furthermore, the wet deposition measurement network provides a detailed and comprehensive database only for the USA, while there are large data gaps in other regions. Nevertheless, in comparison with other models the obtained agreement with the measurements is very good. Especially because the model performs very well for the USA, where both emission data and measurements are of high quality and representativeness, it can be concluded, that the model representation of wet deposition processes is quite accurate.

6.4.2 Simulations with different scavenging mechanisms

6.4.2.1 Simulation setup

For this study three simulations have been performed. All use the submodels described in Section 2.2. The selected convection scheme is T1, since it is the default of the ECHAM5/MESSy model. The horizontal resolution is T42 with 31 vertical layers (the model top layer is at 10 hPa). The integration period is the year 2000, with three months of spin-off in advance. A weak data assimiliation technique is applied, only prescribing the sea surface temperature and nudging the surface pressure using meteorological data from ECMWF - analyses. The differences between the simulations are only in the description of the scavenging of the gas phase species:

- The SCAV_SCM simulation: scavenging and cloud and precipitation chemistry is explicitely calculated using the KPP mechanism with a so-called minimum set of chemical reactions (see the reactions labeled with **Scm** in the SCAV reaction tables in Appendix C);
- The SCAV_EASY simulation: the scavenging is simplified, and described by assuming only Henry's law gas partitioning for all considered species, not taking any chemical reaction and interaction between the species in the aqueous phase into account;
- The SCAV_COM simulation: a comprehensive set of chemical and uptake reactions are considered using the KPP differential equation solver (see the reactions labeled with **Sc** in the SCAV reaction tables in Appendix C).

The scavenging submodel applied in the three simulations is an improved version of the one used in the EVAL simulation with a better description of the precipitation liquid water content and the pH - value analysis. It is described in Section 6.2 and in Tost et al. (2006).
Since the simulation setup is slightly different from the simulations described in the Sections 3.3.1 and 6.3.1, and the nudging technique is applied in the simulations of this chapter, modifications of the precipitation patterns compared to Section 3.3.2 may occur, and the precipitation distribution is presented in Figure 6.14. For the detailed analysis of

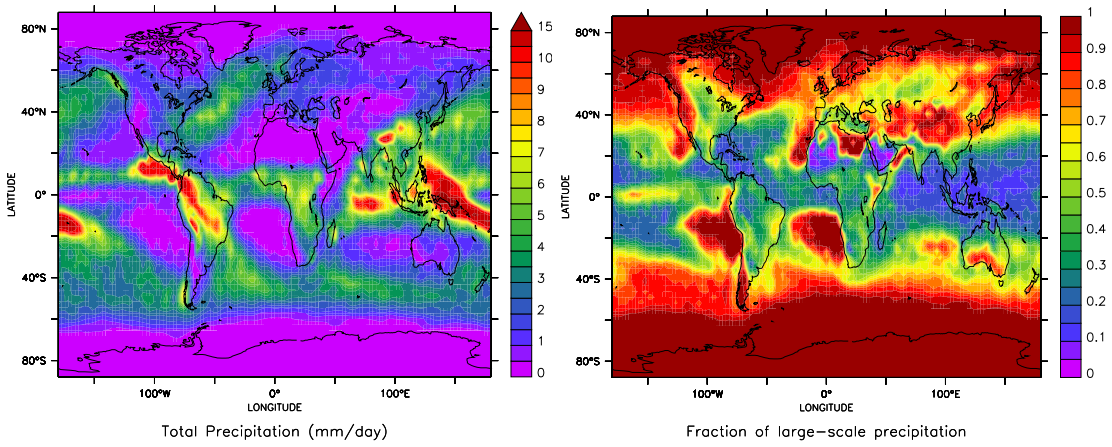

Figure 6.14: Total rain flux and fraction of large-scale compared to total precipitation

the precipitation patterns the reader is referred to Chapter 3. Since it is important for the scavenging and wet deposition, these graphics are merely a reminder of the precipitation distribution. Additionally, it shows only the liquid precipitation at the surface (neglecting snow), indicating the regions with effective aqueous phase chemistry. The right panel of Figure 6.14 shows the fraction of the large-scale rain of the total liquid precipiptation. In the tropics the convective precipitation is dominant ($> 90\%$), while further polewards the large-scale rainfall becomes increasingly important. In some regions of the subtropics there is almost no convective precipitation and also in the central Pacific ITCZ the large-scale scheme contributes substantially to the total rainfall. With the help of this figure the importance of the contribution of the individual precipitation producing parts of the model to the wet deposition can be addressed. Additionally, a weighting factor for the total precipitation pH can be calculated and applied (see Section 6.4.2.2.2).

6.4.2.2 Results

6.4.2.2.1 Wet deposition fluxes

In this section the differences in the wet deposition fluxes between the individual simulations are analysed.

For this purpose the annual deposition of nitrate, NH_x, and sulphate are compared to the observations, previously used in Section 6.4.1. A statistical analysis is performed with the help of a Taylor diagram in Figure 6.15. The 'star' symbol denotes the standard deviation - correlation - relationship of the SCAV_SCM, the 'plus' for the SCAV_EASY and the 'diamond' for the SCAV_COM simulation. Red denotes nitrate, blue NH_x and green sulphate. For all three compounds the SCAV_SCM and SCAV_COM simulation show similar values while the SCAV_EASY simulation shows significantly lower values for the normalised standard deviation, indicating an underestimation of the spatial variation. However, for nitrate and sulphate the correlation is still similar to the other two simulations. For the NH_x compounds, the SCAV_EASY simulation fails completely, since the symbol is close to the origin. Even though the data is correlated with $R > 0.5$, the normalised standard deviation is very small.

With this improved scheme (relative to the EVAL simulation of Section 6.4.1), the normalised standard deviation is close to one for nitrate and sulphate in the simulations using liquid phase chemistry, while for ammonia and ammonium it is 0.91 for SCAV_COM and

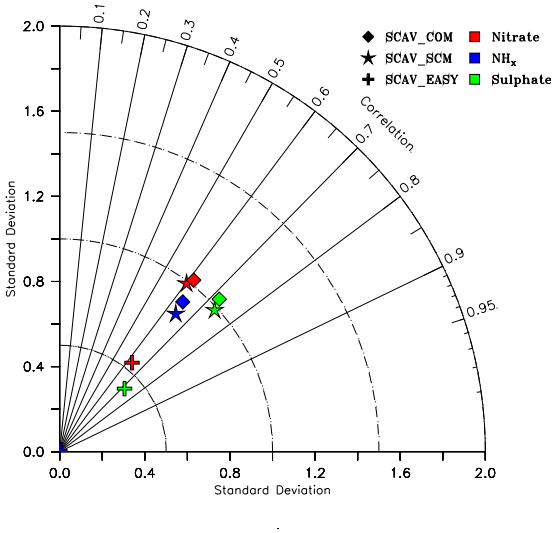

Figure 6.15: Taylor diagram for the three simulations compared with the observations described in Section 6.4.1 for nitrate, NH_x and sulphate.

0.85 for SCAV_SCM. The correlation R is above 0.6 for nitrate, 0.63 for ammonia, and 0.72 for sulphate for both SCAV_SCM and SCAV_COM. With respect to the correlation SCAV_EASY is similar for nitrate and sulphate, but significantly lower for NH_x. Compared with Section 6.4.1 for the EVAL simulation there is a significant improvement with respect to the variation in terms of the normalised standard deviation. The corrections in the scheme result in a much better description of the amplitude of the spatial variation. However, the correlation achieves comparable values.
The SCAV_EASY simulation indicates considerable weaknesses especially for NH_x, but also worse results for nitrate and sulphate with respect to the amplitude of the variation.

Table 6.3: Global sink processes for several species in the individual simulations

Species	SCAV_SCM		SCAV_EASY		SCAV_COM	
	DRY	WET	DRY	WET	DRY	WET
Nitrate Tg N/yr	22.53	32.30	34.76	14.99	22.48	32.10
NH_x Tg N/yr	19.05	37.09	41.00	0.21	19.03	37.01
Sulphate Tg S/yr	5.64	48.54	3.59	32.01	5.47	43.66
H_2O_2 Tg/yr	195.0	94.75	213.0	103.1	173.9	77.88
HCHO Tg/yr	43.1	1.10	43.84	1.11	41.73	0.95
HCOOH Tg/yr	13.82	6.01	18.18	0.16	17.32	9.88

In addition, the global total deposition is analysed in Table 6.3. Since sometimes differences in the wet deposition are compensated by dry deposition the values for both sink processes are presented. In this table the sedimentation part is included in the dry deposition.
For nitrate, the wet deposition is the main contribution in the SCAV_SCM and SCAV_COM simulation, while in the SCAV_EASY simulation the wet deposition is reduced by half, and dry deposition is much more important. Nevertheless, the total deposition sums up to about 54 Tg N/yr for the first two simulations, and 49 Tg N/yr for SCAV_EASY.

Since in the SCAV_EASY simulation the dissociation of nitric acid is ignored, the total wet deposition, including aqueous phase HNO_3 and NO_3^-, is weaker. This dissociation decreases the aqueous concentration of HNO_3; otherwise the uptake into the aqueous phase is determined by Henry's law only, considering gas phase diffusion limitations. However, even for a species with a high solubility such as nitric acid, the dissociation is of relevance since without it the wet deposition is substantially reduced.
For NH_x the wet deposition of SCAV_EASY is almost negligible, as indicated in Figure 6.15. The total deposition is significantly lower, even though the dry deposition partly compensates the failure of the wet deposition scheme. This is a consequence of the lower solubility of ammonia. Without dissociation, NH_4^+ cannot be formed. Consequently, the uptake into the droplets is less efficient. However, in reality in an acidic environment almost all NH_3 is converted to NH_4^+, allowing enhanced uptake of gaseous ammonia. The sulphate dry deposition is of minor importance in all simulations, originating from the aerosol sedimentation. Since in the SCAV_EASY simulation there is no conversion of SO_2 into SO_4^{2-} in the liquid phase, the wet deposition in this simulation is significantly lower than in the other two simulations, again underestimating the absolute values. For H_2O_2 dry deposition is more important than wet deposition in all simulations. The wet deposition in the SCAV_COM simulation is lowest, because in the comprehensive aqueous phase chemistry mechanism several reactions consuming this compound (including the photolytical destruction within the droplets) are taken into account. While in SCAV_SCM there is only the SO_2 oxidation (Equation 1.11), in SCAV_EASY there is no chemical sink in the aqueous phase. The lower consumption in the liquid phase leads to higher gas phase concentrations and consequently higher dry deposition. Taking into account aqueous phase chemical sinks does not only modify the importance of the other sink processes, but also the total sink (about 290 Tg for SCAV_SCM, 316 Tg for SCAV_EASY, and only 250 Tg for SCAV_COM).
Formaldehyde with only medium solubility shows very similar values in all simulations. Since there is no difference in the considered reactions in the simulations SCAV_SCM and SCAV_EASY, the values are very similar. In SCAV_COM there are reactions consuming HCHO in the liquid phase, and the lower gaseous H_2O_2 concentrations lead to slightly lower gas phase production and subsequent wet deposition.
Formic acid, finally, shows a similar behaviour as NH_x because it is also of medium solubility. By ignoring the dissociation only very limited uptake is possible (in SCAV_EASY). The SCAV_COM simulation shows significantly higher values for both dry and wet deposition resulting from the modified oxidation capacity of the atmosphere in the gas phase.

In addition to the statistical analysis and the global total values, the absolute values of the annual wet deposition for the same compounds as in Table 6.3 of the SCAV_COM simulation are presented in the left panels of the Figures 6.16 to 6.21. The middle panels show the differences to the SCAV_COM simulation of the SCAV_SCM simulation, while the right panels depict the absolute values for the SCAV_EASY simulation. Due to the partly very high differences to the SCAV_COM simulation a difference plot of these two simulations dose not give much information.
The nitrate wet deposition in Figure 6.16 shows a similar picture as in Figure 6.11 with slightly higher values east of the North American east coast. The deposition in Central Africa is significantly lower than in the EVAL simulation, corresponding better with local observations. In Europe slightly higher values are calculated, again in better agreement with the observations. The regions of main differences of SCAV_SCM to SCAV_COM

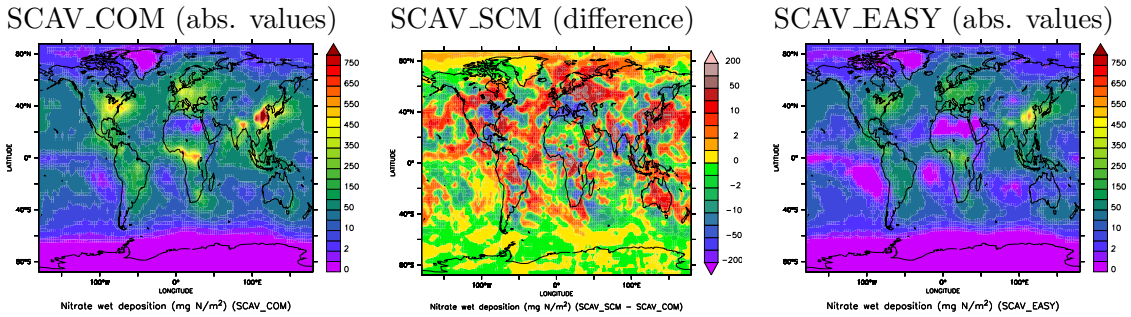

Figure 6.16: Nitrate annual wet deposition in mg N / m^2 of the SCAV_COM simulation (left), the absolute difference of SCAV_SCM to SCAV_COM (middle), and the absolute values for the SCAV_EASY simulation (right).

are in the eastern USA and western Europe with lower values in SCAV_SCM and higher values in Central Africa, northeastern North America and eastern Europe. Even though there are differences in many locations, these are mainly small compared to the absolute values of the nitrate deposition. The SCAV_EASY simulation shows almost everywhere significantly lower values for the reasons mentioned above.

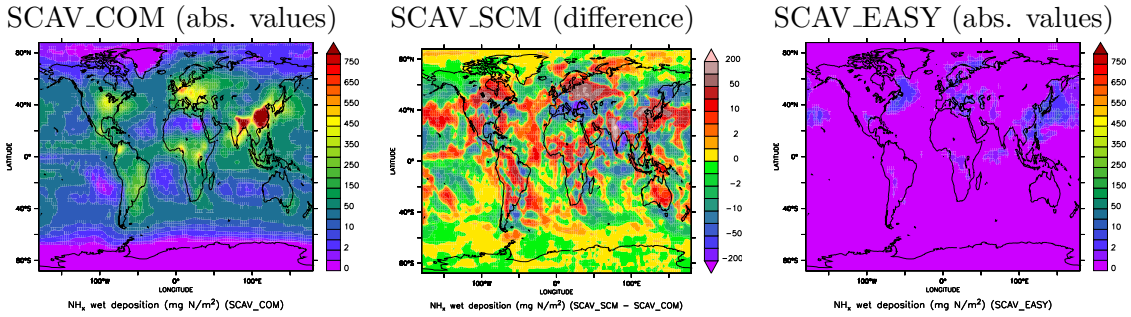

Figure 6.17: NH_x annual wet deposition in mg N / m^2 of the SCAV_COM simulation (left), the absolute difference of SCAV_SCM to SCAV_COM (middle), and the absolute values for the SCAV_EASY simulation (right).

Figure 6.17 shows similar pictures for ammonia and ammonium. As for nitrate, the SCAV_COM simulation seems to capture better the values over western and central Europe than the EVAL simulation. The maximum deposition occurs in East Asia. The main differences between the SCAV_COM and SCAV_SCM simulation occur in eastern Europe, India, and on the Chinese east coast with higher values in SCAV_SCM, and lower values over the Mediterranean and southern China. The deposition differences over the Pacific are twofold. In the storm tracks and the ITCZ there is more deposition in SCAV_SCM while there is less in the subtropics and north of the northern storm tracks. Since the precipitation patterns are quite similar in these two simulations, these differences cannot be attributed to differences in precipitation. A possible indication can rather be found in the pH - value which is presented and anaylsed in Section 6.4.2.2.2. There is slightly more acidity in the precipitation in those regions in the SCAV_SCM simulation, leading to a faster production of NH_4^+ and therefore a possibly higher uptake of gaseous NH_3. However, this explanation is arguable. The differences in the maximum deposition regions of East Asia are hard to evaluate since the emissions in this region are highly uncertain

and the observational data is scarce. Therefore it is difficult to determine which simulation performs better compared to observations in that region. As already mentioned, the SCAV_EASY simulation fails completely in describing NH_x wet deposition. However, ammonia does not affect the other gaseous consitutents due to the selected gas phase chemistry mechanism and no aqueous phase reactions in SCAV_EASY.

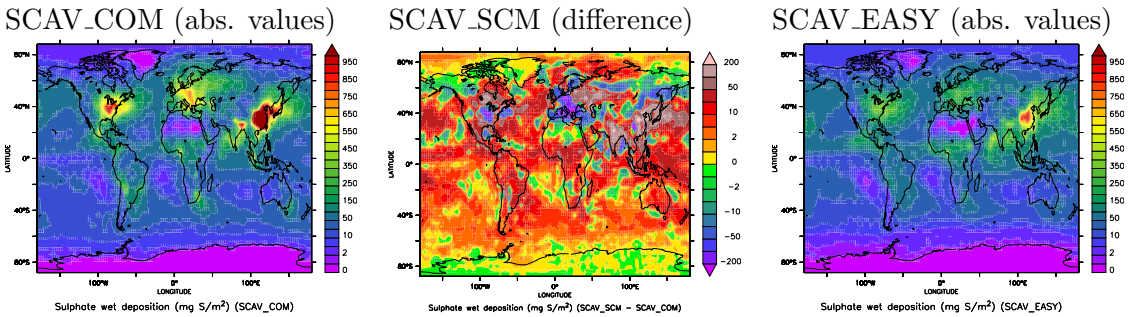

Figure 6.18: Sulphate annual wet deposition in mg S / m^2 of the SCAV_COM simulation (left), the absolute difference of SCAV_SCM to SCAV_COM (middle), and the absolute values for the SCAV_EASY simulation (right).

For sulphate (Figure 6.18), the highest wet deposition is calculated for East Asia with secondary maxima in the eastern USA and central Europe. The overall picture looks quite similar as in the EVAL simulation (compare Figure 6.13). The correlation with the observations is similar and the normalised standard deviation close to one, leading to a relatively good match of model and observations. There is globally more sulphate wet deposition in the SCAV_SCM simulation as a consequence of neglecting the sulphate consuming reactions in the simplified aqueous phase chemistry. The main regions with significantly lower sulphate deposition in the SCAV_COM simulation are eastern Canada, eastern Europe and East Asia, while over western Europe and the western USA lower values than in the SCAV_COM simulation are simulated. Since these are the same regions where the differences in the nitrate deposition occur, the interactions of sulphate and nitrate in the aqueous phase have an impact. Additionally, the differences in H_2O_2 as one of the main oxidants of sulphur dioxide are an considerable factor. In the SCAV_EASY simulation the spatial distribution of the wet deposition is similar, but again the fluxes are much smaller. This can be explained by the missing aqueous phase oxidation. The reaction pathway of oxidising SO_2 to H_2SO_4 in the gas phase is much slower and less efficient, leading to lower concentrations to be scavenged.
The general distribution of hydrogen peroxide (H_2O_2, shown in Figure 6.19) wet deposition looks relatively similar for all three simulations. With decreasing complexity of the scavenging mechanism the absolute values increase. This is explained by neglecting the H_2O_2 consuming reactions in the liquid phase. However, this has a strong impact on the gas phase, due to the changed oxidising capacity of the atmosphere, i.e., higher OH radical concentrations in the gas phase. There are only very few regions with lower deposition fluxes in the SCAV_SCM simulation. The largest differences occur in regions with strong precipitation. This is a consequence of the more efficient uptake of reaction partners and consequently faster H_2O_2(aq) consuming reactions in SCAV_COM. Additionally, in the tropics with strong incoming solar radiation the photolysis of hydrogen peroxide in the liquid phase is an important additional sink in the SCAV_COM simulation. The SCAV_EASY simulation has no chemical loss of H_2O_2 in the aqueous phase and therefore

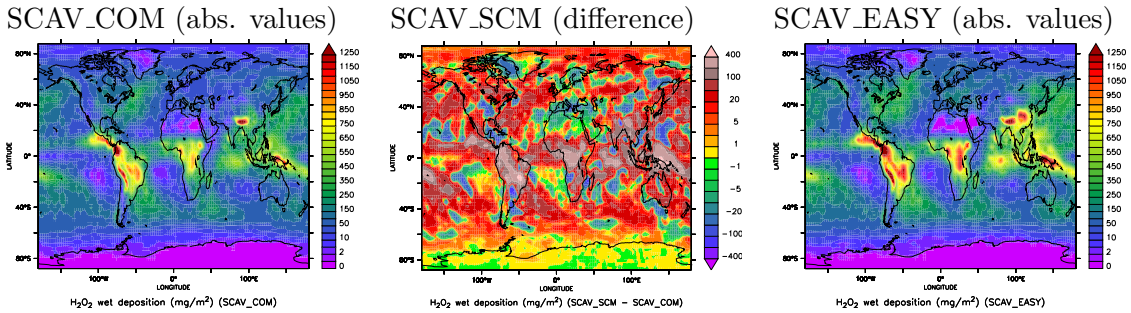

Figure 6.19: H_2O_2 annual wet deposition in mg / m^2 of the SCAV_COM simulation (left), the absolute difference of SCAV_SCM to SCAV_COM (middle), and the absolute values for the SCAV_EASY simulation (right).

shows the highest deposition fluxes.

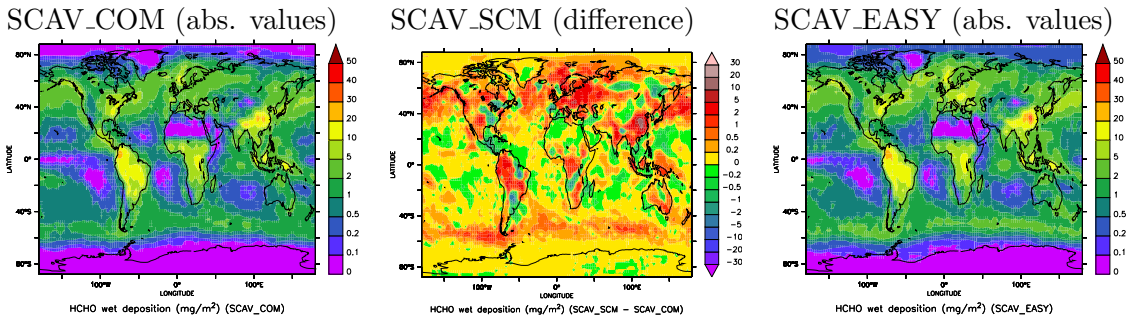

Figure 6.20: HCHO annual wet deposition in mg / m^2 of the SCAV_COM simulation (left), the absolute difference of SCAV_SCM to SCAV_COM (middle), and the absolute values for the SCAV_EASY simulation (right).

The main wet deposition of formaldehyde occurs in Amazonia, Central Africa and southeast Asia, as can be seen in Figure 6.20. This is consistent with the gas phase concentrations, which are highest over the tropical continents as a result of isoprene oxidation. Additionally, HCHO is directly emitted into the atmosphere. Due to its longer lifetime (several hours to days, depending on incoming solar radiation (Jacobson, 2002)), and only moderate solubility it can be transported into the storm tracks where it is finally deposited. As already indicated in Table 6.3 the wet deposition of HCHO is almost identical in all simulations. Since there is only one reaction consuming HCHO in the liquid phase ($HCHO + OH \rightarrow HCOOH + HO_2$) in the SCAV_COM simulation, and the OH(aq) concentration is relatively small, this is only of minor importance. This reaction results in small differences between SCAV_SCM and SCAV_COM. In addition, the modified oxidising capacity induced by the aqueous phase chemistry affects the gas phase mixing ratios and results in differences between the individual simulations much stronger, resulting in the differences seen in the other panels of Figure 6.20.
Last, but not least, the wet deposition of formic acid is analysed in Figure 6.21. The highest values are calculated in the tropics, i.e., consistently in regions with the highest precipitation fluxes. Since the sources are mainly continental, the wet deposition is highest over the continents of Amazonia, Southern Asia and Indonesia. It is chemically more reactive and more soluble than HCHO, at least if the dissociation of this weak acid is

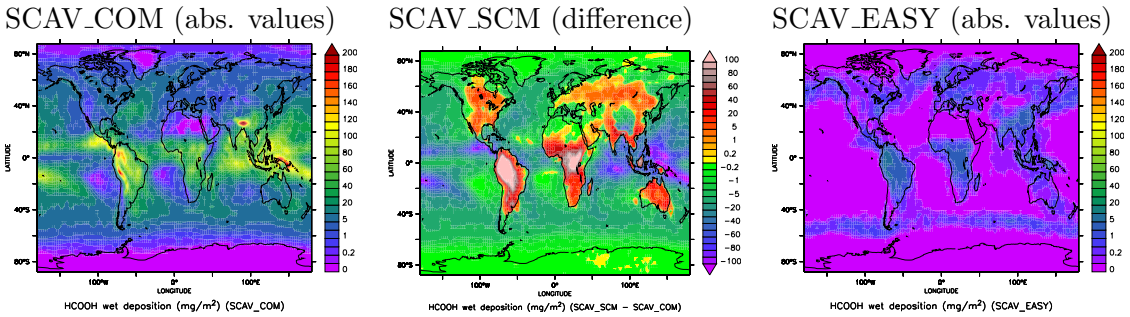

Figure 6.21: HCOOH annual wet deposition in mg / m^2 of the SCAV_COM simulation (left), the absolute difference of SCAV_SCM to SCAV_COM (middle), and the absolute values for the SCAV_EASY simulation (right).

considered. Therefore, the wet deposition occurs closer to the sources. The SCAV_SCM simulation shows significantly higher values over the tropical continents of Amazonia and Central Africa than the SCAV_COM simulation. In the northern hemisphere slightly higher deposition fluxes are calculated in the SCAV_SCM simulation. On the other hand, over Indonesia and almost everywhere over the ocean the wet deposition is lower than in the SCAV_COM simulation, especially in the tropics where the difference is substantial. This is again a consequence of the additional chemical reactions in the liquid phase that are neglected in the SCAV_SCM simulation, both having a direct and indirect influence on the oxidation capacity of the atmosphere. Similar to NH_x, the SCAV_EASY simulation fails in the wet deposition because of the missing dissociation of this only moderately soluble compound leading to an overestimation of gaseous HCOOH. However, compared to the SCAV_SCM simulation this is mainly balanced by a higher dry deposition.

6.4.2.2.2 pH - value analysis of clouds and precipitation

Figure 6.22 compares the annual zonal averages of the large-scale (upper row) and convective (lower row) cloud pH - value for the SCAV_SCM simulation (left) and SCAV_COM (right). In contrast to previous studies the H^+ concentration is not diagnosed from the sum of the anions but determined directly as a result of the dissociation and neutralisation reactions. To compute an average H^+ concentration in the clouds, the individual values are weighted with the cloud water content. Finally, the average pH is calculated according to Equation 1.8 from this average H^+ concentration in the cloud water.
Due to the CO_2 content of the atmosphere and less ammonia emissions than acidic pollutants the cloud pH is always acidic. The scale reaches from pH - values of three to six, with pH 7 representing neutral water.
Low acidity, i.e., high pH - values, occur in the southern hemisphere and the tropics, while lower pH - values dominate the northern hemisphere. This is mostly due to the fact that most of the anthropogenic, industrial pollutants (NO_x and SO_2) are emitted in the industrialised countries of the northern hemisphere. With increasing altitude the acidity increases, since with lower temperatures the liquid cloud water decreases, because the clouds mostly consist of ice particles. Therefore the amount of available water is smaller, resulting in higher concentrations of pollutants. This is also the reason for a poleward decrease of the cloud pH. In the zonal average, the large-scale clouds can reach the surface. In the model this is similar to fog, which is not treated separately by the microphysical

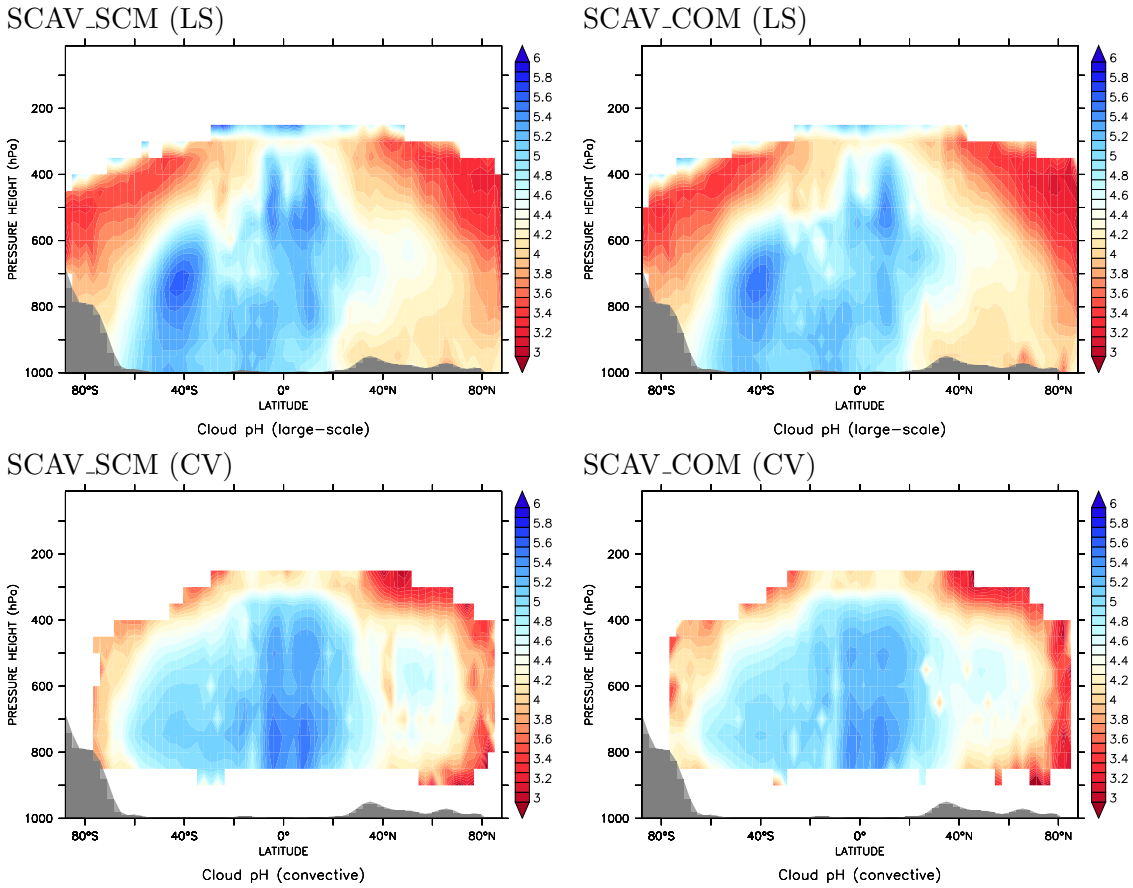

Figure 6.22: Annual zonal average of the cloud pH - values in the vertical cross section for the SCAV_SCM (left) and SCAV_COM (right) simulation. The upper row shows the pH - value of large-scale clouds, and the lower row of convective clouds. The grey area depicts the zonal average orography.

cloud routines. Since fog is mostly more acidic than actual clouds, an increase in the pH - value can be found in the more polluted northern hemisphere from the surface to the levels between 800 and 600 hPa altitude.
The convective cloud pH shows a sharp cutoff at about 850 hPa. Below this level there are no or not enough values to calculate a zonal average. This results from a simplification in the current scheme. The convective cloud water is not calculated explicitely in some convection parameterisations. Therefore, only the fraction of the cloud water which is converted to precipitation is used instead. In the T1 convection scheme no precipitation is formed below 1500 m altitude above the surface (compare Equation 3.10). This results in an underestimation of the convective cloud water, and therefore in too low nucleation scavenging. However, for the wet deposition the nucleation scavenging is correctly calculated, since only this fraction of the scavenged compounds is incorporated in the wet deposition flux. Therefore, only the cloud processing of air is underestimated by this simplification. As for the large scale, a difference in the acidity can be seen from the South to the North: on the southern hemisphere the pH - values are generally higher. In the tropics, where deep convection is dominant and a large amount of water is available, the pH - values are highest. Further northwards there is an increase in the acidity in the subtropics, where

almost no convection occurs. In the northern storm tracks (40° to 60°N) with substantial convective activity, the pH slightly increases above 700 hPa. In the polar regions the convective cloud water content is very low, resulting in low pH - values.
The differences in both convective and large scale cloud pH between the SCAV_SCM and SCAV_COM simulation are very small. Overall, in the SCAV_COM simulation the cloud water is slightly more acidic. This results from taking into account more chemical species and reactions in the aqueous phase. However, the differences are small, and with respect to the cloud pH the computationally cheaper (see Section 6.4.2.2.4) SCAV_SCM simulation seems to give almost the same results.
Due to the dissolved acidic species in the precipitation, resulting from scavenging and precipitation chemistry, the pH - value can also be determined for rain water. Figure 6.23 shows the large-scale (upper row) and convective (middle row) precipitation pH for the SCAV_SCM (left) and SCAV_COM (right) simulation. The lower row depicts the total rain pH, as a precipitation-weighted average from both types of rainfall. Similar to the analysis for the cloud acidity a precipitation weighted average H^+ concentration is calculated and from that the pH is determined. Similar to the pictures for cloud pH the scale is defined from 3.5 to 6.5, i.e., completely in the acidic regime.
The large-scale precipitation shows high values of acidity (red color) over the eastern USA, over Europe and east Asia. Additionally, there are low pH - values in Central and South Africa and over the Sahara. It is important to distinguish the two factors controlling the pH. There are high, acid producing emissions in America, Europe and east Asia on the one hand, and on the other hand very low precipitation amounts occur in northern Africa and northern Europe, where there is either no rain or the precipitation is mostly falling as snow. In the tropics pH - values are mostly higher, especially over the ocean.
The convective rain pH shows high acidity in North America, Europe, and parts of East Asia. Additionally, there are low pH - values at the South American and African east coast. The latter regions as well as the polar regions are characterised by low convective precipitation values (compare Figure 6.14). The regions in the northern hemisphere are more strongly influenced by the industrial emissions. The lower pH - values in Central Africa result mostly from the NO_x emissions from biomass burning.
The lower row of Figure 6.23 depicts the composite of both the convective and large-scale parts. This is comparable to measurements, because in reality a distinction between large-scale and convective rain is not possible. Indeed, the total rain pH - value is, similar to the fractions, mostly dominated by the acidic emissions in the northern hemisphere.
The differences between the two simulations are relatively small. They are most pronounced in the Sahara, where almost no precipitation occurs at all. In the tropical Pacific the pH is slightly higher in the SCAV_SCM simulation, while over Australia the precipitation is more acidic. In the generally more acidic regions of North America and Europe the pH values are slightly lower in the SCAV_COM simulation.
Note however, that in these simulations aerosol chemistry is not considered. Even though the scavenging of aerosol sulphate, nucleated from the gas phase, or generated from evaporating precipitation and clouds is treated, the chemical composition of the seasalt particles is ignored. This includes the release of HCl and HBr from the aerosol into the gas phase and their subsequent scavenging, and the alkaline composition of the seasalt aerosol itself due to the content of HCO_3^- (Kerkweg, 2005). Nevertheless, compared to the amount of acidity originating from oxidated sulphur and nitrogen, it is expected that this is less significant for the precipitation pH. Moreover, the lowest pH - values are calculated mostly over land, where seasalt aerosol has no major influence. Furthermore, alkaline components

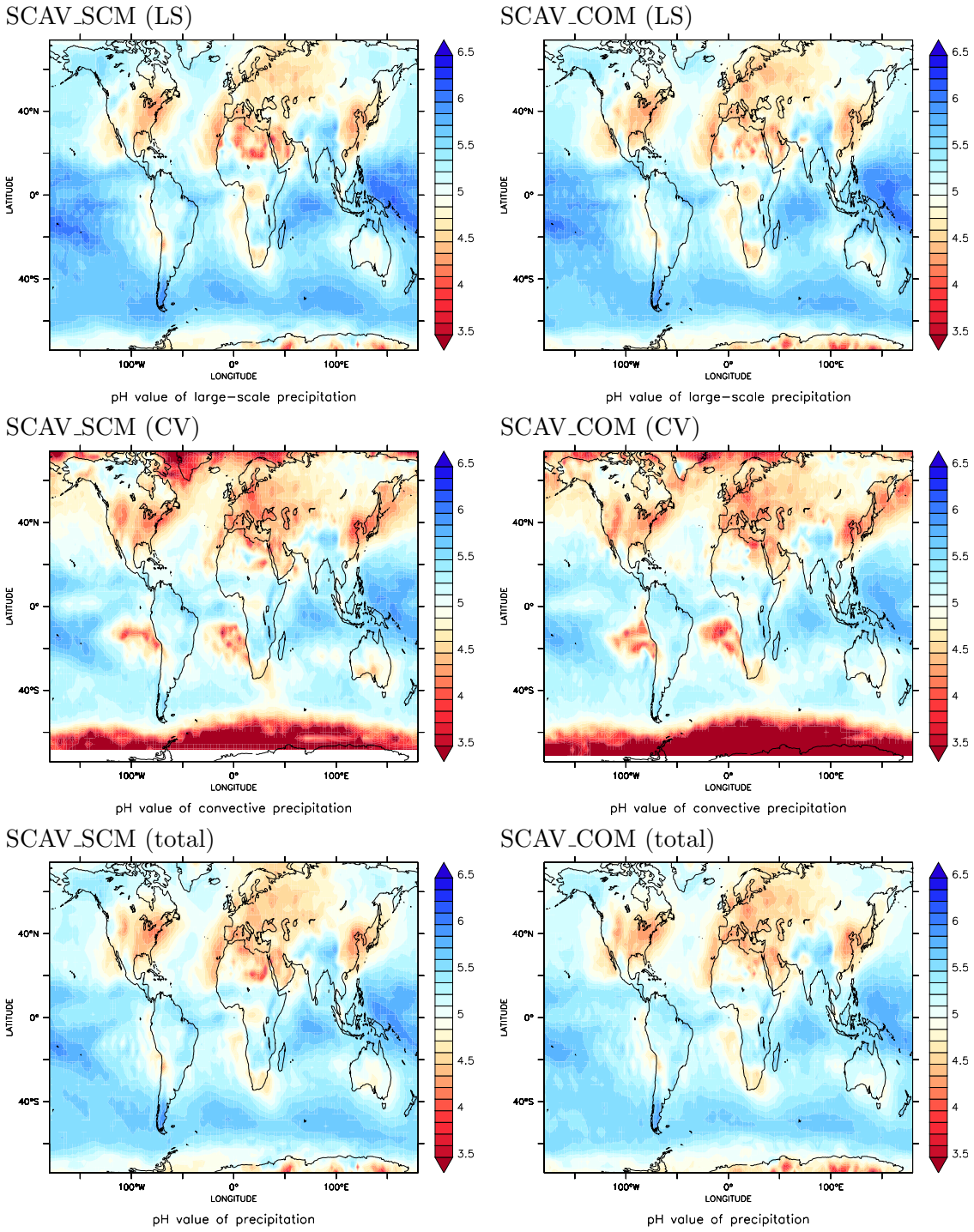

Figure 6.23: Rain pH - values at the surface for the SCAV_SCM (left) and SCAV_COM (right) simulation. The upper row shows the pH - values of large-scale rain, the middle row the pH - values of convective rain and the lower row the precipitation weighted total rain pH - values.

of mineral dust aerosols are also neglected.
A comparison with observed pH - values is presented in Figure 6.24 using data from the

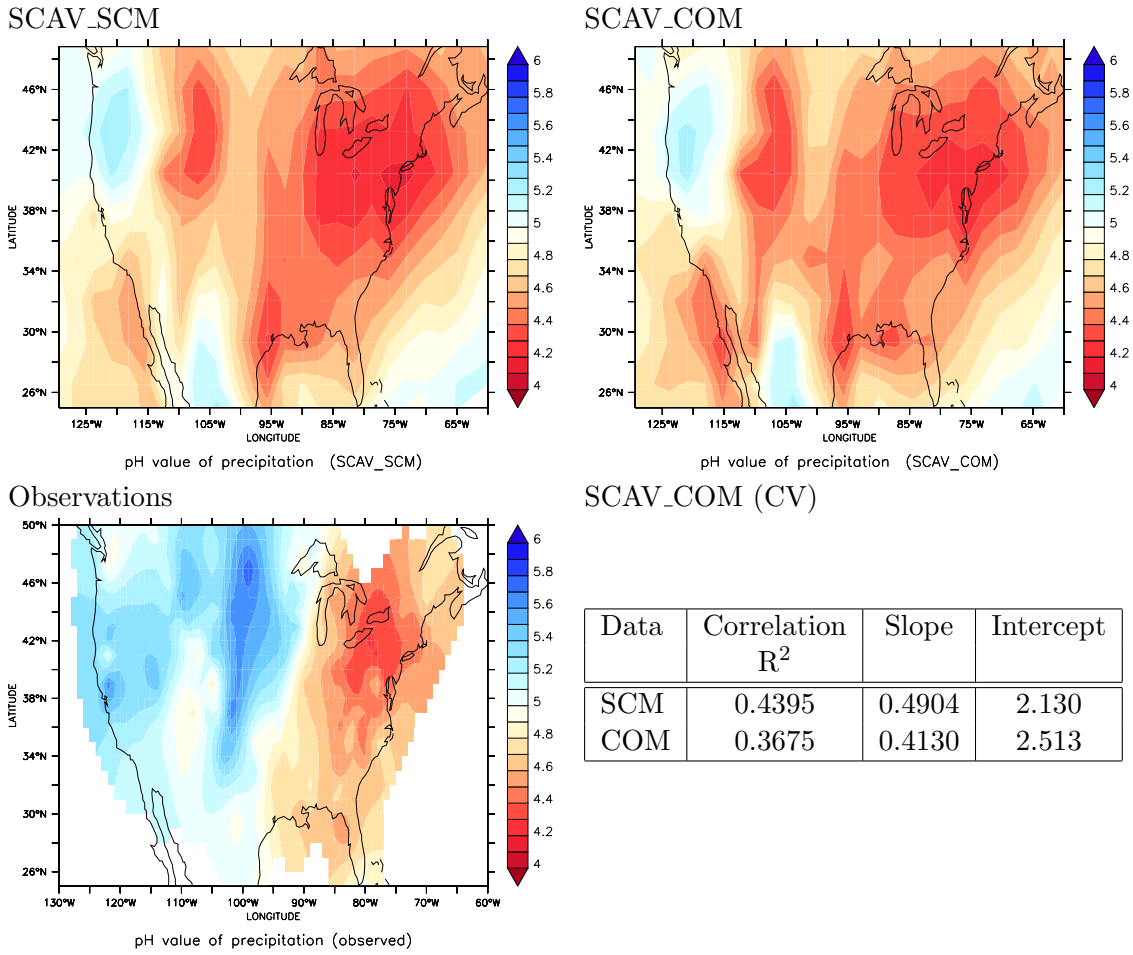

Data	Correlation R^2	Slope	Intercept
SCM	0.4395	0.4904	2.130
COM	0.3675	0.4130	2.513

Figure 6.24: Rain pH - values at the surface for the SCAV_SCM (upper left) and SCAV_COM (upper right) simulation in the USA. In the lower row the corresponding observed average pH (left) and the statisical comparison (right) is shown.

NADP network for the simulation year 2000. Since the meteorology is nudged for this year, a detailed point to point comparison of the annual average pH is possible. From the observations of the wet deposition flux of H^+ and the observed precipitation amount an annual average pH of the precipitation is calculated. The same values as in Figure 6.23 are shown in the upper row for the SCAV_SCM (left) and SCAV_COM (right) for the USA. In the lower row, the precipitation pH calculated from the observations is presented. Additionally, the corresponding statistics are shown in the table in the lower right panel. For comparison, the station observations are gridded and interpolated on a 1° x 1° grid. The pictures in the upper row show only small differences: SCAV_SCM has slightly lower values in the eastern USA, while in the westerly regions there is less acidity than in SCAV_COM. However, the observations look very different: in the eastern USA the low pH - values are represented by the model, but in the western USA the observations show significantly higher pH - values of almost one pH unit, especially in the midwestern regions and California. An analysis of the individual factors controlling the pH (wet deposition of H^+ and precipitation, both not displayed) shows that both are not represented well by the model: the simulated wet deposition of H^+ is effectively larger from 100° to 110°W by

a factor of more than two. In the coarse resolution of the model this affects the midwest in general. Additionally, in Texas and the surrounding states the precipitation is underestimated by the model, while further north in the midwest the precipitation is captured sufficiently well, taking into account the coarser model resolution. Close to the west coast some observations of high precipitation, leading to high pH - values, are considered which are not captured by the model at all. A similar feature occurs in the observations around 105°W from 36° to 42°N. Overall, the lower pH - values in the western USA predicted by the model, but not occuring in the observations, are mostly in regions with very low precipitation.
The statistics are slightly better for the SCAV_SCM simulation with a higher correlation of $R^2 = 0.44$ compared to $R^2 = 0.37$. A slope closer to 1 is calculated for the SCAV_SCM simulation. This is a consequence of the better performance in the west and midwest USA. In summary, the general features of the pH - value distribution are represented in regions with high rainfall, while in regions with low precipitation the performance is worse.

6.4.2.2.3 Influence on gas phase constituents

In this section the influences of the different scavenging mechanisms on gas phase species are investigated. Since wet deposition is most effective in the lower troposphere due the precipitation falling through this layers and many species have their sources at the surface, the annual average surface mixing ratios are compared. For this purpose the SCAV_COM simulation is used as a reference and relative differences are shown for the other simulations with the exception of SO_2, for which absolute differences are shown.

Ozone

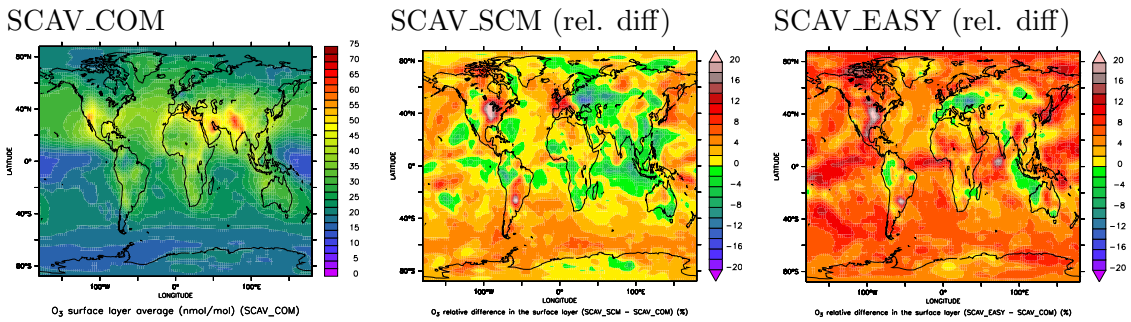

Figure 6.25: Average surface layer mixing ratios of O_3 in nmol/mol of the SCAV_COM simulation (left) and the relative difference in % of SCAV_SCM (middle) and SCAV_EASY (right).

The ozone distribution shows highest annual average values in the Middle East and over Tibet (partly related to the high altitude of the latter region) with secondary maxima in California and the Mediterranean. The values are very similar to the results from the long-term EVAL simulation (Jöckel et al., 2006), even though a vertical resolution only roughly representing the stratosphere is selected in the studies of this section.
The middle panel of Figure 6.25 shows the relative differences in % of the surface ozone of the SCAV_SCM to the SCAV_COM simulation. There are some regions where less ozone is simulated than in the reference simulation, especially in eastern Europe and northwestern Siberia, southeast Asia and the Indian Ocean with maximum differences of about 10% to

15%. Almost everywhere in the ITCZ there are only small differences of ±2%. In the eastern USA and northern Argentina more than 20% more ozone occurs. In western Europe the surface ozone mixing ratio is higher by more than 10% in the SCAV_SCM simulation. Over most of the extratropical oceans slightly higher ozone mixing ratios occur in the range of 5%.
The differences of the SCAV_EASY to the SCAV_COM simulation are much more uniform. With the exception of very few regions (Europe, especially the eastern parts, south west of Indonesia) almost everywhere higher mixing ratios are calculated in the simulation with the simplified scavenging approach. Only in eastern Europe approximately 10% lower mixing ratios occur, while elsewhere more than 5% higher O_3 are predicted by the model. In some regions of the ITCZ and the SPCZ (regions, where convective scavenging is substantial) the differences reach more than 15%. In the eastern USA the differences are even higher than 20%.
Most of the differences correlate with differences in formic acid wet deposition and similar compounds. As a consequence of the different scavenging of the ozone precursors, the ozone formation is affected.
In contrast to the other species treated in detail in this section, O_3 does not have decreasing but increasing mixing ratios with altitude, due to the strong ozone formation in the stratosphere. Therefore in addition to the surface distribution the vertical distribution of zonal average mixing ratios is analysed in Figure 6.26.

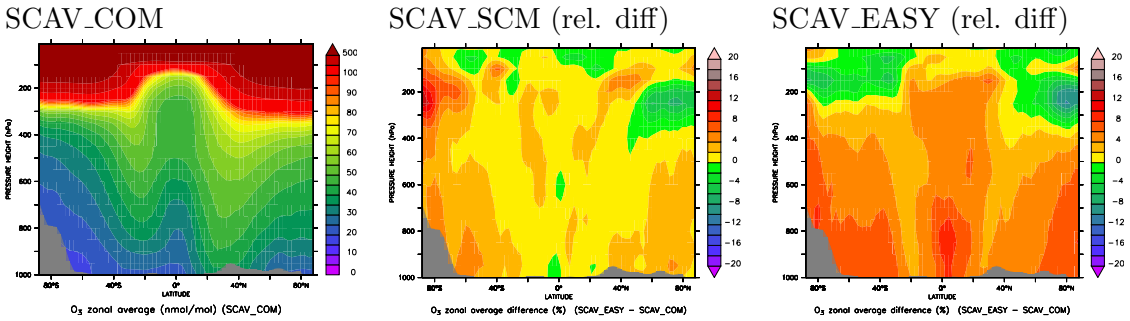

Figure 6.26: Vertical cross section of the zonal and annual averaged O_3 mixing ratios in nmol/mol of the SCAV_COM simulation (left) and the relative difference in % of SCAV_SCM (middle) and SCAV_EASY (right). The grey area depicts the zonal mean orography.

The left panel shows the absolute values of the SCAV_COM simulation. The increasing values with altitude are reproduced well. Mixing ratios of more than 100 nmol/mol mark the tropopause region. In the tropics air with low mixing ratios of ozone is transported up into the upper troposphere by convection. The region around 20°S and 30°N are characterised by the large scale subsidence of the Hadley cell, transporting O_3-rich air downwards combined with efficient photochemical ozone formation in the subtropics. This seems to be more efficient in the northern hemisphere due to the coincidence of this transport and higher surface mixing ratios as seen in Figure 6.25. Towards the north pole the gradient towards the stratosphere is less steep, compared with the cleaner southern hemisphere, resulting from more pollution and subsequent photochemical ozone production.
The middle panel of Figure 6.26 shows the differences simulated with the less comprehensive aqueous phase chemistry in the SCAV_SCM simulation. Whereas in the surface mixing ratios of Figure 6.25 it was unclear whether there is more or less O_3 in the reference

simulation, this graph shows generally higher ozone values in the SCAV_SCM simulation. Although in the zonal average the difference is less than 5%, for specific longitudes this differences can be larger. The difference in ozone hardly changes with altitude in the tropics and midlatitudes, while in the polar region the effect above 300 hPa is much stronger. However, in these region this altitude already represents the lower stratosphere. Even though there is hardly any liquid water for aqueous phase chemistry, some modifications in the lower troposphere can propagate into the UTLS region and have a strong impact there.
The comparison of the SCAV_EASY simulation shows all over the troposphere higher values than in SCAV_COM. The differences are most pronounced in the midlatitudes and tropics, while in the subtropics with only little precipitation they are less distinct. They result from the overall change of the chemical composition of the atmosphere induced by the altered scavenging of some ozone precursors, e.g., HCOOH and HNO_3, oxidants, e.g., H_2O_2 and to a minor part also from the neglection of e.g., SO_2 oxidation in clouds and precipitation by ozone in the liquid phase. As a consequence of the modified chemical composition in the UTLS the ozone mixing ratios in the lower stratosphere are lower by up to 10% in the extratropical regions.

HCHO

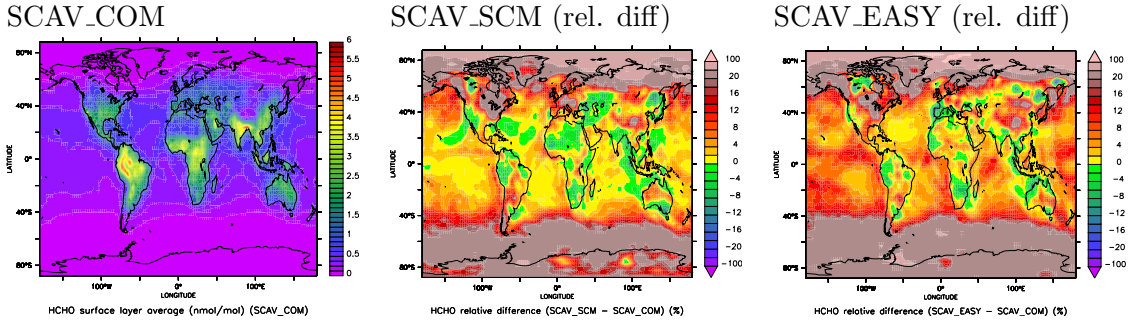

Figure 6.27: Average surface layer mixing ratios of HCHO in nmol/mol of the SCAV_COM simulation (left) and the relative difference in % of SCAV_SCM (middle) and SCAV_EASY (right).

Since formaldehyde is moderately soluble and therefore scavenged, but also important for ozone formation, the similar pictures as for ozone at the the surface are presented in Figure 6.27. The left panel shows the absolute values in nmol/mol. Highest values are obtained in India and southeast Asia, Amazonia and Central Africa. Additionally, medium values are obtained in the southern USA and Middle East. HCHO is directly emitted from industrial sources (responsible for the values in China and the USA), but it is also a product of the oxidation chain of almost all higher hydrocarbons and therefore also strongly influenced by isoprene emissions (responsible for the high values in the tropics). Further polewards the OH concentrations decrease, leading to a weaker chemical HCHO production. Furthermore, the biogenic emissions of the NMHCs are lower in these regions, also leading to a weaker chemical source of formaldehyde.
As seen in Figure 6.20 the wet deposition fluxes do not differ much between the individual simulations. Similarly, the HCHO gas phase mixing ratios in the tropics do not differ by more than 5% for SCAV_SCM. Only in Central Europe and the eastern USA, the

differences reach values higher than 20%. South of 45°S and north of 60°N the relative differences become larger due to the low absolute values in these regions.
The comparison with the SCAV_EASY simulation yields in general a similar result. The differences in the tropics are in the ITCZ up 10%. In China and eastern North America more than 20% higher values are simulated, while in the polar regions the differences exceed even 50% to 100%, resulting in an overall higher surface mixing ratios in the SCAV_EASY simulation. Only very few and small regions are characterised by lower values compared to the SCAV_COM simulation.
Overall, the effect of a different description of the aqueous phase chemistry on HCHO is substantial in the regions with significant concentrations, even though the direct effect is relatively small. It is the indirect effect of a modified oxidising capacity of the atmosphere which affects the surface mixing ratios of this compound.

H_2O_2

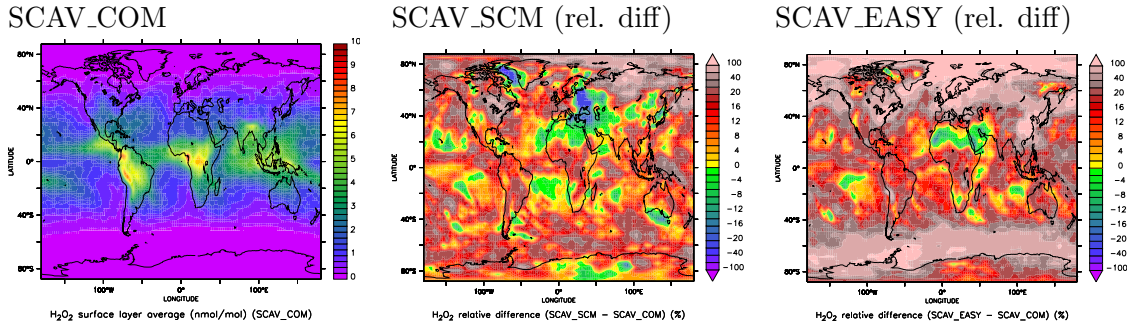

Figure 6.28: Average surface layer mixing ratios of H_2O_2 in nmol/mol of the SCAV_COM simulation (left) and the relative difference in % of SCAV_SCM (middle) and SCAV_EASY (right).

H_2O_2 is of special importance since it is highly soluble and therefore efficiently influenced by the scavenging and aqueous phase chemistry. It is a main oxidant in the liquid phase, especially for SO_2. In the gas phase, it is an oxidant as well as a source for the main oxidant OH. Figure 6.28 shows in the left panel the surface mixing ratio in the SCAV_COM simulation. Corresponding to the water vapour content of the atmosphere and the incoming solar radiation, highest mixing ratios occur in the tropics. Since one of the main sources is the self-reaction of HO_2 ($HO_2 + HO_2 \rightarrow H_2O_2 + O_2$), and HO_2 is a product of oxidation by OH, the highest values occur in the regions of strong VOC emissions and their subsequent oxidation by OH, i.e., the tropical continents (in order of abundance: Amazonia, Central Africa and southeast Asia).
As already seen in Figure 6.19 the wet deposition fluxes are substantially different between SCAV_COM and SCAV_SCM. Similar results occur in the surface gas phase mixing ratios. Only in the subsidence regions with only very weak precipitation very low differences are detected. In eastern Europe and over the ocean between northern Canada and Greenland lower values of more than 20% are simulated in the SCAV_SCM simulation. Almost everywhere else, significantly higher values occur in this simulation: in the tropical ITCZ and the SPCZ these differences are higher than 30%. In the eastern USA and the polar regions even differences of more than 100% occur. However, it must be emphasised that in the polar regions the absolute values are very small.

In the SCAV_EASY simulation this is even more pronounced. First there are no regions with substantially lower values than in the SCAV_COM simulation, and second in the tropics the values are up to 30% higher than in SCAV_COM. Further polewards the regions with large differences (> 100%) are much more widespread.
This is a general result of the combined gas phase and aqueous phase chemistry. Due to the comprehensive interactions and feedbacks, it cannot be directly attributed to one specific process or reaction. In general it is concluded that there is a high dependence of the surface mixing ratios of H_2O_2 on the scavenging description.

SO_2

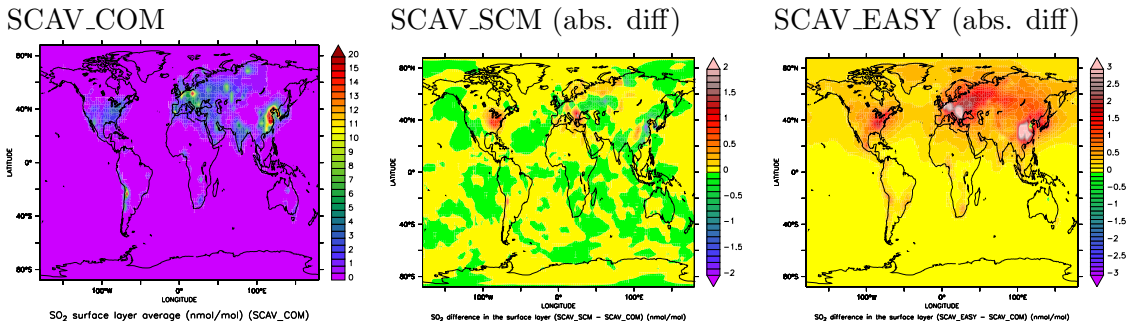

Figure 6.29: Average surface layer mixing ratios of SO_2 in nmol/mol of the SCAV_COM simulation (left) and the absolute difference in nmol/mol of SCAV_SCM (middle) and SCAV_EASY (right).

The last compound analysed in this section is SO_2. Since the absolute values are spatially very variable, relative differences are not very insightful, because they reach numbers of several thousand % in regions with almost negligible absolute mixing ratios. Therefore, in Figure 6.29 the absolute differences are shown. The left panel depicts the absolute values of the sulphur dioxide surface mixing ratio. The highest values occur in eastern China, with secondary maxima in Europe and Chile. These secondary maxima are mostly very punctual and caused by local emission sources. In most parts of Europe and the USA, as well as in the Middle East, India and the western part of Russia lower mixing ratios are found.
The comparison with the SCAV_SCM shows only small differences, less than 2 nmol/mol in the maximum regions. The only regions with significant differences are in the eastern USA, Europe and China, while in the other regions the differences are mostly much smaller ($\pm$ 0.1 nmol/mol). Overall, the conversion of SO_2 to sulphate and subsequent scavenging is considered in both simulations. The small differences result from slightly different uptake into the aqueous phase caused by a different rate of the oxidation to sulphate. This originates from the altered H_2O_2 and O_3 mixing ratios in the gas phase and consequently the aqueous phase. Additionally, the small differences in the acidity of the cloud and rain water modify the reaction speed.
The SCAV_EASY simulation shows everywhere higher mixing ratios for SO_2. In Europe and China the differences are larger than 3 nmol/mol, but also in the USA and more generally in the entire northern hemisphere higher values are calculated by this model simulation. This results from a weaker uptake into the liquid phase. Since the gas phase

oxidation to H_2SO_4 is much slower and the scavenging is significantly reduced, the atmospheric lifetime of SO_2 is increased, and transport into remote regions is possible. However, transport across the ITCZ into the southern hemisphere cannot be detected in the surface regions, because for such long-range transport via the upper troposphere in the tropics and subsequent subsidence in the southern hemisphere (about one year for the interhemispheric exchange time) the lifetime is not long enough.

In summary, a high dependence of the surface mixing ratios on the choice of complexity for the scavenging and aqueous phase chemistry has been found. Since all species interact directly or indirectly with each other, some of the distinctions and reasons are somehow artificial. For ozone, taking into account both surface mixing ratios and the zonal average vertical distribution, the more comprehensive the liquid phase chemistry is calculated the lower are the obtained mixing ratios. The variations are mainly around 5 to 10%, but in some regions they are substantially higher. Since the scavenging and wet deposition is relatively small due to its low solubility, the major differences result from the indirect effects of an altered oxidation capacity of the atmosphere. The SO_2 oxidation contributes slightly to the differences. The effects of the scavenging description on HCHO also result mainly from the altered gas phase composition and are therefore only indirect effects. The processes in the aqueous phase contribute even less than for O_3, since it hardly takes part in chemical reactions in the droplets. The differences between the individual simulations are less pronounced than for most of the other compounds. For H_2O_2 the gas phase surface mixing ratios decrease significantly with a more detailed cloud and precipitation chemistry, partially up to 30% in the regions with the highest absolute values. This results from both reactions in the liquid phase and altered gas phase composition. The surface mixing ratios of SO_2 are similar in both SCAV_COM and SCAV_SCM because both consider the dissociation and liquid phase oxidation to sulphate. Neglecting this processes, as in SCAV_EASY, results in substantially higher mixing ratios close to the emission sources and further downwind. Therefore, the aqueous phase chemistry is mainly responsible for the differences between the three simulations. A further discussion and comparison with measurements follows later on in Section 6.5.

6.4.2.2.4 Computational costs

The computational requirements can roughly be estimated from the average time used per time step for the three simulations on a 128 CPU supercomputer (IBM P4) for a horizontal resolution of T42 with 31 vertical layers presented in Table 6.4. Surprisingly, the SCAV_EASY simulation is even slightly slower than the SCAV_SCM simulation, even though in SCAV_EASY the KPP generated code is not used. This can be explained by the used gas phase mechanism. Due to an inconsistent removal of some gaseous constituents, the chemical differential equation system solved in the MECCA submodel becomes more stiff, and therefore more integration steps, using longer computation time, are required for the numerical solution. It cannot be guaranteed that the times in Table 6.4 are not influenced by other processes running on the computer, since they result from logfile output only. No detailed flow trace analysis has been performed. However, the differences between these two simulations are sufficiently small on this specific architecture that the use of at least SCAV_SCM is recommended for future calculations. The higher computational costs for SCAV_COM are required by the larger number of species and reactions in the liquid phase chemical mechanism. Especially because this differential equation system has to be solved several times (convective and large scale clouds and precipitation) the increase

in the complexity of the process description leads to the higher computational costs. It must be individually decided for a specific study if the impact of clouds and precipitation chemistry is of importance.

Table 6.4: Computational Costs for the three simulations.

Simulation	average time used per time step
SCAV_SCM	≈ 3.50 s
SCAV_EASY	≈ 3.55 s
SCAV_COM	≈ 4.15 s

6.4.3 Aerosol scavenging

The scavenging and wet deposition of aerosols is investigated for seasalt particles. In contrast to the ^{210}Pb deposition in Section 6.3 sticking to an idealised aersosol, in this section the aerosol is calculated explicitely with the M7 (Section 2.2.2.5) submodel. The emissions originate from the ONLEM (Section 2.2.2.4) submodel using a wind speed dependent parameterisation (Guelle et al., 2001). While M7 calculates the microphysical properties and distributes the emissions onto the individual modes, the sink processes are calculated by the submodels DRYDEP (dry deposition), SEDI (sedimentation), and SCAV (wet deposition).
Since there is no global observational dataset available, the model results from SCAV_SCM simulation are compared with other model results from the AEROCOM project[2]. Since the meteorology of the other two simulations (SCAV_COM and SCAV_EASY) is very similar due to the nudging and the seasalt aerosol is chemically inactive in this studies, their results are almost identical.

ECHAM5/MESSy AEROCOM MEDIAN

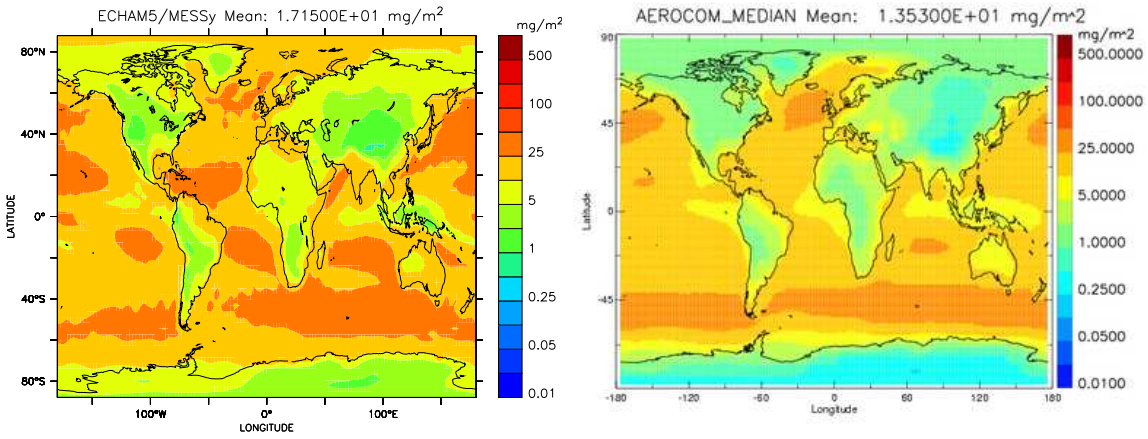

Figure 6.30: Average seasalt column burden in mg/m^2 of the SCAV_SCM simulation (left), and the AEROCOM median (right, from: `http://nansen.ipsl.jussieu.fr/AEROCOM/data.html`).

Figure 6.30 shows the simulated seasalt column burdens in mg/m^2 for the simulation

[2] `http://nansen.ipsl.jussieu.fr/AEROCOM`

SCAV_SCM in the left panel, and the median from the AEROCOM Experiment A simulations (right panel). This Experiment A is a model intercomparison of global atmospheric chemistry climate and chemistry transport models, with each model using their own emissions, boundary conditions, etc., to simulate the atmospheric aerosols. Since the data is not publically available, only a comparison of the pictures on almost the same color scale is possible. The mean value of the seasalt burden of ECHAM5/MESSy is 17.15 mg/m^2, while the AEROCOM A median is slightly lower with 13.53 mg/m^2. Ignoring the most extreme simulations the mean values show a high variability of 8.91 mg/m^2 to 35.66 g/m^2. The overall features of the aerosol column burden of the AEROCOM median are also produced by ECHAM5/MESSy. The highest values are found in the northern and southern storm tracks. However, in the SCAV_SCM simulation, higher values are found in the subsidence regions of the subtropics, i.e., regions with almost no precipitation. Since there is consequently almost no wet depostion in these areas, the main sink is reduced. Almost everywhere over the contintents the values of the SCAV_SCM simulation are higher, denoted by the next color category. Since the values over the continents are in general relatively low because of the lack of emissions, this is a consequence of the general high bias (see global average above), which is more pronounced for the lower values over the continents on the logarithmic color scale. Overall, the spatial distribution patterns are represented rather similarly.
The high bias cannot be explained by the emissions only. For the SCAV_SCM simulation the global mean value is about 10.97 g/(m^2 yr), while in the AEROCOM simulations it ranges between 4.28 g/(m^2 yr) to 236.55 g/(m^2 yr). For the AEROCOM Experiment B (i.e., with prescribed identical emissions) a global mean value of 15.72 g/(m^{2}yr) is proposed. Unfortunately there is no median column burden available for this experiment, but the pictures for the individual simulations (not shown here) indicate even slightly higher values than in the SCAV_SCM simulation. Summarising, it can be concluded that the column burden is acceptably represented by the model assuming the AEROCOM median as a reference.

ECHAM5/MESSy

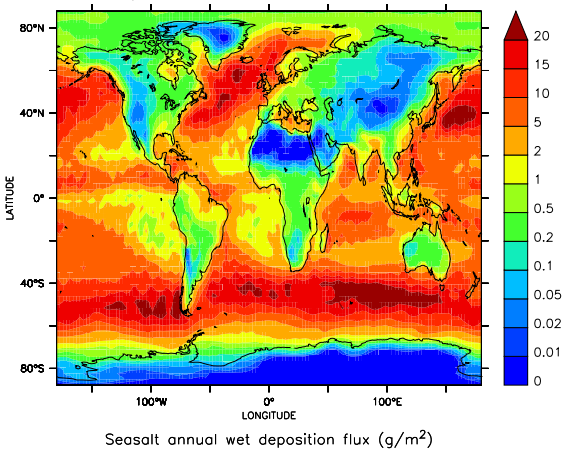

AEROCOM Exp A

Model (Selection of participating models of AEROCOM)	Global Mean Seasalt wet deposition [g / (m^2 yr)]
ECHAM5/MESSy	5.59
ARQM	8.90
GISS	1.57
KYU Sprintars	4.19
LOA Lille	2.21
LSCE INCA	4.74
UMI	2.14
MPI_HAM	5.43

Figure 6.31: Annual seasalt wet deposition flux in g/m^2 of the SCAV_SCM simulation (left) and global average values for several models participating in AEROCOM (right) (from: http://nansen.ipsl.jussieu.fr/AEROCOM/data.html).

An analysis of the wet deposition flux for seasalt aerosol is performed with the help of

Figure 6.31. The left panel depicts the annual wet deposition of the coarse and accumulation mode seasalt aerosol particles in g/m^2. As for most of the gaseous species the highest deposition values are found in areas where both the concentrations are high and additionally high precipitation fluxes occur. Both conditions are fulfilled in the storm track regions resulting in the highest wet deposition fluxes. Due to the strong precipitation in the ITCZ there are much higher deposition values than in the subtropics. Especially in the subsidence regions, the wet deposition is smaller by a factor of up to 10, resulting from the very low precipitation in these regions. Over the continents the wet deposition is much lower, due to the lower seasalt concentrations. There is almost no wet deposition of seasalt over Antarctica, since there is only very weak precipitation. Especially, because in the polar regions the precipitation is falling as snow, the scavenging of aerosol particles is less effective. In Australia, there is only light precipitation resulting in low deposition fluxes, even though a considerable amount of seasalt is transported from the oceans over the continent. This corroborates that wet deposition is the most important sink process, because in absence of precipitation higher burdens are calculated over the continents, where no emission occurs, than over other continents where rainfall is simulated.
For an analysis of this issue, the global mean wet deposition is calculated. The comparison with some wet deposition amounts from the AEROCOM Experiment A are shown in the table in the right panel of Figure 6.31. The wet deposition of seasalt in SCAV_SCM is 5.59 g/(m^2 yr). The dry deposition sink is about 3.64 g/(m^2 yr), with additional 1.78 g/(m^2 yr) from sedimentation, showing that the total wet deposition is more than 50% of all the sinks. The sinks sum up to 11.01 g/(m^2 yr), balancing the emissions of 10.97 g/(m^2 yr). Roughly, the spatial distribution is similar in most of the AEROCOM Experiment A. The absolute values range from 1.57 g/(m^2 yr) to 8.90 g/(m^2 yr), showing also that the absolute value of ECHAM5/MESSy is within the range of other models.

Concluding it can be stated that the wet deposition of aerosol species can be simulated properly, with a high dependence on the aerosol concentrations and the precipitation patterns. The simulation of aerosol content of the atmosphere is within the range of other state-of-the-art global aerosol models.

6.5 Discussion

One weakness of the scavenging scheme is the neglect of the scavenging of gaseous components by snow and the uptake on cloud ice. Due to the treatment of supercooled water in the large-scale cloud scheme, there is mostly a mixture of both liquid and solid water in the large-scale precipitation. Therefore, there is almost always a small reduction of the gas phase mixing ratios by large-scale precipitation, independent of whether it is snow or water. Only in the polar regions, where almost no rainfall occurs, the scavenging of gas phase species is underestimated. The convective precipitation formation lacks the explicit microphysical processes. Therefore, either rain or snow is produced determined by the environmental temperature around the convective cloud. To overcome this problem, it is assumed that a fraction of the convective cloud ice and snow consists of supercooled water. This fraction is linearly decreasing with temperature, reaching zero at minus 35° C. At this low temperature usually all water is frozen (Pruppacher and Klett, 2000). A scavenging scheme that includes the uptake of gaseous species by snow and ice into a cloud resolving model has been applied in the studies of Salzmann (2005), showing an important dependence on the profile of the species to be scavenged. The approach of Lawrence

and Crutzen (1998), who assume a similar process sequence as in the aqueous phase, but with a lower 'Henry coefficient', might be appropriate, but the value of this coefficient is highly uncertain. Additionally, the retention coefficient, i.e., the amount of a tracer that stays inside a freezing droplet and is not released into the gas phase, is not known for most compounds. This has been discussed by Barth et al. (2001) for convective events. However, in their studies idealised tracers of various solubility are used and they find a high dependence on this coefficient, while Lawrence and Crutzen (1998) assign minor importance to such a factor. Salzmann (2005) shows that it is very much dependent of the initial vertical profile of such a species. If the scavenging affects the tracers already in the lower atmosphere, a significant fraction of the species is directly scavenged and wet deposited. Therefore it cannot be transported into the upper troposphere.
This leads to another key problem in a model system using the operator-splitting technique. If the convective transport is treated independent of the scavenging, the wet deposition is either over- or underestimated. If scavenging is followed by the convective transport, the vertical distribution of a species with its source in the boundary layer is not represented correctly, and the uptake can only occur in the lowest troposphere. Alternatively, if the tracer is transported first and afterwards the scavenging is calculated, a large fraction of the tracer is already transported into the upper troposphere by convection and the scavenging is too weak due to the low water content in the high altitudes. A better approach combines information of transport and scavenging. However, since the scavenging depends on the aqueous concentrations from the layers above, and the upward transport on the mixing ratios from the layers below, this issue can only be solved iteratively. In the combination of the submodels SCAV and CVTRANS a first order iteration is applied (see Section 6.2.5). First the transport is calculated to the top level of rain production, then the scavenging scheme is applied, and subsequently, the second part of the transport calculation is performed. For a direct coupling of both processes, the transport being a direct source or sink for each species, the whole column must be treated at once for the aqueous phase chemistry, but this becomes computationally very expensive.

The studies of Section 6.3 do not represent a real atmosphere since the chemical production and loss of the species are neglected. These species are idealised, but have the characteristics, e.g., the solubility, of the real compounds. Both, the different precipitation distributions and the different convective transport affect the mixing ratios and wet deposition of the idealised compounds. For species with low solubility the different transport is of highest importance. For species of high solubility the occurence of precipitation determines the wet deposition patterns, while the strength of the rain events is of secondary relevance. The species of medium solubility are both affected by the differences in transport and the precipitation both strength and spatial distribution.
In contrast to the studies of Doherty et al. (2005), in which the influence of convective transport on ozone and its precursors is investigated by either applying convective transport or not, the studies of Section 6.3 investigate the differences arising from the transport using different convection parameterisation schemes, and are therefore not comparable. The low importance of the ice scavenging as discussed by Salzmann (2005) and mentioned above for the HNO_3-like species is confirmed in this study.
The transport and scavenging of soluble and insoluble compounds in a convective cloud is investigated by Mari et al. (2000). They confirm the importance of the scavenging of H_2O_2 in the liquid phase. The scavenging of SO_2 is highly dependent on the pH, due to the dependance of the oxidation rate on the aqueous H^+ concentration. A direct comparison

is not possible, since in contrast to Section 6.3 Mari et al. (2000) apply comprehensive chemistry and the effect of single clouds, while in Figure 6.5 a long term average profile of three species is shown. However, qualitatively the decrease of the mixing ratios by the clouds, partly assigned to impaction and partly to nucleation scavenging are even higher for HCHO than in their study. For an insoluble tracer like CO and O_3 the transport into the upper troposphere results in a well mixed state throughout the troposphere if no chemical sinks are taken into account. In contrast, the mixing ratios of HNO_3 are almost completely depleted in the middle and upper troposhere, as analysed in the studies of Section 6.3 and of Mari et al. (2000).

In studies using comprehensive gas phase chemistry, but an alternative scavenging mechanism, the real state of the atmosphere is simulated. The results shown in Figures 6.25 and 6.26 are consistent with the conclusions of Barth et al. (2002), that ozone is approximately reduced by 6% in the cloud capped boundary layer if cloud chemsitry is taken into account. In the SCAV_EASY simulation with only a rough description of aqueous phase chemistry, the O_3 mixing ratios are about 5% higher. Even though the simulations setups are very different (global and cloud resolving model), the results of Barth et al. (2002) are generally confirmed. The pH dependence of ozone depletion by liquid phase chemistry cannot be confirmed in detail. This would require a detailed analysis of data with a very high temporal resolution to investigate the short-term fluctuations in the ozone production dependent on variations of the cloud pH, which are not available from the simulations of this thesis. Globally, the O_3 surface mixing ratios are less decreased by the comprehensive aqueous phase chemistry than in Barth et al. (2002), but the latter simulations only cover a 20° by 20° region around Hawaii, and are therefore not representative for the whole globe. Nevertheless, the global influence of the aqueous phase chemistry on ozone is within the same range.
Compared with the results of Liang and Jacob (1997), the effect of using a comprehensive cloud and precipitation chemistry is stronger in the simulations of Section 6.4.2. Even though both simulations, SCAV_COM and SCAV_SCM include a basic liquid phase chemistry, the differences of the simulated annual average surface mixing ratios are larger than in the results of Liang and Jacob (1997). They support their results by three-dimensional calculations for North America, where the differences between the two simulations (SCAV_COM and SCAV_EASY) of the present is study are largest. While in the model results of Liang and Jacob (1997) the summer maximum is located around 100°W with a secondary maximum in California, the highest mixing ratios of the SCAV_COM simulation are at the American west coast. In the SCAV_SCM simulation a second maximum occurs in summer at about 100°W, but the mixing ratio is a few nmol/mol lower than in California. Overall, the amplitude of the seasonal cycle is larger, but in all seasons higher ozone mixing ratios are calculated compared to the study of Liang and Jacob (1997). However, as Barth et al. (2001) stated, the cloud properties are only crudely parameterised in the work of Liang and Jacob (1997). This affects the cloud chemistry because of the dependence of the transfer reaction speed on the droplet properties. In contrast, the aqueous phase chemistry mechanism is even more comprehensive than in the SCAV_COM simulation, though all the major reactions are similar.
The results of Lelieveld and Crutzen (1991) show a higher dependence of O_3 on cloud chemistry. Since they compare results without cloud chemistry with the effects of clouds and liquid phase chemistry, a comparison with the differences between the simulations of this section (SCAV_COM, SCAV_SCM, and SCAV_EASY) is difficult because the different

scavenging schemes both take the effects of clouds and simplified cloud and precipitation chemistry into account. The findings of Lelieveld and Crutzen (1991) can be compared better to the differences of SCAV_COM to the SCAV_EASY simulation, even though this simulation considers an effective sink of HNO_3 and N_2O_5. Therefore the effect of clouds on the tropospheric chemistry appears to be much stronger in the work of Lelieveld and Crutzen (1991) than indicated in the results of this thesis. Similar to the studies mentioned above, the cloud properties are only roughly parameterised and the studies are performed with box models and varying cloud properties from a global cloud data set. This is hardly comparable with the results of a consistent global atmospheric chemistry general circulation model. Consequently, the global influence of liquid phase chemistry on O_3 is concluded to be smaller than proposed by Lelieveld and Crutzen (1991), but has more importance than described by Liang and Jacob (1997), especially under specific conditions on a local to regional scale.
The results of the effect on ozone are comparable with the study of Matthijsen et al. (1997) who find reductions of O_3 induced by cloud chemistry effects of about 5% overall, but locally in the boundary layer these can reach almost 20%. In their model studies, the aqueous phase chemistry contains also reactions with Cu^+ and Fe^{2+}, which are not considered in the SCAV_COM reaction set. Overall, they find higher influence of the cloud and precipitation chemistry than Liang and Jacob (1997), comparable to the findings in this Section. Additionally, they mention cloud pH values over Europe, ranging from 3 to 6, again comparable to the results of Section 6.4.2.2.2. However, the results of Matthijsen et al. (1997) are also obtained with a regional model.
The studies of Liu et al. (1997) analyse the effect of individual clouds and precipitation events and also the effect of cloud processing of air masses by passing through a series of clouds and precipitations events. Since the latter process represents better the real atmospheric conditions, their results are comparable with the findings of the present section. It is shown that in the vertical profiles of H_2O_2 the precipitation removal is substantial in both daytime and in nighttime conditions by a single cloud. The scavenging of hydrogen peroxide is taken into account in all three simulations SCAV_COM, SCAV_SCM and SCAV_EASY. Since hydrogen peroxide is highly soluble, its depletion by scavenging is comparable with the results for HNO_3. In Section 6.3.2.1 an almost complete depletion in the middle troposphere has been analysed for this compound. The influence of detailed cloud chemistry on the differences in hydrogen peroxide surface mixing ratios is still substantial as analysed from Figure 6.28. For ozone Liu et al. (1997) conclude that one single cloud event is almost negligible due to its low solubility, but a series of clouds (precipitating and non-precipitating), comparable with real atmospheric conditions in which air undergoes several times the processing by clouds, can have a significant (not directly quantified) impact on O_3 mixing ratios. This is comparable to the result from the ozone mixing ratio analysis of Section 6.4.2.2.3.

Vertical profiles from several measurement campaigns, compiled by Emmons et al. (2000), are compared with the model results of Section 6.4.2. The individual observed profiles are averaged for each measurement campaign (temporally) and region (spatially). Since, there is only one year of simulation, but the measurement campaigns have been performed in various years, no point-to-point comparison can be performed. However, the average vertical profiles for one region of the measurements are compared with average profiles for the model results in the same region. Since many compounds are highly variable, the standard deviation of both observations and model are taken into account while determin-

ing the correlation and normalised standard deviation as well as for the bias (variability weighted statistical analysis).

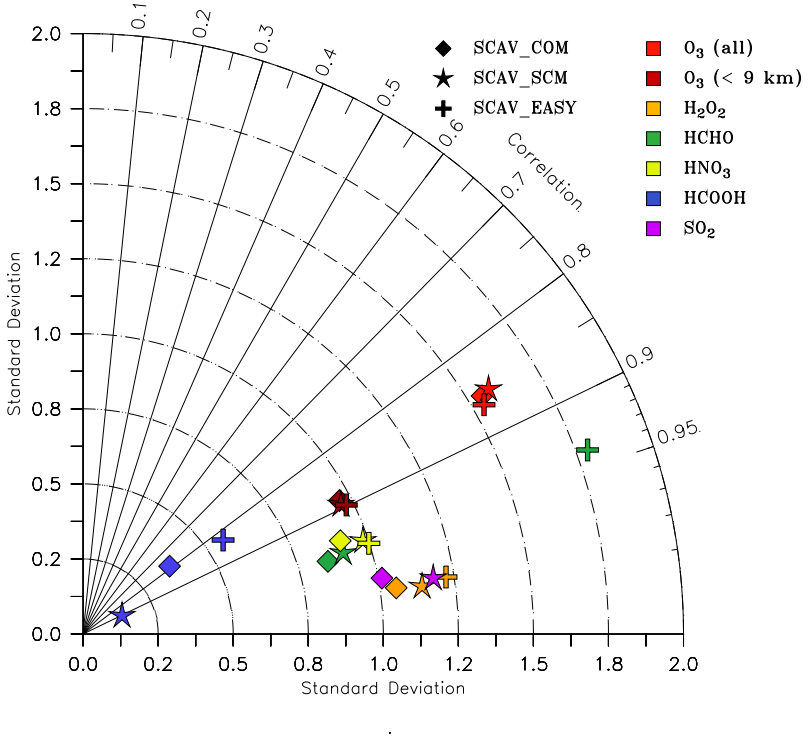

Figure 6.32: Taylor diagram for O_3, HNO_3 and HCHO of the Emmons et al. (2000)-database correlated to the individual SCAV simulations.

Table 6.5: Bias in units of geometric average standard deviation of both model and observations for the individual species in the three simulations.

Species	SCAV_COM	SCAV_SCM	SCAV_EASY
O_3	0.25	0.30	0.38
O_3 below 9 km	0.10	0.15	0.25
H_2O_2	-0.01	0.03	0.16
HCHO	0.13	0.21	0.29
HNO_3	-0.22	-0.22	0.41
HCOOH	-0.37	-4.59	-0.04
SO_2	-1.18	-1.01	1.81

The correlation and normalised standard deviation for all three simulations are displayed in Figure 6.32 for total O_3, O_3 below 9 km, HNO_3, HCHO, HCOOH, and SO_2 in a Taylor diagram for the three simulations of Section 6.4.2. These are marked with the different symbols, while the individual species are marked with different colors. In addition to the correlation and the standard deviation, the bias is listed in Table 6.5. These three quantities provide a general view of the model performance.
For O_3 the calculations are performed for all values (red) and the values below 9 km (dark red), separately. While the values including measurements up to 12 km altitude show a

correlation above 0.85, but a normalised standard deviation of more than 1.5 for all three simulations, the data considering values from the lower and middle troposphere only are correlated more strongly (almost 0.9) with the normalised σ of almost 1. From the horizontal patterns and the amplitude of the temporal and spatial variability there is hardly any difference between SCAV_COM, SCAV_SCM and SCAV_EASY. However, the more comprehensive liquid phase chemistry in the model the smaller is the bias. This shows that for a good representation of tropospheric ozone in the model system the aqueous phase chemistry is a requirement.
The comparison of the H_2O_2 (orange) observations with the model results yield a very high correlation (> 0.99). The normalised standard deviation decreases from around 1.2 for the SCAV_EASY simulation to 1.05 for SCAV_COM. Additionally, there is almost no bias for the SCAV_COM model setup, while in SCAV_EASY a substantial overestimation occurs.
The HCHO (green) mixing ratios are captured well by the model in the SCAV_COM and SCAV_SCM simulation (correlation around 0.95 and normalised σ around 0.9). In the SCAV_EASY simulation the amplitude of the variability in time and space is much higher (> 1.8). The bias is lowest in the SCAV_COM simulation compared to SCAV_SCM and SCAV_EASY.
The gaseous nitric acid (yellow) is simulated best in the SCAV_EASY simulation with respect to correlation and normalised standard deviation, but SCAV_SCM is almost identical and the SCAV_COM simulation only slightly worse (all correlated higher than 0.93 and σ between 0.9 and 1.0). The bias is identical in SCAV_COM and SCAV_SCM, both slightly underestimating the atmospheric mixing ratios. The bias of SCAV_EASY is higher and shows an overestimation of HNO_3.
The model performance for formic acid HCOOH (blue) is less satisfying in all three simulations. Even though the correlation is higher than 0.8 in all cases, the spatial and temporal variability is substantially underestimated. However, the SCAV_EASY simulation performs best with a σ around 0.6, while for SCAV_COM it is only around 0.35 and for SCAV_SCM even only 0.1. The bias is worst for SCAV_SCM, while in SCAV_COM it is much smaller and even smaller in SCAV_EASY. Even though formic acid wet deposition is only very weak in the SCAV_EASY simulation (compare Figure 6.21), the gas phase mixing ratio seems to be captured best in this setup. This is expected to result from compensating errors in the complex chemical system. An additional reason for the high bias in the simulations taking aqueous phase chemistry into account might be the underestimation of the direct HCOOH emissions.
The last analysed compound is SO_2. Since the normalised σ for SCAV_EASY is about 6, it is not displayed in Figure 6.32. The correlation is also worse for this simulation compared to the very high values of R (> 0.99) in both simulations taking the liquid phase oxidation into account. The amplitutde of the variability in time and space is captured better in SCAV_COM and SCAV_SCM, with improved performance for SCAV_COM. The bias is relatively high compared to the other compounds. Both SCAV_COM and SCAV_SCM underestimate the gas phase mixing ratios, while SCAV_EASY overestimates it.

As shown in Section 6.4.2.2.1, the representation of the wet deposition fluxes of the three major compounds (NO_3^-, NH_x and SO_4^{2-}) is very similar in both SCAV_COM and SCAV_SCM, with a slightly better correlation in SCAV_SCM, but a better representation of the amplitude of the spatial variation in SCAV_COM. The results of SCAV_EASY are much worse with respect to the total amount and the amplitude of the spatial variation.

The robustness of the results of Section 6.4.2 is supported by the application of the SCAV_SCM scheme in the long-term coupled chemistry climate simulation EVAL (Jöckel et al., 2006) and the analysis in Section 6.4.1.

With respect to both wet deposition and gas phase mixing ratios, the SCAV_COM simulation using comprehensive aqueous phase chemistry is overall rated as best simulation in representing the observed values. For long-term chemistry simulations, the computationally cheaper SCAV_SCM setup might be sufficient, while the SCAV_EASY scavenging mechanism might be acceptable only if the impact of the tropospheric chemistry is less important for the results of a particular study. However, since it is not computationally cheaper, at least on the architecture used in this thesis work, its application is not recommended. A possible improvement for the SCAV_EASY scheme would be the application of 'effective Henry coefficients', which include the dissociation of species in the liquid phase. However, this also induces errors, since the effective dissociation is dependent on the pH - value of the solution, determined by the concentrations of the dissolved acidic species. In a previous version of the SCAV_EASY mechanism, constant (estimated) scavenging coefficients have been applied for individual species, but this resulted in even worse agreement with the observations. Potentially, parameterised scavenging coefficients for trace gases, as proposed by Asman (1995), are useful to determine the sink process by wet deposition, but are less appropriate to investigate the influence of cloud and precipitation chemistry on the trace gas budgets of the atmosphere.

Chapter 7

Conclusions

The results of Section 3 show that replacing the convection parameterisation in a global chemistry climate model is possible without major consequences for the atmospheric global vertically averaged temperature over the given simulation period of 6 years, even though the precipitation patterns are highly dependent on the selected convection scheme. While generally the zonal and the main features of the longitudinal precipitation distribution, as derived from observations, are reproduced by all convection schemes considered, some parameterisations yield better results than the others. The "best performing" convection scheme of this study is that of the ECMWF (IFS cycle 29r1b) (Tompkins et al., 2004) with both shallow convection closures (traditional and Grant and Brown (1999)), because it compares most closely with the GPCP observational dataset.
On the other hand, the water vapour column values are slightly overestimated with the ECMWF convection scheme, whereas the best agreement with observational data from GOME/SSMI is obtained with the Tiedtke-Nordeng (Tiedtke, 1989; Nordeng, 1994) convection scheme. However, the results of most of the other schemes show only small differences, that are consistent, e.g., the Bechtold et al. (2001) scheme which produces more precipitation in the tropics, shows lower water vapour columns in these regions.
The evaporation patterns are similar in all simulations with the different convection parameterisations; however, the absolute values differ substantially.
The effects of the modified hydrological cycle result in changes in the 3-D temperature fields. For the surface temperature the replacement of the convection scheme results in global changes that are of the order of the observed temperature increase over the last century, with locally substantially larger differences. No "tuning" of the model energy budget has been applied for the individual simulation setups, since the main focus of this study was to test the robustness of the simulated hydrological cycle and meteorology against changes in the convection parameterisation.

The changes in convective transport caused by the alternative convection parameterisations do not greatly alter the overall distribution of trace compounds, as analysed with ^{222}Rn, even though the calculated convective mass fluxes show significant differences. However, although the vertical profiles of radon compared with observations differ substantially, they are within the range of the observed high variability.

A high dependence of the convective cloud top height on the selected convection parameterisation is determined in Chapter 5. The resulting lightning distribution shows large differences among the individual simulations. An acceptable agreement of the simulated

flash frequency distributions with observations has been achieved, even though with none of the convection parameterisations the observations and model results are highly correlated; the best performance with respect to the simulated flash frequency is obtained with the ECMWF scheme. In all case studies, the overall flash frequency has to be rescaled as in most models (i.e., "tuned"), depending on resolution and the selected convection parameterisation.

A new comprehensive submodel (SCAV) for scavenging and cloud and precipitation chemistry of aerosols and trace gases has been developed (Tost et al., 2006). Compared to previous approaches the new scheme is physically more consistent, thus a subject to a larger number of feedbacks, and accounts for a larger number of multiphase processes. Its application under idealised conditions shows general agreement with other model studies. The influence of atmospheric convection parameterisations on scavenging and wet deposition is determined by the varying precipitation distribution and its intensity, and the variable strength of the convective transport. The differences in the wet deposition between the individual simulations are substantial for both highly and moderately soluble compounds, while species with a low solubility are less affected. The vertical redistribution in regions where convection plays a dominant role is more variable for species of low and medium solubility, while for highly soluble compounds the average vertical profiles are very similar. If these species are emitted at the surface, they hardly reach the upper troposphere, but are efficiently removed by nucleation and impaction scavenging in the lower and middle troposphere.
Under realistic conditions, acceptable agreement with observations of wet deposition is achieved in a comprehensive simulation over several years (Section 6.4.1). The analysis of the model results for several regions of the globe, comparing with data from the respective measurement networks, yields a much better representation of the wet deposition fluxes in the dense observation network of the USA, while e.g., in Europe only the main characteristics of the deposition patterns are captured.
Based on this analysis the SCAV submodel has been improved. Three different simulations with various complexity of the scavenging and liquid phase chemistry have been performed and analysed: SCAV_COM includes comprehensive aqueous phase chemistry, SCAV_SCM reduced (minimum) liquid phase chemistry, and SCAV_EASY simulates scavenging based on Henry's law, only. The wet deposition patterns of these three simulations are analysed as well as the effect on gas phase species. The simulated wet deposition with SCAV_SCM and SCAV_COM of the main acidic and alkaline compounds nitrate, NH_x, and sulphate is very similar. In both simulations a better representation of, both, the correlation and the spatial variability has been achieved compared to the simulation of Section 6.4.1. A distinction between better performance with respect to the wet deposition is hardly possible for the SCAV_COM and SCAV_SCM simulation for the compounds for which observations are available. The SCAV_EASY simulates much reduced wet deposition due to neglecting the acid-base-reactions in the liquid phase; for dissociating compounds of medium solubility (NH_3 and HCOOH) it fails completely. Therefore, it is not recommended for future studies.
The differences resulting from the different scavenging mechanisms lead to a modified chemical composition of the atmosphere, including the oxidation capacity of the atmosphere by altered H_2O_2 and consequently OH mixing ratios. Therefore, differences in the gas phase constituents have been analysed. For ozone the SCAV_COM simulation with the comprehensive aqueous phase chemistry results in generally lower ozone mixing ratios.

However, this effect is globally smaller than expected from a previous study (Lelieveld and Crutzen, 1991), but larger than proposed in another (Liang and Jacob, 1997).
A comparison with observed vertical profiles shows a good agreement for several compounds. For most of the species the bias is lowest in the simulation with the SCAV_COM mechanism. Likewise, the correlation is highest and the normalised standard deviation is close to 1. This indicates that a detailed description of the liquid phase chemistry is relevant for the trace gas budgets of the troposphere. This also includes the UTLS region, in which the chemical composition is affected through both convective transport and scavenging. Due to the interaction with the stratosphere, a detailed description of the aqueous phase chemistry is therefore important for the chemical trace gas budget of the entire atmosphere. The SCAV_SCM has proven applicable in a long-term chemical simulation, and, since the differences to the SCAV_COM simulation are mainly within a few %, it can be applied in future studies, in which the main focus is on other aspects of atmospheric chemistry. However, the SCAV_EASY scheme results mostly in higher deviations from the observed gas phase mixing ratios, in addition to weaknesses with respect to wet deposition as mentioned above.
The simulation of the wet deposition of the atmospheric aerosol is compared with other state-of-the-art models, and an acceptable agreement has been obtained. Even though in previous studies with simplified parameterisations of scavenging and aqueous phase chemistry the simulated trace gas budgets have been in 'acceptable' agreement with observations, comparisons with measurement data have been based on a limited number of compounds. The present scheme accounts for a much larger range of compounds and processes, so that model tuning becomes redundant, thus establishing a much improved framework for prognostic studies.

Outlook

The convection scheme intercomparison can be improved by applying identical input parameters to all convection schemes at the same time. This would eliminate the differences in the dynamics which originate from the different convection parameterisations. However, only one of the schemes of such a simulation can couple back to the model dynamics. From this approach also an ensemble calculation of convection from different parameterisations can be achieved.
The description of the convective transport as a plume ensemble, as proposed by Lawrence and Rasch (2005), for all convection parameterisations might be better suited to simulate the effect of convection on the mixing ratios of trace gases in the convective clouds and the outflow regions.
A direct effect of the individual convection schemes on chemical trace species can be revealed only in a simulation series with comprehensive gas and aqueous phase chemistry. In contrast to the idealised studies, these results can be compared with observations to determine the "best performing" convection scheme with respect to trace gas distributions.
The additional implementation of the scavenging and uptake of trace species on snow and ice crystals is a desirable future development, improvement and completion of the scavenging submodel, as developed in this thesis work.
The process of aerosol nucleation scavenging will be improved in future, when the aerosol is not diagnostically removed by the clouds, but prognostically considered in the condensation process by determining the number of cloud condensation nuclei (e.g., Lohmann

et al., 1999). The amount of cloud condensation nuclei removed from the atmosphere can be calculated from the precipitation formation process. However, even though theoretically such an approach is possible, given an accurate description of the atmospheric aerosol, its application in a coupled chemistry climate model will likely result in significant changes in the cloud and consequently precipitation distributions.
The aqueous phase chemistry mechanism will be further developed, including transition metal chemistry, which might be of importance for liquid phase oxidation processes (Deguillaume et al., 2004). Furthermore, simulations with comprehensive multiphase chemistry in the atmospheric aerosol (Kerkweg, 2005), as well as in cloud and precipitation (this thesis work) will reveal the overall impact of, both, the aerosol and cloud chemistry on the atmospheric trace gas budgets.

Even though the meteorological and chemical conditions are rather complex by themselves, the atmospheric sciences should not be treated as an isolated field of science. The future of modelling is likely to move towards comprehensive Earth System Models (ESM), which comprise not only the atmosphere, but other subsystems of the Earth, e.g., the ocean, vegetation and land cover, and the cryosphere. Especially the interaction with the biosphere will gain importance in the field of atmospheric sciences, since it is known that atmosphere-surface interactions, affected by the terrestrial and marine biota, strongly influence meteorological and chemical conditions, and vice versa. Additionally, the impact of mankind on the atmospheric climate system will be subject to a growing interest, as well as the effects of climate change on mankind due to health effects of atmospheric pollution, acid deposition and socio-economic aspects.

Appendix A

Description of the statistical methods

The statistics that are applied in this thesis are mostly standard. For completeness they are shortly presented in this section, based on basic text books of statistical analysis (e.g., Wilks, 2005). Additionally, it is referred to the article of Taylor (2001).
The used quantities are:

- The mean value $\overline{f}$:
  It is defined by the sum of all values f_n, divided by the number of valid points N:

$$\overline{f} = \frac{1}{N} \sum_{n=1}^{N} f_n. \tag{A.1}$$

- The bias $\overline{E}$:
  It is defined by the difference of the mean values of the simulation $\overline{f}$ and the reference $\overline{r}$.

$$\overline{E} = \overline{f} - \overline{r}. \tag{A.2}$$

- The root mean square RMS E:
  It is defined by the square-rooted sum of the squared differences of the values of the simulation f_n and the reference r_n:

$$E = \sqrt{\frac{1}{N} \sum_{n=1}^{N} (f_n - r_n)^2}. \tag{A.3}$$

  This quantity can be resolved into two components: the bias $\overline{E}$ and the centered RMSE E', defined as follows:

$$E' = \sqrt{\frac{1}{N} \sum_{n=1}^{N} [(f_n - \overline{f}) - (r_n - \overline{r})])^2}. \tag{A.4}$$

  These two components add quadratically to yield E:

$$E^2 = \overline{E}^2 + E'^2. \tag{A.5}$$

  In this work, always E' is used, when the RMSE is mentioned.

- The linear regression ($Y = m \cdot x + b$) with m as the slope and b the intercept with the Y-axis. These two parameters are calculated by:

$$m = \frac{\sum_{n=1}^{N} f_n r_n - N\overline{f}\overline{r}}{\sum_{n=1}^{N} r_n^2 - N\overline{r}^2} \tag{A.6}$$

$$b = \overline{f} - m\overline{r} \tag{A.7}$$

Additionally, the Taylor diagrams (Taylor, 2001) are applied using the geometrical relationship between the correlation R, the RMSE E' and the standard deviations σ_f and σ_r, that are defined by:

$$\sigma_f = \sqrt{\frac{1}{N}\sum_{n=1}^{N}(f_n - \overline{f})^2} \tag{A.8}$$

The correlation R (in the tables usually R^2 is used) is defined by:

$$R = \frac{\frac{1}{N}\sum_{n=1}^{N}(f_n - \overline{f})(r_n - \overline{r})}{\sigma_f \sigma_r} \tag{A.9}$$

The relationship

$$E'^2 = \sigma_f^2 + \sigma_r^2 - 2\sigma_f\sigma_r R \tag{A.10}$$

and the law of cosine result in a geometric relationship between the four quantities of Equation A.10. It is common to use the standard deviation of the observations to normalise the standard deviation of the model calculations. Therefore the standard deviation in a Taylor diagram is ideally around 1 resulting in a more limited range on the radius axis. A typical Taylor diagram is shown in Figure A.1. The distance from the origin determines

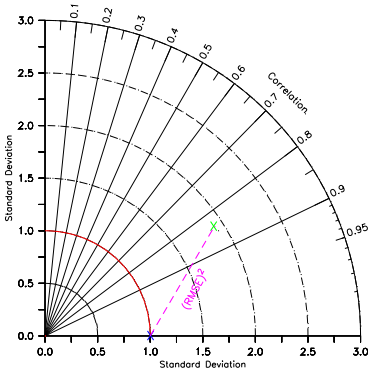

Figure A.1: Taylor Diagram, showing the correlation and normalised standard deviation of two datasets.

the normalised standard deviation. Therefore the perfect match would be on the circle with radius 1 (red line). The angle depicts the correlation. A perfect match between the two datasets would be the blue cross, indicating the normalized standard deviation of 1 and the correlation of 1. The distance of a point from this point results in the RMSE E'^2 as a consequence of Equation A.10 in the units of standard deviation.

Appendix B

Abbreviations and variable definitions

Table B.1: Acronyms and abbreviations

Acronym	**Description**
AMIP	Atmospheric Model Intercomparison Project
B1	Convection simulation with the Bechtold convection scheme without cloud ice
B2	Convection simulation with the Bechtold convection scheme including cloud ice
CAPE	convective available potential energy
CCM	chemistry climate model
CCM3	version 3 of the community climate model
CONVECT	convection submodel of MESSy
CRM	Cloud Resolving Model
CTM	Chemistry Transport Model
CVTRANS	convective tracer transport submodel of MESSy
C_T1	simulation applying the T1 convection scheme with tracer transport and scavenging
C_EC	simulation applying the EC2 convection scheme with tracer transport and scavenging
C_ZH	simulation applying the ZH convection scheme with tracer transport and scavenging
C_ZHW	simulation applying the ZHW convection scheme with tracer transport and scavenging
C_B2	simulation applying the B2 convection scheme with tracer transport and scavenging
DLR	Deutsches Zentrum für Luft- und Raumfahrt
EC	Convection simulation with the ECMWF convection scheme with the operational shallow convection closure
EC2	Convection simulation with the ECMWF convection scheme with the classical shallow convection closure
ERA40	40 year dataset of meteorological reanalysis
GCM	General Circulation Model
GPCP	Global Precipitation Climatology Project
ECHAM5	climate model
ECMWF	European Center for Medium-range Weather Forecast
IFS	Integrated Forecast System at ECMWF

Table B.1: Acronyms and abbreviations

Acronym	**Description**
ITCZ	Inner Tropical Convergence Zone
KPP	Kinetic PreProcessor
LCL	Lifting condensation level
LFC	Level of free convection
CTL	Cloud Top Layer
LNOX	NO_x emissions produced by lightning and the respective MESSy submodel
M7	aerosol microphysics submodel
MA-ECHAM5	middle atmosphere version of the ECHAM5 model
MATCH	Model of Atmospheric Transport and Chemistry
MESSy	Modular Earth Submodel System
MPI-C	Max-Planck-Institute for Chemistry, Mainz, Germany
MPI-MET	Max-Planck-Institute for Meteorology, Hamburg, Germany
NMHC	Non-Methane HydroCarbons
NWP	numerical weather prediction
SCAV	scavenging submodel of MESSy
SCAV_COM	scavenging simulation with comprehensive aqueous phase chemistry
SCAV_EASY	scavenging simulation with Henry's law equilibrium
SCAV_SCM	scavenging simulation with minimum aqueous phase chemistry
SCM	single Column Model
SPCZ	South Pacific Convergence Zone
SST	Sea Surface Temperature
T1	Convection simulation with the Tiedtke (Nordeng) convection scheme, the reference simulation
T2	Convection simulation with the Tiedtke (original) convection scheme
T3	Convection simulation with the Tiedtke (hybrid) convection scheme
ZH	Convection simulation with the Zhang-McFarlane-Hack convection scheme
ZHW	Convection simulation with the Zhang-McFarlane-Hack convection scheme with enhanced evaporation

Table B.2: Variables and units

Variable	**Description**	**Unit**
b	buoyancy	$m/(s^2\ K^2)$
c	concentration of a chemical species	$molecules/cm^3_{air}$
c_u	condensation of water vapour in the updraft	1/s
CAPE	convective available potential energy	J/kg
D_d	detrainment into the downdraft	$kg/(m^2\ s)$
D_g	gas diffusion coefficient in air	m^2/s
D_p	particle diffusion	m^2/s
D_u	detrainment into the updraft	$kg/(m^2\ s)$
e_d	evaporation of detrained water	1/s
e_l	evaporation of cloud water	1/s
e_p	evaporation of precipitation water	1/s
E	impaction scavenging efficiency	1/s
E_d	entrainment into the downdraft	$kg/(m^2\ s)$
E_u	entrainment into the updraft	$kg/(m^2\ s)$

Table B.2: Variables and units

Variable	**Description**	**Unit**
f_{Slinn}	Slinn correction factor for sedimentation velocity	1
f_{Cun}	Cunningham slip flow correction factor	1
ff_{obs}	observed global flash frequency	1/s
ff_{model}	modelled global flash frequency	1/s
$F(\lambda)$	spectral actinic flux	W/(m^2 s)
F_{drydep}	dry deposition flux	molecules/(m^2 s)
F_{rain}	precipitation flux	kg/(m^2 s)
$F^a(\lambda)$	spectral actinic flux for a purely absorbing atmosphere	W/(m^2 s)
g	gravitational acceleration	m/s^2
G_p	precipitation formation	kg_{water}/kg_{air}
G(X)	relaxation coefficient for quantity X	1/s
h	moist static energy	J/kg
H_x	inverse dimensionless Henry coeeficient	1
J_x	photolysis rate coefficient for species X	1/s
$J_{i,x}$	photolysis rate coefficient for species X in the spectral interval i	1/s
$J^a_{i,x}$	photolysis rate coefficient for species X in the spectral interval i for a purely absorbing atmosphere	1/s
k_{mt}	phase transfer rate	1/s
$k_{exf:f}$	forward phase transfer reaction rate	1/s
$k_{exf:b}$	backward phase transfer reaction rate	1/s
L	latent heat of condenstation	J/kg
LWC	liquid water content	kg_{water}/kg_{air}
M_u	updraft mass flux	kg/(m^2 s)
M_d	downdraft mass flux	kg/(m^2 s)
M(X)	mixing ratio for species X	kg/kg
M_u(X)	updraft mixing ratio for species X	kg/kg
$M_u d$(X)	updraft detraining mixing ratio for species X	kg/kg
p	pressure	Pa
p_0	reference pressure	Pa
p_e	fraction of entrained air that is detrained in the same level	1
q	specific humidity	kg_{water}/kg_{air}
q_u	specific humidity in the updraft	kg_{water}/kg_{air}
q_d	specific humidity in the downdraft	kg_{water}/kg_{air}
Q_r	radiation tendency on the budget of the dry static energy	J/(kg s)
r	radius of a particle or droplet	m
r_c^u	updraft cloud water	kg_{water}/kg_{air}
r_c^u	updraft cloud ice	kg_{water}/kg_{air}
R	gas constant for dry air	J/(mol K)
R_{aero}	aerodynamic resistance	s/m
R_{surf}	surface resistance	s/m
R_{qbr}	resistance of a quais-laminar boundary layer	s/m
R_r	precipitation formation rate for Zhang convection	kg/(m^2 s)
R_0	updraft radius	m
Re	Reynolds number	1
RH	relative humidity	1
RF	rescaling Factor for flash frequencies	1
s	dry static energy	J/kg
s_d	dry static energy in the downdraft	J/kg
s_u	dry static energy in the updraft	J/kg
St	Stokes number	1

Table B.2: Variables and units

Variable	**Description**	**Unit**
Sc	Schmidt number	1
t	time	s
T	temperature	K
T_v	virtual temperature	K
v	wind vector	m/s
$\bar{v}$	mean molecular diffusion velocity from Boltzmann distribution	m/s
v_t	terminal sedimentation velocity	m/s
v_{tr}	transition velocity	m/s
v_{Stokes}	Stokes velocity	m/s
v_d	dry deposition velocity	m/s
w	vertical velocity of air	m/s
z	altitude	m
z_d	downdraft top height	m
β	overshoot parameter from Hack convection	1
δ_i	ratio of the actinic fluxes for a purely absorbing to the real atmosphere	1
η	dynamic viscosity	kg /(m s)
λ_w	wavelength	m
λ_d	fractional entrainment rate for Zhang convection	1
λ	mean free path of air	m
ν	kinematic viscosity	m^2/s
ρ	air density	kg/m^3
ρ_{aero}	aerosol density	kg/m^3
σ_x	absorption cross section of species X	m^2
σ_{cv}	fractional convective cloud cover	1
σ	standard deviation of a variable	as the corresponding variable
τ	convective adjustment time	s
Δr_r	rain formation	kg_{water}/kg_{air}
Δr_s	snow formation	kg_{water}/kg_{air}
Λ_B	aerosol nucleation scavenging efficiency	1/s
$\Phi_x(\lambda)$	quantum yield of species X at wavelength λ	1
Θ	potential temperature	K

Appendix C

SCAV Reaction Tables

Table C.1: Heterogeneous reactions

#	labels	reaction	rate coefficient
H1000f	Sc	$O_2 \rightarrow O_2(aq)$	`k_exf(KPP_O2)`
H1000b	Sc	$O_2(aq) \rightarrow O_2$	`k_exb(KPP_O2)`
H1001f	ScScm	$O_3 \rightarrow O_3(aq)$	`k_exf(KPP_O3)`
H1001b	ScScm	$O_3(aq) \rightarrow O_3$	`k_exb(KPP_O3)`
H2100f	Sc	$OH \rightarrow OH(aq)$	`k_exf(KPP_OH)`
H2100b	Sc	$OH(aq) \rightarrow OH$	`k_exb(KPP_OH)`
H2101f	Sc	$HO_2 \rightarrow HO_2(aq)$	`k_exf(KPP_HO2)`
H2101b	Sc	$HO_2(aq) \rightarrow HO_2$	`k_exb(KPP_HO2)`
H2102f	ScScm	$H_2O_2 \rightarrow H_2O_2(aq)$	`k_exf(KPP_H2O2)`
H2102b	ScScm	$H_2O_2(aq) \rightarrow H_2O_2$	`k_exb(KPP_H2O2)`
H3100f	Sc	$NO \rightarrow NO(aq)$	`k_exf(KPP_NO)`
H3100b	Sc	$NO(aq) \rightarrow NO$	`k_exb(KPP_NO)`
H3101f	Sc	$NO_2 \rightarrow NO_2(aq)$	`k_exf(KPP_NO2)`
H3101b	Sc	$NO_2(aq) \rightarrow NO_2$	`k_exb(KPP_NO2)`
H3102f	Sc	$NO_3 \rightarrow NO_3(aq)$	`k_exf(KPP_NO3)`
H3102b	Sc	$NO_3(aq) \rightarrow NO_3$	`k_exb(KPP_NO3)`
H3200f	ScScm	$NH_3 \rightarrow NH_3(aq)$	`k_exf(KPP_NH3)`
H3200b	ScScm	$NH_3(aq) \rightarrow NH_3$	`k_exb(KPP_NH3)`
H3201	ScScm	$N_2O_5 \rightarrow HNO_3(aq) + HNO_3(aq)$	`k_exf_N2O5 * C(KPP_H2O_l)`
H3202f	Sc	$HONO \rightarrow HONO(aq)$	`k_exf(KPP_HONO)`
H3202b	Sc	$HONO(aq) \rightarrow HONO$	`k_exb(KPP_HONO)`
H3203f	ScScm	$HNO_3 \rightarrow HNO_3(aq)$	`k_exf(KPP_HNO3)`
H3203b	ScScm	$HNO_3(aq) \rightarrow HNO_3$	`k_exb(KPP_HNO3)`
H3204f	Sc	$HNO_4 \rightarrow HNO_4(aq)$	`k_exf(KPP_HNO4)`
H3204b	Sc	$HNO_4(aq) \rightarrow HNO_4$	`k_exb(KPP_HNO4)`
H4100f	ScScm	$CO_2 \rightarrow CO_2(aq)$	`k_exf(KPP_CO2)`
H4100b	ScScm	$CO_2(aq) \rightarrow CO_2$	`k_exb(KPP_CO2)`
H4101f	ScScm	$HCHO \rightarrow HCHO(aq)$	`k_exf(KPP_HCHO)`
H4101b	ScScm	$HCHO(aq) \rightarrow HCHO$	`k_exb(KPP_HCHO)`
H4102f	Sc	$CH_3O_2 \rightarrow CH_3OO(aq)$	`k_exf(KPP_CH3O2)`
H4102b	Sc	$CH_3OO(aq) \rightarrow CH_3O_2$	`k_exb(KPP_CH3O2)`
H4103f	ScScm	$HCOOH \rightarrow HCOOH(aq)$	`k_exf(KPP_HCOOH)`
H4103b	ScScm	$HCOOH(aq) \rightarrow HCOOH$	`k_exb(KPP_HCOOH)`
H4104f	ScScm	$CH_3OOH \rightarrow CH_3OOH(aq)$	`k_exf(KPP_CH3OOH)`
H4104b	ScScm	$CH_3OOH(aq) \rightarrow CH_3OOH$	`k_exb(KPP_CH3OOH)`
H4105f	Sc	$CH_3OH \rightarrow CH_3OH(aq)$	`k_exf(KPP_CH3OH)`

Table C.1: Heterogeneous reactions

#	labels	reaction	rate coefficient
H4105b	Sc	$CH_3OH(aq) \rightarrow CH_3OH$	`k_exb(KPP_CH3OH)`
H4200f	ScScm	$CH_3COOH \rightarrow CH_3COOH(aq)$	`k_exf(KPP_CH3COOH)`
H4200b	ScScm	$CH_3COOH(aq) \rightarrow CH_3COOH$	`k_exb(KPP_CH3COOH)`
H4201f	Sc	$CH_3CHO \rightarrow CH_3CHO(aq)$	`k_exf(KPP_CH3CHO)`
H4201b	Sc	$CH_3CHO(aq) \rightarrow CH_3CHO$	`k_exb(KPP_CH3CHO)`
H4202f	Sc	$PAN \rightarrow PAN(aq)$	`k_exf(KPP_PAN)`
H4202b	Sc	$PAN(aq) \rightarrow PAN$	`k_exb(KPP_PAN)`
H4300f	Sc	$CH_3COCH_3 \rightarrow CH_3COCH_3(aq)$	`k_exf(KPP_CH3COCH3)`
H4300f	Sc	$CH_3COCH_3(aq) \rightarrow CH_3COCH_3$	`k_exb(KPP_CH3COCH3)`
H6000f	Sc	$Cl_2 \rightarrow Cl_2(aq)$	`k_exf(KPP_Cl2)`
H6000b	Sc	$Cl_2(aq) \rightarrow Cl_2$	`k_exb(KPP_Cl2)`
H6200f	ScScm	$HCl \rightarrow HCl(aq)$	`k_exf(KPP_HCl)`
H6200b	ScScm	$HCl(aq) \rightarrow HCl$	`k_exb(KPP_HCl)`
H6201f	Sc	$HOCl \rightarrow HOCl(aq)$	`k_exf(KPP_HOCl)`
H6201b	Sc	$HOCl(aq) \rightarrow HOCl$	`k_exb(KPP_HOCl)`
H7000f	Sc	$Br_2 \rightarrow Br_2(aq)$	`k_exf(KPP_Br2)`
H7000b	Sc	$Br_2(aq) \rightarrow Br_2$	`k_exb(KPP_Br2)`
H7200f	ScScm	$HBr \rightarrow HBr(aq)$	`k_exf(KPP_HBr)`
H7200b	ScScm	$HBr(aq) \rightarrow HBr$	`k_exb(KPP_HBr)`
H7201f	Sc	$HOBr \rightarrow HOBr(aq)$	`k_exf(KPP_HOBr)`
H7201b	Sc	$HOBr(aq) \rightarrow HOBr$	`k_exb(KPP_HOBr)`
H7600f	Sc	$BrCl \rightarrow BrCl(aq)$	`k_exf(KPP_BrCl)`
H7600b	Sc	$BrCl(aq) \rightarrow BrCl$	`k_exb(KPP_BrCl)`
H9100f	ScScm	$SO_2 \rightarrow SO_2(aq)$	`k_exf(KPP_SO2)`
H9100b	ScScm	$SO_2(aq) \rightarrow SO_2$	`k_exb(KPP_SO2)`
H9200	ScScm	$H_2SO_4 \rightarrow H_2SO_4(aq)$	`k_exf(KPP_H2SO4)`

Notes:
The forward (`k_exf`) and backward (`k_exb`) rate coefficients are calculated in the file `messy_scav_base.f90` using the accommodation coefficients (Table C.3) and Henry's law coefficients (Table C.2) as described in Section 6.2.1.

Table C.2: Henry's Law Coefficients

Species	$K_0[M/atm]$	$-\Delta_{sol}H/R[K]$	Reference
HNO_3	$1.7 \cdot 10^5$	8694	Lelieveld and Crutzen (1991)
H_2O_2	$1.0 \cdot 10^5$	6338	Lind and Kok (1994)
CH_3OOH	$3.0 \cdot 10^2$	5322	Lind and Kok (1994)
HCHO	$7.0 \cdot 10^3$	6425	Chameides (1984)
HCOOH	$3.7 \cdot 10^3$	5700	Lelieveld and Crutzen (1991)
CH_3COOH	$5.5 \cdot 10^3$	5894	Khan et al. (1995)
O_3	$1.2 \cdot 10^{-2}$	2560	Chameides (1984)
SO_2	1.2	3120	Chameides (1984)
H_2SO_4	$1.0 \cdot 10^{11}$	-	
N_2O_5	1.4	-	Ervens et al. (2003)
PAN	5.0	-	Holdren et al. (1984)
OH	$3.0 \cdot 10^1$	4300	Hanson et al. (1992)
HONO	$4.9 \cdot 10^1$	4780	Chameides (1984)
CO_2	$3.1 \cdot 10^{-2}$	2423	Chameides (1984)
NH_3	58.0	4085	Chameides (1984)
HO_2	$3.9 \cdot 10^3$	5900	Hanson et al. (1992)
NO_3	2.0	2000	Thomas et al. (1993)

Table C.2: Henry's Law Coefficients

Species	$K_0[M/atm]$	$-\Delta_{sol}H/R[K]$	Reference
NO_2	$6.4 \cdot 10^{-3}$	2500	Lee and Schwartz (1981), for temperature dependence Chameides (1984)
HNO_4	$1.2 \cdot 10^{4}$	6900	Régimbal and Mozurkewich (1997)
CH_3OH	$2.20 \cdot 10^{2}$	5390	Snider and Dawson (1985)
CH_3CHO	$1.14 \cdot 10^{1}$	6254	Betterton and Hoffmann (1988a)
CH_3O_2	6.0	5600	Lelieveld and Crutzen (1991)
$C_2H_5O_2$	6.0	87	Ervens et al. (2003)
NO	$1.9 \cdot 10^{-3}$	1480	Schwartz and White (1981)
CH_3COCH_3	$3.52 \cdot 10^{1}$	3800	Zhou and Mopper (1990)
HCl	1.2	9001	Brimblecombe and Clegg (1989)
HBr	1.3	10239	Brimblecombe and Clegg (1989)
HOCl	$6.7 \cdot 10^{2}$	5862	Huthwelker et al. (1995)
HOBr	$9.3 \cdot 10^{1}$	5862	Vogt et al. (1996)
BrCl	$9.4 \cdot 10^{-1}$	5600	Bartlett and Margerum (1999)
Cl_2	$9.1 \cdot 10^{-2}$	2500	Wilhelm et al. (1977)
Br_2	$7.6 \cdot 10^{-1}$	4094	Dean (1992)
DMSO	$5.0 \cdot 10^{4}$	6425	De Bruyn et al. (1994)
O_2	$1.3 \cdot 10^{-3}$	1500	Lide and Frederikse (1995)

Table C.3: Accommodation Coefficients

Species	α^0	$-\Delta_{sol}H/R[K]$	Reference
HNO_3	0.5	-	Abbatt and Waschewsky (1998)
H_2O_2	0.077	2769	Worsnop et al. (1989)
CH_3OOH	$4.5 \cdot 10^{-3}$	3273	Magi et al. (1997)
HCHO	0.043	-	DeMore et al. (1997)
HCOOH	0.014	3978	DeMore et al. (1997)
CH_3COOH	$1.9 \cdot 10^{-2}$	5894	
O_3	$2.0 \cdot 10^{-3}$	-	DeMore et al. (1997)
SO_2	0.11	-	DeMore et al. (1997)
H_2SO_4	0.65	-	Pöschl et al. (1998)
N_2O_5	0.1	-	DeMore et al. (1997)
PAN	0.1	-	estimated
OH	$1.0 \cdot 10^{-2}$	-	Takami et al. (1998)
HONO	$4.0 \cdot 10^{-2}$	-	DeMore et al. (1997)
CO_2	0.01	2000	estimated
NH_3	$6.0 \cdot 10^{-2}$	-	DeMore et al. (1997)
HO_2	0.2	-	DeMore et al. (1997)
NO_3	$4.0 \cdot 10^{-2}$	-	Rudich et al. (1996)
NO_2	$1.5 \cdot 10^{-3}$	-	Ponche et al. (1993)
HNO_4	0.1	-	DeMore et al. (1997)
CH_3OH	0.1	-	estimated
CH_3CHO	0.03	-	estimated, Ervens et al. (2003)
CH_3O_2	0.01	2000	estimated
$C_2H_5O_2$	$8.2 \cdot 10^{-3}$	-	estimated, Ervens et al. (2003)
NO	0.1	-	estimated
CH_3COCH_3	$1.9 \cdot 10^{-2}$	-	Ervens et al. (2003)
HCl	0.074	3072	Schweitzer et al. (2000)
HBr	0.031	3940	Schweitzer et al. (2000)
HOCl	0.5	-	estimated
HOBr	0.5	-	estimated

Table C.3: Accommodation Coefficients

Species	α^0	$-\Delta_{sol}H/R[K]$	Reference
BrCl	0.033	-	estimated
Cl_2	0.038	6546	Hu et al. (1995)
Br_2	0.038	6546	Hu et al. (1995)
DMSO	0.048	2578	De Bruyn et al. (1994)
O_2	0.01	2000	estimated

Table C.4: Acid-base and other eqilibria

#	labels	reaction	$K_0[M^{m-n}]$	$-\Delta H/R[K]$
EQ20	Sc	$HO_2 \rightleftharpoons O_2^- + H^+$	1.6E-5	
EQ21	ScScm	$H_2O \rightleftharpoons H^+ + OH^-$	1.0E-16	-6716
EQ30	ScScm	$NH_4^+ \rightleftharpoons H^+ + NH_3$	5.88E-10	-2391
EQ31	Sc	$HONO \rightleftharpoons H^+ + NO_2^-$	5.1E-4	-1260
EQ32	ScScm	$HNO_3 \rightleftharpoons H^+ + NO_3^-$	15	8700
EQ33	Sc	$HNO_4 \rightleftharpoons NO_4^- + H^+$	1.E-5	
EQ40	ScScm	$CO_2 \rightleftharpoons H^+ + HCO_3^-$	4.3E-7	-913
EQ41	ScScm	$HCOOH \rightleftharpoons H^+ + HCOO^-$	1.8E-4	
EQ42	ScScm	$CH_3COOH \rightleftharpoons H^+ + CH_3COO^-$	1.75E-5	-46
EQ61	ScScm	$HCl \rightleftharpoons H^+ + Cl^-$	1.7E6	6896
EQ62	Sc	$HOCl \rightleftharpoons H^+ + ClO^-$	3.2E-8	
EQ71	ScScm	$HBr \rightleftharpoons H^+ + Br^-$	1.0E9	
EQ72	Sc	$HOBr \rightleftharpoons H^+ + BrO^-$	2.3E-9	-3091
EQ90	ScScm	$SO_2 \rightleftharpoons H^+ + HSO_3^-$	1.7E-2	2090
EQ91	ScScm	$HSO_3^- \rightleftharpoons H^+ + SO_3^{2-}$	6.0E-8	1120
EQ92	ScScm	$HSO_4^- \rightleftharpoons H^+ + SO_4^{2-}$	1.2E-2	2720
EQ93	ScScm	$H_2SO_4 \rightleftharpoons H^+ + HSO_4^-$	1.0E3	

Notes:

EQ20 Weinstein-Lloyd and Schwartz (1991)
EQ21 Chameides (1984)
EQ30 Chameides (1984)
EQ31 Schwartz and White (1981)
EQ32 Davis and de Bruin (1964)
EQ33 Warneck (1999)
EQ40 Chameides (1984)
EQ41 Weast (1980)
EQ42 see note
EQ61 Marsh and McElroy (1985)
EQ62 Lax (1969)
EQ71 Lax (1969)
EQ72 Kelley and Tartar (1956)
EQ90 Chameides (1984)
EQ91 Chameides (1984)
EQ92 Seinfeld and Pandis (1998)
EQ93 Seinfeld and Pandis (1998)

Table C.5: Aqueous phase reactions

#	labels	reaction	$k_0\ [M^{1-n}s^{-1}]$	$-E_a/R[K]$
A1000	Sc	$O_3 + O_2^- \rightarrow OH + OH^-$	1.5E9	
A2100	Sc	$OH + O_2^- \rightarrow OH^-$	1.0E10	
A2101	Sc	$OH + OH \rightarrow H_2O_2$	5.5E9	
A2102	Sc	$HO_2 + O_2^- \rightarrow H_2O_2 + OH^-$	1.0E8	-900
A2103	Sc	$HO_2 + OH \rightarrow H_2O$	7.1E9	
A2104	Sc	$HO_2 + HO_2 \rightarrow H_2O_2$	9.7E5	-2500
A2105	Sc	$H_2O_2 + OH \rightarrow HO_2$	2.7E7	-1684
A3100	Sc	$NO_2^- + O_3 \rightarrow NO_3^-$	5.0E5	-6950
A3101	Sc	$NO_2 + NO_2 \rightarrow HNO_3 + HONO$	1.0E8	

Table C.5: Aqueous phase reactions (...continued)

#	labels	reaction	k_0 $[M^{1-n}s^{-1}]$	$-E_a/R[K]$
A3102	Sc	$NO_4^- \rightarrow NO_2^-$	8.0E1	
A3200	Sc	$NO_2 + HO_2 \rightarrow HNO_4$	1.8E9	
A3201	Sc	$NO_2^- + OH \rightarrow NO_2 + OH^-$	1.0E10	
A3202	Sc	$NO_3 + OH^- \rightarrow NO_3^- + OH$	8.2E7	-2700
A3203	Sc	$HONO + OH \rightarrow NO_2$	1.0E10	
A3204	Sc	$HONO + H_2O_2 \rightarrow HNO_3$	4.6E3	-6800
A4100	Sc	$CO_3^- + O_2^- \rightarrow HCO_3^- + OH^-$	6.5E8	
A4101	Sc	$CO_3^- + H_2O_2 \rightarrow HCO_3^- + HO_2$	4.3E5	
A4102	Sc	$HCOO^- + CO_3^- \rightarrow 2\ HCO_3^- + HO_2$	1.5E5	
A4103	Sc	$HCOO^- + OH \rightarrow OH^- + HO_2 + CO_2$	3.1E9	-1240
A4104	Sc	$HCO_3^- + OH \rightarrow CO_3^-$	8.5E6	
A4105	Sc	$HCHO + OH \rightarrow HCOOH + HO_2$	7.7E8	-1020
A4106	Sc	$HCOOH + OH \rightarrow HO_2 + CO_2$	1.1E8	-991
A4107	Sc	$CH_3OO + O_2^- \rightarrow CH_3OOH + OH^-$	5.0E7	
A4108	Sc	$CH_3OO + HO_2 \rightarrow CH_3OOH$	4.3E5	
A4109	Sc	$CH_3OH + OH \rightarrow HCHO + HO_2$	9.7E8	
A4110a	Sc	$CH_3OOH + OH \rightarrow CH_3OO$	2.7E7	-1715
A4110b	Sc	$CH_3OOH + OH \rightarrow HCHO + OH$	1.1E7	-1715
A9100	Sc	$SO_3^- + O_2 \rightarrow SO_5^-$	1.5E9	
A9101	ScScm	$SO_3^{2-} + O_3 \rightarrow SO_4^{2-}$	1.5E9	-5300
A9102	Sc	$SO_4^- + O_2^- \rightarrow SO_4^{2-}$	3.5E9	
A9103	Sc	$SO_4^- + SO_3^{2-} \rightarrow SO_3^- + SO_4^{2-}$	4.6E8	
A9104	Sc	$SO_5^- + O_2^- \rightarrow HSO_5^- + OH^-$	2.3E8	
A9200	Sc	$SO_3^{2-} + OH \rightarrow SO_3^- + OH^-$	5.5E9	
A9201	Sc	$SO_4^- + OH \rightarrow HSO_5^-$	1.0E9	
A9202	Sc	$SO_4^- + HO_2 \rightarrow SO_4^{2-} + H^+$	3.5E9	
A9203	Sc	$SO_4^- + H_2O \rightarrow SO_4^{2-} + H^+ + OH$	1.1E1	-1110
A9204	Sc	$SO_4^- + H_2O_2 \rightarrow SO_4^{2-} + H^+ + HO_2$	1.2E7	
A9205	Sc	$HSO_3^- + O_2^- \rightarrow SO_4^{2-} + OH$	3.0E3	
A9206	ScScm	$HSO_3^- + O_3 \rightarrow SO_4^{2-} + H^+$	3.7E5	-5500
A9207	Sc	$HSO_3^- + OH \rightarrow SO_3^-$	4.5E9	
A9208	Sc	$HSO_3^- + HO_2 \rightarrow SO_4^{2-} + OH + H^+$	3.0E3	
A9209	ScScm	$HSO_3^- + H_2O_2 \rightarrow SO_4^{2-} + H^+$	5.2E6	-3650
A9210	Sc	$HSO_3^- + SO_4^- \rightarrow SO_3^- + SO_4^{2-} + H^+$	8.0E8	
A9212	Sc	$HSO_3^- + HSO_5^- \rightarrow 2\ SO_4^{2-} + 2\ H^+$	7.1E6	
A9300	Sc	$SO_3^{2-} + NO_2 \rightarrow SO_4^{2-} + 2\ HONO - NO_2$	2.0E7	
A9301	Sc	$SO_4^- + NO_3^- \rightarrow SO_4^{2-} + NO_3$	5.0E4	
A9302	Sc	$SO_4^{2-} + NO_3 \rightarrow NO_3^- + SO_4^-$	1.0E5	
A9303	Sc	$HSO_3^- + NO_2 \rightarrow HSO_4^- + 2\ HONO - NO_2$	2.0E7	
A9304	Sc	$HSO_3^- + NO_3 \rightarrow SO_3^- + NO_3^- + H^+$	1.4E9	-2000
A9305	Sc	$HSO_3^- + HNO_4 \rightarrow HSO_4^- + NO_3^- + H^+$	3.1E5	
A9400	Sc	$SO_3^{2-} + HCHO \rightarrow CH_2OHSO_3^- + OH^-$	1.4E4	
A9401	Sc	$SO_3^{2-} + CH_3OOH \rightarrow SO_4^{2-} + CH_3OH$	1.6E7	-3800
A9402	Sc	$HSO_3^- + HCHO \rightarrow CH_2OHSO_3^-$	4.3E-1	
A9403	Sc	$HSO_3^- + CH_3OOH \rightarrow SO_4^{2-} + H^+ + CH_3OH$	1.6E7	-3800
A9404	Sc	$CH_2OHSO_3^- + OH^- \rightarrow SO_3^{2-} + HCHO$	3.6E3	

Notes:

A1000: Sehested et al. (1983)
A2100: Sehested et al. (1968)
A2101: Buxton et al. (1988)
A2102: Christensen and Sehested (1988)
A2103: Sehested et al. (1968)
A2104: Christensen and Sehested (1988)
A2105: Christensen et al. (1982)
A3100: Damschen and Martin (1983)
A3101: Lee and Schwartz (1981)
A3102: Warneck (1999)
A3200: Warneck (1999)
A3201: Wingenter et al. (1999)
A3202: Exner et al. (1992)
A3203: Barker et al. (1970)
A3204: Damschen and Martin (1983)
A4100: Ross et al. (1992)
A4101: Ross et al. (1992)
A4102: Ross et al. (1992)
A4103: Chin and Wine (1994)
A4104: Ross et al. (1992)
A4105: Chin and Wine (1994)
A4106: Chin and Wine (1994)
A4107: Jacob (1986)
A4108: Jacob (1986)
A4109: Buxton et al. (1988)
A4110a,b: Jacob (1986)
A9100: Huie and Neta (1987)
A9101: Hoffmann (1986)
A9102: Jiang et al. (1992)
A9103: Huie and Neta (1987)
A9104: Buxton et al. (1996)
A9200: Buxton et al. (1988)
A9201: Jiang et al. (1992)
A9202: Jiang et al. (1992)
A9203: Herrmann et al. (1995)
A9204: Wine et al. (1989)
A9205: D. Sedlak, pers. comm. (1993)
A9206: Hoffmann (1986)
A9207: Buxton et al. (1988)
A9208: D. Sedlak, pers. comm. (1993)
A9209: Martin and Damschen (1981)
A9210: Huie and Neta (1987)
A9212: Betterton and Hoffmann (1988b)
A9300: Clifton et al. (1988)
A9301: Exner et al. (1992)
A9302: Logager et al. (1993)
A9303: Clifton et al. (1988)
A9304: Exner et al. (1992)
A9305: Warneck (1999)
A9400: Boyce and Hoffmann (1984)
A9401: Lind et al. (1987)
A9402: Boyce and Hoffmann (1984)
A9403: Lind et al. (1987)
A9404: Seinfeld and Pandis (1998)

Table C.6: Photolysis reactions

#	labels	reaction	rate coefficient
PH2100	Sc	$H_2O_2 + h\nu \rightarrow 2\ OH$	`JX(ip_H2O2) * 2.33`

Notes: J-values are calculated with an external module and then supplied to the SCAV chemistry

Appendix D

MECCA Reaction Tables

Table D.1: Gas phase reactions

#	reaction	rate coefficient
G1000	$O_2 + O(^1D) \rightarrow O(^3P) + O_2$	3.2E-11*EXP(70./temp)
G1001	$O_2 + O(^3P) \rightarrow O_3$	6.E-34*((temp/300.)**(-2.4))*cair
G1002	$O_3 + O(^1D) \rightarrow 2\ O_2$	1.2E-10
G1003	$O_3 + O(^3P) \rightarrow 2\ O_2$	8.E-12*EXP(-2060./temp)
G01Diag	$O_3(s) \rightarrow LO_3(s)$	k_O3s
G2100	$H + O_2 \rightarrow HO_2$	k_3rd(temp,cair,5.7E-32,1.6,7.5E-11,0.,0.6)
G2101	$H + O_3 \rightarrow OH$	1.4E-10*EXP(-470./temp)
G2102	$H_2 + O(^1D) \rightarrow H + OH$	1.1E-10
G2103	$OH + O(^3P) \rightarrow H$	2.2E-11*EXP(120./temp)
G2104	$OH + O_3 \rightarrow HO_2$	1.7E-12*EXP(-940./temp)
G2105	$OH + H_2 \rightarrow H_2O + H$	5.5E-12*EXP(-2000./temp)
G2106	$HO_2 + O(^3P) \rightarrow OH$	3.E-11*EXP(200./temp)
G2107	$HO_2 + O_3 \rightarrow OH$	1.E-14*EXP(-490./temp)
G2108a	$HO_2 + H \rightarrow 2\ OH$	0.69*8.1E-11
G2108b	$HO_2 + H \rightarrow H_2$	0.29*8.1E-11
G2108c	$HO_2 + H \rightarrow O(^3P) + H_2O$	0.02*8.1E-11
G2109	$HO_2 + OH \rightarrow H_2O$	4.8E-11*EXP(250./temp)
G2110	$HO_2 + HO_2 \rightarrow H_2O_2$	k_HO2_HO2
G2111	$H_2O + O(^1D) \rightarrow 2\ OH$	2.2E-10
G2112	$H_2O_2 + OH \rightarrow H_2O + HO_2$	2.9E-12*EXP(-160./temp)
G3100	$N + O_2 \rightarrow NO + O(^3P)$	1.5E-11*EXP(-3600./temp)
G3101	$N_2 + O(^1D) \rightarrow O(^3P) + N_2$	1.8E-11*EXP(110./temp)
G3102a	$N_2O + O(^1D) \rightarrow 2\ NO$	6.7E-11
G3102b	$N_2O + O(^1D) \rightarrow N_2 + O_2$	4.9E-11
G3103	$NO + O_3 \rightarrow NO_2 + O_2$	3.E-12*EXP(-1500./temp)
G3104	$NO + N \rightarrow O(^3P) + N_2$	2.1E-11*EXP(100./temp)
G3105	$NO_2 + O(^3P) \rightarrow NO + O_2$	5.6E-12*EXP(180./temp)
G3106	$NO_2 + O_3 \rightarrow NO_3 + O_2$	1.2E-13*EXP(-2450./temp)
G3107	$NO_2 + N \rightarrow N_2O + O(^3P)$	5.8E-12*EXP(220./temp)
G3108	$NO_3 + NO \rightarrow 2\ NO_2$	1.5E-11*EXP(170./temp)
G3109	$NO_3 + NO_2 \rightarrow N_2O_5$	k_NO3_NO2
G3110	$N_2O_5 \rightarrow NO_2 + NO_3$	k_NO3_NO2/(3.E-27*EXP(10990./temp))

Table D.1: Gas phase reactions (... continued)

#	reaction	rate coefficient
G3200	NO + OH → HONO	k_3rd(temp,cair,7.E-31,2.6, 3.6E-11,0.1,0.6)
G3201	NO + HO_2 → NO_2 + OH	3.5E-12*EXP(250./temp)
G3202	NO_2 + OH → HNO_3	k_3rd(temp,cair,2.E-30,3., 2.5E-11,0.,0.6)
G3203	NO_2 + HO_2 → HNO_4	k_NO2_HO2
G3204	NO_3 + HO_2 → NO_2 + OH + O_2	3.5E-12
G3205	HONO + OH → NO_2 + H_2O	1.8E-11*EXP(-390./temp)
G3206	HNO_3 + OH → H_2O + NO_3	k_HNO3_OH
G3207	HNO_4 → NO_2 + HO_2	k_NO2_HO2/(2.1E-27*EXP(10900./ temp))
G3208	HNO_4 + OH → NO_2 + H_2O	1.3E-12*EXP(380./temp)
G4100	CH_4 + $O(^1D)$ → .75 CH_3O_2 + .75 OH + .25 HCHO + .4 H + .05 H_2	1.5E-10
G4101	CH_4 + OH → CH_3O_2 + H_2O	1.85E-20*EXP(2.82*log(temp) -987./temp)
G4102	CH_3OH + OH → HCHO + HO_2	7.3E-12*EXP(-620./temp)
G4103a	CH_3O_2 + HO_2 → CH_3OOH	4.1E-13*EXP(750./temp) /(1.+1./497.7*EXP(1160./temp))
G4103b	CH_3O_2 + HO_2 → HCHO + H_2O + O_2	4.1E-13*EXP(750./temp) /(1.+497.7*EXP(-1160./temp))
G4104	CH_3O_2 + NO → HCHO + NO_2 + HO_2	2.8E-12*EXP(300./temp)
G4105	CH_3O_2 + NO_3 → HCHO + HO_2 + NO_2	1.3E-12
G4106a	CH_3O_2 + CH_3O_2 → 2 HCHO + 2 HO_2	9.5E-14*EXP(390./temp) /(1.+1./26.2*EXP(1130./temp))
G4106b	CH_3O_2 + CH_3O_2 → HCHO + CH_3OH	9.5E-14*EXP(390./temp) /(1.+26.2*EXP(-1130./temp))
G4107	CH_3OOH + OH → .7 CH_3O_2 + .3 HCHO + .3 OH + H_2O	k_CH3OOH_OH
G4108	HCHO + OH → CO + H_2O + HO_2	9.52E-18*EXP(2.03*log(temp) +636./temp)
G4109	HCHO + NO_3 → HNO_3 + CO + HO_2	3.4E-13*EXP(-1900./temp)
G4110	CO + OH → H + CO_2	1.57E-13 + cair*3.54E-33
G4111	HCOOH + OH → HO_2	4.E-13
G4200	C_2H_6 + OH → $C_2H_5O_2$ + H_2O	1.49E-17*temp*temp*EXP(-499./ temp)
G4201	C_2H_4 + O_3 → HCHO + .22 HO_2 + .12 OH + .23 CO + .54 HCOOH + .1 H_2	1.2E-14*EXP(-2630./temp)
G4202	C_2H_4 + OH → .6666667 $CH_3CH(O_2)CH_2OH$	k_3rd(temp,cair,1.E-28,0.8, 8.8E-12,0.,0.6)
G4203	$C_2H_5O_2$ + HO_2 → C_2H_5OOH	7.5E-13*EXP(700./temp)
G4204	$C_2H_5O_2$ + NO → CH_3CHO + HO_2 + NO_2	2.6E-12*EXP(365./temp)
G4205	$C_2H_5O_2$ + NO_3 → CH_3CHO + HO_2 + NO_2	2.3E-12
G4206	$C_2H_5O_2$ + CH_3O_2 → .75 HCHO + HO_2 + .75 CH_3CHO + .25 CH_3OH	1.6E-13*EXP(195./temp)
G4207	C_2H_5OOH + OH → .3 $C_2H_5O_2$ + .7 CH_3CHO + .7 OH	k_CH3OOH_OH
G4208	CH_3CHO + OH → $CH_3C(O)OO$ + H_2O	5.6E-12*EXP(270./temp)
G4209	CH_3CHO + NO_3 → $CH_3C(O)OO$ + HNO_3	1.4E-12*EXP(-1900./temp)
G4210	CH_3COOH + OH → CH_3O_2	4.E-13*EXP(200./temp)

Table D.1: Gas phase reactions (... continued)

#	reaction	rate coefficient
G4211a	$CH_3C(O)OO + HO_2 \rightarrow CH_3C(O)OOH$	4.3E-13*EXP(1040./temp) /(1.+1./37.*EXP(660./temp))
G4211b	$CH_3C(O)OO + HO_2 \rightarrow CH_3COOH + O_3$	4.3E-13*EXP(1040./temp) /(1.+37.*EXP(-660./temp))
G4212	$CH_3C(O)OO + NO \rightarrow CH_3O_2 + NO_2$	8.1E-12*EXP(270./temp)
G4213	$CH_3C(O)OO + NO_2 \rightarrow PAN$	k_PA_NO2
G4214	$CH_3C(O)OO + NO_3 \rightarrow CH_3O_2 + NO_2$	4.E-12
G4215a	$CH_3C(O)OO + CH_3O_2 \rightarrow HCHO + HO_2 + CH_3O_2 + CO_2$	0.9*2.E-12*EXP(500./temp)
G4215b	$CH_3C(O)OO + CH_3O_2 \rightarrow CH_3COOH + HCHO + CO_2$	0.1*2.E-12*EXP(500./temp)
G4216	$CH_3C(O)OO + C_2H_5O_2 \rightarrow .82\ CH_3O_2 + CH_3CHO + .82\ HO_2 + .18\ CH_3COOH$	4.9E-12*EXP(211./temp)
G4217	$CH_3C(O)OO + CH_3C(O)OO \rightarrow 2\ CH_3O_2 + 2\ CO_2 + O_2$	2.5E-12*EXP(500./temp)
G4218	$CH_3C(O)OOH + OH \rightarrow CH_3C(O)OO$	k_CH3OOH_OH
G4219	$NACA + OH \rightarrow NO_2 + HCHO + CO$	5.6E-12*EXP(270./temp)
G4220	$PAN + OH \rightarrow HCHO + NO_2$	2.E-14
G4221	$PAN \rightarrow CH_3C(O)OO + NO_2$	k_PAN_M
G4300	$C_3H_8 + OH \rightarrow .82\ C_3H_7O_2 + .18\ C_2H_5O_2 + H_2O$	1.65E-17*temp*temp*EXP(-87./temp)
G4301	$C_3H_6 + O_3 \rightarrow .57\ HCHO + .47\ CH_3CHO + .33\ OH + .26\ HO_2 + .07\ CH_3O_2 + .06\ C_2H_5O_2 + .23\ CH_3C(O)OO + .04\ CH_3COCHO + .06\ CH_4 + .31\ CO + .22\ HCOOH + .03\ CH_3OH$	6.5E-15*EXP(-1900./temp)
G4302	$C_3H_6 + OH \rightarrow CH_3CH(O_2)CH_2OH$	k_3rd(temp,cair,8.E-27,3.5, 3.E-11,0.,0.5)
G4303	$C_3H_6 + NO_3 \rightarrow ONIT$	4.6E-13*EXP(-1155./temp)
G4304	$C_3H_7O_2 + HO_2 \rightarrow C_3H_7OOH$	k_PrO2_HO2
G4305	$C_3H_7O_2 + NO \rightarrow .96\ CH_3COCH_3 + .96\ HO_2 + .96\ NO_2 + .04\ C_3H_7ONO_2$	k_PrO2_NO
G4306	$C_3H_7O_2 + CH_3O_2 \rightarrow CH_3COCH_3 + .8\ HCHO + .8\ HO_2 + .2\ CH_3OH$	k_PrO2_CH3O2
G4307	$C_3H_7OOH + OH \rightarrow .3\ C_3H_7O_2 + .7\ CH_3COCH_3 + .7\ OH$	k_CH3OOH_OH
G4308	$CH_3CH(O_2)CH_2OH + HO_2 \rightarrow CH_3CH(OOH)CH_2OH$	6.5E-13*EXP(650./temp)
G4309	$CH_3CH(O_2)CH_2OH + NO \rightarrow .98\ CH_3CHO + .98\ HCHO + .98\ HO_2 + .98\ NO_2 + .02\ ONIT$	4.2E-12*EXP(180./temp)
G4310	$CH_3CH(OOH)CH_2OH + OH \rightarrow .5\ CH_3CH(O_2)CH_2OH + .5\ CH_3COCH_2OH + .5\ OH + H_2O$	3.8E-12*EXP(200./temp)
G4311	$CH_3COCH_3 + OH \rightarrow CH_3COCH_2O_2 + H_2O$	1.33E-13+3.82E-11*EXP(-2000./temp)
G4312	$CH_3COCH_2O_2 + HO_2 \rightarrow CH_3COCH_2O_2H$	8.6E-13*EXP(700./temp)
G4313	$CH_3COCH_2O_2 + NO \rightarrow NO_2 + CH_3C(O)OO + HCHO$	2.9E-12*EXP(300./temp)
G4314	$CH_3COCH_2O_2 + CH_3O_2 \rightarrow .5\ CH_3COCHO + .5\ CH_3OH + .3\ CH_3C(O)OO + .8\ HCHO + .3\ HO_2 + .2\ CH_3COCH_2OH$	7.5E-13*EXP(500./temp)

Table D.1: Gas phase reactions (... continued)

#	reaction	rate coefficient
G4315	$CH_3COCH_2O_2H$ + OH → .3 $CH_3COCH_2O_2$ + .7 CH_3COCHO + .7 OH	k_CH3OOH_OH
G4316	CH_3COCH_2OH + OH → CH_3COCHO + HO_2	3.E-12
G4317	CH_3COCHO + OH → $CH_3C(O)OO$ + CO	8.4E-13*EXP(830./temp)
G4318	MPAN + OH → CH_3COCH_2OH + NO_2	3.2E-11
G4319	MPAN → MVKO2 + NO_2	k_PAN_M
G4320	$C_3H_7ONO_2$ + OH → CH_3COCH_3 + NO_2	6.2E-13*EXP(-230./temp)
G4400	C_4H_{10} + OH → $C_4H_9O_2$ + H_2O	1.81E-17*temp*temp*EXP(114./temp)
G4401	$C_4H_9O_2$ + CH_3O_2 → .88 $CH_3COC_2H_5$ + .68 HCHO + 1.23 HO_2 + .12 CH_3CHO + .12 $C_2H_5O_2$ + .18 CH_3OH	k_PrO2_CH3O2
G4402	$C_4H_9O_2$ + HO_2 → C_4H_9OOH	k_PrO2_HO2
G4403	$C_4H_9O_2$ + NO → .84 NO_2 + .56 $CH_3COC_2H_5$ + .56 HO_2 + .28 $C_2H_5O_2$ + .84 CH_3CHO + .16 ONIT	k_PrO2_NO
G4404	C_4H_9OOH + OH → .15 $C_4H_9O_2$ + .85 $CH_3COC_2H_5$ + .85 OH + .85 H_2O	k_CH3OOH_OH
G4405	MVK + O_3 → .45 HCOOH + .9 CH_3COCHO + .1 $CH_3C(O)OO$ + .19 OH + .22 CO + .32 HO_2	.5*(1.36E-15*EXP(-2112./temp) +7.51E-16*EXP(-1521./temp))
G4406	MVK + OH → MVKO2	.5*(4.1E-12*EXP(452./temp) +1.9E-11*EXP(175./temp))
G4407	MVKO2 + HO_2 → MVKOOH	1.82E-13*EXP(1300./temp)
G4408	MVKO2 + NO → NO_2 + .25 $CH_3C(O)OO$ + .25 CH_3COCH_2OH + .75 HCHO + .25 CO + .75 HO_2 + .5 CH_3COCHO	2.54E-12*EXP(360./temp)
G4409	MVKO2 + NO_2 → MPAN	.25*k_3rd(temp,cair,9.7E-29, 5.6,9.3E-12,1.5,0.6)
G4410	MVKO2 + CH_3O_2 → .5 CH_3COCHO + .375 CH_3COCH_2OH + .125 $CH_3C(O)OO$ + 1.125 HCHO + .875 HO_2 + .125 CO + .25 CH_3OH	2.E-12
G4411	MVKO2 + MVKO2 → CH_3COCH_2OH + CH_3COCHO + .5 CO + .5 HCHO + HO_2	2.E-12
G4412	MVKOOH + OH → MVKO2	3.E-11
G4413	$CH_3COC_2H_5$ + OH → MEKO2	1.3E-12*EXP(-25./temp)
G4414	MEKO2 + HO_2 → MEKOOH	k_PrO2_HO2
G4415	MEKO2 + NO → .985 CH_3CHO + .985 $CH_3C(O)OO$ + .985 NO_2 + .015 ONIT	k_PrO2_NO
G4416	MEKOOH + OH → .8 MeCOCO + .8 OH + .2 MEKO2	k_CH3OOH_OH
G4417	ONIT + OH → $CH_3COC_2H_5$ + NO_2 + H_2O	1.7E-12
G4500	ISOP + O_3 → .28 HCOOH + .65 MVK + .1 MVKO2 + .1 $CH_3C(O)OO$ + .14 CO + .58 HCHO + .09 H_2O_2 + .08 CH_3O_2 + .25 OH + .25 HO_2	7.86E-15*EXP(-1913./temp)
G4501	ISOP + OH → ISO2	2.54E-11*EXP(410./temp)
G4502	ISOP + NO_3 → ISON	3.03E-12*EXP(-446./temp)
G4503	ISO2 + HO_2 → ISOOH	2.22E-13*EXP(1300./temp)
G4504	ISO2 + NO → .88 NO_2 + .88 MVK + .88 HCHO + .88 HO_2 + .12 ISON	2.54E-12*EXP(360./temp)

Table D.1: Gas phase reactions (... continued)

#	reaction	rate coefficient
G4505	ISO2 + CH_3O_2 → .5 MVK + 1.25 HCHO + HO_2 + .25 CH_3COCHO + .25 CH_3COCH_2OH + .25 CH_3OH	2.E-12
G4506	ISO2 + ISO2 → 2 MVK + HCHO + HO_2	2.E-12
G4507	ISOOH + OH → MVK + OH	1.E-10
G4508	ISON + OH → CH_3COCH_2OH + NACA	1.3E-11
G6100	Cl + O_3 → ClO	2.3E-11*EXP(-200./temp)
G6101	ClO + O(^{3}P) → Cl	3.E-11*EXP(70./temp)
G6102	ClO + ClO → Cl_2O_2	k_ClO_ClO
G6103	Cl_2O_2 → ClO + ClO	k_ClO_ClO/(1.27E-27*EXP(8744./temp))
G6200	Cl + H_2 → HCl + H	3.7E-11*EXP(-2300./temp)
G6201a	Cl + HO_2 → HCl	1.8E-11*EXP(170./temp)
G6201b	Cl + HO_2 → ClO + OH	4.1E-11*EXP(-450./temp)
G6202	Cl + H_2O_2 → HCl + HO_2	1.1E-11*EXP(-980./temp)
G6203a	ClO + OH → Cl + HO_2	7.4E-12*EXP(270./temp)
G6203b	ClO + OH → HCl	6.E-13*EXP(230./temp)
G6204	ClO + HO_2 → HOCl	2.7E-12*EXP(220./temp)
G6205	HCl + OH → Cl + H_2O	2.6E-12*EXP(-350./temp)
G6206	HOCl+ OH → ClO + H_2O	3.E-12*EXP(-500./temp)
G6300	ClO + NO → NO_2 + Cl	6.4E-12*EXP(290./temp)
G6301	ClO + NO_2 → $ClNO_3$	k_3rd(temp,cair,1.8E-31,3.4,1.5E-11,1.9,0.6)
G6303	$ClNO_3$ + O(^{3}P) → ClO + NO_3	2.9E-12*EXP(-800./temp)
G6304	$ClNO_3$ + Cl → Cl_2 + NO_3	6.5E-12*EXP(135./temp)
G6400	Cl + CH_4 → HCl + CH_3O_2	9.6E-12*EXP(-1360./temp)
G6401	Cl + HCHO → HCl + CO + HO_2	8.1E-11*EXP(-30./temp)
G6402	Cl + CH_3OOH → CH_3O_2 + HCl	5.7E-11
G6403	ClO + CH_3O_2 → HO_2 + Cl + HCHO	3.3E-12*EXP(-115./temp)
G6404	CCl_4 + O(^{1}D) → ClO + 3 Cl	3.3E-10
G6405	CH_3Cl + O(^{1}D) → OH + Cl	1.65E-10
G6406	CH_3Cl + OH → H_2O + Cl	2.4E-12*EXP(-1250./temp)
G6407	CH_3CCl_3 + O(^{1}D) → OH + 3 Cl	3.E-10
G6408	CH_3CCl_3 + OH → H_2O + 3 Cl	1.6E-12*EXP(-1520./temp)
G6500	CF_2Cl_2 + O(^{1}D) → ClO + Cl	1.4E-10
G6501	$CFCl_3$ + O(^{1}D) → ClO + 2 Cl	2.3E-10
G7100	Br + O_3 → BrO	1.7E-11*EXP(-800./temp)
G7101	BrO + O(^{3}P) → Br + O_2	1.9E-11*EXP(230./temp)
G7102a	BrO + BrO → Br + Br	2.4E-12*EXP(40./temp)
G7102b	BrO + BrO → Br_2	2.8E-14*EXP(869./temp)
G7200	Br + HO_2 → HBr	1.5E-11*EXP(-600./temp)
G7201	BrO + HO_2 → HOBr	3.4E-12*EXP(540./temp)
G7202	HBr + OH → Br + H_2O	1.1E-11
G7203	HOBr + O(^{3}P) → OH + BrO	1.2E-10*EXP(-430./temp)
G7301	BrO + NO → Br + NO_2	8.8E-12*EXP(260./temp)
G7302	BrO + NO_2 → $BrNO_3$	k_BrO_NO2
G7400	Br + HCHO → HBr + CO + HO_2	1.7E-11*EXP(-800./temp)
G7403	CH_3Br + OH → H_2O + Br	2.35E-12*EXP(-1300./temp)
G7603a	BrO + ClO → Br + OClO	9.5E-13*EXP(550./temp)
G7603b	BrO + ClO → Br + Cl	2.3E-12*EXP(260./temp)
G7603c	BrO + ClO → BrCl	4.1E-13*EXP(290./temp)

Table D.1: Gas phase reactions (... continued)

#	reaction	rate coefficient
G9200	SO_2 + OH → H_2SO_4 + HO_2	`k_3rd(temp,cair,3.E-31,3.3, 1.5E-12,0.,0.6)`
G9400a	DMS + OH → CH_3SO_2 + HCHO	`1.13E-11*EXP(-253./temp)`
G9400b	DMS + OH → DMSO + HO_2	`k_DMS_OH`
G9401	DMS + NO_3 → CH_3SO_2 + HNO_3 + HCHO	`1.9E-13*EXP(520./temp)`
G9402	DMSO + OH → .6 SO_2 + HCHO + .6 CH_3O_2 + .4 HO_2 + .4 CH_3SO_3H	`1.E-10`
G9403	CH_3SO_2 → SO_2 + CH_3O_2	`1.9E13*EXP(-8661./temp)`
G9404	CH_3SO_2 + O_3 → CH_3SO_3	`3.E-13`
G9405	CH_3SO_3 + HO_2 → CH_3SO_3H	`5.E-11`

Notes:
Rate coefficients for three-body reactions are defined via the function `k_3rd`(T, M, k_0^{300}, n, $k_{\rm inf}^{300}$, m, $f_{\rm c}$). In the code, the temperature T is called `temp` and the concentration of "air molecules" M is called `cair`. Using the auxiliary variables $k_0(T)$, $k_{\rm inf}(T)$, and $k_{\rm ratio}$, `k_3rd` is defined as:

$$k_0(T) = k_0^{300} \times \left(\frac{300\text{K}}{T}\right)^n \quad \text{(D.1)}$$

$$k_{\rm inf}(T) = k_{\rm inf}^{300} \times \left(\frac{300\text{K}}{T}\right)^m \quad \text{(D.2)}$$

$$k_{\rm ratio} = \frac{k_0(T)M}{k_{\rm inf}(T)} \quad \text{(D.3)}$$

$$\texttt{k\_3rd} = \frac{k_0(T)M}{1+k_{\rm ratio}} \times f_{\rm c}^{\left(\frac{1}{1+(\log_{10}(k_{\rm ratio}))^2}\right)} \quad \text{(D.4)}$$

A similar function, called `k_3rd_iupac` here, is used by Atkinson et al. (2005) for three-body reactions. It has the same function parameters as `k_3rd` and it is defined as:

$$k_0(T) = k_0^{300} \times \left(\frac{300\text{K}}{T}\right)^n \quad \text{(D.5)}$$

$$k_{\rm inf}(T) = k_{\rm inf}^{300} \times \left(\frac{300\text{K}}{T}\right)^m \quad \text{(D.6)}$$

$$k_{\rm ratio} = \frac{k_0(T)M}{k_{\rm inf}(T)} \quad \text{(D.7)}$$

$$N = 0.75 - 1.27 \times \log_{10}(f_{\rm c}) \quad \text{(D.8)}$$

$$\texttt{k\_3rd\_iupac} = \frac{k_0(T)M}{1+k_{\rm ratio}} \times f_{\rm c}^{\left(\frac{1}{1+(\log_{10}(k_{\rm ratio})/N)^2}\right)} \quad \text{(D.9)}$$

G1000: Sander et al. (2003)
G1001: Sander et al. (2003)
G1002: Sander et al. (2003), path leading to 2 $O(^3P)$ + O_2 neglected
G1003: Sander et al. (2003)
G01Diag: Roelofs and Lelieveld (1997), `k_O3s = (1.7E-12*EXP(-940./temp))*C(KPP_OH)+(1.E-14*EXP(-490./temp))*C(KPP_HO2)+J_O1D*2.2E-10*C(KPP_H2O)/(3.2E-11*EXP(70./temp)*C(KPP_O2)+1.8E-11*EXP(110./temp)*C(KPP_N2)+2.2E-10*C(KPP_H2O))`
G2100: Sander et al. (2003)
G2101: Sander et al. (2003)
G2102: Sander et al. (2003)
G2103: Sander et al. (2003)
G2104: Sander et al. (2003)
G2105: Sander et al. (2003)
G2106: Sander et al. (2003)
G2107: Sander et al. (2003)
G2108a,b,c: Sander et al. (2003), branching ratio from Hack et al., see note B5 of Sander et al. (2003)
G2109: Sander et al. (2003)
G2110: Christensen et al. (2002), Kircher and Sander (1984), The rate coefficient is: `k_HO2_HO2 = (1.5E-12*EXP(19./temp)+1.7E-33*EXP(1000./temp)*cair)* (1.+1.4E-21*EXP(2200./temp)`

`*C(KPP_H2O)`. The value for the first (pressure-independent) part is from Christensen et al. (2002), the water term from Kircher and Sander (1984)
G2111: Sander et al. (2003)
G2112: Sander et al. (2003)
G3100: Sander et al. (2003)
G3101: Sander et al. (2003)
G3102a: Sander et al. (2003)
G3102b: Sander et al. (2003)
G3103: Sander et al. (2003)
G3104: Sander et al. (2003)
G3105: Sander et al. (2003)
G3106: Sander et al. (2003)
G3107: Sander et al. (2003)
G3108: Sander et al. (2003)
G3109: Sander et al. (2003). The rate coefficient is: `k_NO3_NO2 = k_3rd(temp,cair,2.E-30,4.4,1.4E-12,0.7,0.6)`.
G3110: Sander et al. (2003). The rate coefficient is defined as backward reaction divided by equilibrium constant.
G3200: Sander et al. (2003)
G3201: Sander et al. (2003)
G3202: Sander et al. (2003)
G3203: Sander et al. (2003). The rate coefficient is: `k_NO2_HO2 = k_3rd(temp,cair,1.8E-31,3.2,4.7E-12,1.4,0.6)`.
G3204: Sander et al. (2003)
G3205: Sander et al. (2003)
G3206: Sander et al. (2003). The rate coefficient is: `k_HNO3_OH = 2.4E-14 * EXP(460./temp) + 1./ ( 1./(6.5E-34 * EXP(1335./temp) *cair) + 1./(2.7E-17 * EXP(2199./temp)) )`
G3207: Sander et al. (2003). The rate coefficient is defined as backward reaction divided by equilibrium constant.
G3208: Sander et al. (2003)
G4100: Sander et al. (2003)
G4101: Atkinson (2003)
G4102: Sander et al. (2003)
G4103a,b: Sander et al. (2003), product distribution is from Elrod et al. (2001)
G4104: Sander et al. (2003)
G4105: Atkinson et al. (1999)
G4106a: Sander et al. (2003)
G4106b: Sander et al. (2003)
G4107: Sander et al. (2003). The rate coefficient is: `k_CH3OOH_OH = 3.8E-12*EXP(200./temp)`
G4108: Sivakumaran et al. (2003)
G4109: Sander et al. (2003), same temperature dependence assumed as for $CH_3CHO+NO_3$
G4110: McCabe et al. (2001)
G4111: Sander et al. (2003)
G4200: Atkinson (2003)
G4201: Sander et al. (2003), product distribution is from von Kuhlmann (2001) (see also Neeb et al. (1998))
G4202: Sander et al. (2003)
G4203: Sander et al. (2003)
G4204: Sander et al. (2003)
G4205: Atkinson et al. (1999)
G4206: Rate coefficient calculated by von Kuhlmann (pers. comm. 2004) using self reactions of CH_3OO and C_2H_5OO from Sander et al. (2003) and geometric mean as suggested by Madronich and Calvert (1990) and Kirchner and Stockwell (1996). The product distribution (branching=0.5/0.25/0.25) is calculated by von Kuhlmann (pers. comm. 2004) based on Villenave and Lesclaux (1996) and Tyndall et al. (2001).
G4207: Same value as for **G4107:** $CH_3OOH+OH$ assumed.
G4208: Sander et al. (2003)
G4209: Sander et al. (2003)
G4210: Sander et al. (2003)
G4211a: Tyndall et al. (2001)
G4211b: Tyndall et al. (2001)
G4212: Tyndall et al. (2001)
G4213: Tyndall et al. (2001). The rate coefficient is: `k_PA_NO2 = k_3rd(temp,cair,8.5E-29,6.5,1.1E-11,1.,0.6)`.
G4214: Canosa-Mas et al. (1996)
G4215a: Sander et al. (2003)
G4215b: Sander et al. (2003)
G4216: `1.0E-11` from Atkinson et al. (1999), temperature dependence from Kirchner and Stockwell (1996)
G4217: Tyndall et al. (2001)
G4218: Same value as for **G4107:** $CH_3OOH+OH$ assumed.
G4219: According to Pöschl et al. (2000), the same value as for $CH_3CHO+OH$ can be assumed.
G4220: 50% of the upper limit given by Sander et al. (2003), as suggested by von Kuhlmann (2001)
G4221: Sander et al. (2003). The rate coefficient is: `k_PAN_M = k_PA_NO2/9.E-29*EXP(-14000./temp)`, i.e. the rate coefficient is defined as backward reaction divided by equilibrium constant.
G4300: Atkinson (2003)
G4301: Sander et al. (2003), product distribution is for terminal olefin carbons from Zaveri and Peters (1999)
G4302: Atkinson et al. (1999)
G4303: Atkinson et al. (1999)
G4304: Atkinson (1997). The rate coefficient is: `k_PrO2_HO2 = 1.9E-13*EXP(1300./temp)`. Value for generic RO_2 + HO_2 reaction from Atkinson (1997) is used.
G4305: Atkinson et al. (1999). The rate coefficient is: `k_PrO2_NO = 2.7E-12*EXP(360./temp)`
G4306: Kirchner and Stockwell (1996). The rate coefficient is: `k_PrO2_CH3O2 = 9.46E-14*EXP(431./temp)`. The product distribution is from von Kuhlmann (2001).
G4307: Same value as for **G4107:** $CH_3OOH+OH$ assumed.
G4308: Müller and Brasseur (1995)
G4309: Müller and Brasseur (1995), products are

from von Kuhlmann (2001)
G4310: Müller and Brasseur (1995)
G4311: Sander et al. (2003)
G4312: Tyndall et al. (2001)
G4313: Sander et al. (2003)
G4314: Tyndall et al. (2001)
G4315: Same value as for **G4107:** CH_3OOH+OH assumed.
G4316: Atkinson et al. (1999)
G4317: Tyndall et al. (1995)
G4318: Orlando et al. (2002)
G4319: Same value as for PAN assumed.
G4320: Atkinson et al. (1999)
G4400: Atkinson (2003)
G4401: Same value as for propyl group assumed (`k_PrO2_CH3O2`).
G4402: Same value as for propyl group assumed (`k_PrO2_HO2`).
G4403: Same value as for propyl group assumed (`k_PrO2_NO`).
G4404: Same value as for **G4107:** CH_3OOH+OH assumed.
G4405: Pöschl et al. (2000)
G4406: Pöschl et al. (2000)
G4407: Pöschl et al. (2000)
G4408: Pöschl et al. (2000)
G4409: Pöschl et al. (2000). The factor 0.25 was recommended by Uli Poeschl (pers. comm. 2004).
G4410: von Kuhlmann (2001)
G4411: Pöschl et al. (2000)
G4412: Pöschl et al. (2000)
G4413: Atkinson et al. (1999)
G4414: Same value as for propyl group assumed (`k_PrO2_HO2`).
G4415: Same value as for propyl group assumed (`k_PrO2_NO`).
G4416: Same value as for **G4107:** CH_3OOH+OH assumed.
G4417: Atkinson et al. (1999), value for $C_4H_9ONO_2$ used here.
G4500: Pöschl et al. (2000)
G4501: Pöschl et al. (2000)
G4502: Pöschl et al. (2000)
G4503: Boyd et al. (2003), same temperature dependence assumed as for other RO_2+HO_2 reactions
G4504: Pöschl et al. (2000), yield of 12 % $RONO_2$ assumed as suggested in Table 2 of Sprengnether et al. (2002).
G4505: von Kuhlmann (2001)
G4506: Pöschl et al. (2000)
G4507: Pöschl et al. (2000)
G4508: Pöschl et al. (2000)
G6100: Sander et al. (2003)
G6101: Sander et al. (2003)
G6102: Atkinson et al. (2005). The rate coefficient is: `k_ClO_ClO = k_3rd_iupac(temp,cair,2.E-32, 4.,1.E-11,0.,0.45)`.
G6103: Sander et al. (2003). The rate coefficient is defined as backward reaction divided by equilibrium constant.
G6200: Sander et al. (2003)
G6201a: Sander et al. (2003)
G6201b: Sander et al. (2003)
G6202: Sander et al. (2003)
G6203a: Sander et al. (2003)
G6203b: Sander et al. (2003)
G6204: Sander et al. (2003). At low temperatures, there may be a minor reaction channel leading to O_3+HCl. See Finkbeiner et al. (1995) for details. It is neglected here.
G6205: Sander et al. (2003)
G6206: Sander et al. (2003)
G6300: Sander et al. (2003)
G6301: Sander et al. (2003)
G6303: Sander et al. (2003)
G6304: Sander et al. (2003)
G6400: Sander et al. (2003)
G6401: Sander et al. (2003)
G6402: Sander et al. (2003)
G6403: Sander et al. (2003)
G6404: Sander et al. (2003)
G6405: Sander et al. (2003), average of reactions with CH_3Br and CH_3F (B. Steil, pers. comm., see also note A15 in Sander et al. (2003)).
G6406: Sander et al. (2003)
G6407: Sander et al. (2003), extrapolated from reactions with CH_3CF_3, CH_3CClF_2, and CH_3CCl_2F (B. Steil, pers. comm., see also note A15 in Sander et al. (2003)).
G6408: Sander et al. (2003)
G6500: Sander et al. (2003)
G6501: Sander et al. (2003)
G7100: Sander et al. (2003)
G7101: Sander et al. (2003)
G7102a: Sander et al. (2003)
G7102b: Sander et al. (2003)
G7200: Sander et al. (2003)
G7201: Sander et al. (2003)
G7202: Sander et al. (2003)
G7203: Sander et al. (2003)
G7301: Sander et al. (2003)
G7302: Sander et al. (2003). The rate coefficient is: `k_BrO_NO2 = k_3rd(temp,cair,5.2E-31,3.2, 6.9E-12,2.9,0.6)`.
G7400: Sander et al. (2003)
G7403: Sander et al. (2003)
G7603a: Sander et al. (2003)
G7603b: Sander et al. (2003)
G7603c: Sander et al. (2003)
G9200: Sander et al. (2003)
G9400a: Atkinson et al. (2003); Abstraction path. The assumed reaction sequence (omitting H_2O and O_2 as products) according to Yin et al. (1990) is:

$$\begin{aligned} DMS + OH &\rightarrow CH_3SCH_2 \\ CH_3SCH_2 + O_2 &\rightarrow CH_3SCH_2OO \\ CH_3SCH_2OO + NO &\rightarrow CH_3SCH_2O + NO_2 \\ CH_3SCH_2O &\rightarrow CH_3S + HCHO \end{aligned}$$

$$\begin{aligned} CH_3S + O_3 &\rightarrow CH_3SO \\ CH_3SO + O_3 &\rightarrow CH_3SO_2 \end{aligned}$$

$$\begin{aligned} DMS + OH &\quad CH_3SO_2 + HCHO \\ +NO + 2O_3 &\rightarrow +NO_2 \end{aligned}$$

Neglecting the effect on O_3 and NO_x, the remaining reaction is:

$$DMS + OH + O_3 \rightarrow CH_3SO_2 + HCHO$$

G9400b: Atkinson et al. (2003); Addition path. The rate coefficient is: `k_DMS_OH = 1.0E-39*EXP(5820./temp)*C(KPP_O2)/ (1.+ 5.0E-30*EXP(6280./temp)*C(KPP_O2))`.
G9401: Atkinson et al. (2003)
G9402: Hynes and Wine (1996)
G9403: Barone et al. (1995)
G9404: Barone et al. (1995)
G9405: Barone et al. (1995)

Table D.2: Photolysis reactions

#	reaction	rate coefficient
J1000	$O_2 + h\nu \rightarrow O(^3P) + O(^3P)$	`JX(ip_O2)`
J1001a	$O_3 + h\nu \rightarrow O(^1D)$	`JX(ip_O1D)`
J1001b	$O_3 + h\nu \rightarrow O(^3P)$	`JX(ip_O3P)`
J2100	$H_2O + h\nu \rightarrow H + OH$	`JX(ip_H2O)`
J2101	$H_2O_2 + h\nu \rightarrow 2\ OH$	`JX(ip_H2O2)`
J3100	$N_2O + h\nu \rightarrow O(^1D)$	`JX(ip_N2O)`
J3101	$NO_2 + h\nu \rightarrow NO + O(^3P)$	`JX(ip_NO2)`
J3102	$NO + h\nu \rightarrow N + O(^3P)$	`JX(ip_NO)`
J3103a	$NO_3 + h\nu \rightarrow NO_2 + O(^3P)$	`JX(ip_NO2O)`
J3103b	$NO_3 + h\nu \rightarrow NO$	`JX(ip_NOO2)`
J3104	$N_2O_5 + h\nu \rightarrow NO_2 + NO_3$	`JX(ip_N2O5)`
J3200	$HONO + h\nu \rightarrow NO + OH$	`JX(ip_HONO)`
J3201	$HNO_3 + h\nu \rightarrow NO_2 + OH$	`JX(ip_HNO3)`
J3202	$HNO_4 + h\nu \rightarrow .667\ NO_2 + .667\ HO_2 + .333\ NO_3 + .333\ OH$	`JX(ip_HNO4)`
J4100	$CH_3OOH + h\nu \rightarrow HCHO + OH + HO_2$	`JX(ip_CH3OOH)`
J4101a	$HCHO + h\nu \rightarrow H_2 + CO$	`JX(ip_COH2)`
J4101b	$HCHO + h\nu \rightarrow H + CO + HO_2$	`JX(ip_CHOH)`
J4102	$CO_2 + h\nu \rightarrow CO + O(^3P)$	`JX(ip_CO2)`
J4200	$C_2H_5OOH + h\nu \rightarrow CH_3CHO + HO_2 + OH$	`JX(ip_CH3OOH)`
J4201	$CH_3CHO + h\nu \rightarrow CH_3O_2 + HO_2 + CO$	`JX(ip_CH3CHO)`
J4202	$CH_3C(O)OOH + h\nu \rightarrow CH_3O_2 + OH$	`JX(ip_PAA)`
J4203	$NACA + h\nu \rightarrow NO_2 + HCHO + CO$	`0.19*JX(ip_CHOH)`
J4204	$PAN + h\nu \rightarrow CH_3C(O)OO + NO_2$	`JX(ip_PAN)`
J4300	$C_3H_7OOH + h\nu \rightarrow CH_3COCH_3 + HO_2 + OH$	`JX(ip_CH3OOH)`
J4301	$CH_3COCH_3 + h\nu \rightarrow CH_3C(O)OO + CH_3O_2$	`JX(ip_CH3COCH3)`
J4302	$CH_3COCH_2OH + h\nu \rightarrow CH_3C(O)OO + HCHO + HO_2$	`0.074*JX(ip_CHOH)`
J4303	$CH_3COCHO + h\nu \rightarrow CH_3C(O)OO + CO + HO_2$	`JX(ip_CH3COCHO)`
J4304	$CH_3COCH_2O_2H + h\nu \rightarrow CH_3C(O)OO + HO_2 + OH$	`JX(ip_CH3OOH)`
J4305	$MPAN + h\nu \rightarrow CH_3COCH_2OH + NO_2$	`JX(ip_PAN)`
J4306	$C_3H_7ONO_2 + h\nu \rightarrow CH_3COCH_3 + NO_2 + HO_2$	`3.7*JX(ip_PAN)`
J4400	$C_4H_9OOH + h\nu \rightarrow OH + .67\ CH_3COC_2H_5 + .67\ HO_2 + .33\ C_2H_5O_2 + .33\ CH_3CHO$	`JX(ip_CH3OOH)`
J4401	$MVK + h\nu \rightarrow CH_3C(O)OO + HCHO + CO + HO_2$	`0.019*JX(ip_COH2) +.015*JX(ip_ CH3COCHO)`
J4402	$MVKOOH + h\nu \rightarrow OH + .5\ CH_3COCHO + .25\ CH_3COCH_2OH + .75\ HCHO + .75\ HO_2 + .25\ CH_3C(O)OO + .25\ CO$	`JX(ip_CH3OOH)`
J4403	$CH_3COC_2H_5 + h\nu \rightarrow CH_3C(O)OO + C_2H_5O_2$	`0.42*JX(ip_CHOH)`

Table D.2: Photolysis reactions (... continued)

#	reaction	rate coefficient
J4404	MEKOOH + hν → $CH_3C(O)OO$ + CH_3CHO + OH	JX(ip_CH3OOH)
J4405	MeCOCO + hν → 2 $CH_3C(O)OO$	2.15*JX(ip_CH3COCHO)
J4406	ONIT + hν → NO_2 + .67 $CH_3COC_2H_5$ + .67 HO_2 + .33 $C_2H_5O_2$ + .33 CH_3CHO	3.7*JX(ip_PAN)
J4500	ISOOH + hν → MVK + HCHO + HO_2 + OH	JX(ip_CH3OOH)
J4501	ISON + hν → MVK + HCHO + NO_2 + HO_2	3.7*JX(ip_PAN)
J6000	Cl_2 + hν → Cl + Cl	JX(ip_Cl2)
J6100	Cl_2O_2 + hν → 2 Cl	1.4*JX(ip_Cl2O2)
J6101	OClO + hν → ClO + O(^{3}P)	JX(ip_OClO)
J6200	HCl + hν → Cl + H	JX(ip_HCl)
J6201	HOCl + hν → OH + Cl	JX(ip_HOCl)
J6301	$ClNO_3$ + hν → Cl + NO_3	JX(ip_ClNO3)
J6400	CH_3Cl + hν → Cl + CH_3O_2	JX(ip_CH3Cl)
J6401	CCl_4 + hν → 4 Cl	JX(ip_CCl4)
J6402	CH_3CCl_3 + hν → 3 Cl	JX(ip_CH3CCl3)
J6500	$CFCl_3$ + hν → 3 Cl	JX(ip_CFCl3)
J6501	CF_2Cl_2 + hν → 2 Cl	JX(ip_CF2Cl2)
J7000	Br_2 + hν → Br + Br	JX(ip_Br2)
J7200	HOBr + hν → Br + OH	JX(ip_HOBr)
J7301	$BrNO_3$ + hν → Br + NO_3	JX(ip_BrNO3)
J7400	CH_3Br + hν → Br + CH_3O_2	JX(ip_CH3Br)
J7500	CF_3Br + hν → Br	JX(ip_CF3Br)
J7600	BrCl + hν → Br + Cl	JX(ip_BrCl)
J7601	CF_2ClBr + hν → Br + Cl	JX(ip_CF2ClBr)

Notes: J-values are calculated with an external module and then supplied to the MECCA chemistry
J6100: Stimpfle et al. (2004) claim that the combination of absorption cross sections from Burkholder et al. (1990) and the Cl_2O_2 formation rate coefficient by Sander et al. (2003) can approximately reproduce the observed Cl_2O_2/ClO ratios and ozone depletion. They give an almost zenith-angle independent ratio of 1.4 for Burkholder et al. (1990) to Sander et al. (2003) J-values. The IUPAC recommendation for the Cl_2O_2 formation rate is about 5 to 15 % less than the value by Sander et al. (2003) but more than 20 % larger than the value by Sander et al. (2000). The J-values by Burkholder et al. (1990) are within the uncertainty range of the IUPAC recommendation.

Table D.3: Heterogeneous reactions on climatological aerosols

#	reaction	rate coefficient
PSC200	N_2O_5 + H_2O → HNO_3 + HNO_3	khet_N2O5_H2O
PSC410	HOCl + HCl → Cl_2 + H_2O	khet_HOCl_HCl
PSC420	$ClNO_3$ + HCl → Cl_2 + HNO_3	khet_ClNO3_HCl
PSC421	$ClNO_3$ + H_2O → HOCl + HNO_3	khet_ClNO3_H2O
PSC510	HOBr + HBr → Br_2 + H_2O	khet_HOBr_HBr
PSC520	$BrNO_3$ + H_2O → HOBr + HNO_3	khet_BrNO3_H2O
PSC540	$ClNO_3$ + HBr → BrCl + HNO_3	khet_ClNO3_HBr
PSC541	$BrNO_3$ + HCl → BrCl + HNO_3	khet_BrNO3_HCl
PSC542	HOCl + HBr → BrCl + H_2O	khet_HOCl_HBr
PSC543	HOBr + HCl → BrCl + H_2O	khet_HOBr_HCl

Notes: These reaction rates are calculated with the HETCHEM submodel and then supplied to the MECCA chemistry (see `http://www.messy-interface.org` for details).

Bibliography

Abbatt, J. P. D. and Waschewsky, G. C. G.: Heterogeneous interactions of HOBr, HNO_3, O_3, and NO_2 with deliquescent NaCl aerosols at room temperature, J. Phys. Chem. A, 102, 3719–3725, 1998.

Adler, R. F., Huffman, G. J., Chang, A., Ferraro, R., Xie, P., Janowiak, J. E., Rudolf, B., Schneider, U., Curtis, S., Bolvin, D., Gruber, A., Susskind, J., Arkin, P., and Nelkin, E.: The Version-2 Global Precipitation Climatology Project (GPCP) Monthly Precipitation Analysis (1979 - Present), J. Hydrometeorology, 4, 1147–1167, 2003.

Alheit, R. R., Flossmann, A. I., and Pruppacher, H. R.: A theoretical Study of the Wet Removal of Atmospheric Pollutants. Part IV: The Uptake and Redistribution of Aerosol Paricles through Nucleation and Impaction Scavenging by Growing Cloud Drops and Ice Particles, J. Atmos. Sci., 47, 870–887, 1990.

Allen, D. J. and Pickering, K. E.: Evaluation of lightning flash rate parameterizations for use in a global chemical transport model, J. Geophys. Res., 107, 4711, doi:10.1029/2002JD002066, 2002.

Andronache, C.: Estimated variability of below-cloud aerosol removal by rainfall for observed aerosol size distributions, Atmos. Chem. Phys., 3, 131–143, 2003.

Andronache, C.: Estimates of sulfate aerosol wet scavenging coefficient for locations in the Eastern United States, Atmos. Environ., 38, 795–804, 2004.

Arakawa, A.: The Cumulus Parameterization Problem: Past, Present, and Future, J. Clim., 17, 2493–2525, 2004.

Arakawa, A. and Schubert, W. H.: Interaction of a Cumulus Cloud Ensemble with the Large-Scale Envirnoment, Part I, J. Atmos. Sci., 31, 674–701, 1974.

Asman, W. A. H.: Parameterization of below-cloud scavenging of highly soluble gases under convective conditions, Atmos. Environ., 29, 1359–1368, 1995.

Atkinson, R.: Gas-phase tropospheric chemistry of volatile organic compounds: 1. Alkanes and alkenes, J. Phys. Chem. Ref. Data, 26, 215–290, 1997.

Atkinson, R.: Kinetics of the gas-phase reactions of OH radicals with alkanes and cycloalkanes, Atmos. Chem. Phys., 3, 2233–2307, 2003.

Atkinson, R., Baulch, D. L., Cox, R. A., Hampson, Jr., R. F., Kerr, J. A., Rossi, M. J., and Troe, J.: Summary of evaluated kinetic and photochemical data for atmospheric chemistry: Web version August 1999, `http://www.iupac-kinetic.ch.cam.ac.uk/`, 1999.

Atkinson, R., Baulch, D. L., Cox, R. A., Crowley, J. N., Hampson, R. F., Hynes, R. G., Jenkin, M. E., Rossi, M. J., and Troe, J.: Evaluated kinetic and photochemical data for atmospheric chemistry: Part 1 - gas phase reactions of O_x, HO_x, NO_x and SO_x species, Atmos. Chem. Phys. Discuss., 3, 6179–6699, 2003.

Atkinson, R., Baulch, D. L., Cox, R. A., Crowley, J. N., Hampson, Jr., R. F., Hynes, R. G., Jenkin, M. E., Kerr, J. A., Rossi, M. J., and Troe, J.: Summary of evaluated kinetic and photochemical data for atmospheric chemistry: Web version March 2005, `http://www.iupac-kinetic.ch.cam.ac.uk/`, 2005.

Baker, M. B., Corbin, R. G., and Latham, J.: The influence of entrainment on the evolution of cloud droplet spectra: I. A model of inhomogeneous mixing, Q. J. R. Meteorol. Soc., 106, 581–598, 1980.

Balkanski, Y., Schulz, M., Claquin, T., Moulin, C., and Ginoux, P.: Global Emissions of Mineral Aerosol: Formulation and Validation using Satellite Imagery, in: Emissions of Atmospheric Trace Compounds, edited by Granier, C., pp. 239–267, Kluwer Academic Publishers, 2004.

Barker, G. C., Fowles, P., and Stringer, B.: Pulse radiolytic induced transient electrical conductance in liquid solutions, Trans. Faraday Soc., 66, 1509–1519, 1970.

Barone, S. B., Turnipseed, A. A., and Ravishankara, A. R.: Role of adducts in the atmospheric oxidation of dimethyl sulfide, Faraday Discuss., 100, 39–54, 1995.

Barth, M. C., Stuart, A. L., and Skamarock, W. C.: Numerical simulations of the July 10, 1996, Stratospheric-Tropospheric Experiment: Radiation, Aerosols, and Ozone (STERAO)-Deep Convection experiment storm: Redistribution of soluble stracers, J. Geophys. Res., 106, 12 381–12 400, 2001.

Barth, M. C., Hess, P. G., and Madronich, S.: Effect of marine boundary layer clouds on tropospheric chemistry as analyzed in a regional chemistry transport model, J. Geophys. Res., 107, 4126, doi:10.1029/2001JD000468, 2002.

Bartlett, W. P. and Margerum, D. W.: Temperature dependencies of the Henry's law constant and the aqueous phase dissociation constant of bromine chloride, Environ. Sci. Technol., 33, 3410–3414, 1999.

Bateman, H.: Solution of a system of differential equations occuring in the theory of radiactive transformation, in: Proc. Cambridge Philos. Soc., 1910.

Bates, D. V.: Ambient ozone and mortality, Epidemiology, 16, 427–429, 2005.

Beard, K. V. and Pruppacher, H. R.: A determination of the terminal velocity and drag of small water drops by means of a wind tunnel, J. Atmos. Sci., 26, 1066–1971, 1969.

Bechtold, P., Bazile, E., Guichard, F., Mascart, P., and Richard, E.: A mass-flux convection scheme for regional and global models, Q. J. R. Meteorol. Soc., 127, 869–886, 2001.

Bechtold, P., Chaboureau, J.-P., Beljaars, A., Betts, A. K., Köhler, M., Miller, M., and Redelsperger, J.-L.: The simulation of the diurnal cycle of convective precipitation over land in a global model, Q. J. R. Meteorol. Soc., 130, 3119–3137, 2004.

Beirle, S., Platt, U., Wenig, M., and Wagner, T.: NO_x production by lightning estimated with GOME, Adv. Space Res., 34, 793–797, 2004.

Bell, N., Hsu, L., Jacob, D. J., Schultz, M. G., Blake, D. R., Butler, J. H., King, D. B., Lobert, J. M., and Maier-Reimer, E.: Methyl iodide: Atmospheric budget and use as a tracer of marine convection in global models, J. Geophys. Res., 107, 4340, doi:10.1029/2001JD001151, 2002.

Bengtsson, L., Hodges, K. I., and Hagemann, S.: Sensitivity of large-scale atmospheric analyses to humidity observations and its impact on the global water cycle and tropical and extratropical weather systems in ERA40, Tellus, 56A, 202–217, 2004.

Best, A. C.: The size distribution of raindrops, Q. J. R. Meteorol. Soc., 76, 16–36, 1950.

Betterton, E. A. and Hoffmann, M. R.: Henry's law constants of some environmentally important aldehydes, Environ. Sci. Technol., 22, 1415–1418, 1988a.

Betterton, E. A. and Hoffmann, M. R.: Oxidation of aqueous SO_2 by peroxymonosulfate, J. Phys. Chem., 92, 5962–5965, 1988b.

Bjerkness, J.: Saturated-adiabatic ascent of air through dry-adiabatically descending environment, Q. J. R. Meteorol. Soc., 64, 325–330, 1938.

Bott, A. and Carmichael, G. R.: Multiphase chemistry in a microphysical radiation fog model - a numerical study, Atmos. Environ., 27, 503–522, 1993.

Bouwman, A., Lee, D., Asman, W., Dentener, F., van der Hoek, K., and Olivier, J.: A global high-resolution emission inventory for ammonia, Global Biogeochem. Cycles, 11, 561–587, 1997.

Boyce, S. D. and Hoffmann, M. R.: Kinetics and mechanism of the formation of hydroxymethanesulfonic acid at low pH, J. Phys. Chem., 88, 4740–4746, 1984.

Boyd, A. A., Flaud, P.-M., Daugey, N., and Lesclaux, R.: Rate constants for $RO_2 + HO_2$ reactions measured under a large excess of HO_2, J. Phys. Chem. A, 107, 818–821, 2003.

Brasseur, G. P., Kiehl, J. T., Müller, J.-F., Schneider, T., Granier, C., Tie, X., and Hauglustaine, D.: Past and future changes in global tropospheric ozone: Impact on radiative forcing, Geophys. Res. Lett., 25, 3807–3810, 1998.

Brimblecombe, P. and Clegg, S. L.: Erratum, J. Atmos. Chem., 8, 95, 1989.

Brinkop, S. and Sausen, R.: A modified mass-flux scheme for convection which maintains positive tracer concentrations, Tech. Rep. 67, Institut für Physik der Atmosphäre DLR, 1996.

Brühl, C.: The impact of the future scenarios for methane and other chemically active gases on the GWP of methane, Chemosphere, 26, 731–738, 1993.

Buchholz, J.: Simulations of Physics and Chemistry of Polar Stratospheric Clouds in a General Circulation Model, Ph.D. thesis, Johannes Gutenberg-Universität Mainz, Germany, 2005.

Burkholder, J. B., Orlando, J. J., and Howard, C. J.: Ultraviolet absorption cross sections of Cl_2O_2 between 210 and 410 nm, J. Phys. Chem., 94, 687–695, 1990.

Burrows, J. P., Weber, M., Buchwitz, M., Rozanov, V. V., Ladstädter-Weissenmayer, A., Richter, A., de Beek, R., Hoogen, R., Bramstedt, K., Eichmann, K.-U., and und D. Perner, M. E.: The Global Ozone Monitoring Experiment (GOME): Mission Concept and First Scientific Results, J. Atmos. Sci., 56, 151–175, 1999.

Buxton, G. V., Greenstock, C. L., Helman, W. P., and Ross, A. B.: Critical review of rate constants for reactions of hydrated electrons, hydrogen atoms and hydroxyl radicals ($\cdot OH/\cdot O^-$) in aqueous solution, J. Phys. Chem. Ref. Data, 17, 513–886, 1988.

Buxton, G. V., McGowan, S., Salmon, G. A., Williams, J. E., and Wood, N. D.: A study of the spectra and reactivity of oxysulphur-radical anions involved in the chain oxidation of S(IV): A pulse and γ-radiolysis study, Atmos. Environ., 30, 2483–2493, 1996.

Canosa-Mas, C. E., King, M. D., Lopez, R., Percival, C. J., Wayne, R. P., Shallcross, D. E., Pyle, J. A., and Daele, V.: Is the reaction between $CH_3(O)O_2$ and NO_3 important in the night-time troposphere?, J. Chem. Soc. Faraday Trans., 92, 2211–2222, 1996.

Chameides, W. L.: The photochemistry of a remote marine stratiform cloud, J. Geophys. Res., 89D, 4739–4755, 1984.

Chang, J. S., Brost, R. A., Isaksen, I. S. A., Madronich, S., Middleton, P., Stockwell, W. R., and Walcek, C. J.: A Three-Dimensional Eulerian Acid Deposition Model: Physical Concepts and Formulation, J. Geophys. Res., 92, 14 681–14 700, 1987.

Chin, M. and Wine, P. H.: A temperature-dependent competitive kinetics study of the aqueous-phase reactions of OH radicals with formate, formic acid, acetate, acetic acid, and hydrated formaldehyde, in: Aquatic and Surface Photochemistry, edited by Helz, G. R., Zepp, R. G., and Crosby, D. G., pp. 85–96, A. F. Lewis, NY, 1994.

Christensen, H. and Sehested, K.: HO_2 and O_2^- radicals at elevated temperatures, J. Phys. Chem., 92, 3007–3011, 1988.

Christensen, H., Sehested, K., and Corfitzen, H.: Reactions of hydroxyl radicals with hydrogen peroxide at ambient and elevated temperatures, J. Phys. Chem., 86, 1588–1590, 1982.

Christensen, L. E., Okumura, M., Sander, S. P., Salawitch, R. J., Toon, G. C., Sen, B., Blavier, J.-F., and Jucks, K. W.: Kinetics of $HO_2 + HO_2 \rightarrow H_2O_2 + O_2$: Implications for stratospheric H_2O_2, Geophys. Res. Lett., 29, doi:10.1029/2001GL014525, 2002.

Christian, H. J., Blakeslee, R. J., Goodman, S. J., Mach, D. A., Stewart, M. F., Buechler, D. E., Koshak, W. J., Hall, J. M., Boek, W. L., Driscoll, K. T., and Boccippio, D. J.: The Lightning Imaging Sensor, in: Proceedings of the 11th International Conference on Atmospheric Electricity, Guntersville, Alabama, June 7-11, pp. 746–749, 1999.

Christian, H. J., Blakeslee, R. J., Boccippio, D. J., Boeck, W. L., Buechler, D. E., Driscoll, K. T., Goodman, S. J., Hall, J. M., Koshak, W. J., Mach, D. M., and Stewart, M. F.: Global frequency and distribution of lightning as observed from space by the Optical Transient Detector, J. Geophys. Res., 108, 4005, doi:10.1029/2002JD002347, 2003.

Clifton, C. L., Altstein, N., and Huie, R. E.: Rate constant for the reaction of NO_2 with sulfur(IV) over the pH range 5.3–13, Environ. Sci. Technol., 22, 586–589, 1988.

Collins, W. J., Derwent, R. G., Johnson, C. E., and Stevenson, D. S.: A comparison of two schemes of convective transport of chemical species in a Lagrangian global chemistry model, Q. J. R. Meteorol. Soc., 128, 991–1009, 2002.

Crutzen, P. J. and Lawrence, M. G.: The Impact of Precipitation Scavenging on the Transport of Trace Gases: A 3-Dimensional Model Sensitivity Study, J. Atmos. Chem., 37, 81–112, 2000.

Damian, V., Sandu, A., Damian, M., Potra, F., and Carmichael, G. R.: The kinetic preprocessor KPP - a software environment for solving chemical kinetics, Comput. Chem. Eng., 26, 1567–1579, 2002.

Damschen, D. E. and Martin, L. R.: Aqueous aerosol oxidation of nitrous acid by O_2, O_3 and H_2O_2, Atmos. Environ., 17, 2005–2011, 1983.

Davis, Jr., W. and de Bruin, H. J.: New activity coefficients of 0-100 per cent aqueous nitric acid, J. Inorg. Nucl. Chem., 26, 1069–1083, 1964.

De Bruyn, W. J., Shorter, J. A., Davidovits, P., Worsnop, D. R., Zahniser, M. S., and Kolb, C. E.: Uptake of gas-phase sulfur species methanesulfonic acid, dimethylsulfoxide, and dimethyl sulfone by aqueous surfaces, J. Geophys. Res., 99D, 16 927–16 932, 1994.

Dean, J. A.: Lange's Handbook of Chemistry, McGraw-Hill, Inc., 1992.

Deguillaume, L., Leriche, M., Monod, A., and Chaumerliac, N.: The role of transition metal ions on HO_x radicals in clouds: a numerical evaluation of its impact on multiphase chemistry, Atmos. Chem. Phys., 4, 95–110, 2004.

DeMore, W. B., Sander, S. P., Golden, D. M., Hampson, R. F., Kurylo, M. J., Howard, C. J., Ravishankara, A. R., Kolb, C. E., and Molina, M. J.: Chemical kinetics and photochemical data for use in stratospheric modeling. Evaluation number 12, JPL Publication 97-4, Jet Propulsion Laboratory, Pasadena, CA, 1997.

Dentener, F.: Heterogeneous Chemistry in the Troposphere, Ph.D. thesis, Universiteit Utrecht, 1993.

Doherty, R. M., Stevenson, D. S., Collins, W. J., and Sanderson, M. G.: Influence of convective transport on tropospheric ozone and its precursors in a chemistry-climate model, Atmos. Chem. Phys. Discuss., 5, 3747–3771, 2005.

Donner, L. J., Seman, C. J., Hemler, R. S., and Fan, S.: A Cumulus Parameterization Including Mass Fluxes, Convective Vertical Velocities, and Mesoscale Effects: Thermodynamic and Hydrological Aspects in a General Circulation Model, J. Clim., 14, 3444–3463, 2001.

Doswell, C. A. and Markowski, P. M.: Is Buoyancy a Relative Quantity, Mon. Weather Rev., 132, 853–863, 2004.

Eitzen, Z. A. and Randall, D. A.: Numerical Simulations of Interactions between Gravity Waves and Deep Moist Convection, J. Atmos. Sci., 62, 1480–1496, 2005.

Elrod, M. J., Ranschaert, D. L., and Schneider, N. J.: Direct kinetics study of the temperature dependence of the CH_2O branching channel for the CH_3O_2 + HO_2 reaction, Int. J. Chem. Kinetics, 33, 363–376, 2001.

Emanuel, K. A. and Zivkovic-Rothman, M.: Development and Evaluation of a Convection Scheme for Use in Climate Models, J. Atmos. Sci., 56, 1766–1782, 1999.

Emmons, L. K., Hauglustaine, D. A., Müller, J.-F., carroll, M. A., Brasseur, G. P., Brunner, D., Staehelin, J., Thouret, V., and Marenco, A.: Data composites of airborne observations of tropospheric ozone and its precursors, J. Geophys. Res., 105, 20 497–20 538, 2000.

Ervens, B., George, C., Williams, J. E., Boxton, G. V., Salmon, G. A., Bydder, M., Wilkinsons, F., Dentener, F., Mirabel, P., Wolke, R., and Herrmann, H.: CAPRAM 2.4 (MODAC mechanism): An extended and condensed tropospheric aqueous phase mechanism and its application, J. Geophys. Res., 108, 4426, doi:10.1029/2002JD002202, 2003.

Exner, M., Herrmann, H., and Zellner, R.: Laser-based studies of reactions of the nitrate radical in aqueous solution, Ber. Bunsenges. Phys. Chem., 96, 470–477, 1992.

Fahey, K. M. and Pandis, S. N.: Optimizing model performance: variable size resolution in cloud chemistry modeling, Atmos. Environ., 35, 4471–4478, 2001.

Fahey, K. M. and Pandis, S. N.: Size-resolved aqueous-phase atmospheric chemistry in a three-dimensional chemical transport model, J. Geophys. Res., 108, 4690, doi:10.1029/2003JD003564, 2003.

Feichter, J., Kjellström, E., Rohde, H., Dentener, F., Lelieveld, J., and Roelofs, G.-J.: Simulation of the tropospheric sulfur cycle in a global climate model, Atmos. Environ., 30, 1693–1707, 1996.

Finkbeiner, M., Crowley, J. N., Horie, O., Müller, R., Moortgat, G. K., and Crutzen, P. J.: Reaction between HO_2 and ClO: Product formation between 210 and 300 K, J. Phys. Chem., 99, 16 264–16 275, 1995.

Flossmann, A. I. and Pruppacher, H. R.: A theoretical Study of the Wet Removal of Atmospheric Pollutants. Part III: The Uptake, Redistribution, and Deposition of $(NH_4)_2SO_4$ Particles by a Convective Cloud using a Two-Dimensional Cloud Dynamics Model, J. Atmos. Sci., 45, 1857–1871, 1988.

Flossmann, A. I., Hall, W. D., and Pruppacher, H. R.: A theoretical Study of the Wet Removal of Atmospheric Pollutants. Part I: The Redistribution of Aerosol Particles captured through Nucleation and Impaction Scavenging by Growing Cloud Drops, J. Atmos. Sci., 42, 583–606, 1985.

Flossmann, A. I., Pruppacher, H. R., and Topalian, J. H.: A theoretical Study of the Wet Removal of Atmospheric Pollutants. Part II: The Uptake and Redistribution of $(NH_4)_2SO_4$ Particles and SO_2 Gas Simultaneously Scavenged by Growing Cloud Drops, J. Atmos. Sci., 44, 2912–2923, 1987.

Franzblau, E. and Popp, C. J.: Nitrogen oxides produced from lightning, J. Geophys. Res., 94, 11 089–11 104, 1989.

Frössling: The evaporating of falling drops, Beitr. Geophys., 52, 170–216, 1938.

Fu, Q., Krueger, S. K., and Liou, K. N.: Interactions of Radiation and Convection in Simulated Tropical Cloud Clusters, J. Atmos. Sci., 52, 1310–1328, 1995.

Gamache, J. F. and Houze, jr., R. A.: Water budget of a Mesoscale Convective System in the Tropics, J. Atmos. Sci., 40, 1835–1850, 1983.

Ganzeveld, L. and Lelieveld, J.: Dry deposition parametrization in a chemistry general circulation model and its influence on the distribution of reactive trace gases, J. Geophys. Res., 100, 20 999–21 012, 1995.

Ganzeveld, L., Lelieveld, J., and Roelofs, G.-J.: A dry deposition parameterization for sulfur oxides in a chemistry and general circulation model, J. Geophys. Res., 103, 5679–5694, 1998.

Ganzeveld, L. N., Lelieveld, J., Dentener, F. J., Krol, M. C., Bouwman, A. J., and Roelofs, G.-J.: Global soil-biogenic NOx emissions and the role of canopy processes, J. Geophys. Res., 107, 2002a.

Ganzeveld, L. N., Lelieveld, J., Dentener, F. J., Krol, M. C., and Roelofs, G.-J.: Atmosphere-biosphere trace gas excanges simulated with a single-column model, J. Geophys. Res., 107, 2002b.

Gidel, L. T.: Cumulus Cloud Transport of Transient Tracers, J. Geophys. Res., 88, 6587–6599, 1983.

Goodman, S. N.: The methodologic ozone effect, Epidemiology, 16, 430–435, 2005.

Grabowski, W. W.: An Improved Framework for Superparameterization, J. Atmos. Sci., 61, 1940–1952, 2004.

Grabowski, W. W. and Smolarkiewicz, P. K.: CRCP: a Cloud Resolving Convection Parameterization for modeling the tropical convecting atmosphere, Physica, 133D, 171–178, 1999.

Grant, A. L. M. and Brown, A. R.: A similarity hypothesis for shallow-cumulus transports, Q. J. R. Meteorol. Soc., 125, 1913–1936, 1999.

Gregory, D., Morcrette, J.-J., Jakob, C., Beljaars, C. M., and Stockdale, T.: Revision of convection, radiation and cloud schemes in the ECMWF Integrated Forecasting System, Q. J. R. Meteorol. Soc., 126, 1685–1710, 2000.

Grell, G. A. and Deeveny, D.: A generalized approach to parameterizing convection combining ensemble and data assimilation techniques, Geophys. Res. Lett., 29, 1693, doi:10.1029/2002GL015311, 2002.

Grewe, V., Brunner, D., Dameris, M., Grenfell, J. L., Hein, R., Shindell, D., and Staehelin, J.: Origin and variability of upper tropospheric nitrogen oxides and ozone at northern mid-latitudes, Atmos. Environ., 35, 3421–3433, 2001.

Guelle, W., Schulz, M., Balkanski, Y., and Dentener, F.: Influence of the source formulation on modeling the atmospheric global distribution of sea salt aerosol, J. Geophys. Res., 106, 27 509–27 524, 2001.

Hack, J. J.: Parameterization of moist convection in the National Center for Atmospheric Research community climate model (CCM2), J. Geophys. Res., 99, 5551–5568, 1994.

Hagemann, S., Arpe, K., Bengtsson, L., and Kirchner, I.: Validation of precipitation from ERA40 and an ECHAM4.5 simulation nudged with ERA40 data, Tech. rep., 3. Workshop on Re-analysis, 5-9 November 2001 ERA-40 Project Report Series, Reading, UK, 2002.

Hagemann, S., Arpe, K., and Roeckner, E.: Evaluation of the hydrological cycle in the ECHAM5 model, J. Clim., p. in press, 2006.

Hanson, D. R., Burkholder, J. B., Howard, C. J., and Ravishankara, A. R.: Measurement of OH and HO_2 radical uptake coefficients on water and sulfuric acid surfaces, J. Phys. Chem., 96, 4979–4985, 1992.

Hass, H., Ebel, A., Feldmann, H., Hakobs, H. J., and Memmesheimer, M.: Evaluation studies with a regional chemical transport model (EURAD) using air quality data from the EMEP monitoring network, Atmos. Environ., 27A, 867–887, 1993.

Herrmann, H., Reese, A., and Zellner, R.: Time resolved UV/VIS diode array absorption spectroscopy of SO_x^- (x=3, 4, 5) radical anions in aqueous solution, J. Mol. Struct., 348, 183–186, 1995.

Hoffmann, M. R.: On the kinetics and mechanism of oxidation of aquated sulfur dioxide by ozone, Atmos. Environ., 20, 1145–1154, 1986.

Holdren, M. W., Spicer, C. W., and Hales, J. M.: Peroxyacetyl nitrate solubility and decomposition rate in acidic water, Atmos. Environ., 18, 1171–1173, 1984.

Holton, J. R., Haynes, P. H., McIntyre, M. E., and Pfister, L.: Stratosphere-Troposphere Exchange, Rev. Geophys., 33, 403–439, 1995.

Houghton, J. T., Ding, Y., Griggs, D. J., Nouger, M., van der Linden, P. J., Dai, X., Maskell, K., and Johnson, C. A.: IPCC - Climate Change 2001: The Scientific Basis. Contribution of Working Group I to the third Assessment Report of the Intergovernmental Panel on Climate Change, Cambridge University Press, 2001.

Houze, jr., R. A.: Mesoscale Convective Systems, Reviews of Geophysics, 42, RG4003, doi: 8755-1209/2004RG000150, 2004.

Hu, J. H., Shi, Q., Davidovits, P., Worsnop, D. R., Zahniser, M. S., and Kolb, C. E.: Reactive uptake of Cl_2(g) and Br_2(g) by aqueous surfaces as a function of Br^- and I^- ion concentration: The effect of chemical reaction at the interface, J. Phys. Chem., 99, 8768–8776, 1995.

Huebert, B. J., Bates, T., Russel, P. B., shi, G., Kim, Y. J., Kawamura, K., Carmichael, G., and Nakajima, T.: An overview of ACE-Asia: Strategies for quantifying the relationshops between Asian aerosols and their climatic impacts, J. Geophys. Res., 108, 8633, doi: 10.1029/2003JD003550, 2003.

Huffman, G. J., Adler, R. F., Arkin, P., Chang, A., Ferraro, R., Gruber, A., Janowiak, J., McNab, A., Rudolf, B., and Schneider, U.: The Global Precipitation Climatology Project (GPCP) Combined Precipitation Dataset, Bullet. Amer. Meteor. Soc., 78, 5–20, 1997.

Huie, R. E. and Neta, P.: Rate constants for some oxidations of S(IV) by radicals in aqueous solutions, Atmos. Environ., 21, 1743–1747, 1987.

Huthwelker, T., Clegg, S. L., Peter, T., Carslaw, K., Luo, B. P., and Brimblecombe, P.: Solubility of HOCl in water and aqueous H_2SO_4 to stratospheric temperatures, J. Atmos. Chem., 21, 81–95, 1995.

Hynes, A. J. and Wine, P. H.: The atmospheric chemistry of dimethylsulfoxide (DMSO) kinetics and mechanism of the OH + DMSO reaction, J. Atmos. Chem., 24, 23–37, 1996.

Jacob, D. J.: Chemistry of OH in remote clouds and its role in the production of formic acid and peroxymonosulfate, J. Geophys. Res., 91D, 9807–9826, 1986.

Jacob, D. J.: Heterogeneous chemistry and tropospheric ozone, Atmos. Environ., 34, 2131–2159, 2000.

Jacob, D. J. and Prather, M. J.: Radon-222 as a test of convective transport in a general circulation model, Tellus, 42B, 118–134, 1990.

Jacob, D. J., Logan, J. A., Yevich, R. M., Gardner, G. M., Spivakovsky, C. M., Wofsy, S. C., Munger, J. W., Sillman, S., Prather, M. J., Rodgers, M. O., Westberg, H., and Zimmerman, P. R.: Simulation of Summertime Ozone over North America, J. Geophys. Res., 98, 14 797–14 816, 1993.

Jacob, D. J., Prather, M. J., Rasch, P. J., Shia, R.-L., Balkanski, Y. J., Beagley, S. R., Bergmann, D. J., Blackshear, W. T., Brown, M., Chiba, M., Chipperfield, M. P., de Grandpre, J., Dignon, J. E., Feichter, J., Genthon, C., Grose, W. L., Kasibhatla, P. S., Köhler, I., Kritz, M. A., Law, K., Penner, J. E., Ramonet, M., Reeves, C. E., Rotman, D. A., Stockwell, D. Z., van Velthoven, P. F., Verver, G., Wild, O., Yang, H., and Zimmermann, P.: Evaluation and intercomparison of global atmospheric transport models using ^{222}Rn and other short-lived tracers, J. Geophys. Res., 102, 5953–5970, 1997.

Jacobson, M. Z.: Atmopsheric Pollution, Cambridge University Press, 2002.

Jakob, C. and Siebesma, A. P.: A New Subcloud Model for Mass-Flux Convection Schemes: Influence on Triggering, Updraft Properties, and Model Climate, Mon. Weather Rev., 131, 2765–2778, 2003.

Jeuken, A. B. M., Siegmund, P. C., Heijboer, L. C., Feichter, J., and Bengtsson, L.: On the potential of assimilating meteorological analyses in a global climate model for the purpose of model validation, J. Geophys. Res., 101, 16 939–16 950, 1996.

Jiang, P.-Y., Katsumura, Y., Nagaishi, R., Domae, M., Ishikawa, K., Ishigure, K., and Yoshida, Y.: Pulse radiolysis study of concentrated sulfuric acid solutions. Formation mechanism, yield and reactivity of sulfate radicals, J. Chem. Soc. Faraday Trans., 88, 1653–1658, 1992.

Jöckel, P.: Technical Note: Recursive rediscretisation of geo-scientific data in multiple dimensions in the Modular Earth Submodel System (MESSy) data import interface, Atmos. Chem. Phys. Discuss., submitted, 2006.

Jöckel, P., von Kuhlmann, R., Lawrence, M., Steil, B., Brenninkmeijer, C., Crutzen, P., Rasch, P., and Eaton, B.: On a fundamental problem in implementing flux-form advection schemes for tracer transport in 3-dimensional general circulation and chemistry transport models, Q. J. R. Meteorol. Soc., 127, 1035–1052, 2001.

Jöckel, P., Sander, R., Kerkweg, A., Tost, H., and Lelieveld, J.: Technical Note: The Modular Earth Submodel System (MESSy) - a new approach towards Earth System Modeling, Atmos. Chem. Phys., 5, 433–444, 2005.

Jöckel, P., Tost, H., Pozzer, A., and the MESSy-Team: Evaluation of the atmospheric chemistry GCM ECHAM5/MESSy: Consistnent simulation of ozone in the stratosphere and troposphere, Atmos. Chem. Phys. Discuss., in preparation, 2006.

Kain, J. S. and Fritsch, J. M.: A One-Dimensional Entraining/Detraining Plume model and its Application in convective Parameterization, J. Atmos. Sci., 47, 2784–2801, 1990.

Kaiser, J.: Mounting evidence indicts fine-particle pollution, Sci. China, 307, 1858–1861, 2005.

Kelley, C. M. and Tartar, H. V.: On the system: bromine-water, J. Am. Chem. Soc., 78, 5752–5756, 1956.

Kerkweg, A.: Global Modelling of Atmospheric Halogen Chemistry in the Marine Boundary Layer, Ph.D. thesis, Rheinische Friedrich-Wilhelms-Universität Bonn, Germany, 2005.

Kerkweg, A., Sander, R., Tost, H., and Jöckel, P.: Technical Note: Implementation of prescribed (OFFLEM), calculated (ONLEM), and pseudo-emissions (TNUDGE) of chemical species in the Modular Earth Submodel System (MESSy), Atmos. Chem. Phys. Discuss., submitted, 2006.

Khan, I., Brimblecombe, P., and Clegg, S. L.: Solubilities of pyruvic acid and the lower (C_1-C_6) carboxylic acids. Experimental determination of equilibrium vapour pressures above pure aqueous and salt solutions, J. Atmos. Chem., 22, 285–302, 1995.

Kircher, C. C. and Sander, S. P.: Kinetics and mechanism of HO_2 and DO_2 disproportionations, J. Phys. Chem., 88, 2082–2091, 1984.

Kirchner, F. and Stockwell, W. R.: Effect of peroxy radical reactions on the predicted concentrations of ozone, nitrogenous compounds, and radicals, J. Geophys. Res., 101D, 21 007–21 022, 1996.

Krishnamurti, T. N. and Sanjay, J.: A new approach to the cumulus parametrization issue, Tellus, 55A, 275–300, 2003.

Kritz, M. A., Rosner, S. W., Kelly, K. K., Loewenstein, M., and Chan, K. R.: Radon Measurements in the Lower Tropical Stratosphere: Evidence for Rapid Vertical Transport Dehydration of Tropospheric Air, J. Geophys. Res., 98, 8725–8736, 1993.

Kritz, M. A., Rosner, S. W., and Stockwell, D. Z.: Validation of an off-line three-dimensional chemical transport model using observed radon profiles: 1. Observations, J. Geophys. Res., 103, 8425–8432, 1998.

Kuo, H. L.: Further Studies of the Parameterization of the Influence of Cumulus Convection on Large-Scale Flow, J. Atmos. Sci., 31, 1232–1240, 1974.

Labrador, L. J.: Sensitivity of Tropospheric Chemistry to the Source of NO_x from Lightning: Sensitivity Simulations with the Global 3D Global Chemistry Model for Atmospheric Transport and Chemistry MATCH-MPIC, Ph.D. thesis, Ruprechts-Karls Universität Heidelberg, 2005.

Labrador, L. J., v. Kuhlmann, R., and Lawrence, M. G.: Strong sensitivity of the global mean OH concentration and the tropospheric oxidizing efficiency to the source of NO_x from lightning, Geophys. Res. Lett., 31, L06 102, doi:10.1029/2003GL019229, 2004.

Labrador, L. J., v. Kuhlmann, R., and Lawrence, M. G.: The effects of lightning-produced NO_x and its vertical distribution on atmospheric chemistry: sensitivity simulations with MATCH-MPIC, Atmos. Chem. Phys., 5, 1815–1834, 2005.

Landgraf, J. and Crutzen, P. J.: An efficient method for online calculations of photolysis and heating rates, J. Atmos. Sci., 55, 863–878, 1998.

Lang, R. and Lawrence, M. G.: Improvement of the vertical humidity distribution in the chemistry-transport model MATCH through increased evaporation of convective precipitation, Geophys. Res. Lett., 32, L17 812, doi:10.1029/2005GL023172, 2005a.

Lang, R. and Lawrence, M. G.: Evaluation of the hydrological cycle of MATCH driven by NCEP reanalysis data: comparison with GOME water vapor measurements, Atmos. Chem. Phys., 5, 887–908, 2005b.

Lawrence, M. G. and Crutzen, P. J.: The impact of cloud particle gravitational settling on soluble trace gas distributions, Tellus, 50B, 263–289, 1998.

Lawrence, M. G. and Rasch, P. J.: Tracer transport in deep convective updrafts: plume ensemble versus bulk formulations, J. Atmos. Sci., 62, 2880–2894, 2005.

Lawrence, M. G., Crutzen, P. J., Rasch, P. J., Eaton, B. E., and Mahowald, N. M.: A model for studies of troposhperic chemistry: Description, global distributions and evaluation, J. Geophys. Res., 104, 26 245–26 277, 1999.

Lax, E.: Taschenbuch für Chemiker und Physiker, Springer Verlag, Berlin, 1969.

Lee, M.-I., Kang, I.-S., and Mapes, B. E.: Impacts of Cumulus Convection Parameterization on Aqua-planet AGCM Simulations of Tropical Intraseasonal Variability, J. Met. Soc. Japan, 81, 963–992, 2003.

Lee, Y.-N. and Schwartz, S. E.: Reaction kinetics of nitrogen dioxide with liquid water at low partial pressure, J. Phys. Chem., 85, 840–848, 1981.

Lelieveld, J. and Crutzen, P. J.: The Role of Clouds in Tropospheric Chemistry, J. Atmos. Chem., 12, 229–267, 1991.

Lelieveld, J., Crutzen, P. J., and Brühl, C.: Climate effects of atmospheric methane, Chemosphere, 26, 739–768, 1993.

Leriche, M., Dequillaume, L., and Chaumerliac, N.: Modeling study of strong acids formation and partitioning in a polluted cloud during wintertime, J. Geophys. Res., 108, 4433, doi:10.1029/2002JD002950, 2003.

Levine, S. Z. and Schwartz, S. E.: In-cloud and below-cloud scavenging of nitric acid vapor, Atmos. Environ., 16, 1725–1734, 1982.

Liang, J. and Jacob, D. J.: Effect of aqueous phase cloud chemistry on tropospheric ozone, J. Geophys. Res., 102, 5993–6001, 1997.

Lide, D. R. and Frederikse, H. P. R., eds.: CRC Handbook of Chemistry and Physics, 76th Edition, CRC Press, Inc., Boca Raton, FL, 1995.

Lin, J. W.-B. and Neelin, J. D.: Influence of a stochastic moist convective parameterization on tropical climate variability, Geophys. Res. Lett., 27, 3691–3694, 2000.

Lin, J. W.-B. and Neelin, J. D.: Considerations for Stochastic Convective Parameterization, J. Atmos. Sci., 59, 959–975, 2002.

Lin, J. W.-B. and Neelin, J. D.: Toward stochastic deep convective parameterization in general circulation models, Geophys. Res. Lett., 30, 1162, doi:10.1029/2002GL016203, 2003.

Lin, S.-J. and Rood, R.: Multidimensional Flux-Form Semi-Lagrangian Transport Schemes, Mon. Weather Rev., 124, 2046–2070, 1996.

Lind, J. A. and Kok, G. L.: Correction to "Henry's law determinations for aqueous solutions of hydrogen peroxide, methylhydroperoxide, and peroxyacetic acid" by John A. Lind and Gregory L. Kok, J. Geophys. Res., 99D, 21 119, 1994.

Lind, J. A., Lazrus, A. L., and Kok, G. L.: Aqueous phase oxidation of sulfur(IV) by hydrogen peroxide, methylhydroperoxide, and peroxyacetic acid, J. Geophys. Res., 92D, 4171–4177, 1987.

Liss, P. S. and Merlivat, L.: Air sea gas exchange rates: Introduction and Synthesis, in: The Role of Air-Sea Exchange in Geochemical Cycling, edited by Buat-Menard, P., pp. 113–127, D. Reidel Publishing Company, 1986.

Liu, C. and Moncrieff, M. W.: Effects of Convectively Generated Gravity Waves and Rotation on the Organization of Convection, J. Atmos. Sci., 61, 2218–2227, 2004.

Liu, H., Jacob, D. J., Bey, I., and Yantosca, R. M.: Contraints from ^{210}Pb and ^{7}Be on wet deposition and transport in a global three-dimensional chemical tracer model driven by assimilated meteorological fields, J. Geophys. Res., 106, 12 109–12 128, 2001.

Liu, S. C., McAfee, J. R., and Cicerone, R. J.: Radon 222 and Tropospheric Vertical Transport, J. Geophys. Res., 89, 7291–7297, 1984.

Liu, X., Mauersberger, G., and Möller, D.: The effects of cloud processes on the tropospheric photochemistry: an improvement of the EURAD model with a coupled gaseous and aqueous chemical mechanism, Atmos. Environ., 31, 3119–3135, 1997.

Logager, T., Sehested, K., and Holcman, J.: Rate constants of the equilibrium reactions SO_4 + $HNO_3 \rightleftharpoons HSO_4^-$ + NO_3 and SO_4 + $NO_3 \rightleftharpoons SO_4^{2-}$ + NO_3, Radiat. Phys. Chem., 41, 539–543, 1993.

Lohmann, U. and Feichter, J.: Global indirect aerosol effects: a review, Atmos. Chem. Phys., 5, 715–737, 2005.

Lohmann, U. and Roeckner, E.: Design and performance of a new cloud microphysics scheme developed for the ECHAM general circulation model, Climate Dynamics, 12, 557–572, 1996.

Lohmann, U., Feichter, J., Chuang, C. C., and Penner, J. E.: Predicition of the number of cloud droplets in the ECHAM GCM, J. Geophys. Res., 104, 9169–9198, 1999.

Madden, R. A. and Julian, P. R.: Observations of the 40-50-Day Tropical Oscillation - A Review, Mon. Weather Rev., 122, 814–837, 1994.

Madronich, S. and Calvert, J. G.: Permutation reactions of organic peroxy radicals in the troposphere, J. Geophys. Res., 95D, 5697–5715, 1990.

Magi, L., Schweitzer, F., Pallares, C., Cherif, S., , Mirabel, P., and George, C.: Investigation of the uptake rate of ozone and methyl hydroperoxide by water surfaces, J. Phys. Chem. A, 101, 4943–4949, 1997.

Mahowald, N. M., Rasch, P. J., and Prinn, R. G.: Cumulus parameterizations in chemical transport models, J. Geophys. Res., 100, 26 173–26 189, 1995.

Mahowald, N. M., Rasch, P. J., Eaton, B. E., Whittlestome, S., and Prinn, R. G.: Transport of ^{222}radon to the remote troposphere using the Modell of Atmospheric Transport and Chemistry and assimilated winds from ECMWF and the National Center for Environmental Prediction/NCAR, J. Geophys. Res., 102, 28 139–28 151, 1997.

Manabe, S. and Strickler, R. F.: Thermal Equilibrium of the Atmosphere with a Convective Adjustment, J. Atmos. Sci., 21, 361–385, 1964.

Manabe, S., Smagorinsky, J., and Strickler, R. F.: Simulated climatology of a general circulation model with a hydrological cycle, Month. Weather Rev., 93, 769–798, 1965.

Mapes, B. E.: Gregarious Tropical convection, J. Atmos. Sci., 50, 2026–2037, 1993.

Mapes, B. E., Warner, T. T., Xu, M., and Gochis, D. J.: Comparisons of Cumulus Parameterizations and Entrainment using Domain-Mean Wind Divergence in a regional model, J. Atmos. Sci., 61, 1284–1295, 2004.

Mari, C., Jacob, D. J., and Bechtold, P.: Transport and scavenging of soluble gases in a deep convective cloud, J. Geophys. Res., 105, 22 255–22 267, 2000.

Marsh, A. R. W. and McElroy, W. J.: The dissociation constant and Henry's law constant of HCl in aqueous solution, Atmos. Environ., 19, 1075–1080, 1985.

Martin, L. R. and Damschen, D. E.: Aqueous oxidation of sulfur dioxide by hydrogen peroxide at low pH, Atmos. Environ., 15, 1615–1621, 1981.

Martinsson, B. G., Frank, G., Cederfelt, S.-I., Swietlicki, E., Berg, O. H., Zhou, J., Bower, K. N., Bradbury, C., Birmili, W., Stratmann, F., Wendisch, M., Wiedensohler, A., and Yuskiewicz, B. A.: Droplet nucleation and growth in orographic clouds in relation to the aerosol population, Atmos. Res., 50, 289–315, 1999.

Mason, J. B.: The Physics of Clouds, Oxford University Press, 1971.

Matthijsen, J., Builtjes, P. J. H., Meijer, E. W., and Boersen, G.: Modelling cloud effects on ozone on a regional scale: a case study, Atmos. Environ., 31, 3227–3238, 1997.

Mauzerall, D. L., Sultan, B., Kim, N., and Bradford, D. F.: NO_x emissions from large point sources: variability in ozone production, resulting health damages and economic costs, Atmos. Environ., 39, 2851–2866, 2005.

McCabe, D. C., Gierczak, T., Talukdar, R. K., and Ravishankara, A. R.: Kinetics of the reaction OH + CO under atmospheric conditions, Geophys. Res. Lett., 28, 3135–3138, 2001.

Monahan, E. C.: The Ocean as a Source for Atmospheric Particles, in: The Role of Air-Sea Exchange in Geochemical Cycling, edited by Buat-Menard, P., pp. 129–163, D. Reidel Publishing Company, 1986.

Monod, A. and Carlier, P.: Impact of clouds on the tropospheric ozone budget: Direct effect of multiphase photochemistry of soluble organic compounds, Atmos. Environ., 33, 4431–4446, 1999.

Moore, H. E., Poet, S. E., and Martell, E. A.: ^{222}Rn, ^{210}Pb, ^{210}Bi and ^{210}Po Profiles and Aerosol residence Times versus Altitude, J. Geophys. Res., 78, 7065–7075, 1973.

Mullendore, G. L., Durran, D. R., and Holton, J. R.: Cross-Tropopause tracer transport in midlatitude convection, J. Geophys. Res., 110, D06 113, doi:10.1029/2004JD005059, 2005.

Müller, J.-F. and Brasseur, G.: IMAGES: A three-dimensional chemical transport model of the global troposphere, J. Geophys. Res., 100D, 16 445–16 490, 1995.

Naveau, P. and Moncrieff, M. W.: A probabilistic description of convective mass fluxes and its relationship to extreme-value theory, Q. J. R. Meteorol. Soc., 129, 2217–2232, 2003.

Neeb, P., Horie, O., and Moortgat, G. K.: The ethene-ozone reaction in the gas phase, J. Phys. Chem. A, 102, 6778–6785, 1998.

Nober, F. J. and Graf, H. F.: A new convective cloud field model based on principles of self-organisation, Atmos. Chem. Phys., 5, 2749–2759, 2005.

Noël, S., Buchwitz, M., Bovensmann, H., Hoogen, R., and Burrows, J. P.: Atmospheric Water Vapor Amounts Retrieved from GOME Satellite Data, Geophys. Res. Lett., 26, 1841–1844, 1999.

Nordeng, T. E.: Extended versions of the convective parametrization scheme at ECMWF and their impact on the mean and transient activity of the model in the tropics, Tech. Rep. 206, ECWMF, 1994.

Olivié, D.: On the Role of Convection and Turbulence for Tropospheric Ozone and its Precursors, Ph.D. thesis, Technische Universiteit Eindhoven, 2005.

Orlando, J. J., Tyndall, G. S., Bertman, S. B., Chen, W., and Burkholder, J. B.: Rate coefficient for the reaction of OH with CH_2=C(CH_3)C(O)OONO_2 (MPAN), Atmos. Environ., 36, 1895–1900, 2002.

Pickering, K. E., Wang, Y., Tao, W.-K., Price, C., and Müller, J.-F.: Vertical distribution of lightning NO_x for use in regional and chemical transport models, J. Geophys. Res., 103, 31 203–31 216, 1998.

Ponche, J. L., George, C., and Mirabel, P.: Mass transfer at the air/water interface: Mass accommodation coefficients of SO_2, HNO_3, NO_2 and NH_3, J. Atmos. Chem., 16, 1–21, 1993.

Pöschl, U., Canagaratna, M., Jayne, J. T., Molina, L. T., Worsnop, D. R., Kolb, C. E., and Molina, M. J.: Mass accommodation coefficient of H_2SO_4 vapor on aqueous sulfuric acid surfaces and gaseous diffusion coefficient of H_2SO_4 in N_2/H_2O, J. Phys. Chem. A, 102, 10 082–10 089, 1998.

Pöschl, U., von Kuhlmann, R., Poisson, N., and Crutzen, P. J.: Development and intercomparison of condensed isoprene oxidation mechanisms for global atmospheric modeling, J. Atmos. Chem., 37, 29–52, 2000.

Pressyanov, D. S.: Short solution of the radioactive decay chain equations, Am. J. Phys., 70, 444–445, 2002.

Price, C. and Rind, D.: A simple Lightning Parametrization for Calculating Global Lightning Distributions, J. Geophys. Res., 97, 9919–9933, 1992.

Price, C. and Rind, D.: Modeling Global Lightning Distributions in a General Circulation Model, Mon. Weather Rev., 122, 1930–1939, 1994.

Price, C., Penner, J., and Prather, M.: NO_x from lightning, 1. Global distribution based on lightning physics, J. Geophys. Res., 102, 5929–5941, 1997.

Pruppacher, H. R. and Klett, J. D.: Microphysics of Clouds and Precipitation, Kluwer Academic Publishers, 2000.

Ramanathan, V., Crutzen, P. J., Kiehl, J. T., and Rosenfeld, D.: Aerosols, Climate and the Hydrological Cycle, Science, 294, 2119–2124, 2001.

Randall, D., Khairoutdinov, M., Arakawa, A., and Grabowski, W.: Breaking the cloud parameterization deadlock, Bullet. Amer. Meteor. Soc., 84, 1547–1564, 2003.

Rasch, P. J., Mahowald, N. M., and Eaton, B. E.: Representations of transport, convection and the hydrologic cycle in chemical transport models: Implications for the modeling of short-lived and soluble species, J. Geophys. Res., 102, 28 127–28 138, 1997.

Rasch, P. J., Feichter, J., Law, K., Mahowald, N., Penner, J., Benkovitz, C., Genthon, C., Giannakopoulos, C., Kasibhatla, P., Koch, D., Levy, H., Maki, T., Prather, M., roberts, D. L., Roelofs, G.-J., Stevenson, D., Stockwell, Z., Taguchi, S., Kritz, M., Chipperfield, M., Baldocchi, D., McMurry, P., Barrie, L., Balkanski, Y., Chatfield, R., Kjellström, E., Lawrence, M., Lee,

H. N., Lelieveld, J., Noone, K. J., Seinfeld, J., Stenchikov, G., Schwartz, S., Walcek, C., and Williamson, D.: A comparison of scavenging and deposition processes in global models: results from the WCRP Cambridge Workshop of 1995, Tellus, 52B, 1025–1056, 2000.

Régimbal, J.-M. and Mozurkewich, M.: Peroxynitric acid decay mechanisms and kinetics at low pH, J. Phys. Chem. A, 101, 8822–8829, 1997.

Respondek, P. S., Flossmann, A. I., Alheit, R. R., and Pruppacher, H. R.: A theoretical Study of the Wet Removal of Atmospheric Pollutants. Part V: The Uptake, Redistribution, and Deposition of $(NH_4)_2SO_4$ Particles by a Convective Cloud Containing Ice, J. Atmos. Sci., 52, 2121–2132, 1995.

Ridley, B. A., Dye, J. E., Walega, J. G., Zheng, J., Grahek, F. E., and Rison, W.: On the production of active nitrogen by thunderstorms over New Mexico, J. Geophys. Res., 101, 20 985–21 005, 1996.

Riedel, E.: Anorganische Chemie, de Gruyter, 1999.

Roeckner, E., Bäuml, G., Bonaventura, L., Brokopf, R., Esch, M., Giorgetta, M., Hagemann, S., Kirchner, I., Kornblue, L., Manzini, E., Rhodin, A., Schleese, U., Schulzweida, U., and Tompkins, A.: The atmospheric general circulation model ECHAM5: Part 1, Tech. Rep. 349, Max-Planck-Institut für Meteorologie, 2003.

Roeckner, E., Brokopf, R., Esch, M., Giorgetta, M., Hagemann, S., Kornblue, L., Manzini, E., Schleese, U., and Schulzweida, U.: The atmospheric general circulation model ECHAM5: Part 2, Tech. Rep. 354, Max-Planck-Institut für Meteorologie, 2004.

Roelofs, G.-J. and Lelieveld, J.: Distribution and budget of O_3 in the troposphere calculated with a chemistry general circulation model, J. Geophys. Res., 100, 20 983–20 998, 1995.

Roelofs, G.-J. and Lelieveld, J.: Model study of the influence of cross-tropopause O_3 transports of tropospheric O_3 levels, Tellus, 49B, 38–55, 1997.

Ross, A. B., Mallard, W. G., Helman, W. P., Bielski, B. H. J., Buxton, G. V., Cabelli, D. E., Greenstock, C. L., Huie, R. E., and Neta, P.: NDRL-NIST Solution Kinetics Database: - Ver. 1, National Institute of Standards and Technology, Gaithersburg, MD, 1992.

Rudich, Y., Talukdar, R. K., Imamura, T., Fox, R. W., and Ravishankara, A. R.: Uptake of NO_3 on KI solutions: Rate coefficient for the $NO_3 + I^-$ reaction and gas-phase diffusion coefficients for NO_3, Chem. Phys. Lett., 261, 467–473, 1996.

Ruggaber, A., Dlugi, R., Bott, A., Forkel, R., Herrmann, H., and Jacobi, H.-W.: Modelling of radiation quantities and photolysis frequencies in the aqueous phase in the troposphere, Atmos. Environ., 31, 3137–3150, 1997.

Salzmann, M.: Influences of deeep convective cloud systems on tropospheric trace gases and photochemistry over the tropical West Pacific: A modeling case study, Ph.D. thesis, Johannes Gutenberg-Universität Mainz, Germany, 2005.

Sanak, J., Gaudry, A., and Lambert, G.: Size distribution of ^{210}Pb aerosols over the ocean, Geophys. Res. Lett., 8, 1067–1069, 1981.

Sander, R.: Modeling atmospheric chemistry: Interactions between gas-phase species and liquid cloud/aerosol particles, Surv. Geophys., 20, 1–31, 1999.

Sander, R., Kerkweg, A., Jöckel, P., and Lelieveld, J.: Technical Note: The new comprehensive atmospheric chemistry module MECCA, Atmos. Chem. Phys., 5, 445–450, 2005.

Sander, S. P., Friedl, R. R., DeMore, W. B., Golden, D. M., Kurylo, M. J., Hampson, R. F., Huie, R. E., Moortgat, G. K., Ravishankara, A. R., Kolb, C. E., and Molina, M. J.: Chemical kinetics and photochemical data for use in stratospheric modeling. Supplement to evaluation 12: Update of key reactions. Evaluation number 13, JPL Publication 00-3, Jet Propulsion Laboratory, Pasadena, CA, `http://jpldataeval.jpl.nasa.gov/`, 2000.

Sander, S. P., Finlayson-Pitts, B. J., Friedl, R. R., Golden, D. M., Huie, R. E., Kolb, C. E., Kurylo, M. J., Molina, M. J., Moortgat, G. K., Orkin, V. L., and Ravishankara, A. R.: Chemical Kinetics and Photochemical Data for Use in Atmospheric Studies, Evaluation Number 14, JPL Publication 02-25, Jet Propulsion Laboratory, Pasadena, CA, 2003.

Sandu, A. and Sander, R.: Technical Note: Simulating chemical systems in Fortran90 and Matlab with the Kinetic PreProcessor KPP-2.1, Atmos. Chem. Phys. Discuss., 5, 8689–8714, 2005.

Sandu, A., Verwer, J. G., Blom, J. G., Spee, E. J., Carmichael, G. R., and Potra, F. A.: Benchmarking stiff ODE solvers for atmospheric chemistry problems II: Rosenbrock solvers, Atmos. Environ., 31, 3459–3472, 1997a.

Sandu, A., Verwer, J. G., Loon, M. V., Carmichael, G. R., Potra, F. A., Dabdub, D., and Seinfeld, J. H.: Benchmarking stiff ODE solvers for atmospheric chemistry problems–I. implicit vs explicit, Atmos. Environ., 31, 3151–3166, 1997b.

Schery, S. D. and Wasiolek, M. A.: Modeling radon flux from the earth's surface, in: Radon and Thoron in the Human Environment, Proceedings of the 7th Tohwa University International Symposium, edited by Katase and Shimo, World Scientific, Singapore, 1998.

Schmitt, A. and Brunner, B.: Emissions from aviation and their development over time, in: Pollutants from air traffic - results of atmospheric research 1992-1997. Final Report on the BMBF Verbundprogramm "Schadstoffe in der Luftfahrt", Tech. report, DLR - Mitteilung 97-04, pp. 1–301, 1997.

Schwartz, S. E.: Mass-transport considerations pertinent to aqueous phase reactions of gases in liquid-water clouds, in: Chemistry of Multiphase Atmospheric Systems, NATO ASI Series, Vol. G6, edited by Jaeschke, W., pp. 415–471, Springer Verlag, Berlin, 1986.

Schwartz, S. E. and White, W. H.: Solubility equilibria of the nitrogen oxides and oxyacids in dilute aqueous solution, in: Advances in Environmental Science and Engineering, edited by Pfafflin, J. R. and Ziegler, E. N., vol. 4, pp. 1–45, Gordon and Breach Science Publishers, NY, 1981.

Schweitzer, F., Mirabel, P., and George, C.: Uptake of hydrogen halides by water droplets, J. Phys. Chem. A, 104, 72–76, 2000.

Sehested, K., Rasmussen, O. L., and Fricke, H.: Rate constants of OH with HO_2, O_2^-, and $H_2O_2^+$ from hydrogen peroxide formation in pulse-irradiated oxygenated water, J. Phys. Chem., 72, 626–631, 1968.

Sehested, K., Holcman, J., and Hart, E. J.: Rate constants and products of the reactions of e_{aq}^-, O_2^- and H with ozone in aqueous solutions, J. Phys. Chem., 87, 1951–1954, 1983.

Seinfeld, J. H. and Pandis, S. N.: Atmospheric Chemistry and Physics, John Wiley & Sons, 1998.

Siqueira, J. R. and Machado, L. A. T.: Influence of the Frontal Systems on the Day-to-Day Convection Variability over South America, J. Clim., 17, 1754–1766, 2004.

Sivakumaran, V., Hölscher, D., Dillon, T. J., and Crowley, J. N.: Reaction between OH and HCHO: temperature dependent rate coefficients (202-399 K) and product pathways (298 K), Phys. Chem. Chem. Phys., 5, 4821–4827, 2003.

Slinn, S. A. and Slinn, W. G. N.: Predictions for particle deposition on natural waters, Atmos. Environ., 14, 1013–1016, 1980.

Slinn, W. G. N.: Atmospheric Sciences and Power Production - 1979, chap. 11, Precipitation Scavenging, U.S. Department of Energy, Washington, D.C., 1983.

Snider, J. R. and Dawson, G. A.: Tropospheric light alcohols, carbonyls, and acetonitrile: Concentrations in the southwestern United States and Henry's law data, J. Geophys. Res., 90D, 3797–3805, 1985.

Sprengnether, M., Demerjian, K. L., Donahue, N. M., and Anderson, J. G.: Product analysis of the OH oxidation of isoprene and 1,3-butadiene in the presence of NO, J. Geophys. Res., 107D, doi:10.1029/2001JD000716, 2002.

Steil, B., Dameris, M., Brühl, C., Crutzen, P. J., Grewe, V., Ponater, M., and Sausen, R.: Development of a chemistry module for GCMs: first results of a multiannual integration, Ann. Geophys., 16, 205–228, 1998.

Stensrud, D. J. and Anderson, J. L.: Is Midlatitude Convection an Active or a Passive Player in Producing Global Circulation Patterns, J. Clim., 14, 2222–2237, 2001.

Stevenson, D. S., Johnson, C. E., Collins, W. J., Derwent, R. G., Shine, K. P., and Edwards, J. M.: Evolution of tropspheric ozone radiative forcing, Geophys. Res. Lett., 25, 3819–3822, 1998.

Stier, P., Feichter, J., Kinne, S., Kloster, S., Vignati, E., Wilson, J., Ganzeveld, L., Tegen, I., Werner, M., Balkanski, Y., Schulz, M., and Boucher, O.: The Aerosol-Climate Model ECHAM5-HAM, Atmos. Chem. Phys., 5, 1125–1156, 2005.

Stimpfle, R. M., Wilmouth, D. M., Salawitch, R. J., and Anderson, J. G.: First measurements of ClOOCl in the stratosphere: The coupling of ClOOCl and ClO in the Arctic polar vortex, J. Geophys. Res., 109, doi:10.1029/2003JD003811, 2004.

Stockwell, D. Z., Kritz, M. A., Chipperfield, M. P., and Pyle, J. A.: Validation of an off-line three-dimensional chemical transport model using observed radon profiles: 2. Model results, J. Geophys. Res., 103, 8433–8445, 1998.

Stockwell, D. Z., Giannakopoulos, C., Plantevin, P.-H., Carver, G. D., Chipperfield, M. P., Law, K. S., Pyle, J. A., Shallcross, D. E., and Wang, K.-Y.: Modelling NO_x from lightning and its impact on global chemical fields, Atmos. Environ., 33, 4477–4493, 1999.

Sun, Y., Zuhang, G., Wang, Y., Zaho, X., Li, J., Wang, Z., and An, Z.: Chemical composition of dust storms in Beijing and implications for the mixing of mineral aerosol with pollution aerosol on the pathway, J. Geophys. Res., 110, D24 209, doi:10.1029/2005JD006054, 2005.

Svenningsson, B., Hansson, H.-C., Martinsson, B., Wiedensohler, A., Swietlicki, E., Cederfelt, S.-I., Wendisch, M., Bower, K. N., Choularton, T. W., and Colvile, R. N.: Cloud droplet nucleation scavenging in relation to the size and hygroscopic behaviour of aerosol particles, Atmos. Environ., 31, 2463–2475, 1997.

Takami, A., Kato, S., Shimono, A., and Koda, S.: Uptake coefficient of OH radical on aqueous surface, Chem. Phys., 231, 215–227, 1998.

Taylor, K. E.: Summarizing multiple aspects of model preformance in a single diagram, J. Geophys. Res., 106, 7183–7192, 2001.

Thomas, K., Volz-Thomas, A., and Kley, D.: Zur Wechselwirkung von NO_3-Radikalen mit wässrigen Lösungen: Bestimmung des Henry- und des Massenakkomodationskoeffizienten, Ph.D. thesis, Institut für Chemie und Dynamik der Geosphäre 2, Forschungszentrum Jülich GmbH, FRG, 1993.

Thomas, R. J., Krehbiel, P. R., Rison, W., Hamlin, T., Boccippio, D. J., Goodman, S. J., and Christian, H. J.: Comparison of ground-based 3-dimensional lightning mapping observations with satellite-based LIS observations in Oklahoma, Geophys. Res. Lett., 27, 1703–1706, 2000.

Tie, X., Zhang, R., Brasseur, G., Emmons, L., and Lei, W.: Effects of lightning on reactive nitrogen and nitrogen reservoir species in the troposphere, J. Geophys. Res., 106, 3167–3178, 2001.

Tiedtke, M.: A Comprehensive Mass Flux Scheme for Cumulus Parametrization in Large-Scale Models, Mon. Weather Rev., 117, 1779–1800, 1989.

Tompkins, A. M.: A prognostic parameterization for the subgrid-scale variability of water vapor and clouds in large-scale models and its use to diagnose cloud cover, J. Atmos. Sci., 59, 1917–1942, 2002.

Tompkins, A. M., Bechtold, P., Beljaars, A. C. M., Benedetti, A., Cheinet, S., Janiskova, M., Köhler, M., Lopez, P., and Morcrette, J.-J.: Moist physical processes in the IFS: Progress and Plans, Tech. Rep. 452, ECWMF, 2004.

Tost, H., Jöckel, P., Kerkweg, A., Sander, R., and Lelieveld, J.: Technical Note: A new comprehensive SCAVenging submodel for global atmospheric chemistry modelling, Atmos. Chem. Phys., 6, 565–574, 2006.

Trenberth, K. E. and Stepaniak, D. P.: Seamless Poleward Atmospheric Energy Transport and Implications for the Hadley Circulation, J. Clim., 16, 3706–3722, 2003.

Tyndall, G. S., Staffelbach, T. A., Orlando, J. J., and Calvert, J. G.: Rate coefficients for the reactions of OH radicals with methylglyoxal and acetaldehyde, Int. J. Chem. Kinetics, 27, 1009–1020, 1995.

Tyndall, G. S., Cox, R. A., Granier, C., Lesclaux, R., Moortgat, G. K., Pilling, M. J., Ravishankara, A. R., and Wallington, T. J.: The atmospheric chemistry of small organic peroxy radicals, J. Geophys. Res., 106D, 12 157–12 182, 2001.

van Aalst, M.: Dynamics and Transport in the Stratosphere: Simulations with a General Circulation Model, Ph.D. thesis, Universiteit Utrecht, 2005.

Vehmakäki, H., Kulmala, M., Napario, I., Lehtinen, K. E. J., Timmreck, C., Noppel, M., and Laaksonen, A.: An improved parametrization for sulfuric acid-water nucleation rates for tropospheric and stratospheric conditions, J. Geophys. Res., 107, 4622, doi:10.1029/2002JD002184, 2002.

Vignati, E., Wilson, J., and Stier, P.: M7: An efficient size-resolved aerosol microphysics module for large-scale aerosol transport models, J. Geophys. Res., 109, D22 202, doi:10.1029/2003JD004485, 2004.

Villenave, E. and Lesclaux, R.: Kinetics of the cross reactions of CH_3O_2 and $C_2H_5O_2$ radicals with selected peroxy radicals, J. Phys. Chem., 100, 14 372–14 382, 1996.

Vogt, R., Crutzen, P. J., and Sander, R.: A mechanism for halogen release from sea-salt aerosol in the remote marine boundary layer, Nature, 383, 327–330, 1996.

von Glasow, R., Sander, R., Bott, A., and Crutzen, P. J.: Modeling halogen chemistry in the marine boundary layer. 1. Cloud-free MBL, J. Geophys. Res., 107, 4341, doi:10.1029/2002JD000942, 2002a.

von Glasow, R., Sander, R., Bott, A., and Crutzen, P. J.: Modeling halogen chemistry in the marine boundary layer. 2. Interactions with sulfur and the cloud-covered MBL, J. Geophys. Res., 107, 4323, doi:10.1029/2002JD000943, 2002b.

von Kuhlmann, R.: Tropospheric photochemistry of ozone, its precursors and the hydroxyl radical: A 3D-modeling study considering non-methane hydrocarbons, Ph.D. thesis, Johannes Gutenberg-Universität, Mainz, Germany, 2001.

von Kuhlmann, R., Lawrence, M. G., and Crutzen, P. J.: A model for studies of tropospheric ozone and nonmethane hydrocarbons: Model description and ozone results, J. Geophys. Res., 108, 4294, doi:10.1029/2002JD002893, 2003.

Wang, C. and Chang, J. S.: A Three-Dimensional Numerical Model of Cloud Dynamics, Microphysics and Chemistry: 3. Redistribution of Pollutants, J. Geophys. Res., 98, 16 787–16 798, 1993a.

Wang, C. and Chang, J. S.: A Three-Dimensional Numerical Model of Cloud Dynamics, Microphysics and Chemistry: 4. Cloud and Precipitation Chemistry, J. Geophys. Res., 98, 16 799–16 808, 1993b.

Wang, C. and Crutzen, P. J.: Impact of a simulated severe local storm on the redistribution of sulfur dioxide, J. Geophys. Res., 100, 11 357–11 367, 1995.

Warneck, P.: The relative importance of various pathways for the oxidation of sulfur dioxide and nitrogen dioxide in sunlit continental fair weather clouds, Phys. Chem. Chem. Phys., 1, 5471–5483, 1999.

Warner, J.: On Steady-State One-Dimensional Models of Cumulus Convection, J. Atmos. Sci., 27, 1035–1040, 1970.

Weast, R. C., ed.: CRC Handbook of Chemistry and Physics, 61st Edition, CRC Press, Inc., Boca Raton, FL, 1980.

Weinstein-Lloyd, J. and Schwartz, S. E.: Low-intensity radiolysis study of free-radical reactions in cloudwater: H_2O_2 production and destruction, Environ. Sci. Technol., 25, 791–800, 1991.

Wentz, F. J.: A well-calibtrated ocean algorithm for special sensor microwave/imager, J. Geophys. Res., 102, 8703–8718, 1997.

Wilcox, E. M.: Spatial and Temporal Scales of Precipitation Tropical Cloud Systems in Satellite Imagery and the NCAR CCM3, J. Clim., 16, 3545–3559, 2003.

Wilhelm, E., Battino, R., and Wilcock, R. J.: Low-pressure solubility of gases in liquid water, Chem. Rev., 77, 219–262, 1977.

Wilkins, E. T.: Air pollution aspects of the London fog of December 1952 - Discussion, Q. J. R. Meteorol. Soc., 80, 267–271, 1954.

Wilks, D. S.: Statistical Methods in the Atmospheric Sciences, Elsevier, Academic Press, 2005.

Wilson, J., Cuvelier, C., and Raes, F.: A modelling study of global mixed aerosol fields, J. Geophys. Res., 106, 34 081–34 108, 2001.

Wine, P. H., Tang, Y., Thorn, R. P., Wells, J. R., and Davis, D. D.: Kinetics of aqueous phase reactions of the SO_4^- radical with potential importance in cloud chemistry, J. Geophys. Res., 94D, 1085–1094, 1989.

Wingenter, O. W., Sive, B. C., Blake, N. J., and Rowland, F. S.: Atomic chlorine concentrations determined from ethane and hydroxyl measurements made over the Central Pacific Ocean, Eos, Trans. AGU (Abstract Supplement), 80/46, F149–F150, 1999.

Worsnop, D. R., Zahniser, M. S., Kolb, C. E., Gardner, J. A., Watson, L. R., van Doren, J. M., Jayne, J. T., and Davidovits, P.: The temperature dependence of mass accommodation of SO_2 and H_2O_2 on aqueous surfaces, J. Phys. Chem., 93, 1159–1172, 1989.

Xie, P. and Arkin, P.: Global Precipitation: A 17-year Monthly Analysis Based on Gauge Observations, Satellite Estimates and Numerical Model Outputs, Bullet. Amer. Meteor. Soc., 78, 2539–2558, 1997.

Xie, S., Xu, K., Cederwall, R. T., Bechtold, P., Del Genio, A. D., Klein, S. A., Cripe, D. G., Ghan, S. J., Gregory, D., Iacobellis, S. F., Krueger, S. K., Lohmann, U., Petch, J. C., Randall, D. A., Rotstayn, L. D., Somerville, R. C. J., Sud, Y. C., von Salzen, K., Walker, G. K., Wolf, A., Yio, J. J., Zhang, G. J., and Zhang, M.: Intercomparison and evaluation of cumulus parameterizations under summertime midlatitude continental conditions, Q. J. R. Meteorol. Soc., 128, 1095–1135, 2002.

Yanai, M., Esbensen, S., and Chu, J.-H.: Determination of Bulk Properties of Tropical Cloud Clusters from Large-Scale Heat and Moisture Budgets, J. Atmos. Sci., 30, 611–627, 1973.

Yano, J.-I., Guichard, F., Lafore, J.-P., Redelsperger, J.-L., and Bechtold, P.: Estimations of Mass Fluxes for Cumulus Parameterizations from High-Resolution Spatial Data, J. Atmos. Sci., 61, 829–842, 2004.

Yin, F., Grosjean, D., and Seinfeld, J. H.: Photooxidation of dimethyl sulfide and dimethyl disulfide. I: Mechanism development, J. Atmos. Chem., 11, 309–364, 1990.

Yin, Y., Parker, D. J., and Carslaw, K. S.: Simulation of trace gas redistribution by convective clouds - Liquid phase processes, Atmos. Chem. Phys., 1, 19–36, 2001.

Yu, S., Kasibhatla, P. S., Wright, D. L., Schwartz, S. E., McGraw, R., and Deng, A.: Moment-based simulation of microphysical properties of sulfate aerosols in the eastern United States: Model description, evaluation, and regional analysis, J. Geophys. Res., 108, 4353, doi:10.1029/2002JD002890, 2003.

Zaucker, F., Daum, P. H., Wetterauer, U., Berkowitz, C., Kromer, B., and Broecker, W. S.: Atmospheric ^{222}Rn measurements during the 1993 NARE Intensive, J. Geophys. Res., 101, 29 149–29 164, 1996.

Zaveri, R. A. and Peters, L. K.: A new lumped structure photochemical mechanism for large-scale applications, J. Geophys. Res., 104D, 30 387–30 415, 1999.

Zhang, G. J. and McFarlane, N. A.: Sensitivity of Climate Simulations to the Parameterization of Cumulus Convection in the Canadian Climate Centre General Circulation Model, Atmosphere-Ocean, 33, 407–446, 1995.

Zhou, X. and Mopper, K.: Apparent partition coefficients of 15 carbonyl compounds between air and seawater and between air and freshwater; Implications for air-sea exchange, Environ. Sci. Technol., 24, 1864–1869, 1990.

Acknowledgements

First of all I want to thank my supervisor Prof. Jos Lelieveld for incorporating me into the working group of atmospheric modelling and the freedom he gave me about choosing research topics of my interest for this thesis work. Additional thanks to him and his wife Tineke for the nice PhD program they set up within this institute.
Secondly, I am grateful to Prof. Andreas Bott, my second supervisor, for his helpful comments and the opportunity to do my PhD at the University of Bonn.
Very special thanks go to Dr. Patrick Jöckel for the 'day-to-day' advision. Whenever, I ran into problems it was good to know, that you are there and always willing to give a helping hand. Furthermore, I like to thank you for stepping in as my official 'day-to-day' advisor, after you did the job anyway and for letting me take part in the realisation of your MESSy idea.
Thanks to Dr. Astrid Kerkweg for the sharing of thoughts and ideas, testing and applying my code and all the fruitful hints.
Dr. Rolf Sander has been helping out to increase my, at the beginning very limited, knowledge of atmospheric chemistry and I thank you for the discussion and advision time you wasted on me.
I thank Dr. Mark Lawrence, my present group leader, for his shared interested and help in my research topics and the useful advices and code contribution for the convective transport part.
Thanks to Andrea Pozzer for his help with the visualisation of the vertical profiles of measurements and model results.
Special acknowledegements got the computer people at the institute, most of all Klaus Egenolf, who were mostly helpful in the technical problems occuring in computer work.
Thanks go also to the rest of the MESSy-Team for their comments and for testing my computer code developments.
I like to thank my previous and actual roommates Sandra, Sarah, Domenico, Meryem, Michael and Joachim for the nice atmosphere in our office, reaching beyond the world of modelling and science.
Furthermore all colleagues at MPI made this institute a nice place to work in pleasant company.

Special thanks go to my parents for the opportunities, they gave me, their support and advice, the freedom of my own decisions and all further things without I would not have been able to make it.
Thanks also to my friends, especially Linda, for their support and encouragement, but even more for the world beyond science and for caring about me.....

Additionally, I would like to thank the people, that provided me with measurement data to perform proper comparison of my model output with observations. Therefore many thanks go to Rüdiger Lang for the monthly GPCP and water vapour column data, to Frank Dentener for the wet deposition data and to Dirk Olivié for the Radon profiles. Furthermore, I acknowledge the work of people that compiled some of the data sets, but I did not get to know personally, yet: the trace gas vertical profiles originate from the work of L. Emmons and co-workers, and the lightning observation data were produced by the NASA LIS/OTD Science Team with H. J. Christian as pricincipal investigator.